

**UNIVERSIDAD COMPLUTENSE DE MADRID**  
**FACULTAD DE CIENCIAS QUÍMICAS**  
Departamento de Química Inorgánica



**TESIS DOCTORAL**

**Materiales compuestos basados en carbono  
desordenado como electrodos en supercondensadores**

**Composite materials based on disordered carbon as  
supercapacitor electrodes**

MEMORIA PARA OPTAR AL GRADO DE DOCTOR

PRESENTADA POR

**Daniel Arenas Esteban**

Directores

**David Ávila Brande**  
**L. Carlos Otero Díaz**

Madrid  
Ed. electrónica 2019

Universidad Complutense de Madrid  
Facultad de Ciencias Químicas  
Departamento de Química Inorgánica



**Materiales compuestos basados en carbono desordenado  
como electrodos en supercondensadores**

---

**Composite materials based on disordered carbon as  
supercapacitor electrodes**

Daniel Arenas Esteban

Tesis Doctoral

---

Directores:  
David Ávila Brande  
L. Carlos Otero Díaz







UNIVERSIDAD  
COMPLUTENSE  
MADRID

**DECLARACIÓN DE AUTORÍA Y ORIGINALIDAD DE LA TESIS  
PRESENTADA PARA OBTENER EL TÍTULO DE DOCTOR**

D./Dña. Daniel Arenas Esteban,  
estudiante en el Programa de Doctorado Química Avanzada,  
de la Facultad de Ciencias Químicas de la Universidad Complutense de  
Madrid, como autor/a de la tesis presentada para la obtención del título de Doctor y  
titulada:

Materiales compuestos basados en carbono desordenado como electrodos en supercondensadores.  
Composite materials based on disordered carbon as supercapacitor electrodes.

y dirigida por: \_\_\_\_\_  
David Ávila Brande  
L. Carlos Otero Díaz

**DECLARO QUE:**

La tesis es una obra original que no infringe los derechos de propiedad intelectual ni los derechos de propiedad industrial u otros, de acuerdo con el ordenamiento jurídico vigente, en particular, la Ley de Propiedad Intelectual (R.D. legislativo 1/1996, de 12 de abril, por el que se aprueba el texto refundido de la Ley de Propiedad Intelectual, modificado por la Ley 2/2019, de 1 de marzo, regularizando, aclarando y armonizando las disposiciones legales vigentes sobre la materia), en particular, las disposiciones referidas al derecho de cita.

Del mismo modo, asumo frente a la Universidad cualquier responsabilidad que pudiera derivarse de la autoría o falta de originalidad del contenido de la tesis presentada de conformidad con el ordenamiento jurídico vigente.

En Madrid, a 7 de abril de 2019

Fdo.:

Esta DECLARACIÓN DE AUTORÍA Y ORIGINALIDAD debe ser insertada en  
la primera página de la tesis presentada para la obtención del título de Doctor.



# Dedication

*A mi familia*



# Acknowledgements

En primer lugar quiero agradecer a los directores de esta tesis, el Dr. L. Carlos Otero Díaz y el Dr. David Ávila Brande, su dedicación, supervisión y confianza durante todos estos años. Agradecer a Carlos que a pesar de “no haberme esforzado lo suficiente” en la química estructural, confió en mi desde el primer momento; a David su inestimable ayuda, guía y consejo a lo largo de toda la tesis.

Quisiera extender este agradecimiento al Dr. Esteban Urones Garrote, Dr. Adrian Gómez Herrero y Dr. Javier García García por compartir conmigo su conocimiento y experiencia en Microscopía Electrónica, enseñándome junto a mis directores de tesis todo lo que se en este apasionante campo del cual pretendo seguir aprendiendo. Pero también por su amistad y apoyo durante estos años.

Quiero agradecer también a los organismos responsables que han financiado durante estos años la investigación en que se enmarca esta tesis doctoral a través de sus respectivos proyectos, la Comunidad de Madrid (S-2013/MIT-12753), la Universidad Complutense de Madrid (PR26/16-3B-1) y al Ministerio de Economía Industria y Competitividad (MAT2017-84385-R).

Agradecer a todos los miembros del grupo de “Preparación, caracterización y propiedades de sólidos no moleculares” del Departamento de Química Inorgánica por la buena acogida recibida, haciéndome sentir como en casa desde el primer momento. Gracias también por fomentar todo tipo de actividades científicas en las que he tenido la suerte de participar. Me gustaría mencionar especialmente a Elena Mesa, gracias por hacernos a todos la vida más fácil.

Thanks to Dr. Viola I. Birss for giving me the opportunity to spend four months in her research group at the University of Calgary, where I learned how to perform and interpret the electrochemical characterization of the materials studied in this thesis. And of course, thanks to Dr. Beatriz Molero, for making the above possible and for her hospitality.

## ACKNOWLEDGEMENTS

---

Agradecer al Dr. Javier Carretero su valiosa ayuda, permitiéndome afianzar y expandir mis conocimientos electroquímicos. Por su contagiosa pasión por la química y por todas las discusiones y ánimos que me ha ofrecido en la etapa final de la tesis.

Mencionar a todos los compañeros con los que he compartido camino, y que de alguna manera han contribuido a mi historia en la Complutense, compañeras de cuarto: Rebeca, Elena, Maider y Manar; demás "jóvenes" del super grupo: Xabi, Sara, Alvaro, Rafa, Sanju, Dani, Jesus, Irene, Arturo ...; integrantes del NanoLab: Guille, Maria, Vanesa, Pablo, Joao ...; Andrés, por todos los cafés; Irene, particular profesora de inglés; Anita, Raluca y todos los TFGs y TFGMs que han trabajado conmigo (espero que os hayáis divertido) ... y mucha más gente de la facultad y de fuera de ella con la que he tenido la suerte de coincidir...

¡Gracias a todos por el buen recuerdo que me llevo de estos años!

# Index

<b>Acknowledgements</b>	<b>III</b>
<b>Resumen</b>	<b>VII</b>
<b>Summary</b>	<b>XI</b>
<b>Abbreviations</b>	<b>XV</b>
<b>1 Introduction</b>	<b>1</b>
1.1 Energy storage devices . . . . .	3
1.2 Supercapacitors . . . . .	6
1.2.1 Energy storage mechanism on supercapacitors . . . . .	8
1.2.2 Fundamental parameters . . . . .	11
1.3 Carbon Science . . . . .	13
1.3.1 The sp hybridization: Linear carbon chains . . . . .	14
1.3.2 The sp <sup>2</sup> hybridization: Graphene-like carbons . . . . .	16
1.3.3 The sp <sup>3</sup> hybridization: Nano Diamonds . . . . .	22
1.3.4 Carbon materials as electrodes on supercapacitor devices . . . . .	22
1.3.5 Carbon-based composite materials for supercapacitors . . . . .	26
<b>2 Objectives</b>	<b>39</b>
2.1 General objectives: . . . . .	39
2.2 Specific objectives: . . . . .	39
<b>3 Experimental techniques</b>	<b>41</b>
3.1 Electron microscopy . . . . .	41
3.1.1 Scanning Electron Microscopy (SEM) . . . . .	41
3.1.2 Transmission Electron Microscopy (TEM) . . . . .	43
3.2 Adsorption Isotherms . . . . .	47
3.3 Infrared spectroscopy (IR) . . . . .	51
3.4 Electrochemical Characterization . . . . .	53
3.4.1 Cyclic Voltammetry (CV) . . . . .	55



3.4.2	Galvanostatic Cyclic with Potential Limitation (GCPL) . . .	56
3.4.3	Electrochemical Impedance Spectroscopy (EIS) . . . . .	57
<b>4</b>	<b>Organometallic-derived carbon with embedded metal nano-oxide composites as improved electrode materials for supercapacitors</b>	<b>63</b>
4.1	Nickelocene as precursor of microporous organometallic-derived carbon with confined nickel oxide nanoparticles as supercapacitor electrode . . . . .	65
4.2	New electrode material based on $Mn_3O_4$ nanoparticles embedded in organometallic-derived carbon (ODC) . . . . .	80
<b>5</b>	<b>Lignocellulosic-based activated carbons with ingrained metal or metal oxide nanoparticles as composite supercapacitor electrodes</b>	<b>97</b>
5.1	Walnut shell activated carbon with embedded $MnO_x$ nanoparticles composite with enhanced electrochemical properties . . . . .	98
5.2	Bamboo activated carbon with embedded gold nanoparticles composite as supercapacitor electrode with enhanced volumetric capacitance . . . . .	109
<b>6</b>	<b>Carbon-Gold Nanograpes: A novel and tunable electrode nanomaterial for supercapacitor applications</b>	<b>123</b>
6.1	Carbon-Gold Nanograpes . . . . .	124
<b>7</b>	<b>Summary and Conclusions</b>	<b>139</b>
	<b>Appendix I: List of Publications</b>	<b>143</b>
	<b>Appendix II: List of Presentations</b>	<b>145</b>
	<b>Appendix III: CV</b>	<b>147</b>

# Resumen

Los condensadores electroquímicos de doble capa (EDLC), comúnmente denominados supercondensadores, son dispositivos de almacenamiento electroquímico de energía capaces de proporcionar más energía que un condensador común y cargarse o descargarse más rápido que una batería. Hoy en día, este tipo de dispositivos ha atraído un gran interés debido a tener una excelente reversibilidad, una capacidad de ciclado prácticamente ilimitada ( $>1,000,000$  ciclos) y un modo de operación sencillo, ofreciendo soluciones en aplicaciones donde se requiere un aporte instantáneo de energía. Los esfuerzos e investigaciones actuales tienen como objetivo aumentar su densidad de energía sin perder potencia, para obtener nuevos dispositivos que alcancen o incluso superen la densidad de energía de una batería manteniendo las ventajas propias de los supercondensadores.

El principal mecanismo de almacenamiento de energía en estos dispositivos es la capacidad eléctrica o capacitancia, que se basa en la adsorción reversible de iones de electrolitos sobre la superficie de los electrodos formando una doble capa electroquímica. No ocurren reacciones faradaicas y la energía permanece almacenada en cargas agregadas en la superficie del material del electrodo. Por lo tanto, cuanto mayor sea el área superficial del electrodo, más energía se podría almacenar y es por eso que el carbono desordenado microporoso es el material más comúnmente utilizado como material de electrodo y el que se encuentra en los dispositivos comerciales. Por otro lado, los compuestos capaces de interactuar con el electrolito mediante reacciones redox faradaicas de manera rápida y reversible pueden presentar otro mecanismo similar a la capacitancia para almacenar energía, que por similitud se denomina mecanismo de pseudocapacitancia.

En esta tesis, se han diseñado diferentes estrategias sintéticas con el fin de obtener materiales compuestos basados en carbono desordenado con propiedades electroquímicas mejoradas para su uso como electrodos en supercondensadores.

En primer lugar, la extracción selectiva con cloro gaseoso de los centros metálicos de compuestos organometálicos a temperaturas intermedias, seguida de la

conversión hidrotérmal de los intermedios de reacción constituidos por un material compuesto basado en una matriz de carbono desordenado con una dispersión homogénea de nanopartículas de haluro metálico, ha demostrado ser una ruta sintética excelente y directa para la obtención de materiales compuestos basados en carbones nanoporosos con nanopartículas pseudocapacitivas de óxidos metálicos. Utilizando como precursores niqueloceno ( $\text{Ni}(\text{C}_5\text{H}_5)_2$ ) y acetilacetato de manganeso (II) ( $\text{Mn}(\text{C}_5\text{H}_7\text{O}_2)_2$ ) se han obtenido sendos materiales compuestos formados por una matriz porosa de carbono derivado de organometálico (ODC) con una dispersión homogénea de nanopartículas de  $\text{NiO}$  y  $\text{Mn}_3\text{O}_4$  respectivamente en su interior. Los estudios electroquímicos muestran que en estos materiales este mecanismo pseudocapacitivo parece funcionar en sinergia con el mecanismo puramente capacitivo, mejorando la capacidad de almacenamiento de energía total del material compuesto frente al respectivo material de carbono en un 44 % en el caso del compuesto ODC@NiO (pasando de 47 a 85  $\text{F g}^{-1}$ ) y de un 33 % en el compuesto ODC@ $\text{Mn}_3\text{O}_4$  (de 87 a 130  $\text{F g}^{-1}$ ). Adicionalmente, estas nanopartículas otorgan al compuesto una mayor densidad que el respectivo material de carbono, lo que resulta en una mejora de la capacidad volumétrica. Asimismo, la matriz de carbono proporciona estabilidad mecánica a las nanopartículas.

En segundo lugar, habiéndose observado la mejora lograda con la adición de nanopartículas de óxido metálico, se seleccionaron carbones activados a partir de precursores lignocelulósicos como matriz para el desarrollo de nuevos materiales compuestos mediante la adición de nanopartículas de óxido-metálico o metálicas sintetizadas ex situ. Como materiales precursores para los carbones activados se seleccionaron cascara de nuez gallega (*Juglans regia*) y bambú (*Guadua angustifolia*), debido a su alto contenido de carbono en forma de lignina y la elevada área superficial que desarrollan tras activarlos químicamente. En el caso del carbono activado derivado del bambú la incorporación de un 25 % de nanopartículas de oro (AuNPs) pretendía reducir de forma sustancial la resistencia equivalente en serie (ESR), de forma que aunque se sacrifica la capacidad gravimétrica del material pasando de 100 a 73  $\text{F g}^{-1}$  el aumento de densidad que le otorga al material compuesto la inclusión de las AuNPs contribuye la obtención de una alta capacitancia volumétrica (de 29 a 47  $\text{F cm}^{-3}$ ), proporcionando un valor añadido en términos de su utilidad práctica como material de electrodo en dispositivos móviles. En el caso del carbón activado derivado de nueces gallegas, el material compuesto presenta una ESR aproximadamente 4 veces inferior al carbón activado derivado de bambú, por lo que en este caso se pretendía mejorar las propiedades electroquímicas incorporando únicamente un 1 % de nanopartículas de óxido de manganeso. Los resultados obtenidos para el material compuesto proporcionan no solo una mejora de la capacidad de almacenamiento total del material (de 41 a 59  $\text{F cm}^{-3}$ ), com-

pensando la disminución del área superficial con el mecanismo pseudocapacitivo proporcionado por las nanopartículas de óxido de manganeso, sino una disminución de aproximadamente 6 veces la ESR del dispositivo comparado con el material de carbón.

En el último capítulo, se ha sintetizado un nuevo material compuesto denominado Carbon-Gold Nanograpes, formado por nanoesferas de carbono microporoso con un núcleo de varias nanopartículas de oro, combinando una alta densidad con una gran área superficial. Este nuevo material compuesto proporciona una capacitancia volumétrica similar a nanoesferas de carbono análogas que no tienen un núcleo sólido, con la ventaja de ser un material más denso y, por tanto, más adecuado para dispositivos prácticos. Sin embargo, la capacitancia volumétrica de estos materiales disminuye rápidamente a velocidades de carga/descarga rápidas en una solución de 0,5 M  $\text{H}_2\text{SO}_4$ , tal vez debido a problemas de difusión iónica a través de la estructura porosa del material. Al calentar el nanocompuesto más allá del punto de fusión de la nanopartícula de oro, estas funden y pueden fluir fuera de las nanoesferas de carbono, mejorando la conectividad de la estructura microporosa y mejorando la interacción ion-poro y, por lo tanto, su conductividad iónica. De esta forma, los valores de capacitancia gravimétrica y volumétrica aumentaron a  $210 \text{ F g}^{-1}$  y  $114 \text{ F cm}^{-3}$ , respectivamente, en una celda simétrica de dos electrodos usando 0.5 M  $\text{H}_2\text{SO}_4$  como electrolito. Este trabajo demuestra un nuevo concepto para el control de la estructura microporosa en el diseño de nuevos materiales compuestos de carbono de próxima generación.



# Summary

Electrochemical double layer capacitors (EDLC), commonly referred as supercapacitors, are electrochemical energy storage devices that can provide more energy than a common capacitor and deliver or capture it faster than a battery. Nowadays, this type of devices have attracted considerable interest because they have excellent reversibility, practically unlimited cyclability ( $> 1,000,000$  cycles) and a simple operation mode, offering solutions in applications where a rapid energy boost is required. Current efforts and research are aimed at increasing their energy density without losing power, in order to obtain new devices that reach or even surpass the energy density of a battery while simultaneously maintaining the advantages of supercapacitors.

The main energy storage mechanism in such devices is the electrical capacity or capacitance, which is based on the reversible adsorption of electrolyte ions onto the surface of the electrodes, forming an electrochemical double layer. There is no faradaic reaction and the energy remains stored in aggregated charges at the surface of the electrode material. Therefore, the higher the surface area, the more energy could be stored, and that's why microporous disordered carbon materials are the most commonly used electrodes and the one found in commercial devices. On the other hand, compounds able to interact with the electrolyte by quick and reversible faradaic redox reactions can present a similar behavior for energy storage, which by similarity is called pseudocapacitance mechanism.

In this thesis, different synthetic strategies have been designed in order to obtain composite materials based on disordered carbon with improved electrochemical properties for use as electrodes in supercapacitors.

In first place, the selective metal extraction with gaseous chlorine of the organometallic compounds metal centers at intermediate temperatures, followed by the hydrothermal conversion of the by-product reaction intermediates constituted by a composite material based on a disordered carbon matrix with a homogeneous dispersion of nanoparticles of metal halide, has proved to be an excellent and straight-

forward synthetic route for the direct obtention of composite materials based on nanoporous carbons with pseudo-capacitive metal oxides nanoparticles. Using Niquelocene ( $\text{Ni}(\text{C}_5\text{H}_5)_2$ ) and Manganese (II) acetylacetonate ( $\text{Mn}(\text{C}_5\text{H}_7\text{O}_2)_2$ ) as precursors, composite materials formed by a porous organometallic derived carbon (ODC) with a homogeneous dispersion of NiO and  $\text{Mn}_3\text{O}_4$  nanoparticles respectively embedded were obtained. Electrochemical studies show that in these materials, this pseudo-capacitive mechanism seems to work in synergy with the pure capacitance mechanism, improving the total energy storage capacity of the composite materials compared to their respective carbon material by 44% in the case of the ODC@NiO (going from 47 to 85 F  $\text{g}^{-1}$ ) and 33% in the compound ODC@ $\text{Mn}_3\text{O}_4$  (from 87 to 130 F  $\text{g}^{-1}$ ). Additionally, these nanoparticles endow the composite with a greater density than the respective carbon material, which results in an improvement of the volumetric capacitance. Also, the carbon matrix provides mechanical stability to the nanoparticles.

In second place, having been observed the improvement achieved with the addition of metal-oxide nanoparticles, lignocellulosic activated carbons were selected as matrix for the synthesis of new composite materials by addition of ex-situ synthesized metal-oxide or metal nanoparticles. As precursor materials for the activated carbons, Galician walnut shells (*Juglans regia*) and bamboo (*Guadua angustifolia*) were selected, due to their high carbon content in the form of lignin and the high specific surface area developed after chemical activation. In the case of activated carbon derived from bamboo, the incorporation of 25% of gold nanoparticles (AuNPs) aimed to substantially reduce the equivalent series resistance (ESR) value, so that although the gravimetric capacity of the material is sacrificed from 100 to 73 F  $\text{g}^{-1}$  the increase in density that the inclusion of the AuNPs involved, contribute to the obtention of a high volumetric capacitance (from 29 to 47 F  $\text{cm}^{-3}$ ), providing a higher value in terms of the practical utility of the composite in mobile devices. In the case of activated carbon derived from bamboo, the incorporation of 25 % of gold nanoparticles aimed to substantially reduce the ESR, so that although the gravimetric capacity of the material is sacrificed from 100 to 73 F  $\text{g}^{-1}$  the increase of density that gives the composite material the inclusion of the AuNPs contributes the obtaining of a high volumetric capacitance (from 29 to 47 F  $\text{cm}^{-3}$ ), providing an added value in terms of its practical utility as electrode material in mobile devices. In the case of activated carbon derived from Galician nuts, the composite material presents an ESR approximately 4 times lower than activated carbon derived from bamboo, so in this case it was intended to improve the electrochemical properties by incorporation of only 1% of manganese oxide nanoparticles. The results obtained for the composite material provide not only an improvement of the total storage capacity of the material (from 41 to 59

F cm<sup>-3</sup>), compensating the decrease of the surface area with the pseudocapacitive mechanism provided by the manganese oxide nanoparticles, but a decrease of approximately 6 times the ESR of the device compared to the carbon material.

In the last chapter, a new composite material, denoted as Carbon-Gold Nanograpes, composed of individual microporous carbon nanospheres with a core of several gold nanoparticles, has been successfully synthesized, providing both high density and large surface area. This new composite material gives a volumetric capacitance that is similar to analogous carbon nanospheres that do not have a solid core. As it also has the advantage of a denser material, it is more suitable for use in practical devices. However, it was found that the volumetric capacitance of these materials quickly decreased at fast charge-discharge rates in 0.5 M H<sub>2</sub>SO<sub>4</sub> solution, perhaps due to challenges of access of the electrolyte into the small pore sizes of the nanocarbon. By heating the nanocomposite beyond the gold nanoparticle melting point, the melted gold could be made to flow out of the carbon nanospheres, improving the connectivity of the microporous structure and enhancing ion-pore interaction and thus its ionic conductivity. Overall, the gravimetric and volumetric capacitance values increased to 210 F g<sup>-1</sup> and 114 F cm<sup>-3</sup>, respectively, in a symmetrical two-electrode cell using 0.5 M H<sub>2</sub>SO<sub>4</sub> as the electrolyte. This work demonstrates a new concept for micropore structure control for the design of next generation carbon composite materials.





# Abbreviations

<b>2D-NLDFT</b>	2D Non-Local Density Functional Theory
<b>AFC</b>	Alkaline fuel cell
<b>AFM</b>	Atomic Force Microscopy/Microscope
<b>AuNPs</b>	Gold Nanoparticles
<b>BAC</b>	Bamboo Activated Carbon
<b>BET</b>	Brunauer, Emmett and Teller
<b>CBED</b>	Convergent Beam Diffraction Patterns
<b>CCD</b>	Cyclic Charge-Discharge
<b>CDC</b>	Carbide-Derived Carbon
<b>CNSs</b>	Carbon Nanospheres
<b>CNT</b>	Carbon Nanotubes
<b>CTEM</b>	Conventional Transmission Electron Microscopy
<b>CV</b>	Cyclic Voltammetry
<b>CVD</b>	Chemical Vapor Deposition
<b>DFT</b>	Density Functional Theory
<b>DP</b>	Diffraction Pattern
<b>DDP</b>	Digital Diffraction Pattern
<b>DWCNT</b>	Double Wall Carbon Nanotubes
<b>EDLCs</b>	Electrochemical Double Layer Capacitors
<b>EELS</b>	Electron Energy-Loss Spectroscopy
<b>EIS</b>	Electrochemical Impedance Spectroscopy
<b>ELNES</b>	Energy-Loss Near the Edge Structure
<b>FMT</b>	Fundamental Measure Theory
<b>GCMC</b>	Grand Canonical Monte Carlo
<b>GCPL</b>	Galvanostatic Cyclic with Potential Limitation
<b>GNR</b>	Graphene NanoRibbons
<b>HAADF</b>	High-Angle Annular Dark-Field
<b>HRTEM</b>	High-Resolution Transmission Electron Microscopy
<b>HTHP</b>	High Temperature High Pressure
<b>IEA</b>	International Energy Agency
<b>IUPAC</b>	International Union of Pure and Applied Chemistry
<b>LM</b>	Light Microscopy/Microscope
<b>MFMT</b>	Modified Fundamental Measure Theory
<b>MCFCs</b>	Molten carbonate fuel cells
<b>MWCNT</b>	Multi Wall Carbon Nanotubes
<b>NLDFT</b>	Non-Local Density Functional Theory
<b>NGs</b>	Nanograpes

## ABBREVIATIONS

---

<b>ODC</b>	Organometallic-Derived Carbon
<b>OLC</b>	Onion Like Carbons
<b>PAH</b>	Polycyclic Aromatic Hydrocarbons
<b>PAFC</b>	Phosphoric acid fuel cell
<b>PDA<sub>s</sub></b>	Personal Digital Assistant
<b>PEMFC<sub>s</sub></b>	Proton exchange membrane fuel cells
<b>PGS<sub>s</sub></b>	Polymerized glucose spheres
<b>PSD</b>	Pore Size Distribution
<b>SAED</b>	Selected Area Electron Diffraction
<b>SAFC</b>	Solid acid fuel cell
<b>SC</b>	SuperCapacitor
<b>SCNM</b>	Shaped Carbon Nanomaterials
<b>SEM</b>	Scanning Electron Microscopy/Microscope
<b>SOFC<sub>s</sub></b>	Solid oxide fuel cells
<b>STEM</b>	Scanning Transmission Electron Microscopy/Microscope
<b>SWCNT</b>	Single Wall Carbon Nano Tubes
<b>TEM</b>	Transmission Electron Microscopy/Microscope
<b>WAC</b>	Walnut shell Activated Carbon
<b>XRD</b>	X-ray Powder Diffraction
<b>XEDS</b>	X-ray Energy Dispersive Spectroscopy/Spectrometer
<b>ZLP</b>	Zero Loss Peak

# Chapter 1

## Introduction

The energy demand of the globalized and technological society in which we live is in continuous growth, since both first world countries and those in developing require the consumption of increasingly large amounts of energy to cover the increase in the level of development such as the use of electronic devices, electrification or transports (Figure 1.1). The International Energy Agency (IEA) estimates a 30% of increase in global energy demand by 2040, mainly driven by in developing countries such as India and Southeast Asia (International Energy Agency, 2017). This situation entails an uncomfortable truth: the energy sources that up to now have supported the industrial advances that we enjoy in our world, mainly

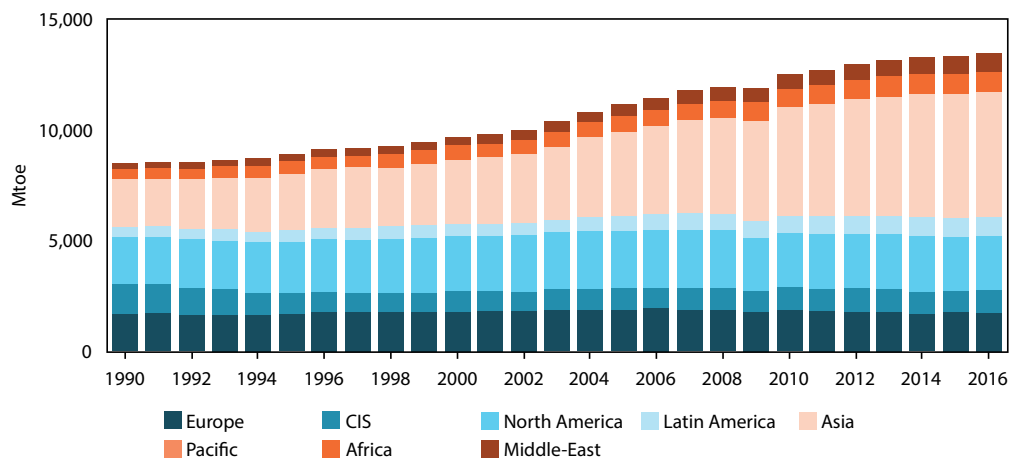


Figure 1.1: Global energy consumption by countries. Home Global Energy Statistical Yearbook 2017 (Enerdata, 2018).

based on fossil fuels, are being depleted. The amount of oil available on the planet is increasingly smaller and more expensive to extract, and therefore it cannot continue to be our main source of energy for the continued exponential growth of our population.

That is not the only problem associated, in addition, due to the indiscriminate use of these fossil fuels, more and more quantities of gases responsible for the so-called greenhouse effect have been released into the atmosphere. Consequently, the global temperature of our planet is increasing year after year, approximately  $1.2\text{ }^{\circ}\text{C}$ , since the pre-industrial times of the years 1961-1990 (Morice *et al.*, 2012). Exceeding the mark of  $1\text{ }^{\circ}\text{C}$ , we are dangerously close to reach and surpass the global limit agreed of  $2\text{ }^{\circ}\text{C}$  above the pre-industrial temperature (Figure 1.2). Although this is the limit that has been set as the highest acceptable risk to assume by environmental organizations and economists, exceeding lower temperatures we are already suffering from natural catastrophes as stronger and more intense hurricanes or the consequences of the melting poles, increasing the sea level by 20 centimeters (NASA, 2018).

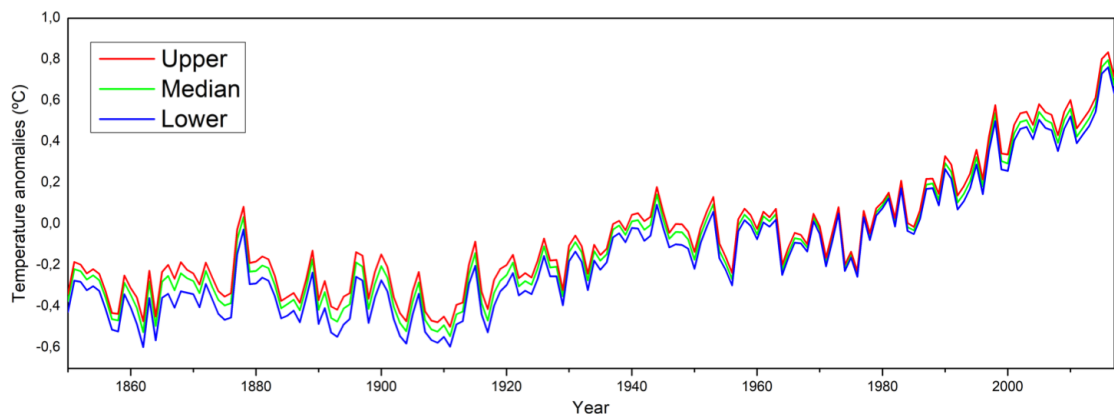


Figure 1.2: Temperature anomalies since 1850 to 2017 (Met Office Hadley Centre, 2017).

This situation requires, as soon as possible, a change in our source of energy production, replacing the fossil fuels by renewable sources of energy that reduces the impact of our society on the environment. Renewable sources are the most economic energy sources of new generation, consequently nowadays many countries are investing in renewable energy plants. China and India lead the production of solar energy, while in the European Union the dominant renewable energy is wind power, where it is also estimated that by 2040 the total renewable energy will represent the 80% of the total energy generated (International Energy Agency, 2017).

But thinking about changing our main source of energy by the renewable ones, their main drawback arises immediately due to the intermittency in their generation. Sunlight can only be used during the day or wind does not blow at demand, in the same way that we cannot locate a waterfall close to our houses to take advantage of hydraulic energy. Figure 1.3 shows the variability and intermittence of sun and wind power during the day. This graph shows an energy system operating in a sunny climate, like that of Spain, with the renewable component being 80% solar power and 20% wind. As well as variability during a typical day, as shown here, renewable power also varies by season and geography.

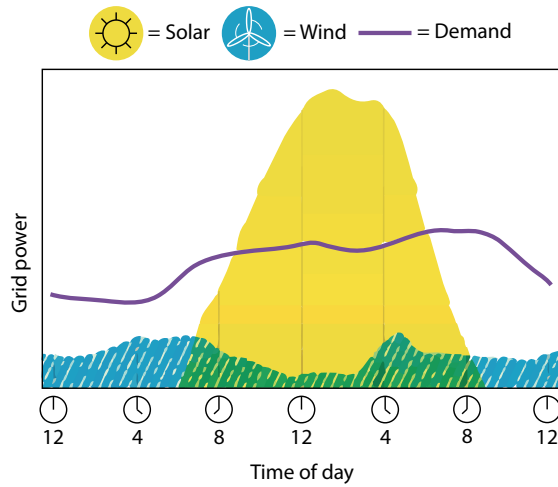


Figure 1.3: Variability of solar and wind power during a typical day (after BP, 2018).

Therefore, the energy storage becomes a critical factor to achieve the balance between the energy demanded and that generated from renewable resources. In this sense, energy storage devices can be employed with the aim of collecting, storing and integrating the excess electricity into the electrical grid upon demand.

## 1.1 Energy storage devices

Energy storage has always been a challenge that has been passed down generations, because electric power has always been the most difficult product to store efficiently. The first attempts to store energy were to pump water from one reservoir to another located in higher altitudes, taking advantage of periods of low energy demand and then releasing moving the turbines and generating energy in periods of high energy demand. It is commonly called hydro-pump, and has been used since the 1920s in Europe and USA. It is still considered a highly efficient storage model, with efficiencies reaching greater than 80% (Energy Storage Association, 2017). However, hydroelectric and hydro-pump storage plants can have an enormous impact on the surrounding environment as they require a great deal of land resources.

From then till now, many technologies and different options have been available to store energy on both short and long-terms. Inductors and capacitors are good examples as short-term storage systems, storing energy in electrostatic or electromagnetic form on electrical circuits. For long-term approach more options are available: batteries and fuel-cells, where chemical redox reactions directly produce electrical energy; fly-wheels, which store kinetic energy by accelerating a rotor in a vacuum enclosure using the surplus energy and considered at present the most efficient storage option in industry reaching up to 93% of efficiency (Boos, 2014); or **supercapacitors**, that store energy in terms of electrostatic form like common capacitors but with greater amount of energy (Kularatna, 2015; Winter & Brodd, 2004), being the topic of the present Thesis. Batteries, fuel-cells and supercapacitors have become the most used and studied storage devices in recent times, because it is easier to create smaller and portable devices to satisfy the increasing demand for its application in hybrid and electric vehicles (Burke & Zhao, 2015) or portable electronic devices such as cell phones, PDAs, and laptops (CAP-XX, 2015).

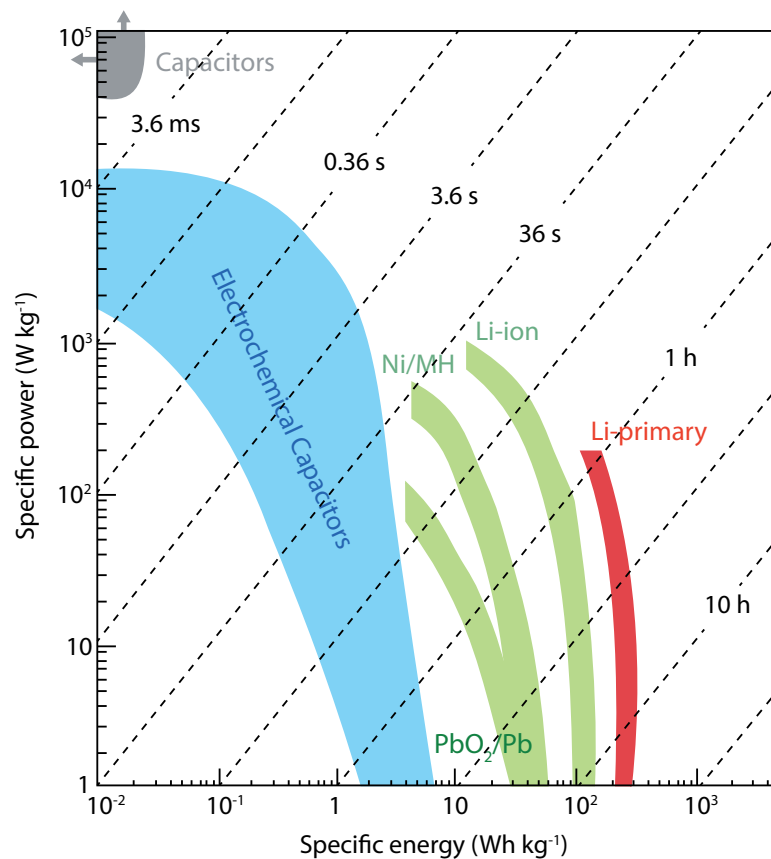


Figure 1.4: Ragone Plot (after Simon & Gogotsi, 2008).

The Ragone plot displayed on Figure 1.4 is commonly used to show the principal differences between batteries and supercapacitors. Batteries, appearing as green and red stripes in the graph since they have high energy density (or specific energy in case of gravimetric measures), however they suffer of low power density or specific power, meaning that the energy cannot be fastly stored and delivered. In the opposite way, supercapacitors, represented by the wide blue stripe in the left of the graph, exhibit lower energy density but higher power density, meaning in this case that they can store less amount of energy but can be delivered very quickly, achieving the highest specific power with the lowest charging times. Making a similarity, a battery would be a long distance runner, it needs a lot of energy released slowly, however a supercapacitor would be a sprinter, it needs just the right energy released very quickly. Thereby, the current applications of supercapacitors are those in which a quick energy boost is needed for a short period of time. As a example, the multinational company AIRBUS uses them in the opening of emergency doors of one of its most commercialized aircraft models the AIRBUS A380 (European Space Agency, 2014) or in the current hybrid vehicles where they can store the fast braking energy generated, reducing fuel consumption. A particular case in Spain is their use on an special catenary-free tram in Seville by the Spanish company TRINELEC. Here, fulfilling the need to remove the catenaries in the tram line when crossing the old town, supercapacitors quickly charge in each tram station the necessary energy to reach the next stop (TRINELEC CAF, 2010).

Batteries can be classified as primary and secondary batteries, depending on whether they are of single-use (galvanic cell, alkaline battery and dry cell) or rechargeables (lead acid battery, lithium ion battery or nickel-cadmium battery) respectively (Dehghani-Sanij *et al.*, 2019). On the other hand, fuel cells come in many varieties depending of their design features such as the fuel kind, operating temperature and the electrolyte substance, which usually defines the type of fuel cell (Proton exchange membrane fuel cells (PEMFCs), Phosphoric acid fuel cell (PAFC), Solid acid fuel cell (SAFC), Alkaline fuel cell (AFC), Solid oxide fuel cells (SOFCs) and Molten carbonate fuel cells (MCFCs) among others) (İnci & Türksöy, 2019).

Having a look to the basic schematic composition of the electrochemical energy storage devices (Figure 1.5) we can notice several similarities: all are composed of two electrodes which work as cathode and anode, where the anode is easily found as the electron donor and the cathode the electron acceptor. Between them there should be an insulator separator, that allows the passage of ions through it but not electrons, that in the case of batteries and fuel cells usually also works as the electrolyte. Finally, if the insulator separator does not work as electrolyte, a



liquid one impregnating everything is needed. But if they are so similar, why do they offer such different properties?. The answer lies in its different mechanisms of storing energy.

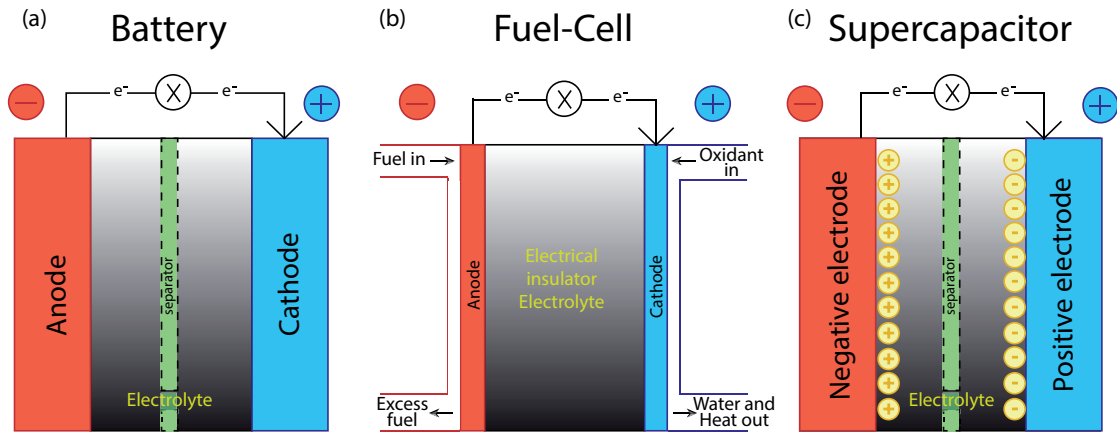


Figure 1.5: Basic scheme of three energy storage devices: battery, fuel-cell and supercapacitor.

Batteries and fuel-cells works basically with redox reactions that occur in their electrodes and the difference between them is that fuel-cells are open systems where the anode and cathode serve as charge-transfer media and/or diffusion layers (depend of the kind of fuel cell) and the active masses are delivered from outside the cell, while batteries are closed systems. In batteries and fuel-cells the charge is stored electrochemically through an exchange of electrons between the electrodes and the electrolyte. As electrons are involved the process is called a Faradaic reaction, since Faraday's law must be fulfilled. The redox reaction takes place on the bulk electrode material, which explains the higher energy density. On the other hand, by involving electron exchange all along the electrode material, provides lower power density. Instead, supercapacitors as we will deeply describe in the next section, work with a different energy storage mechanism called capacitance where the charge is electrostatically stored, without any redox reaction and therefore no Faradaic reactions occurs, offering lower energy density but a higher power density as displayed in the Ragone diagram.

## 1.2 Supercapacitors

A supercapacitor, also called an ultracapacitor or double-layer electric capacitor, is an energy storage device that can provide more energy than a common capacitor

and deliver or capture it faster than a battery. Nowadays, these type of devices has aroused considerable interest because they have excellent reversibility, practically unlimited cyclability ( $> 1,000,000$  cycles) and a simple operation mode. We have just seen that these devices currently offer energy solutions in applications where a rapid energy boost is required, but all currently efforts and research are aimed at increasing the energy density without losing power, in order to obtain more "super" capacitors that reach or even surpass the energy of a battery with also better life-time properties, more difficult to improve on a common battery.

There are many strategies followed for this purpose: increasing the electrode surface area, incorporation of pseudocapacitive materials or even the use of both capacitor and battery type electrodes together with the employment of different types of electrolyte: aqueous, organic or ionic liquids. The rapid proliferation of this type of devices requires an appropriate classification based on the active material on each electrode and the energy storage mechanism, in order to clarify and be able to properly compare different setups, since many times all kind of such devices are included in the general term of supercapacitors, although they work in a very different way from each others. Thereby, supercapacitors can be classified in three general categories: symmetric, asymmetric and hybrid (see Figure 1.6).

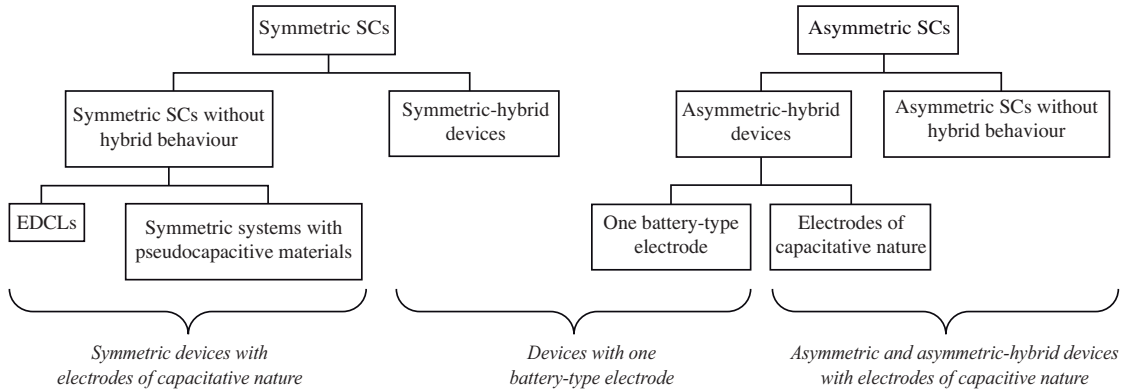


Figure 1.6: Classification of supercapacitors based on the charge storage mechanism and active material in each electrode (after Roldán *et al.*, 2015).

Symmetric devices contain the same active material in each electrode. In this category the classic electrochemical double layer capacitors (EDLCs) that store energy by capacitive mechanism, is the most representative, but also account for other devices with pseudocapacitive mechanism, such as metal oxides or some conductive polymers (Conway *et al.*, 1997; Simon & Gogotsi, 2008) in both electrodes. In addition, there are many studies in materials that can provide both mechanisms in synergy, called hybrid materials, and if a device uses the same hy-

brid material for their two electrodes it is named symmetric-hybrid device. Hybrid and asymmetric terms have been used indiscriminately and often confused. The most reasonable is to use the term asymmetric as opposed to its antonym, ergo for devices built of electrodes of different materials, and the term hybrid for materials that combine different energy storage mechanisms. Therefore, asymmetric supercapacitors with either capacitative (with two different activated carbons) or pseudocapacitative mechanism (for example two different metal oxides) can be described. In the case of asymmetric hybrid supercapacitors where each electrode operates with a different mechanism combining a capacitative material and a pseudocapacitative one (activated carbon/MnO<sub>2</sub> is the common example) or even systems that combine a capacitative-type electrode with a battery-type one that utilizes a rechargeable reaction, being this configuration a promising strategy to improve the energy density of electrochemical capacitors (Roldán *et al.*, 2015).

### 1.2.1 Energy storage mechanism on supercapacitors

As stated before the two main energy storage mechanisms working in supercapacitors are capacitance and pseudocapacitance, however they have not been described in detail yet. Capacitance, that also gives the name to the device, is based on the double layer principle described for the first time by the German physicist Hermann von Helmholtz in 1853, and in 1957 first patented by the General Electric Company (Becker, 1957; Rightmire, 1966). The primary basic concept consists on two facing plates of opposite charges separated by an atomic distance where a controllable surface density of negative or positive charge can arise. Helmholtz broadens this concept to more separated interfaces by placing ions as a charge carrier between the plates and also applied to non metal plates surfaces like semiconductors or colloidal particles. Louis Georges Gouy and David Leonard Chapman, French and English physicists respectively, bring in the thermal fluctuation in their Gouy-Chapman model, as the ions are not fixed charges at the surface as Helmholtz postulated, and the whole electrolyte participates on the process in a diffuse gradient. It was Otto Stern, Nobel laureate in physics in 1943, who mixed both theories identifying two regions on the double layer, the inner Helmholtz layer and the diffuse layer where both contribute to the total capacitance, introducing also the concept that ions are not point charges, they have their own volume plus their hydration shells (the so called Gurney co-sphere radii) correcting the overestimation of capacitance obtained by its predecessors by not taking into account this detail.

Later, D. C, Grahame, from United States, took notice of the different nature of cations and anions: most common cations are smaller than anions and have

stronger dipole interaction with their solvation sphere, so it is more difficult that they lose their shell. Therefore, the Helmholtz layer is divided in two (see Figure 1.7): the inner Helmholtz layer, containing the anions; and the outer Helmholtz layer, where the more solvated cations are located (Conway, 1999).

When a difference of potential (as voltage,  $V$ ) is applied on a supercapacitor, electrons move from the positive to the negative electrode, creating an excess of positive ( $Q^+$ , from electrons that left their holes) and negative ( $Q^-$ , from electrons that arrive) charge on their respective electrodes. This charges separation is unstable and needs to be countered by the corresponding ions of the electrolyte by their electrostatic deposition on the surface of the electrode following the double-layer described above. The current through the electrodes continues flowing until the potential difference between both electrodes become equal to the supply voltage, being this the form in which a supercapacitor stores energy. The ratio between the sum of absolute values of both charges ( $Q = |Q^+| + |Q^-|$ ) on coulombs,  $C$ , and the applied voltage in volts,  $V$ , yields the capacitance in farads,  $F$ .

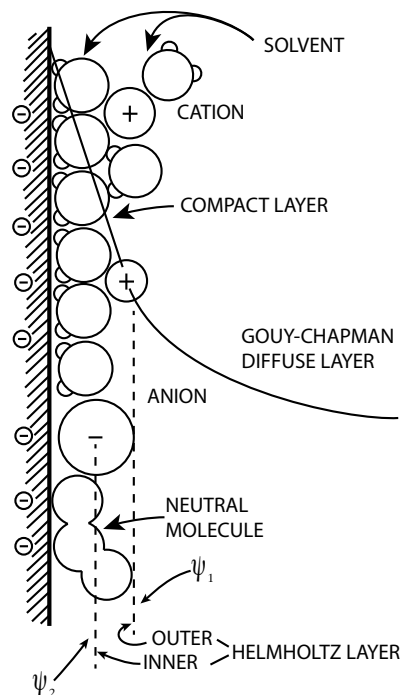


Figure 1.7: Double layer general representation (after Conway, 1999).

$$C = \frac{Q}{V} \quad (1.1)$$

The capacitance formula for a parallel-plate capacitor can also be expressed by the following equation:

$$C = \frac{A\epsilon}{d} \quad (1.2)$$

Where  $A$  is the surface area of the interface between the electrode and the electrolyte in square meters ( $m^2$ ),  $\epsilon$  is the permittivity of the dielectric material and  $d$  is the double layer thickness in meters ( $m$ ). Consequently, the greater the surface area of the electrode, the greater the energy that could be stored.

This is the main difference between supercapacitors and common capacitors, the supercapacitor have much more surface area than its counterpart, as it is made of high surface area materials as electrodes such as activated carbons, while the common capacitor uses metal plates. In the same way, the higher permittivity, the higher capacitance. On the other hand, the greater the distance of the double layer formed at the interface, the smaller the capacitance.

Another type of supercapacitors are based on the so called pseudocapacitance, phenomenon that was firstly discovered by Trasatti and Buzzanca in their studies on the RuO<sub>2</sub> thin films (Trasatti & Buzzanca, 1971) where in a typical cyclic voltammetry experiment (technique in which we will deepen later) the results obtained showed a typical rectangular shape characteristic of a capacitive behavior, and not the expected for a Faradaic process. This process occurs on the electrosorption of ions at the surface of the electrode, involucrating a redox reaction between them, when the electrode surface is able to participate on a reversible redox reaction as for example on metal oxides like RuO<sub>2</sub>. This mechanism has a Faradaic origin, as involves the passage of charge across the double layer formed, in the same way than in batteries, but in this particular case, the charges do not extend through the entire electrode material, but just stay on the surface due to thermodynamic and kinetic reasons, where the redox reaction takes place at very high speed continuously and reversibly. Therefore the charge accepted by the electrode ( $\Delta q$ ) depends on the applied voltage ( $\Delta V$ ), so its derivative relation and thus its electrical behavior is equivalent to the original capacitance (Conway, 1999).

$$C_{\text{pseudo}} = \frac{dq}{dV} \quad (1.3)$$

Additionally, three types of pseudocapacitance can be distinguished: i) the underpotential deposition, where a monolayer of a different metal with a very lower potential than the metal of the electrode is deposited over it; ii) redox pseudocapacitance, in the case of surfaces that participate on the redox reaction like the example of RuO<sub>2</sub>; and iii) intercalation pseudocapacitance, where the ion intercalates into the structure of the electrode to find the redox-active surfaces, but without structural changes on the electrode. In this last case, as there are diffusion problems involved, the charge dependence with the potential is not always linear, so the capacitance is not always constant (Augustyn *et al.*, 2014; Lukatskaya *et al.*, 2016).

Once exposed both storage mechanisms, it should be pointed out that they

are not incompatible, in fact they are always present on this type of devices. It is known that double-layer carbon capacitors exhibit about 1 to 5% of their capacitance as pseudocapacitance from Faradaic reactivity of oxygen groups that always remain in the surface during the synthesis or preparation, and pseudocapacitor devices or even batteries always present a 5 to 10% of electrostatic double layer capacitance component depending on their accessible surface area.

### 1.2.2 Fundamental parameters

Once defined the capacitance in any of the mechanisms previously mentioned, it can be related to the fundamental parameters of a supercapacitor, the energy and the power:

$$E = \frac{1}{2} CV^2 \quad (1.4)$$

$$P = \frac{V^2}{4R_s} \quad (1.5)$$

Where the energy (joules,  $J$ ) that a supercapacitor can store is proportional to the obtained capacitance (farads,  $F$ ) and to the square of the applied potential (volts,  $V$ ), and the power (watts,  $W$ ) is also directly proportional to the square of the potential but in this case, inversely proportional to the internal resistance of the capacitor device (ohms,  $\Omega$ ). The capacitance and the resistance are fundamentally defined by the nature electrode material, meanwhile the voltage depends in a greater extension on the electrolyte type (aqueous, organic or ionic liquid).

In order to desing a good material for electrode in a supercapacitor we need in first place, according to the capacitance equation 1.2 displayed above, a conductive material with a large surface area. In addition, this area must be distributed in a suitable porous structure. Since the energy is stored by the electrostatic deposition of electrolyte ions on the surface of the electrode, these ions must find access to the entire area, and for that, they should fit in the porous structure. A pore size compatible with the ions is required, also taking into account that in the case of using an aqueous electrolyte, a solvation sphere will be formed increasing their size. But even designing a material with the properly pore size for the electrolyte used, also larger pores would be necessary allowing for a faster

circulation of ions throughout the electrode surface (Figure 1.8). If not, the ions would block each other throughout the material, thus interrupting the deposition process and therefore reducing the effective surface area, especially at fast charge and discharge speeds.

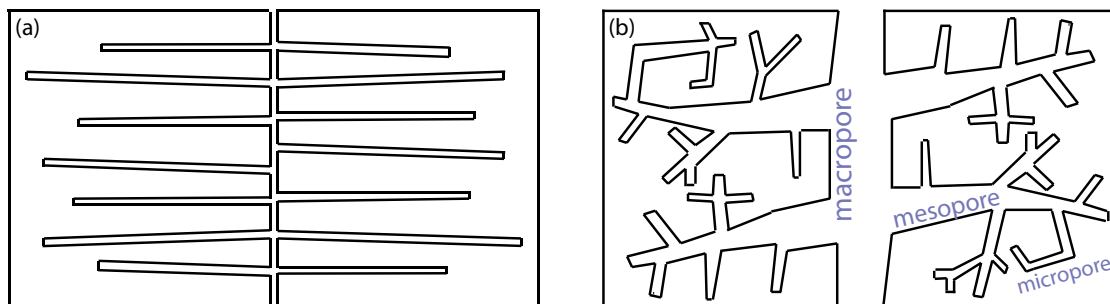


Figure 1.8: (a) Unimodal and (b) multimodal pore structures.

If the capacitance is optimized, focusing on the two equations of this section for energy (1.4) and power (1.5), the applied voltage appears as a key factor in order to maximize both parameters. The electrode material should withstand the applied voltage, but what really limits the applicable potential is the stability of the electrolyte. Aqueous electrolytes are less problematic and easier to manage, but their stability is about one volt. Outside this voltage window, water is hydrolyzed into hydrogen and oxygen, degrading the solvent. On the other hand, organic electrolytes are somewhat more complicated to manage since they require to work on an inert atmosphere, but they can easily resist higher voltages even up to three volts (Zhong *et al.*, 2016).

Finally, it is important to point out that the density of the electrode material is a crucial factor in its applicability. Very often, researchers report impressive gravimetric capacitance values that once the whole device is built up dramatically decreases to a comparable volumetric values previously reported. A material with very high surface area is required, and usually this type of materials presents low density. At the time of manufacturing the electrode to assembly the device, the active material must be, for instance, compressed as a film, losing its great capacity showed on the experimental stage and yielding values similar to those in the commercial ECs made of activated carbon (Gogotsi & Simon, 2011). So, the great challenge on the research of material electrodes for supercapacitors is to design high surface area materials with also high density. Another point to highlight is that, as explained above, volumetric capacitance is a better way to report capacitance values than gravimetric capacitance.

## 1.3 Carbon Science

Carbon is a particular element whose electronic configuration  $1s^2 2s^2 2p^2$  endows it with special properties. Although at first look only two electrons are available to form new bonds, the free energy released when formed allow electron jumps from 2s orbital to the empty 2p orbital, resulting on a new configuration  $1s^2 2s^1 2p_x^1 2p_y^1 2p_z^1$  where now four electrons from four different orbitals are available to form new bonds. That particular configuration also allows the combination or hybridization of s and p orbitals in order to equalize the excited state energy. In such way, when the 2s orbital is combined with the three p orbitals, four new  $sp^3$  orbitals are formed in a tetrahedral configuration, allowing the formation of four  $\sigma$  type single bonds. If the combination is between the 2s orbital and two of the three 2p orbitals, then three new  $sp^2$  orbitals outcome, in a trigonal planar configuration with

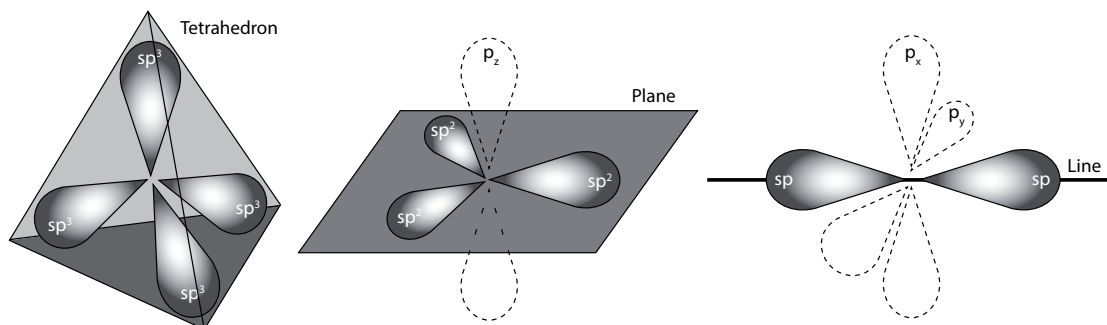


Figure 1.9: Carbon hybrid orbitals.

the remaining p orbital perpendicular to the plane. Two carbon atoms in such configuration form a double bond with the contribution of one  $\sigma$  bond from one  $sp^2$  orbital plus the  $\pi$  bond of the 2p perpendicular orbital. Finally, when the 2s orbital is combined with just one 2p orbital, 2 new sp orbitals are formed, in a linear configuration. In this case, two carbon atoms will form a triple bond by the combination of one  $\sigma$  bond from the sp orbital and two  $\pi$  bonds from the 2p orbitals located perpendicularly from each others (see Figure 1.9).

Different carbon allotropes result by controlling these hybridizations. A three dimension  $sp^3$  hybridization carbon network evolve on the precious diamond form, meanwhile a stacking of the  $sp^2$  planar structure outcome the non so precious graphite. The sp hybridization results on the carbynes, considered the ideal infinite one dimension carbon materials that, although unstable in ambient conditions and chemically very active, are recently attracting the attention of scientists due to their theoretical exciting properties (Bianco *et al.*, 2018). But the world of carbon



allotropes is far from ending here. Previously described materials are considered bulk materials, whereas at the nanoscale other carbon allotropes appear, such as fullerenes,

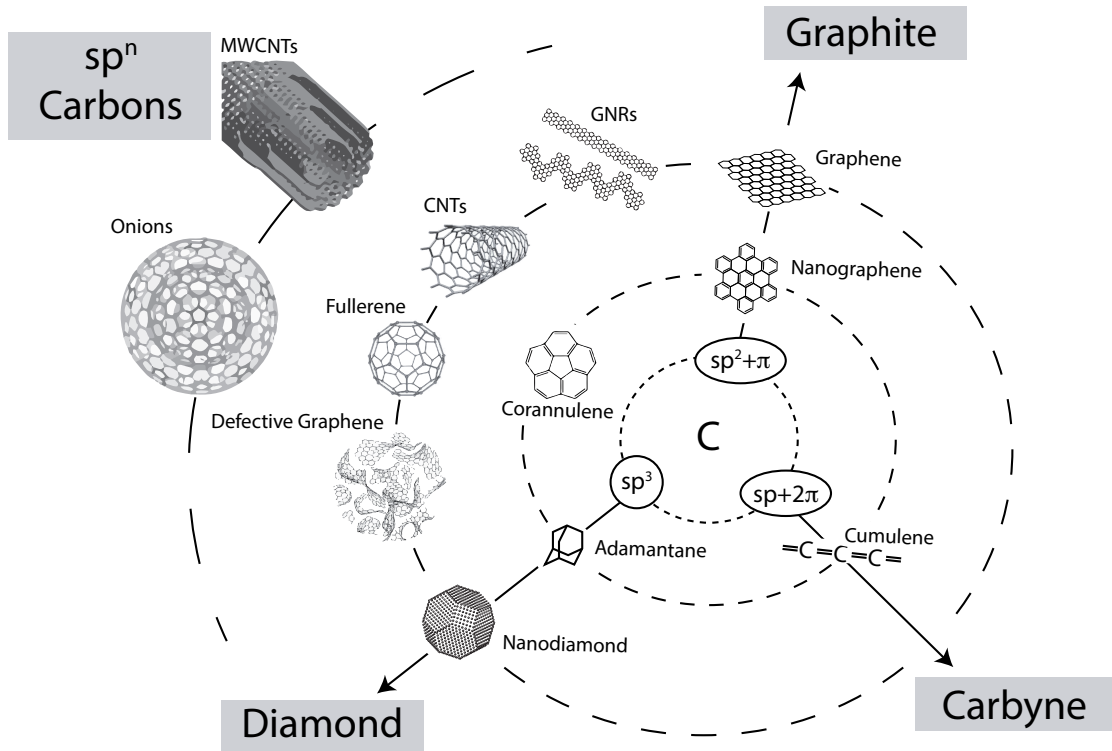


Figure 1.10: Classification of carbon nanostructures from the degree of carbon bond hybridization (modified from Shenderova *et al.* (2002)).

carbon nanotubes (CNT) or graphene appear, topic of thousand of articles. The most often explored system at the nanoscale is the  $sp^2$  planar shape. Fullerenes, CNT, nanohorns and similar nanostructures can be easily explained in terms of a curved graphene layer as their common structural building unit. Conversely,  $sp$  and  $sp^3$  should now be explored more intensively at the nanoscale level. Figure 1.10 show the most representatives carbon structures starting from the three different atomic hybridization and the natural evolution among them.

### 1.3.1 The $sp$ hybridization: Linear carbon chains

Theoretical studies reveal very interesting properties in these linear carbon chains: higher Young's modulus and stiffness than graphene, CNTs and diamond, an ex-

tremely high charges movility based on their intrinsic one dimensional structure and an adjustable bandgap upon strain (Liu *et al.*, 2013; Zhang *et al.*, 2011). Besides, they are important for the understanding of fundamental solid state physics like quantum conductivity.

Linear carbon chains can adopt two different configurations: polyynes and cumulenes (see Figure 1.11). Polyynes are made of alternating triple and single bonds where the two  $\pi$  interactions of each atom are localized in the triple bond resulting on a semiconducting character. While the cumulenes consist on carbon chains with all carbon atoms connected by double bonds, the two  $\pi$  interactions are now localized on both sides of the carbon atom, which endow it with metallic properties.

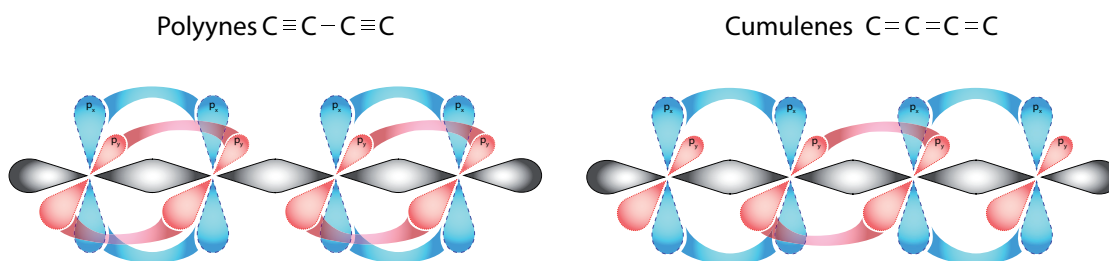


Figure 1.11: Polyynes and cumulenes linear structures.

The synthesis of these linear carbons is not easy due their high reactivity and unstability. The principal attempts to isolate them was trying to trapping them between graphene layers or inside the hollow core of CNTs. In the second case, it has been found that tubular cores in the range between 0.6 to 0.8 nm diameter of multi walled carbon nanotubes (MWCNTs) are optimal for synthesis of linear carbon chains via atmospheric arc discharge in the presence of boron (Kang *et al.*, 2016). More recently, thermal treatment of double-walled carbon nanotubes (DWCNTs) around 1500 °C has been reported for the synthesis of long linear carbon chains (Shi *et al.*, 2016), where metallic properties were found in the composite, even though both the CNTs and the linear carbon chains were semiconductors.

Even so, the study of these carbon materials is in a very first stage, the synthesis mechanism is not well understood and still are many unresolved questions, and their theoretical properties based on their ideal one-dimensional features need to be elucidated. Furthermore, the fabrication of air-stable linear carbon chains without using encapsulation will be one of the biggest challenges to achieve in the near future.

### 1.3.2 The $sp^2$ hybridization: Graphene-like carbons

The graphite bulk material obtained when the carbon atoms are on a  $sp^2$  hybridization is composed of stacked layers of graphene. The  $p_z$  orbitals which remain perpendicular to the graphene planes are responsible of such stacking by Van der Waals forces, and could happen in two different ways, hexagonal (ABABAB...) or rhombohedral (ABCABCABC...) presenting the  $P6_3/mmc$  and  $R\bar{3}m$  spaces groups respectively.

Thus, graphene can be considered as the building block of graphite. Theoretical studies predict the fascinating electronic properties of one single and infinite layer of graphene, a semi-conductor with a band gap close to zero (Wang *et al.*, 2017). But in practice, that infinite planar layer is impossible to obtain. The layers tend to curve, especially if they contain some defects in the carbon network like a pentagon or heptagon instead of an hexagon, or a  $sp^3$ -type carbon that interrupts the planarity, being this effect more probable as the layer increases in size. Therefore, graphene can also be considered the building block of different dimensions carbon nano materials that have been discovered in recent years, becoming the  $sp^2$  the most studied hybridization state at the nanoscale.

#### Zero dimensions nanomaterials

When the layer of graphene is totally curved, **fullerenes** are obtained (Figure 1.12a). Fullerenes are a family of nanomaterials that consists of a hollow cluster formed by a certain number of carbon atoms. The most common of the fullerenes is the structure formed by sixty carbon atoms  $C_{60}$ , synthesized in 1985 by Kroto H.W., Heath J.R., O'Brien S.C., Curl R.F. and Smalley R.E., using the technique of laser vaporization at Rice University (Kroto *et al.*, 1985). A closer inspection at the  $C_{60}$  molecule reveals that each carbon atom is linked to three more atoms forming a truncated icosahedron with twenty hexagons and twelve heptagons, fulfilling the Euler's theorem that determines that every closed structure composed of hexagons and heptagons must contain twelve heptagons and an arbitrary number of hexagons. Five years before (1980) Sumio Iijima first reported transmission electron microscopy images of fullerenes surrounded layer by layer by other icosahedral fullerenes made of a higher number of carbon atoms when studying amorphous carbon films prepared by thermal vacuum deposition (Figure 1.12b). These characteristic shape carbon nanomaterials were called **nanooions** by Ugarte in 1992, who obtained them by intense electron irradiation of carbon

soot under TEM observations (Ugarte, 1992).

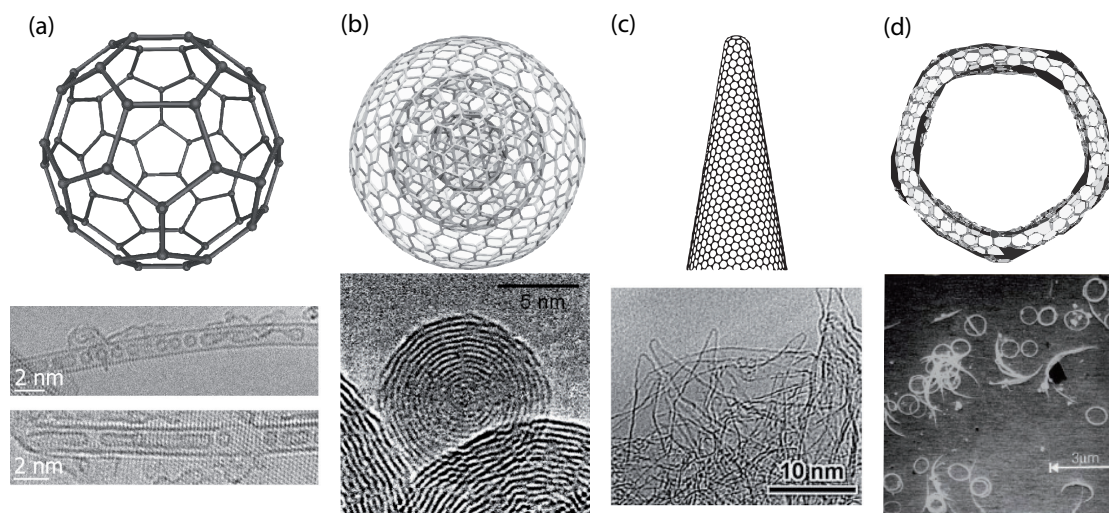


Figure 1.12: Structure schemes and TEM images of (a) fullerenes (Slepchenkov *et al.*, 2017), (b) nanoonions (Camisasca & Giordani, 2017), (c) nanohorns (Iijima *et al.*, 1999) and (d) carbon rings (Martel *et al.*, 1999).

Since the discovery of fullerenes, the number of publications in carbon nano materials increased exponentially, discovering lots of new shapes like the called **nanohorns** (Figure 1.12c), cone shaped aggregates of graphene sheets first reported by Sumio Iijima *et al.* in 1999, synthesized by CO<sub>2</sub> laser ablation and arc discharge without a metal catalyst (Iijima *et al.*, 1999), as well as **carbon rings or toroids** (Figure 1.12d) observed by Smalley and coworkers while examining laser-grown SWCNTs (Lin, 1999; Shaikjee & Coville, 2012). **Graphene clusters, or nanographenes** are one more 0D nanomaterial, also called polycyclic aromatic hydrocarbons (PAHs), which consist on graphene sheets of few carbon atoms synthesized by chemical reactions of hexa-peri and hexacata-hexabenzocoronene derivatives (Delgado *et al.*, 2008; Hahn *et al.*, 2018).

### One dimensions nanomaterials

**Carbon nanotubes** are the most studied one-dimensional carbon nanomaterial based on graphene (Figure 1.13a). Single and multi-wall nanotubes can be easily explained as rolled graphene sheets in a tubular shape. M. Endo and coworkers were the first group to report the existence of these nano shapes by HRTEM trying to produce carbon fibers by a modified chemical vapor deposition (CVD) method

in 1976 (Oberlin *et al.*, 1976), but this paper had not a broad impact at this time because researchers were only focused in carbon nanomaterials after the discovery of fullerenes. In 1991 Sumio Iijima (Iijima, 1991a) confirmed the rolled graphene layer nature of MWCNTs synthesized by using the same method for producing fullerenes, an arc-discharge between graphite electrodes in an inert atmosphere without metal catalyst. Two years later, in 1993, both Iijima's (Iijima & Ichihashi, 1993) and Bethune's groups (Bethune *et al.*, 1993) reported the synthesis of SWCNTs adding during the synthetic process a metal catalyst.

Since the discovery of the first CNTs, researchers have continued with the theoretical and experimental studies of these tubular nano shapes. While the perfect CNT is a rolled hexagonal network layer, structural defects can produce the curvature of the tube. In this sense, **Coiled carbon nanotubes** are a good example (Figure 1.13b), when paired pentagon-heptagon atomic rings arrange themselves periodically within the hexagonal carbon network the tube adopts a spiral shape. Although the formation mechanism is not well understood, the model of localized stresses and anisotropic rates of carbon deposition on catalyst particles is the most widely accepted (Zhang & Li, 2009; Zhang *et al.*, 2000). The insertion of non-hexagonal rings in a particular region of the network also can result on **branched carbon nanotubes**, making possible the constructions of various angles from Y to T shapes (Biró *et al.*, 2004). The CNTs growth direction can also be tuned by the application of an external force originated from an electric field (Nojeh *et al.*, 2004) or gas flow (Jin *et al.*, 2007), yielding the called **regularly bent carbon nanotubes**. Another example of different shape CNTs are the **carbon nanotubes with beads**: beads coated with amorphous or polycrystalline carbon on the surface, adopting various shapes such as spheres, cubes or other polyhedra. It is believed that those beads are formed during the nanotube growth and their shape is related to the type of catalyst seeds (de Heer *et al.*, 2005; Lujun Pan *et al.*, 2001).

Another 1D nano-shaped carbon material that is attracting a lot of attention nowadays is the called **graphene nanoribbons** (GNRs) which consist on a graphene layer in which one of its dimensions has been limited to the nanoscale (Figure 1.13c). The lateral confinement not present in extended graphene endows the GNRs with unusual properties, opening a band gap and controlling quantum states (Bianco *et al.*, 2018). These new properties depend dramatically on the details of the atomic structure of the GNR in such way that the precise control in their synthesis is a crucial parameter in order to harness the full potential of graphene nano-systems and exploit their properties as quantum materials for novel applications.

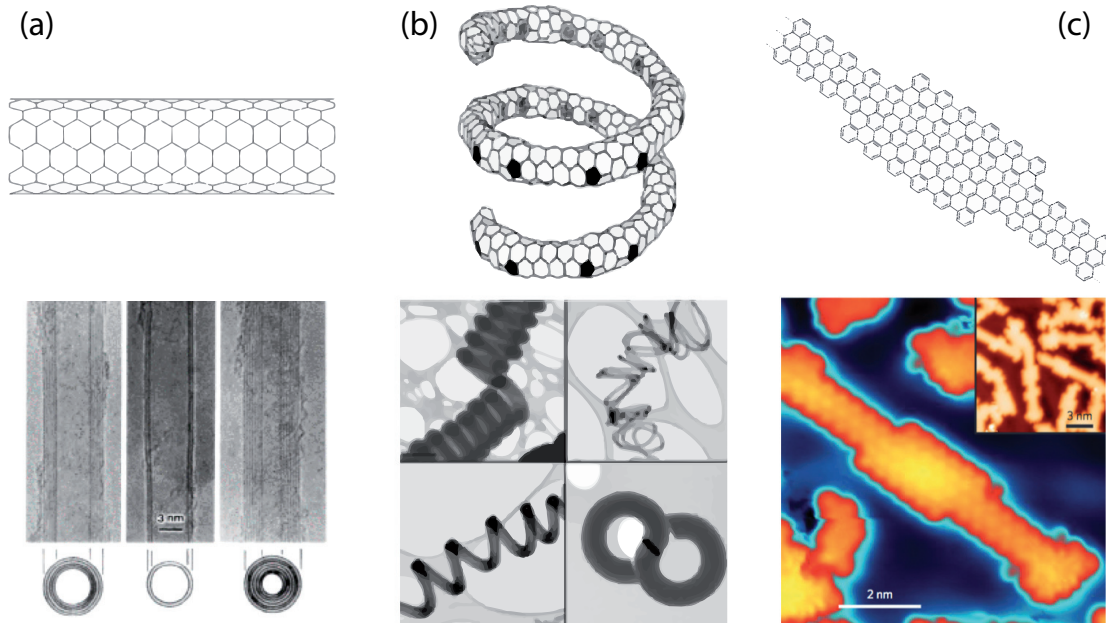


Figure 1.13: Structure Schemes and TEM images of (a) CNTs (Iijima, 1991b) and (b) coiled carbon nanotubes (Shaikjee & Coville, 2012). (c) Structural scheme and AFM image of GNRs (Chen *et al.*, 2015).

Therefore conventional synthesis methods without such precise atomic structure control as chemical vapor deposition (CVD) are excluded. However, recently developments on-surface chemical methods are novel strategies to synthesize these carbon materials. Fasel and Müllen in 2010 (Cai *et al.*, 2010) were pioneers on the surface-assisted bottom-up assembly of small precursor monomers into atomically precise GNRs. In this synthesis method the design of the starting monomer becomes an important step while expanding the family of GNR carbon materials.

## Two dimensions nanomaterials

An infinite two dimensional layer of  $sp^2$  hybridized carbon atoms is what is commonly known as **graphene** (Figure 1.14a). Andrei Geim and Kostya Novoselov were awarded with the Nobel Prize in Physics on 2010 "for groundbreaking experiments regarding the two-dimensional material graphene" (The Nobel Prize, 2010) regarding their discovery in 2004. Since then, graphene has emerged as one of the most popular topic in research because of its extraordinary properties, which have attracted the interest of researchers all over the world. This 2D one-atom thick structure of carbon has as fingerprint a unique electronic structure with lin-

ear dispersion close to the Fermi level. Charge carriers in graphene are better described as massless Dirac fermions, which result in new phenomena (Terrones *et al.*, 2010). Also, bilayers and few-layer-graphene can be included as pseudo 2D carbon structures as transition materials from graphene to graphite with different physicochemical properties than both of them, but where graphene properties can be recovered when stacking disorder is introduced.

Several methods have been reported for graphene synthesis that can be divided into two different approaches: the top-down and the bottom-up. The top-down approach implies the exfoliation of graphite into its graphene sheets, where mechanical exfoliation has been the turning point in the history of graphene and is still the key synthesis technique for obtaining high quality graphene for research purposes, although often entails tedious procedures and low yields (Edwards & Coleman, 2013). Currently, the most common way to produce graphene at large scale in research is in its oxide form following the Hummer's method (Hummers & Offeman, 1958) or derivatives, which consists of a graphite exfoliation by an aggressive acid treatment. On the other hand, the bottom-up approach implements carbon molecules as building blocks for graphene layers acquisition. Even though nowadays it is not suitable for the production of graphene sheets with large surface area, this approach offers the possibility of manufacturing GNRs and nanographenes in large quantities (Warner *et al.*, 2012).

### Three dimensions nanomaterials

As it has been previously described, the stacking of 2D graphene layers results in the 3D graphite, which is the most common carbon structure formed by  $sp^2$  hybridized carbon atoms. However, the layers not always stack in an ordered way, but in random orientations. This concept called turbostatic carbon layers was introduced by B. E. Warren in 1941 (Warren, 1941) while discussing the X-ray diffraction pattern from **carbon black**. Except for 001 reflections, the random orientations prevent the appearance of general  $hkl$  reflections, and for this reason these materials started to be called **disordered carbon materials**. Rosalind E. Franklin in 1951 proposed for the first time a new brilliant structural model for graphitising and non-graphitising carbons (Franklin & Randall, 1951), where the basic structural unit are small graphitic crystallites containing a few layers, which are joined together by cross-links. In graphitising carbons the structural units are approximately parallel to each other and in a non-graphitising carbon are oriented randomly. Years later, the advent of electron microscopy allowed the direct observation of these non-graphitising materials at high resolution giving



rise to a new model in which the structural unit consist on an arrangement of ribbon-shaped layer planes (Ban *et al.*, 1975).

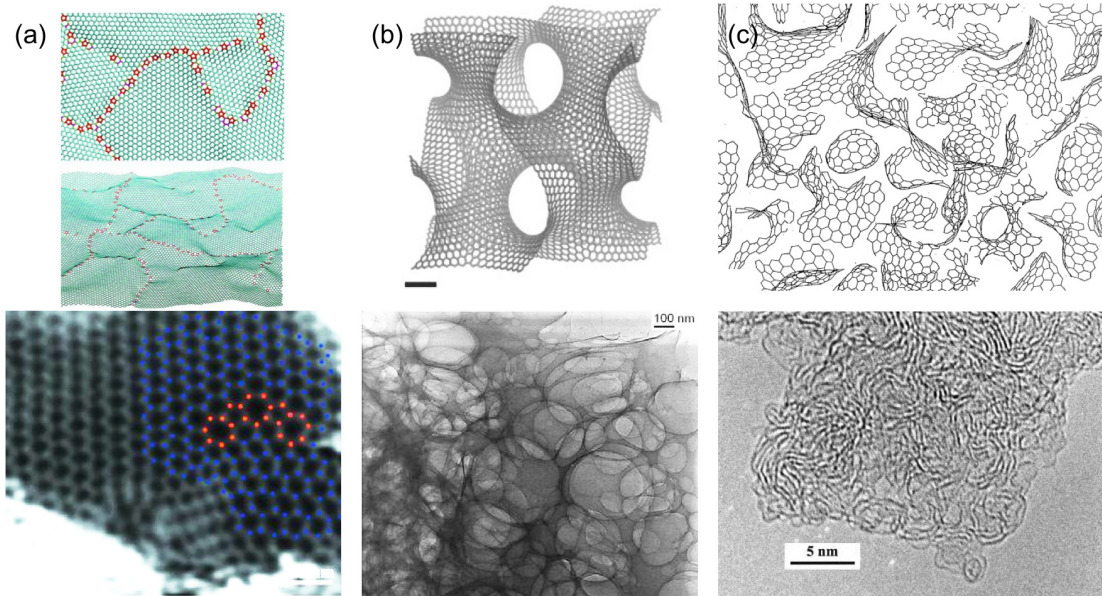


Figure 1.14: Structure scheme and TEM images of (a) graphene layer with some non-hexagonal rings (red) (Guo *et al.*, 2012), (b) Schwarzites (Benedek *et al.*, 2011; Miller *et al.*, 2016) and (c) disordered carbon following the model proposed by Harris and Tsang (Harris, 2004).

So far, the planarity of  $sp^2$  layers has not been questioned, but some researchers pointed out the presence of defects in these layers that break the planarity such as  $sp^3$  bonded atoms and carbon rings with different number than six atoms (Dasgupta & Sathiyamoorthy, 2003). If the graphene layer contains periodic carbon rings with more than six atoms a negative curvature could be produced, obtaining a  $sp^2$  carbon material structurally similar to zeolites that is called **Schwarzites** (Terrones & Terrones, 2003) (Figure 1.14b). In most cases these structural models are ordered, but disordered structures are much more likely in reality, for example the layer curvatures in schwarzites could not be periodic, with result on **carbon nanofoams**, structures that can be visualized as microporous carbons exhibiting nanochannels. These disordered structures (Figure 1.14c) have also been considered in the model proposed by Harris and Tsang in which the structure of non-graphitising carbon consists of discrete fragments of randomly curved carbon sheets (Harris & Tsang, 1997).



### 1.3.3 The $sp^3$ hybridization: Nano Diamonds

The bulk material composed by  $sp^3$  hybridized carbon atoms in an hexagonal close packing is the precious **diamond** with cubic structure in the  $Fd\bar{3}m$  space group. At the nano scale, diamond structures have been found in meteorites and interplanetary dust (Lewis *et al.*, 1987) as well as earth sediments 13,000 years old. The first, although involuntary, **nanodiamonds** produced were in the USSR in the 1960s by detonation, in an attempt of preparing diamond from non-diamond carbon. But until 1980s these works were unknown in the rest of the world and they were not considered of special interest until late 1990s when their possible applications as non-toxic alternative to semiconductor quantum dots in biomedical imaging, magnetic sensors, drug delivery and other areas of medicine began to be discovered (Mochalin *et al.*, 2011).

At present, nanodiamonds can be synthesized by several techniques. In addition of the use of explosion energy, as pioneer researchers in this field, techniques like laser assisted synthesis, high temperature high pressure method (HTHP) or high energy ball milling of microcrystalline diamond are used for industrial production of nanodiamonds. But there are other techniques to obtain nanodiamonds like hydrothermal synthesis, chemical vapour deposition (CVD) synthesis, ion bombardment on graphite, chlorination of carbides or ultrasonic cavitation, among others (Khan, 2018).

### 1.3.4 Carbon materials as electrodes on supercapacitor devices

As mentioned above, carbon materials are classically used as electrodes on electrochemical capacitors (Pandolfo & Hollenkamp, 2006; Simon & Gogotsi, 2013; Zhai *et al.*, 2011; Zhang *et al.*, 2009). Carbon is one of the most flexible elements in structural terms, it can form different structures depending of its possible hybridization  $sp$ ,  $sp^2$  and  $sp^3$  including the combination of both  $sp^n$  as seen above. From all the carbon allotropes, those described below are the most used as electrode materials on supercapacitors because they fit almost all the necessary requirements such as high surface area and conductive properties, low cost (in some cases are obtained from wastes), easy availability, nontoxic nature, environmental friendliness and stability (Figure 1.15).

The  $sp^2/sp^3$  ratio gives an idea of how the graphene layer is curved and struc-


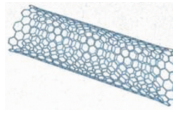
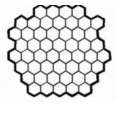
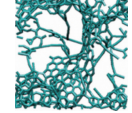
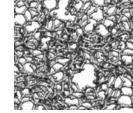

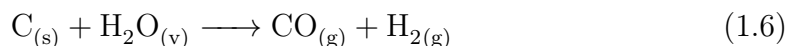
Material	Carbon onions	Carbon nanotubes	Graphene	Activated carbon	Carbide derived carbon	Templated carbon
Dimensionality	0-D	1-D	2-D	3-D	3-D	3-D
Conductivity	High	High	High	Low	Moderate	Low
Volumetric Capacitance	Low	Low	Moderate	High	High	Low
Cost	High	High	Moderate	Low	Moderate	High
Structure						

Figure 1.15: Different carbon structures used in EDLCs (after Simon & Gogotsi, 2013).

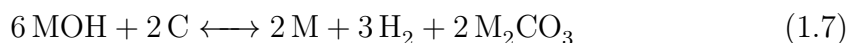
tured in each carbon. In the case of the onion-like carbons (OLCs) the layer is curved in their three dimensions, forming nanoparticles concentric graphene spherical shells, as all its dimensions are limited, it is a zero-dimensional material, and works as a discrete bulk material. These carbons have surface areas up to  $500\text{-}600\text{ m}^2\text{ g}^{-1}$  and very high electrical conductivity, and a capacitance values between  $70\text{-}100\text{ F g}^{-1}$  in alkaline electrolyte (Zhang *et al.*, 2010). If the graphene layers are rolled in one dimension, then SWNTs and MWCNTs are obtained. Capacitances of these materials are between  $100\text{ F g}^{-1}$  for MWCNTs (Niu *et al.*, 1997) to  $180\text{ F g}^{-1}$  for SWCNTs (An *et al.*, 2001) with similar respective surface areas of  $430$  and  $357\text{ m}^2\text{ g}^{-1}$ . OLCs and CNTs are excellent choices for devices with very high power density and a moderate volumetric capacitance, due to their poor density close to  $0.3\text{ g cm}^{-3}$ . Even so, CNTs are extensively used as a base matrix in the search for composite materials in order to increase its energy density without losing power density (Jurewicz *et al.*, 2001; Luo *et al.*, 2017; Yao *et al.*, 2017).

Graphene has a theoretical surface area of about  $2670\text{ m}^2\text{ g}^{-1}$  and its electrical conductivity is the highest of all carbon allotropes. But in practice, it is very difficult to obtain just one single layer and, if this was achieved, the sheets would tend to re-stacking into graphite form during the manufacture of the electrode. In order to have separated sheets a certain shift of  $sp^2$  hybridization into  $sp^3$  is needed, which entails some folding to the sheet, avoiding restacking by forming an amorphous and disordered carbon material. This modification strongly affects to the promising properties of graphene by decreasing the surface area to values similar to those found in CNTs and capacitances of  $100\text{ F g}^{-1}$ . Like CNTs, graphene is widely used as matrix in the development of composite materials. As a particular example, in a composite material made of a mixture of graphene and CNTs in an attempt to avoid the graphene stacking by placing CNTs between the layers (Cheng *et al.*, 2011; Du *et al.*, 2011; Yu & Dai, 2010).

Activated Carbons (AC) are the most representative materials in this field, they have the largest surface area above  $2000 \text{ m}^2 \text{ g}^{-1}$ . These carbons materials are easily produced in large quantities and relatively low cost from fossil fuels like petroleum coke, pitch and coal; but the growing of global energy demand and the increase in awareness of environmental impacts of fossil fuel combustion led to the ACs production from sustainable and renewable natural carbon resources like wood, coconut shells, cellulose, fruit pits or anthracite for example (González-García, 2018). The process to obtain these carbons is divided in two steps: the first one consists of the pyrolysis of the carbon precursor. In this stage, all elements and natural oils typical of the vegetal mass are removed or reduced to their minimum from the material. In a second step, the material is subjected to a physical or chemical activation process. In the physical activation, the carbonized materials is thermally treated between  $400\text{-}1000 \text{ }^\circ\text{C}$  in the presence of inert (Ar,  $\text{N}_2$ ) or oxidizing gases such as water, carbon dioxide or both. Under these conditions carbon reacts yielding  $\text{CO (g)}$  and  $\text{H}_2 \text{ (g)}$ . For example, the activation with water steam can be described by the following reaction:



The release of gases helps maintain the activation temperature and gives rise to the formation of micro, meso and macropores (Sevilla & Mokaya, 2014). One of the most used reagents for chemical activation are NaOH or KOH which react with carbon through the following reaction:

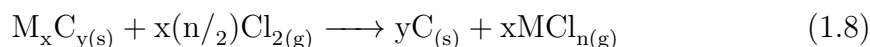


The main advantages of this process over physical activation rely on the high yield, development of microporosity, less energy requirements and activation time, but the cost and environmental impact of the activating agents are the biggest drawbacks.

Nowadays, ACs based supercapacitors give more than  $200 \text{ F g}^{-1}$  in organic electrolytes (Wei *et al.*, 2011) with a density higher than other carbon types of about  $0.4\text{-}0.7 \text{ g cm}^{-3}$ . But the main problem associated to these carbons is that its porosity is totally unpredictable, and as we just seen above, is a critical factor to reach good electrochemical performances. Also, their conductivity is not very high being in the range of  $0.1\text{-}1 \text{ S cm}^{-1}$  depending on the thermal treatment (Zhang *et al.*, 2010). This poor conductivity in comparison with graphite is due to the presence

of oxygenated functional groups developed in the surface during the activation process that localize the charge on their site, decreasing the electronic cloud over the carbon structure. In addition, the lost of planarity within the graphene layers forming the ACs avoiding a free movement of the  $\pi$  electrons together with the formation of insulating voids related to the pores development also contributes to worsen the electrical conductivity of ACs.

On the other hand, although Carbide-derived Carbons can be obtained by several synthetic procedures, such as reaction of calcium carbide with inorganic salts at high temperatures (Nikitin & Gogotsi, 2004), hydrothermal lixiviation of carbides at high temperatures (300-1000 °C) and pressures (2-200 MPa) (Gogotsi & Yoshimura, 1994) or by extraction of the metal atoms of the carbide under vacuum at temperatures around 1200 °C (Kosolapova, 1971), the high-temperature etching with halogens, commonly chlorine, is the most employed. In this methods the metal atoms are removed from the crystalline network by forming the corresponding volatile metal halide yielding a nanostructured carbon material with high surface area and tunable pore size (Chmiola *et al.*, 2010; Gogotsi *et al.*, 2003; Presser *et al.*, 2011; Yushin *et al.*, 2006). The chlorination reaction can be postulated as follows:



Chlorine treatment has successfully been employed for CDC synthesis from a variety of carbide precursors, including SiC, TiC, B<sub>4</sub>C, BaC<sub>2</sub>, CaC<sub>2</sub>, Cr<sub>3</sub>C<sub>2</sub>, Fe<sub>3</sub>C, Mo<sub>2</sub>C, Al<sub>4</sub>C<sub>3</sub>, Nb<sub>2</sub>C, SrC<sub>2</sub>, Ta<sub>2</sub>C, VC, WC, W<sub>2</sub>C, ZrC, ternary carbides such as Ti<sub>2</sub>AlC, Ti<sub>3</sub>AlC<sub>2</sub>, and Ti<sub>3</sub>SiC<sub>2</sub>, and carbonitrides such as Ti<sub>2</sub>AlC<sub>0.5</sub>N<sub>0.5</sub>. Through this method, highly disordered carbon materials with surface areas up to 2000 m<sup>2</sup> g<sup>-1</sup>, similar to the ACs, can be obtained. But in this case, unlike ACs, the pore structure can be tuned. It is not a common rule for all carbides, as each metal reacts in a different way with chlorine, but in some cases like TiC and SiC (the most studied) the pore size can be tuned from 0.6 to 1.1 nm by controlling the temperature synthesis. This is an important advantage in comparison with the ACs, since, as we have seen above, the pore structure of the carbon is a key factor in its electrochemical behaviour. Research in this field has shown that a greater capacitance can be obtained by fitting the pore and electrolyte size. (Chmiola *et al.*, 2006). Additionally, whereas the carbonization process uncontrollable, the metal etching occurs from the outside to the inside of the material allowing the control of carbon growth at the atomic level, layer by layer (see Figure 1.16).

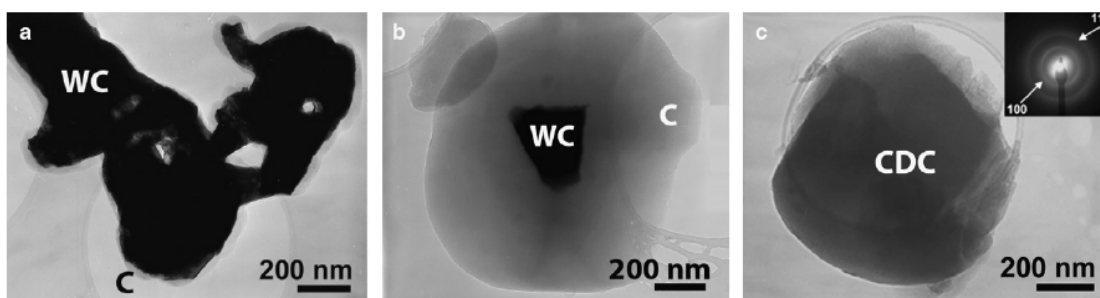


Figure 1.16: Carbonization process of WC at 700 °C, 800 °C and 900 °C (González-García *et al.*, 2010).

Finally, templated porous carbons are a family of nanostructured carbons with well controlled narrow pore size distributions, ordered pore structures, large specific surface areas and an interconnected pore network. They are produced by infiltration of a carbon precursor into the pores of an inorganic template, followed by the carbonization of the organic precursor and removal of the template. In this type of carbon materials the porous structure can be better controlled than in CDCs, similar surface area can be developed and different shapes like nanotubes or spheres, among others, by using different micellar systems or inorganic zeolites templates can be produced (Francois Beguin, 2009). The properties described before, make them promising candidates for supercapacitor electrode materials. In fact electrochemical measurements have reported values of gravimetric capacitance up to 350 F g<sup>-1</sup> in aqueous and 140 F g<sup>-1</sup> in organic electrolytes (Yamada *et al.*, 2007). Even so, their synthesis usually involves several steps and become more tedious and expensive than for the other carbon materials.

### 1.3.5 Carbon-based composite materials for supercapacitors

Pseudocapacitive materials have attracted great interest in the development of supercapacitor electrodes with enhanced energy storage performances. However, this mechanism is only effective in a very thin surface of the material, where the Faradaic reactions occurs. In the particular case of pseudocapacitive metal oxides the poor electronic conductivity of most of them linked to the electrode crack suffered after a certain number of cycles (<10000) (Lokhande *et al.*, 2016) has limited their practical application as electrodes. The design of carbon-based composite materials, where the carbon provides mechanical strength to the supported pseudocapacitive material, better electrical conductivity and its own capacitive component resulted in new materials showing improved capacitive properties. In

addition, these carbon-based composite materials exhibit highest densities yielding improved volumetric capacitances. The Ragone plot displayed in Figure 1.17 shows how the electrochemical performance (especially the energy density) of some typical capacitive and pseudocapacitive materials used as supercapacitors electrodes is improved after the preparation of a carbon-based composite material.

ACs have been widely studied as support for pseudocapacitive metal-oxide nanoparticles such as  $\text{RuO}_2$  (Yang *et al.*, 2015a),  $\text{Zn}_2\text{SnO}_4$  (Jin *et al.*, 2018) or Ni@NiO core/shell structures (Zhang *et al.*, 2014) where beside increase the capacitance value, the cycle life of the electrode is greatly extended. In combination with CNTs, ACs can generate composites able to undergo 50000 cycles with a slight loss of capacitance, instead similar ACs without CNTs where capacitance decrease after 30000 cycles (Borenstien *et al.*, 2013). Meanwhile, CNTs offers a tubular structure with more surface area than solid structures, high electric conductivity and mechanical and chemical stability, making it a good option for a composite electrode. Another example is the composite based on CNTs and  $\text{RuO}_2$  hollow nanospheres yielding high capacitance values up to  $819 \text{ F g}^{-1}$  (Wang *et al.*, 2015) attributed to the good dispersion of ruthenium oxide particles on the carbon nanostructure, and in combination with polymeric species give excellent performance under organic electrolytes (Noked *et al.*, 2012). CNTs also provided a well aligned structure with mechanical stability and high electronic conductivity for the  $\text{MnO}_2$  nanoparticles, enhancing the rate capability of  $\text{MnO}_2$  which trend to decrease due to the collapse of the structure over time (Gao *et al.*, 2015). These composite materials could exhibit high specific capacitance up to  $950 \text{ F g}^{-1}$  achieved in a synthesized composite by the reduction of potassium permanganate under microwave irradiation (Yan *et al.*, 2009).

Graphene and derivatives (graphene oxide (GO) and reduced graphene oxide (rGO)) are the two dimensional carbon materials most used for their combination on a composite material for electrodes on supercapacitors. Higher capacitance values up to  $1365 \text{ F g}^{-1}$  have been reported for a composite consisting on GO with ultrafine  $\text{RuO}_2$  nanoparticles (Yang *et al.*, 2015b), where the layered structure of GO provides excellent sites for  $\text{RuO}_2$  deposition while maintaining the well-defined pathways for ion diffusion. Graphene increases considerably the electrical conductivity of pseudocapacitive metal-oxides like tungsten oxide (Ratha & Rout, 2013), vanadium oxide (Lee *et al.*, 2015), nickel oxide (Chen *et al.*, 2014) or manganese oxides (Chen *et al.*, 2018; Gund *et al.*, 2013; Ye *et al.*, 2013), at the same time that provides a great support with high specific surface area and suitable pore structure.

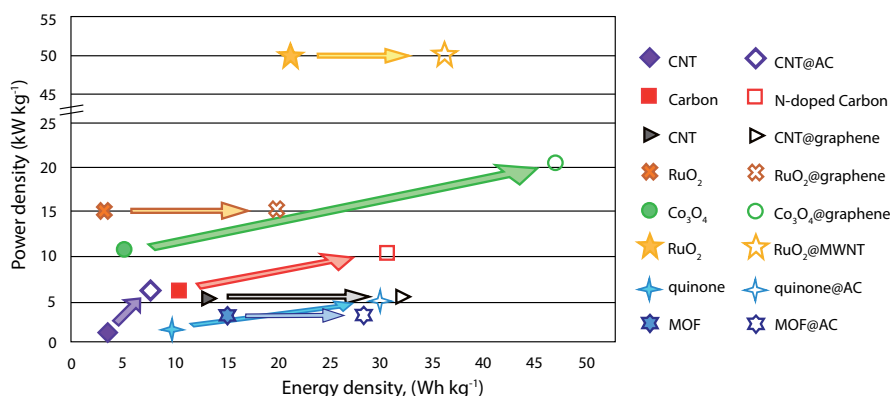


Figure 1.17: Ragone plots of some redox active materials relevant for pseudocapacitive and/or faradaic charge storage and improved composite electrodes comprising these materials in composite structures with carbonaceous materials (after Borenstein *et al.*, 2017).

Carbon aerogels are the 3D structured materials preferred for combining in a composite. For example tungsten oxide nanoparticles dispersed on a mesoporous carbon aerogel shows a capacitance value of  $700 \text{ F g}^{-1}$  compared to  $54 \text{ F g}^{-1}$  of only from  $\text{WO}_3$  nanoparticles (Wang *et al.*, 2014).

Additionally, not only inorganic compounds are considered for the preparation of electrochemically improved composites. There are many organic compounds that exhibit reversible redox reactions in electrochemical systems, which may promote their usage in composite electrodes for energy storage devices. Quinone and its derivatives is one of the most studied and effective organic compounds (Navalpotro *et al.*, 2016; Navarro-Suárez *et al.*, 2017). Such organic molecules can be linked or adsorbed to carbonaceous materials yielding a composite materials with relatively high and stable specific capacitance (Roldán *et al.*, 2011).

## Bibliography

AN, K. H., KIM, W. S., PARK, Y. S., MOON, J.-M., BAE, D. J., LIM, S. C., LEE, Y. S. & LEE, Y. H. (2001). Electrochemical properties of high-power supercapacitors using single-walled carbon nanotube electrodes. *Advanced Functional Materials* **11**(5), 387–392.

AUGUSTYN, V., SIMON, P. & DUNN, B. (2014). Pseudocapacitive oxide materials for high-rate electrochemical energy storage. *Energy and Environmental Science* **7**(5), 1597–1614.

BAN, L. L., CRAWFORD, D. & MARSH, H. (1975). Lattice-resolution electron microscopy in

- structural studies of non-graphitizing carbons from polyvinylidene chloride (pvdc). *Journal of Applied Crystallography* **8**(4), 415–420.
- BECKER, H. I. (1957). Low voltage electrolytic capacitor. US Patent 2800616.
- BENEDEK, G., BERNASCONI, M., CINQUANTA, E., D-ALESSIO, L. & CORATO, M. D. (2011). *Carbon Materials: Chemistry and Physics*. Springer, Dordrecht.
- BETHUNE, D. S., KIANG, C. H., DE VRIES, M. S., GORMAN, G., SAVOY, R., VAZQUEZ, J. & BEYERS, R. (1993). Cobalt-catalysed growth of carbon nanotubes with single-atomic-layer walls. *Nature* **363**, 605–607.
- BIANCO, A., CHEN, Y., CHEN, Y., GHOSHAL, D., HURT, R. H., KIM, Y. A., KORATKAR, N., MEUNIER, V. & TERRONES, M. (2018). A carbon science perspective in 2018: Current achievements and future challenges. *Carbon* **132**, 785–801.
- BIRÓ, L., HORVÁTH, Z., MÁRK, G., OSVÁTH, Z., KOOS, A., BENITO, A., MASER, W. & LAMBIN, P. (2004). Carbon nanotube y junctions: growth and properties. *Diamond and Related Materials* **13**, 241–249.
- BOOS, P. (2014). A technology in review : Energy storage a technology in review : Energy storage.
- BORENSTEIN, A., HANNA, O., ATTIAS, R., LUSKI, S., BROUSSE, T. & AURBACH, D. (2017). Carbon-based composite materials for supercapacitor electrodes: a review. *J. Mater. Chem. A* **5**(25), 12653–12672.
- BORENSTIEN, A., NOKED, M., OKASHY, S. & AURBACH, D. (2013). Composite carbon nanotubes (cnt)/activated carbon electrodes for non-aqueous super capacitors using organic electrolyte solutions. *J. Electrochem. Soc.* **160**(8), A1282–A1285.
- BP (2018). BP Technology Outlook.
- BURKE, A. & ZHAO, H. (2015). Applications of supercapacitors in electric and hybrid vehicles.
- CAI, J., RUFFIEUX, P., JAAFAR, R., BIERI, M., BRAUN, T., BLANKENBURG, S., MUOTH, M., SEITSONEN, A. P., SALEH, M., FENG, X., MÜLLEN, K. & FASEL, R. (2010). Atomically precise bottom-up fabrication of graphene nanoribbons. *Nature* **466**, 470–473.
- CAMISASCA, A. & GIORDANI, S. (2017). Carbon nano-onions in biomedical applications: Promising theranostic agents. *Inorganica Chimica Acta* **468**, 67–76.
- CAP-XX (2015). Cap-xx launches 0.6mm thinline supercapacitors to power wearable, ultra-portable and connected IoT devices. url <https://www.cap-xx.com/929/>. Accessed: 06-09-2018.
- CHEN, L., GUO, X., LU, W., CHEN, M., LI, Q., XUE, H. & PANG, H. (2018). Supercapacitive composite metal oxide electrodes formed with carbon, metal oxides and conducting polymers. *Coordination Chemistry Reviews* **368**, 13–34.



- CHEN, Y., HUANG, Z., ZHANG, H., CHEN, Y., CHENG, Z., ZHONG, Y., YE, Y. & LEI, X. (2014). Synthesis of the graphene/nickel oxide composite and its electrochemical performance for supercapacitors. *International Journal of Hydrogen Energy* **39**(28), 16171–16178.
- CHEN, Y.-C., CAO, T., CHEN, C., PEDRAMRAZI, Z., HABERER, D., DE OTEYZA, D. G., FISCHER, F. R., LOUIE, S. G. & CROMMIE, M. F. (2015). Molecular bandgap engineering of bottom-up synthesized graphene nanoribbon heterojunctions. *Nature Nanotechnology* **10**, 156–160. URL <https://doi.org/10.1038/nnano.2014.307>.
- CHENG, Q., TANG, J., MA, J., ZHANG, H., SHINYA, N. & QINC, L.-C. (2011). Graphene and carbon nanotube composite electrodes for supercapacitors with ultra-high energy density. *Phys. Chem. Chem. Phys.* **13**, 17615–17624.
- CHMIOLA, J., LARGEOT, C., TABERNA, P.-L., SIMON, P. & GOGOTSI, Y. (2010). Monolithic carbide-derived carbon films for micro-supercapacitors. *Science* **328**, 480–483.
- CHMIOLA, J., YUSHIN, G., GOGOTSI, Y., PORTET, C. & TABERNA, P. L. (2006). Anomalous increase in carbon capacitance at pore sizes less than 1 nanometer. *Science* **313**(5794), 1760–1764.
- CONWAY, B. E. (1999). *Electrochemical Supercapacitors*. Kluwer Academic.
- CONWAY, B. E., BIRSS, V. & WOJTOWICZ, J. (1997). The role and utilization of pseudocapacitance for energy storage by supercapacitors. *J. Power Sources* **66**, 1–14.
- DASGUPTA, K. & SATHIYAMOORTHY, D. (2003). Disordered carbon: its preparation, structure, and characterisation. *Materials Science and Technology* **19**(8), 995–1002.
- DE HEER, W. A., PONCHARAL, P., BERGER, C., GEZO, J., SONG, Z., BETTINI, J. & UGARTE, D. (2005). Liquid carbon, carbon-glass beads, and the crystallization of carbon nanotubes. *Science* **307**(5711), 907–910.
- DEGHANI-SANIJ, A., THARUMALINGAM, E., DUSSEAULT, M. & FRASER, R. (2019). Study of energy storage systems and environmental challenges of batteries. *Renewable and Sustainable Energy Reviews* **104**, 192–208.
- DELGADO, J. L., HERRANZ, M. A. & MARTÍN, N. (2008). The nano-forms of carbon. *J. Mater. Chem.* **18**(13), 1417–1426.
- DU, F., YU, D., DAI, L., GANGULI, S., VARSHNEY, V. & ROY, A. K. (2011). Preparation of tunable 3d pillared carbon nanotube-graphene networks for high-performance capacitance. *Chem. Mater.* **23**(21), 4810–4816.
- EDWARDS, R. S. & COLEMAN, K. S. (2013). Graphene synthesis: relationship to applications. *Nanoscale* **5**(1), 38–51.
- ENERDATA (2018). World energy statistical yearbook. url <https://yearbook.enerdata.net/>. Accessed: 06-09-2018.
- ENERGY STORAGE ASSOCIATION (2017). Energy storage technologies. url <http://energystorage.org/energy-storage/energy-storage-technologies>. Accessed: 06-09-2018.

- EUROPEAN SPACE AGENCY (2014). Opening doors to space. url <http://www.esa.int>. Accessed: 06-09-2018.
- FRANCOIS BEGUIN, E. F. (2009). *Carbons for Electrochemical Energy Storage and Conversion Systems*. CRC Press.
- FRANKLIN, R. E. & RANDALL, J. T. (1951). Crystallite growth in graphitizing and non-graphitizing carbons. *Proceedings of the Royal Society A: Mathematical and Physical Sciences* **209**(1097), 196–218.
- GAO, B., LI, X., MA, Y., CAO, Y., HU, Z., ZHANG, X., FU, J., HUO, K. & CHU, P. K. (2015). MnO<sub>2</sub>@TiO<sub>2</sub>/c nanocomposite arrays for high-performance supercapacitor electrodes. *Thin Solid Films* **584**, 61–65.
- GOGOTSI, Y., NIKITIN, A., YE, H., ZHOU, W., FISCHER, J. E., YI, B., FOLEY, H. C. & BARSOUM, M. W. (2003). Nanoporous carbide-derived carbon with tunable pore size. *Nature Materials* **2**, 591.
- GOGOTSI, Y. & SIMON, P. (2011). True performance metrics in electrochemical energy storage. *Science* **334**(6058), 917–918.
- GOGOTSI, Y. G. & YOSHIMURA, M. (1994). Formation of carbon films on carbides under hydrothermal conditions. *Nature* **367**, 628–630.
- GONZÁLEZ-GARCÍA, P. (2018). Activated carbon from lignocellulosics precursors: A review of the synthesis methods, characterization techniques and applications. *Renewable and Sustainable Energy Reviews* **82**, 1393–1414.
- GONZÁLEZ-GARCÍA, P., URONES-GARROTE, E., ÁVILA-BRANDE, D., GÓMEZ-HERRERO, A. & OTERO-DÍAZ, L. C. (2010). Structural study of carbon nanomaterials prepared by chlorination of tungsten carbide and bis (cyclopentadienyl) tungsten dichloride. *Carbon* **48**(13), 3667–3675.
- GUND, G. S., DUBAL, D. P., PATIL, B. H., SHINDE, S. S. & LOKHANDE, C. D. (2013). Enhanced activity of chemically synthesized hybrid graphene oxide/mn<sub>3</sub>o<sub>4</sub> composite for high performance supercapacitors. *Electrochimica Acta* **92**, 205–215.
- GUO, J., MORRIS, J. R., IHM, Y., CONTESCU, C. I., GALLEGO, N. C., DUSCHER, G., PENNYCOOK, S. J. & CHISHOLM, M. F. (2012). Topological defects: Origin of nanopores and enhanced adsorption performance in nanoporous carbon. *Small* **8**(21), 3283–3288.
- HAHN, U., MAISONHAUTE, E. & NIERENGARTEN, J.-F. C. (2018). Twisted n-doped nanographenes: Synthesis, characterization, and resolution. *Angewandte Chemie International Edition* **57**(33), 10635–10639.
- HARRIS, P. & TSANG, S. (1997). High-resolution electron microscopy studies of non-graphitizing carbons. *Philosophical Magazine A* **76**(3), 667–677.
- HARRIS, P. J. F. (2004). Fullerene-related structure of commercial glassy carbons. *Philosophical Magazine* **84**(29), 3159–3167.

- HUMMERS, W. S. & OFFEMAN, R. E. (1958). Preparation of graphitic oxide. *Journal of the American Chemical Society* **80**(6), 1339–1339.
- IJIMA, S. (1991a). Helical microtubules of graphitic carbon. *Nature* **354**, 56–58.
- IJIMA, S. (1991b). Helical microtubules of graphitic carbon. *Nature* **354**, 56–58.
- IJIMA, S. & ICHIHASHI, T. (1993). Single-shell carbon nanotubes of 1-nm diameter. *Nature* **363**, 603–605.
- IJIMA, S., YUDASAKA, M., YAMADA, R., BANDOW, S., SUENAGA, K., KOKAI, F. & TAKAHASHI, K. (1999). Nano-aggregates of single-walled graphitic carbon nano-horns. *Chemical Physics Letters* **309**(3), 165–170.
- İNCI, M. & TÜRKSOY, O. (2019). Review of fuel cells to grid interface: Configurations, technical challenges and trends. *Journal of Cleaner Production* **213**, 1353–1370.
- INTERNATIONAL ENERGY AGENCY (2017). World energy outlook. url <https://www.iea.org/weo2017/>. Accessed: 06-09-2018.
- JIN, K., WANG, Q., CHEN, L., LV, Z., XU, J., HONG, B. & WANG, X. (2018).  $\text{Zn}_2\text{SnO}_4$ /activated carbon composites for high cycle performance supercapacitor electrode. *Journal of Alloys and Compounds* **767**, 419–423.
- JIN, Z., CHU, H., WANG, J., HONG, J., TAN, W. & LI, Y. (2007). Ultralow feeding gas flow guiding growth of large-scale horizontally aligned single-walled carbon nanotube arrays. *Nano Letters* **7**(7), 2073–2079.
- JUREWICZ, K., DELPEUX, S. & BERTAGNA, V. (2001). Supercapacitors from nanotubes/polypyrrole composites. *Chemical Physics Letters* **347**, 36–40.
- KANG, C.-S., FUJISAWA, K., KO, Y.-I., MURAMATSU, H., HAYASHI, T., ENDO, M., KIM, H. J., LIM, D., KIM, J. H., JUNG, Y. C., TERRONES, M., DRESSELHAUS, M. S. & KIM, Y. A. (2016). Linear carbon chains inside multi-walled carbon nanotubes: Growth mechanism, thermal stability and electrical properties. *Carbon* **107**, 217–224.
- KHAN, Z. H. (2018). *Nanomaterials and Their Applications*. Springer Nature Singapore.
- KOSOLAPOVA, T. Y. (1971). *Carbides. Properties, Production, and Applications*. Plenum Press.
- KROTO, H. W., HEATH, J. R., O'BRIEN, S. C., CURL, R. F. & SMALLEY, R. E. (1985). C60: Buckminsterfullerene. *Nature* **318**, 162–163.
- KULARATNA, N. (2015). Energy storage devices: a general overview. In: *Energy Storage Devices for Electronic Systems*. Boston: Academic Press, pp. 1–28.
- LEE, M., WEE, B.-H. & HONG, J.-D. (2015). High performance flexible supercapacitor electrodes composed of ultralarge graphene sheets and vanadium dioxide. *Advanced Energy Materials* **5**(7), 1401890.
- LEWIS, R. S., MING, T., WACKER, J. F., ANDERS, E. & STEEL, E. (1987). Interstellar diamonds in meteorites. *Nature* **326**, 160–162.

- LIN, M.-F. (1999). Thermal properties of carbon toroids. *Journal of the Physical Society of Japan* **68**(11), 3585–3591.
- LIU, M., ARTYUKHOV, V. I., LEE, H., XU, F. & YAKOBSON, B. I. (2013). Carbyne from first principles: Chain of c atoms, a nanorod or a nanorope. *ACS Nano* **7**(11), 10075–10082.
- LOKHANDE, V., LOKHANDE, A., LOKHANDE, C., KIM, J. H. & JI, T. (2016). Supercapacitive composite metal oxide electrodes formed with carbon, metal oxides and conducting polymers. *Journal of Alloys and Compounds* **682**, 381–403.
- LUJUN PAN, TAICHI HAYASHIDA, MEI ZHANG & YOSHIKAZU NAKAYAMA (2001). Field emission properties of carbon tubule nanocoils. *Japanese Journal of Applied Physics* **40**(3B), L235.
- LUKATSKAYA, M. R., DUNN, B. & GOGOTSI, Y. (2016). Architectures for future hybrid energy storage. *Nature Communication* **7**, 1–13.
- LUO, G., LI, H., ZHANG, D., GAO, L. & LIN, T. (2017). Alkaline route for Nb<sub>2</sub>O<sub>5</sub>/carbon nanotubes composite as pseudo-capacitor material with high-rate performance. *Electrochim. Acta* **235**, 175–181.
- MARTEL, R., SHEA, H. R. & AVOURIS, P. (1999). Rings of single-walled carbon nanotubes. *Nature* **398**, 299.
- MET OFFICE HADLEY CENTRE (2017). Median temperature anomaly from 1961-1990 average. url <https://www.metoffice.gov.uk/hadobs/hadcrut4/index.html>. Accessed: 06-09-2018.
- MILLER, D. C., TERRONES, M. & TERRONES, H. (2016). Mechanical properties of hypothetical graphene foams: Giant schwarzites. *Carbon* **96**, 1191–1199.
- MOCHALIN, V. N., SHENDEROVA, O., HO, D. & GOGOTSI, Y. (2011). The properties and applications of nanodiamonds. *Nature Nanotechnology* **7**, 11–23.
- MORICE, C. P., KENNEDY, J. J., RAYNER, N. A. & JONES, P. D. (2012). Quantifying uncertainties in global and regional temperature change using an ensemble of observational estimates: The hadcrut4 data set. *Journal of Geophysical Research: Atmospheres* **117**(D8).
- NASA (2018). Global climate change: Vital signs of the planet. url <https://climate.nasa.gov/>. Accessed: 06-09-2018.
- NAVALPOTRO, P., PALMA, J., ANDERSON, M. & MARCILLA, R. (2016). High performance hybrid supercapacitors by using para-benzoquinone ionic liquid redox electrolyte. *Journal of Power Sources* **306**, 711–717.
- NAVARRO-SUÁREZ, A. M., CASADO, N., CARRETERO-GONZÁLEZ, J., MECERREYES, D. & ROJO, T. (2017). Full-cell quinone/hydroquinone supercapacitors based on partially reduced graphite oxide and lignin/pedot electrodes. *J. Mater. Chem. A* **5**(15), 7137–7143.
- NIKITIN, A. & GOGOTSI, Y. (2004). *Nanostructured carbide-derived carbon*. American Scientific Publishers.

- NIU, C., SICHEL, E. K., HOCH, R., MOY, D. & TENNENT, H. (1997). High power electrochemical capacitors based on carbon nanotube electrodes. *Applied Physics Letters* **70**(11), 1480–1482.
- NOJEH, A., URAL, A., PEASE, R. F. & DAI, H. (2004). Electric-field-directed growth of carbon nanotubes in two dimensions. *Journal of Vacuum Science & Technology B: Microelectronics and Nanometer Structures Processing, Measurement, and Phenomena* **22**(6), 3421–3425.
- NOKED, M., OKASHY, S., ZIMRIN, T. & AURBACH, D. (2012). Composite carbon nanotube/carbon electrodes for electrical double-layer super capacitors. *Angewandte Chemie International Edition* **51**(7), 1568–1571.
- OBERLIN, A., ENDO, M. & KOYAMA, T. (1976). Filamentous growth of carbon through benzene decomposition. *Journal of Crystal Growth* **32**(3), 335–349.
- PANDOLFO, A. G. & HOLLENKAMP, A. F. (2006). Carbon properties and their role in supercapacitors. *J. Power Sources* **157**(1), 11–27.
- PRESSER, V., HEON, M. & GOGOTSI, Y. (2011). Carbide-derived carbons : From porous networks to nanotubes and graphene. *Adv. Funct. Mater.* **21**, 810–833.
- RATHA, S. & ROUT, C. S. (2013). Supercapacitor electrodes based on layered tungsten disulfide-reduced graphene oxide hybrids synthesized by a facile hydrothermal method. *ACS Applied Materials & Interfaces* **5**(21), 11427–11433.
- RIGHTMIRE, R. A. (1966). Electrical energy storage apparatus. US Patent 3288641.
- ROLDÁN, S., BARREDA, D., GRANDA, M., MENÉNDEZ, R., SANTAMARÍA, R. & BLANCO, C. (2015). An approach to classification and capacitance expressions in electrochemical capacitors technology. *Phys. Chem. Chem. Phys.* **17**, 1084–1092.
- ROLDÁN, S., GRANDA, M., MENÉNDEZ, R., SANTAMARÍA, R. & BLANCO, C. (2011). Mechanisms of energy storage in carbon-based supercapacitors modified with a quinoid redox-active electrolyte. *The Journal of Physical Chemistry C* **115**(35), 17606–17611.
- SEVILLA, M. & MOKAYA, R. (2014). Energy storage applications of activated carbons: supercapacitors and hydrogen storage. *Energy Environ. Sci.* **7**, 1250–1280.
- SHAIKJEE, A. & COVILLE, N. J. (2012). The synthesis, properties and uses of carbon materials with helical morphology. *Journal of Advanced Research* **3**(3), 195–223.
- SHENDEROVA, O. A., ZHIRNOV, V. V. & BRENNER, D. W. (2002). Carbon nanostructures. *Critical Reviews in Solid State and Material Sciences* **27**(3-4), 227–356.
- SHI, L., ROHRINGER, P., SUENAGA, K., NIIMI, Y., KOTAKOSKI, J., MEYER, J. C., PETERLIK, H., WANKO, M., CAHANGIROV, S., RUBIO, A., LAPIN, Z. J., NOVOTNY, L., AYALA, P. & PICHLER, T. (2016). Confined linear carbon chains as a route to bulk carbyne. *Nature Materials* **15**, 634–639.
- SIMON, P. & GOGOTSI, Y. (2008). Materials for electrochemical capacitors. *Nature Materials* **7**(11), 845–854.

- SIMON, P. & GOGOTSI, Y. (2013). Capacitive energy storage in nanostructured carbon-electrolyte systems. *Acc. Chem. Res.* **46**(5), 1094–1103.
- SLEPCHENKOV, M. M., KOLESNIKOVA, A. S., SAVOSTYANOV, G. V., NEFEDOV, I. S., ANOSHKIN, I. V., NASIBULIN, A. G. & GLUKHOVA, O. E. (2017). Giga- and terahertz-range nanoemitter based on peapod structure. *Nano Research* **8**(8), 2595–2602.
- TERRONES, H. & TERRONES, M. (2003). Curved nanostructured materials. *New Journal of Physics* **5**(1), 126.
- TERRONES, M., BOTELLO-MÉNDEZ, A. R., CAMPOS-DELGADO, J., LÓPEZ-URÍAS, F., VEGACANTÚ, Y. I., RODRÍGUEZ-MACÍAS, F. J., ELÍAS, A. L., MUÑOZ-SANDOVAL, E., CANOMÁRQUEZ, A. G., CHARLIER, J.-C. & TERRONES, H. (2010). Graphene and graphite nanoribbons: Morphology, properties, synthesis, defects and applications. *Nano Today* **5**(4), 351–372.
- THE NOBEL PRIZE (2010). The nobel prize in physics. url <https://www.nobelprize.org/prizes/physics/2010/summary/>.
- TRAINELEC CAF (2010). FREEDRIVE: catenary-free running. url <http://www.cafpower.com>. Accessed: 06-09-2018.
- TRASATTI, S. & BUZZANCA, G. (1971). Ruthenium dioxide: a new interesting electrode material. solid state structure and electrochemical behaviour. *Journal of Electroanalytical Chemistry and Interfacial Electrochemistry* **29**(2), 4–8.
- UGARTE, D. (1992). Curling and closure of graphitic networks under electron-beam irradiation. *Nature* **359**(6397), 707–709.
- WANG, J., MA, F., LIANG, W. & SUN, M. (2017). Electrical properties and applications of graphene, hexagonal boron nitride (h-bn), and graphene/h-bn heterostructures. *Materials Today Physics* **2**, 6–34.
- WANG, P., XU, Y., LIU, H., CHEN, Y., YANG, J. & TAN, Q. (2015). Carbon/carbon nanotube-supported RuO<sub>2</sub> nanoparticles with a hollow interior as excellent electrode materials for supercapacitors. *Nano Energy* **15**, 116–124.
- WANG, Y.-H., WANG, C.-C., CHENG, W.-Y. & LU, S.-Y. (2014). Dispersing WO<sub>3</sub> in carbon aerogel makes an outstanding supercapacitor electrode material. *Carbon* **69**, 287–293.
- WARNER, J., SCHAFFEL, F., RUMMELI, M. & BACHMATIUK, A. (2012). *Graphene*. Elsevier Oxford.
- WARREN, B. E. (1941). X-ray diffraction in random layer lattices. *Phys. Rev.* **59**(9), 693–698.
- WEI, L., SEVILLA, M., FUERTES, A. B., MOKAYA, R. & YUSHIN, G. (2011). Hydrothermal carbonization of abundant renewable natural organic chemicals for high-performance supercapacitor electrodes. *Advanced Energy Materials* **1**(3), 356–361.
- WINTER, M. & BRODD, R. J. (2004). What are batteries, fuel cells and supercapacitors? *Chemical Reviews* **104**, 4245–4270.

- YAMADA, H., NAKAMURA, H., NAKAHARA, F., MORIGUCHI, I. & KUDO, T. (2007). Electrochemical study of high electrochemical double layer capacitance of ordered porous carbons with both meso/macropores and micropores. *The Journal of Physical Chemistry C* **111**(1), 227–233.
- YAN, J., FAN, Z., WEI, T., CHENG, J., SHAO, B., WANG, K., SONG, L. & ZHANG, M. (2009). Carbon nanotube/MnO<sub>2</sub> composites synthesized by microwave-assisted method for supercapacitors with high power and energy densities. *Journal of Power Sources* **194**(2), 1202–1207.
- YANG, K. S., KIM, C. H. & KIM, B.-H. (2015a). Preparation and electrochemical properties of RuO<sub>2</sub>-containing activated carbon nanofiber composites with hollow cores. *Electrochimica Acta* **174**, 290–296.
- YANG, Y., LIANG, Y., ZHANG, Y., ZHANG, Z., LI, Z. & HU, Z. (2015b). Three-dimensional graphene hydrogel supported ultrafine RuO<sub>2</sub> nanoparticles for supercapacitor electrodes. *New J. Chem.* **39**(5), 4035–4040.
- YAO, Z., MENG, Y., XIA, Q., LI, D., ZHAO, Y. & JIANG, Z. (2017). Synthesis of carbon modified TiO<sub>2</sub> nanotubes composite films by gas thermal penetration as symmetrical and binder-free electrochemical supercapacitor. *J. Alloys Compd.* **721**, 795–802.
- YE, K.-H., LIU, Z.-Q., XU, C.-W., LI, N., CHEN, Y.-B. & SU, Y.-Z. (2013). MnO<sub>2</sub>/reduced graphene oxide composite as high-performance electrode for flexible supercapacitors. *Inorganic Chemistry Communications* **30**, 1–4.
- YU, D. & DAI, L. (2010). Self-assembled graphene/carbon nanotube hybrid films for supercapacitors. *Phys. Chem. Lett.* **1**(2), 467–470.
- YUSHIN, B. G., DASH, R., JAGIELLO, J., FISCHER, J. E. & GOGOTSI, Y. (2006). Carbide-derived carbons : Effect of pore size on hydrogen uptake and heat of adsorption. *Advanced Functional Materials* **16**, 2288–2293.
- ZHAI, Y., DOU, Y., ZHAO, D., FULVIO, P. F., MAYES, R. T. & DAI, S. (2011). Carbon materials for chemical capacitive energy storage. *Adv. Mater.* **23**(42), 4828–4850.
- ZHANG, L. L., ZHOU, R. & ZHAO, X. S. (2009). Carbon-based materials as supercapacitor electrodes. *J. Mater. Chem.* **38**(29), 2520–2531.
- ZHANG, L. L., ZHOU, R. & ZHAO, X. S. (2010). Graphene-based materials as supercapacitor electrodes. *J. Mater. Chem.* **20**(29), 5983–5992.
- ZHANG, M. & LI, J. (2009). Carbon nanotube in different shapes. *Materials Today* **12**(6), 12–18.
- ZHANG, M., YOSHIKAZU NAKAYAMA & LUJUN PAN (2000). Synthesis of carbon tubule nanocoils in high yield using iron-coated indium tin oxide as catalyst. *Japanese Journal of Applied Physics* **39**(12A), L1242–L1244.
- ZHANG, Y., SU, Y., WANG, L., KONG, E. S.-W., CHEN, X. & ZHANG, Y. (2011). A one-dimensional extremely covalent material: monatomic carbon linear chain. *Nanoscale Research Letters* **6**(577).

- ZHANG, Z., HE, Y., ZHOU, Q., HUANG, C., ZHANG, X., GUO, Z., GAO, Y., LIU, J. & CAO, Z. (2014). Unique ni@niocore-shell/ac composite for supercapacitor electrodes. *Electrochimica Acta* **144**, 300–306.
- ZHONG, C., DENG, Y., HU, W., SUN, D., HAN, X., QIAO, J. & ZHANG, J. (2016). *Electrolytes for Electrochemical Supercapacitors*. CRC Press.





# Chapter 2

## Objectives

### 2.1 General objectives:

The objective of this thesis is the synthesis and the structural, textural and electrochemical characterization of nanostructured carbon-based composite materials for their application as electrode materials in supercapacitor devices. These materials, whose structural building block is graphene, are part of the so-called disordered carbons (nanoporous amorphous carbons, activated carbons, ...), because although they do not show long-range order, they do show order on a nanometric scale due to the presence of Disordered or uncorrelated and partially corrugated graphene sheets ( $sp^{2+\delta}$  bond). These materials have a high surface area, high porosity and a narrow micropore size distribution ( $\sim 1\text{nm}$ ). These characteristics make them suitable for application as adsorbents, hydrogen storage devices or, as discussed in this thesis, as electrodes in supercapacitors.

### 2.2 Specific objectives:

- Synthesis of various composite materials by the selective extraction of metals with chlorine gas on organometallic and coordination compounds metal centers followed by the hydrothermal conversion of the by-product reaction intermediates. Obtaining composite materials composed by nanostructured carbon materials with high surface area and controlled pore size as matrix with embedded pseudocapacitive metal oxide nanoparticles.

- Synthesis of lignocellulosic activated carbons of high surface area as well as metal and metal oxide nanoparticles with the aim of mix them in a composite material with improved electrochemical performance, increasing the volumetric capacitance and electric conductivity.
- Design and synthesis of composite material based on microporous carbon and gold nanoparticles with controlled pore size and improved electrochemical properties.
- Given the close relationship between the nanostructure of the materials and their physicochemical properties, a study of the micro and nanostructure will be carried out by means of scanning electron microscopy (SEM) and in detail by high resolution transmission electron microscopy (HRTEM). In addition, the use of XEDS and EELS spectroscopy associated with the transmission microscope will allow us to obtain local composition information.
- Evaluation of the textural properties of the materials prepared by analyzing the adsorption-desorption isotherms, since they provide the specific surface area (BET), the external surface area, the total and micropore volume and the pore size distribution (PSD). A detailed description of the pore structure in terms of size distribution will allow to correlate and predict the properties of the materials in conjunction with the structural study.
- Finally, electrodes with the synthesized materials will be prepared and their electrochemical properties will be evaluated by means of cyclic voltammetry in three-electrode cell configuration, and also cyclic voltammetry together with galvanostatic charge-discharging and impedance measurements in two-electrode cells. Using aqueous (acid, basic and neutral salts) electrolytes, which will allow to determine the specific capacitance of the materials. This parameter indicates the possible application as supercapacitor electrodes in a real device.

# Chapter 3

## Experimental techniques

The observation, study and understanding of the most important features of carbon materials, such as morphology, micro and nano-structure, chemical composition, textural parameters and electrochemical behavior is essential to maximize the performance of the material in certain applications and they are possible due to the combination of different analytic methods. Electron microscopy and its associated analytic techniques (XEDS and EELS) as well as X-ray diffraction, infrared spectroscopy and gas adsorption allows to obtain information about the structure and composition of these materials while the electrochemical techniques like cyclic voltammetry, galvanostatic charge-discharge and impedance spectroscopy provide indispensable information about the electrochemical behavior of the material for their use as electrodes on a supercapacitor device.

The different techniques used in this thesis for the textural, structural, chemical and electrochemical properties of the components are briefly detailed below.

### 3.1 Electron microscopy

#### 3.1.1 Scanning Electron Microscopy (SEM)

Electron microscopes are fundamentally and functionally analogous to light microscopes (LM), replacing the simple optical technology by complicated electronics,

vacuum equipment, voltage supplies and electron optics system. A scanning electron microscope (SEM) can reveal higher levels of detail than a LM with magnification from 10 to 300,000 times. In addition, a SEM have three key advantages against LM (AMMRF, 2019):

- Higher resolution at high magnification; the use of electrons to form the images a resolution value of few nanometers meanwhile the best resolution possible with light is about 200 nm.
- The depth of field (the height of a specimen that appears in focus in an image) of a SEM is 300 times higher than in a LM, endowing the image with a three dimensional appearance.
- Electron interaction with the sample allows the analysis of chemical composition, as well as crystallographic information.

This technique is based on the emission of an electron beam with an energy between 1 and 50 keV and in a vacuum of  $10^{-7}$  bars that is focused on the surface of the sample and continuously scanned over a selected area. As a result of the interaction between incident electrons and the sample, there are a number of outcomes: some electrons are bounced back out of the sample (backscattered electrons), others knock into atoms and displace electrons that, in turn, come out of the sample (secondary electrons); alternatively X-rays, and light or heat (in the sample) can be the result of these interactions.

The micrographs obtained by SEM are the result of two main signals that come from the secondary and backscattered electrons. Secondary electrons signal intensity (with energies of a few tenths of electron-volts) which are emitted from the near surface of the sample, depend directly of the angle of incidence of the electron beam on the surface of the material, in other words, on the topography of the sample. On the other hand, backscattered electrons signal intensity (much higher than for secondary electrons) that are emitted from more deep zones of the sample, depends on the atomic number ( $Z$ ) of the atoms present in the sample, so that the image reveals the difference in chemical composition by contrast difference (I.Goldstein *et al.*, 2003).

Sample preparation is carried out on a copper support where a graphite adhesive tape is placed. In this way two objectives are achieved: fixing the sample to the support and establishing a conductive contact of the electricity between the support and the sample. Since the signal processed comes from the sample

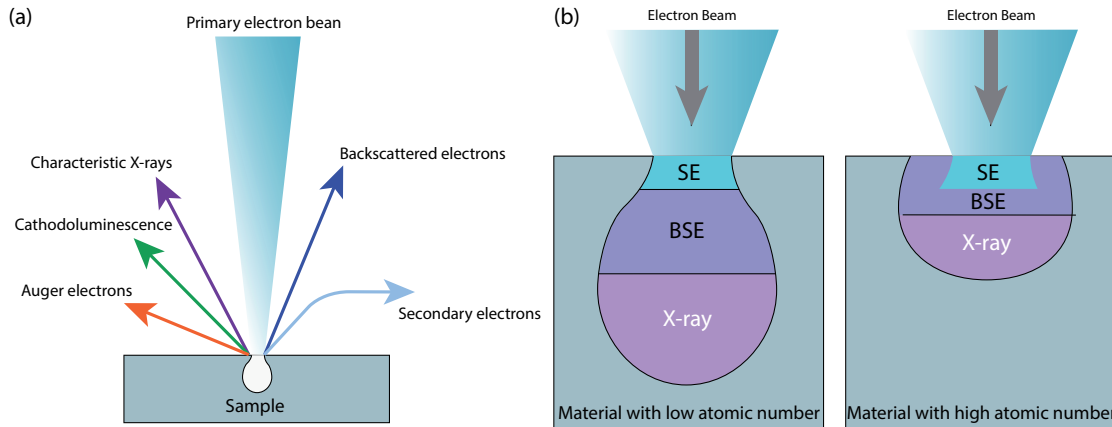


Figure 3.1: (a) Result of the interaction between incident electrons and the sample and (b) difference in interaction depending on the type of material (after AMMRF, 2019).

(after incident beam interaction), this must be conductive to be viewed. If the electrical conductivity of the sample is small, it can be charged as a consequence of the irradiation with the microscope beam, decreasing the quality and resolution of the image. To reduce this effect, the sample is coated with a conductive film (gold, carbon or chromium) that facilitates the discharge of the sample through the metal support.

Using this technique, it was possible to study the morphology, homogeneity and particle size of the samples under study. The micrographs on this thesis were performed in a JEOL JSM 6335F scanning electron microscope operating at voltages from 5 to 20 kV with an average working distance of 15 mm and equipped with an EDS Oxford Instruments X-max detector of 80 mm<sup>2</sup> for analytical studies.

### 3.1.2 Transmission Electron Microscopy (TEM)

Like the SEM, transmission electron microscopes are similar in fundamentals to a LM, with an even more complex equipment and components. The TEM reveals levels of detail and complexity inaccessible by light microscopy allowing detailed micro-structural examination through high-resolution and high magnification imaging as well as the investigation of crystal structures, with image magnifications up to 1,000,000 times in a routine session, able to solve single columns of atoms. In comparison with LM, the TEM provides also three main advantages

(AMMRF, 2019):

- Higher resolution and higher magnification than SEM and LM; resolution better than 0.2 nm is normally achieved in comparison with 5 nm of SEM or 200 nm in a LM.
- Electron diffraction on a periodic structure gives structural information about the sample.
- Like on SEM, the electronic interaction with the sample allows the analysis of chemical composition

On a TEM, the resolution depends directly on the accelerating voltage according to Abbe's equation:

$$d = \frac{0.61\lambda}{n \cdot \sin\alpha} \quad (3.1)$$

where  $d$  is the resolution (the minimum resolvable distance),  $\lambda$  the wavelength of the energy source,  $n$  is the refractive index of the medium and  $\alpha$  the aperture angle. From DeBroglie relation the wavelength of a beam of electrons through a potential field can be calculated from the accelerating voltage using the following equation:

$$\lambda = \frac{1.23}{\sqrt{V}} \quad (3.2)$$

For an electron microscope,  $n$  can be approximated to 1, and  $n \cdot \sin\alpha$  (also called numerical aperture) to  $\alpha$ . Replacing this in the previous equations allows us to directly calculate the highest possible resolution of a microscope knowing the acceleration voltage and the aperture angle with the resulting equation:

$$d = \frac{0.753}{\alpha\sqrt{V}} \text{nm} \quad (3.3)$$

The higher the energy of the electrons, the lower the wavelength and therefore the higher the resolution. In this way, energy of transmission electron microscopes

varies from 40 keV to 3 MeV. But for a higher acceleration voltage, a bigger high voltage generator is required. For example, only two 3 MeV microscopes have been built around the world (one on CEMES-LOE/CNRS in Toulouse, France, and the other on Hitachi in Tokyo, Japan) requiring a two-floor building for their installation. Both of them are currently out of operation. That is why most common microscopes are of 200 keV or 300 keV, which even so, equipped with modern aberration correctors can achieve resolutions up to 0.05 nm.

The electron source is usually a hot filament of tungsten, which emits electrons by thermionic effect, or a field emission source. Some of these electrons are transmitted, another part is scattered and another part gives rise to interactions that produce different phenomena such as light emission, secondary electrons and Auger, X-rays, etc. The transmission electron microscope uses the transmitted/dispersed electrons to form images, diffraction patterns to obtain information about crystal structure and the X-ray emission to know the elemental composition of the sample (Williams & Carter, 2009). Therefore, the operating modes of a transmission electron microscope can be divided into:

- Image formation: It is based on the wave-particle dual nature of the electrons. Considering its wave behavior, when electrons pass across the sample, variations are observed both in the amplitude and in the wave phase and both types of variation give rise to the contrast in the image: amplitude contrast and phase contrast. In most situations both types contribute to the formation of the image but one of them tends to dominate. In the case of amplitude contrast images, bright field or dark field images are obtained, which are originated by the contrast due to the thickness of the sample and the contrast due to the diffraction of the electrons. Phase contrast images are formed by selecting more than one electron beam and are generally associated with high resolution electron microscopy (HRTEM), although this type of contrast is also produced at low magnification. This phase contrast is widely used to obtain images that are directly related to the periodic structure (crystalline planes, extensive defects, etc.) of a crystalline sample.
- Electron diffraction: the electrons, in their wave behavior, can be diffracted

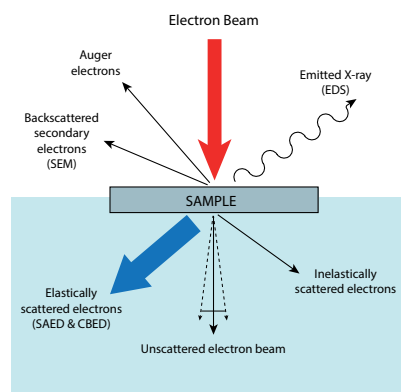


Figure 3.2: Electron emission signals generated by the interaction of the incident beam with a thin material (after AMMRF, 2019).



by crossing a crystalline sample, giving rise to a diffraction pattern that contains information about its crystalline structure. Two main types of diffraction patterns can be obtained: Selected-area electron diffraction patterns (SAED) and convergent beam diffraction patterns (CBED). SAED patterns are very sharp point diagrams that are formed using a parallel electron beam and placing an aperture in the plane of the image to select a certain area. CBED patterns are a set of discs that are formed by focusing the beam on a small area of the sample. The subsequent indexing of the diffraction patterns associates each point of the reciprocal network with a crystalline plane  $hkl$  and from there one can deduce the orientation of the crystal in terms of the zone axes  $[uvw]$  to which the indexed planes belong.

- Microanalysis: associated analytical techniques have been developed that combines the high resolution of an electron microscope with the possibilities of microanalysis of a scanning microscope. The two most commonly used analytical techniques are:
  - Energy Dispersive X-ray Spectroscopy (XEDS): When the incident electron beam impact with the atoms of the material, electrons of inner atomic orbitals of these atoms are plucked from there, which produces the atom ionization. In this situation, electrons from more external orbitals immediately jump to inner hollow orbitals, spreading out the energy equal to the difference between the energies that each electron had in its corresponding orbital. This energy manifests in two ways: Auger electrons or X-rays and is unique for each element. When the intensity of this electromagnetic radiation is represented in relation to its energy, an X-ray spectrum is obtained, consisting of a series of peaks of variable intensity characteristic of the components of the analyzed sample region.
  - Electron Energy Loss Spectroscopy (EELS): This technique is based on the measurement of the energy loss of electrons that interact inelastically with the sample. The measurements in EELS are extraordinarily sensitive to the thickness of the sample, which must be between 5 and 100 nm to reduce the possibility that an electron suffers more than one dispersion. This technique allows to extend the chemical analysis to the light elements ( $Z < 10$ ) something really important since oxygen and carbon are very abundant elements and can not be easily analyzed by XEDS.

In this work, transmission electron microscopy has been used in its image mode to obtain information about the morphology and nanostructure of the materials

obtained in the different synthesis conditions applied, as well as to confirm the formation of composite materials by locating the different nanoparticles used in their corresponding carbon matrix. It has been possible to identify the most stable morphologies as well as the reaction intermediates, which provide information about the process formation of carbon and composite materials. When dealing with direct images at the atomic level, information can be obtained about the graphene sheets disorder degree, which can be related to the textural properties of these materials, as well as the crystalline phases of nanoparticles that have been identified also in combination of microanalysis and diffraction modes.

The conventional TEM images (CTEM), the selected area diffraction patterns and the dispersive energy analysis were obtained in a JEOL JEM 2100 HT microscope operating at 200 keV, equipped with an Oxford Inca EDS spectrometer and an ORIUS SC100 CCD camera. HRTEM images were obtained in a transmission electron microscope JEOL JEM 3000 F, with field emission gun operating at 300 KeV with a point resolution of 0.17 nm, which is coupled with an ENFINA Gatan spectrometer, with a resolution 1.2 eV, where the electron energy loss spectra (EELS) were acquired and a microanalysis system by XEDS Oxford INCA. In STEM mode, it has an ADF detector from Gatan and a HAADF detector for the collection of Z contrast images (Williams & Carter, 2009).

The samples were prepared from a sonicated dispersion, formed by a certain amount of sample in butanol. A drop of each suspension was deposited on a copper grid of 3 mm diameter entre paréntesis, covered with a thin holey carbon film.

## 3.2 Adsorption Isotherms

Since we are preparing materials for its possible application as electrodes in supercapacitors it is essential to perform a textural study of the samples in order to know the surface properties of the material, such as: pore volume, pore size, pore size distribution (PSD) and specific surface area (SSA). According to the IUPAC, three types of pores can be described, depending on their sizes: micropores (<2 nm), mesopores (2-50 nm) and macropores (> 50 nm).

In order to interpret isotherm data, the BET theory developed by S. Brunauer, P.H. Emmett and E. Teller (Brunauer *et al.*, 1938) was the most extensive approximation used for porous materials. That theory starts from the modifications made to the kinetic model of Langmuir isotherm (adsorption of a gas on an adsorbent in

a single layer), allowing to evaluate the mechanism of adsorption in two or more layers and giving information on the amount of active surface area and the size and distribution of pores of the material. The BET model describes the multiple layer adsorption based on the following considerations:

1. The first layer is absorbed similarly to the Langmuir model
2. In the successive layers, the isosteric adsorption heats must be equal to the molar liquefaction heat of the adsorbate at a certain adsorption temperature
3. In all the layers (except the first one) the evaporation-condensation conditions are identical.
4. When  $p = p_0$ , the adsorbate condenses on the surface of the adsorbent and the number of layers tends to infinity.

The equation, known as the BET isotherm in its linear form, is commonly used to graphically represent the experimental data and can be written as follows (Rouquerol *et al.*, 2013):

$$\frac{P}{n_0(p_0 - P)} = \frac{1}{n_m C_m} \left( 1 + \frac{(C_m - 1)P}{p_0} \right) \quad (3.4)$$

Where  $n_0$  and  $p_0$  are the adsorbed amount and the saturation pressure at the equilibrium pressure  $P$ . The  $C_m$  constant, exponentially related to the adsorption heat of the first layer, can be expressed by the following equation:

$$C_m = \exp \left( \frac{(q_I - q_L)}{RT} \right) \quad (3.5)$$

The molar adsorption heats from the first to the  $n$ th layer are represented by  $q_I$  and  $q_L$  respectively. The term  $q_I - q_L$  is interpreted as the net molar adsorption energy. The  $C_m$  value is the responsible for the final shape of the isotherm, being able to take forms of up to six different types depending on the type of pore and the adsorption mechanism (see Figure 3.3) that can be described as follows (Gregg & Sing, 1982):

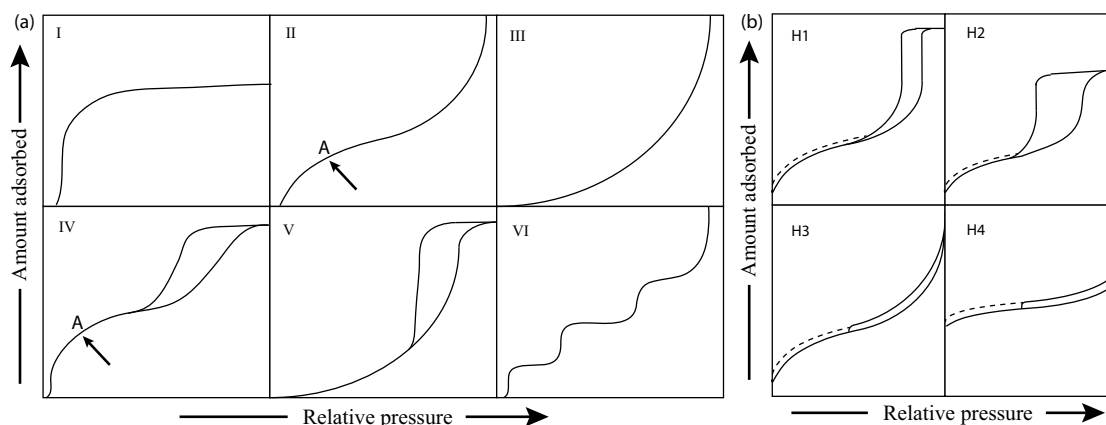


Figure 3.3: (a) The IUPAC classification of adsorption isotherms for solid-gas equilibrium showing both the adsorption and desorption pathways. Note the hysteresis in types IV and V. (b) Schematic representation of different types of hysteresis cycles.

- Type I isotherm is characteristic of microporous solids, where the gas adsorption occurs at low relative pressures in a monolayer form, typical of activated carbon, zeolites, metal-organic frameworks (MOF), etc.
- Type II represents an unrestricted adsorption that evolves from monolayer to multilayer where point "A" marks the stage at which the solid is covered completely by the monolayer and the start of the multilayer takes place. This type of isotherm is very common for non-porous or macroporous adsorbents like  $N_2$  at 77 K over graphite, CNT and carbon black.
- Type III isotherm has a convex shape throughout the entire range of relative pressures. It is relatively rare and is characterized by the presence of balance between the adsorption heat and adsorbent liquefaction, in a low adsorbate-adsorbent interaction.
- Type IV characteristic feature is the presence of the hysteresis cycle (the trajectory described by the adsorption and desorption curves does not follow the same path), which is associated with capillary condensation that occurs in the mesopores and the limited adsorption capacity over a wide range of relative pressures. The initial part of the isotherm is attributed to the transition of the adsorption from monolayer to multilayer, so it follows the same path as the corresponding initial part that presents an isotherm of Type II. This type of isotherms are generally presented in materials that present a wide range of mesoporosity (carbon black compacted under pressure and nanostructured carbons)

- Type V, like the type III isotherm, is characteristic of weak adsorbent-adsorbent interactions, but it differs from the previous one in that the final stretch is not asymptotic, and also has a hysteresis cycle.
- The isotherm type VI is rare. This type of step adsorption occurs only for solids with a very uniform non-porous surface, where each step represents the adsorption in a different layer.

Another important factor of the different isotherms are the hysteresis cycles that are formed since the adsorption and the desorption do not follow the same path. Depending on the hysteresis cycle that is formed, it provides information about the pore type of the material. The hysteresis cycles possible are four where H1 and H4 assume the extremes and in between we can observe the cycles H2 and H3:

- H1; It is a typical parallel and vertical cycle of materials with pore structure produced by agglomeration of spheres of homogeneous size, therefore it will have a narrow pore size distribution. Typical tubular shaped pores open on both sides.
- H2; this type of cycle is common in corpuscular systems, with a pore distribution much more complicated to interpret. It is typical of "bottleneck" pores with large body and narrow neck.
- H3; this type of cycle differs from the two above in that it does not present limits to high pressures. It is of pores produced by plate agglomeration.
- H4; parallel but vertical cycle is typical of pores with slit form, in addition with a type I isotherm indicates the presence of micropores.

The PSD determination of these carbon materials were performed with a different consideration. Since Seaton et al. (Seaton *et al.*, 1989) (the first to propose a procedure to determine the pore size distribution of porous carbons from adsorption isotherms) two decades ago, various approaches for calculating densities of fluids adsorbed in such pores have been employed: starting from the density functional theory (DFT) in its local version to more advanced fluid theories such as non-local density functional theory (NLDFE), the fundamental measure theory (FMT) and its modified versions (MFMT) as well as grand canonical Monte Carlo simulations (GCMC). But whatever the theory used, the essential element that has remained unchanged in most of the carbon PSD analysis applications is

the model of slit pores with energetically uniform flat surfaced walls of infinite extent. In order to better adjust experimental data, the 2D-NLDFT theory was proposed, in which at least two dimensions are required for evaluation of model adsorption isotherms for finite pores, one for finite slit pore, consisting of parallel circular graphene walls, and other for finite slit pore geometries between parallel graphene strips and channels. Results show a better fit of experimental data on porous carbon materials (Jagiello & Olivier, 2013).

The textural characterization of the materials presented in this thesis, has been made by means of the data obtained from the adsorption/desorption isotherms of N<sub>2</sub> at 77 K, which are carried out in a surface area and porosity analyzer Micromeritics ASAP2020. For this purpose, the data derived from two different zones of the isotherm are collected, following the experimental procedure described below:

Before proceeding with the equipment standard degassing, samples with potential corrosive gases adsorbed like Cl<sub>2</sub> or volatile metal chlorides formed during the synthesis, were degassed on a vacuum system equipped with liquid N<sub>2</sub> trap overnight, in order to remove the corrosive gases and prevent the possible damage to the analyzer. Once this step has been completed, a sample of known weight (0.10 - 0.15 g) is placed inside a glass sample holder which is kept under vacuum for 2 h at 110 °C. The purpose is to remove air adsorbed on the material and present in the sample holder. At the end of the degassing time, the amount of sample to be analyzed is obtained by weight difference. The degassed sample is placed in the analysis port of the equipment, the analysis conditions are selected and the isotherm is started. During the standard isotherm, the textural parameters from the isotherms of adsorption-desorption in the area that goes from  $p/p_0$  from 0.005 to 1 are measured. For the PDS, points at lower  $p/p_0$  are needed so data from  $3 \times 10^{-7}$  to 0.005 are also measured in a second isotherm experiment.

### 3.3 Infrared spectroscopy (IR)

Infrared spectroscopy is one of the best tools to solve problems related to molecular structure and chemical identification. The infrared region of the electromagnetic spectrum was discovered by Herschel in 1800, but was not used for analytical purposes until the works of Julius in 1892, and systematically until the 1920s (Olsen, 1990). As shown in Figure 3.4, the infrared region of the spectrum extends between visible light and microwaves, located in the wavelength range between

$7.8 \cdot 10^{-6}$  to  $3 \cdot 10^{-3}$  m.

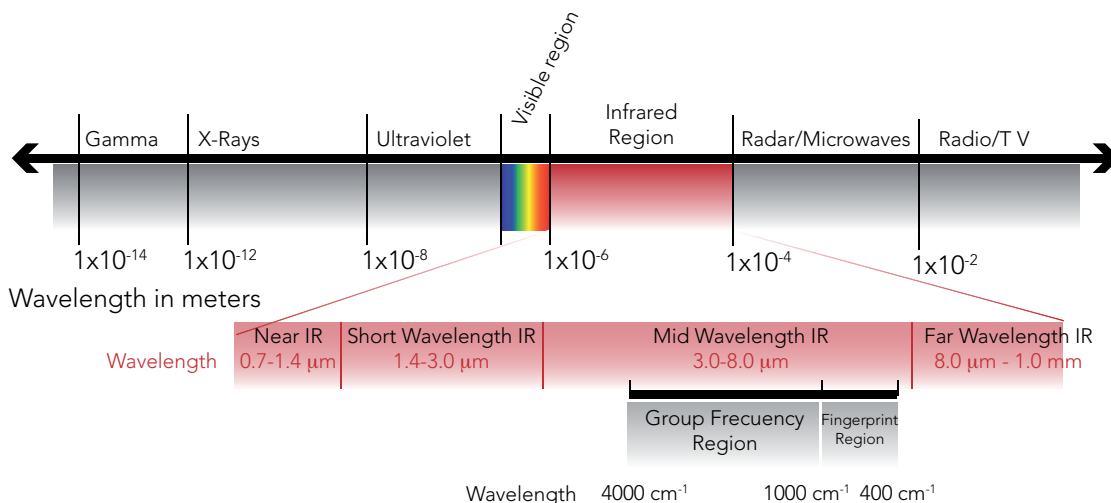


Figure 3.4: The electromagnetic spectrum, highlighting the infrared regions.

The infrared region of the electromagnetic spectrum is divided, into three regions: the near, middle and far infrared, due to their distance from the visible region. Near and short wavelength infrared ( $\lambda = 0.7$  to  $3 \mu\text{m}$ ) are following the visible region. In this zone the absorption bands due to the harmonics of the hydrogen tension vibrations take place. The far infrared ( $\lambda = 10$  to  $8 \mu\text{m}$ ) is close to the radar and microwave region, it has a low energy and a greater information mainly of the rotational transitions, vibrational modes of the crystalline networks and vibrations of the "skeleton" of the molecules. Between them, the mid wavelength infrared ( $\lambda = 8$  to  $3 \mu\text{m}$ ) can be found, very useful to study the fundamental vibrations and the vibrational structure of specific chemical groups. That middle zone can also be divided into two regions: the group frequency, extending from about  $4000$  to  $1000 \text{ cm}^{-1}$ , being the key region for identifying specific chemical groups like carbon-carbon or carbon-oxygen single and double bonds; and the fingerprint region, called like that because is a region of multiple absorption bands which is characteristic of each compound.

In the case of the carbon-based materials studied in this thesis, IR spectroscopy provides information about oxygen functional groups located on their surface, allowing the study of the surface chemistry. The IR spectra collected for this work have been acquired in a Perkin Elmer 100 FT-IR with an Attenuated Total Reflectance accessory (ATR) in the region between  $4000$ - $650 \text{ cm}^{-1}$ .

### 3.4 Electrochemical Characterization

The materials synthesized in this thesis pursue the final objective of being used as electrode materials in supercapacitors, therefore, after structural and textural characterization, their electrochemical performances must be also tested. Two and three-electrode configurations were performed. In the case of the three-electrode cell, the acquired data gives information about the electrochemical behavior of the electrode material, since the working electrode acts as positive and negative electrode at same time. On the other hand, the two-electrode configuration brings information about the supercapacitor device, being this configuration a simulated real device.

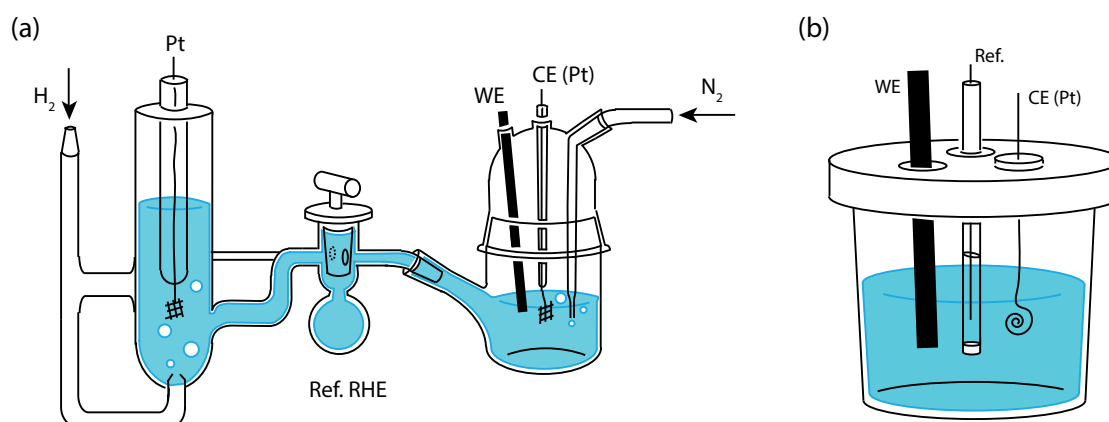


Figure 3.5: Three-electrode cells configuration for (a) RHE and (b) rest of reference electrodes.

The three-electrode cell measurements were performed on a different set-up depending on the reference electrode employed. Figure 3.5a schematically represents the assembly for measurements with Reversible Hydrogen Electrode (RHE) as reference electrode (RE). The principal benefit of the use of this subtype of standard hydrogen electrodes is that the measured potential do not change with the pH so it can be used directly in the electrolyte. The set-up includes a line to constantly pump H<sub>2</sub> in a bulb filled with the electrolyte and a platinum wire, responsible of catalyze the proton reduction. This part is in contact with the cell trough a shut-off valve that allow ions difussion. A glassy carbon rod of 7 mm  $\varnothing$  is used as working electrode (WE), where the material is deposited on the tip in form of an EtOH dispersion with a 1% of Nafion (a sulfonamide tetrafluoroethylene based fluoropolymer-copolymer) as binder. The dispersion, also called ink, is allowed to dry growing in the form of a very thin film on the surface of the rod and the rod is placed in the cell immersed in the electrolyte. A platinized platinum wire is



used as counter electrode (CE), increasing the total surface area which improves reaction kinetics and maximum possible current. The cell is also provided with a  $N_2$  entry for deaerate the electrolyte during the measurements.

In the cases in which different reference electrodes were used like Hg/HgO for specific alkali electrolytes or Ag/AgCl for more general electrolytes, the cell configuration was less sophisticated than the previous one since the  $H_2$  gas pump system is not required. Figure 3.5b shows the three-electrode cell configuration in these cases. Here, the cell can also be deaerate with  $N_2$  before being closed or can incorporate a specific entry for continuous gas flow as described in the previous cell.

The two-electrode set-up was performed on a Swagelok-type cell schematized in Figure 3.6. This type of configuration requires electrodes in form of thin discs, therefore the carbon-based materials, usually obtained in powder form, needs to be processed in a more sophisticated way than the inks prepared above. The carbon-based material is mixed with a 10 wt% of poly(tetrafluoroethylene) (PTFE) as binder in an EtOH dispersion under continuous and vigorous stirring. While the mixture gets dried, the EtOH favors the conformation of PTFE in fine threads that wrap the carbon particles binding them together. As result, the dispersion becomes first a slurry and finally a moldable gum which can be processed to form a thin film. After drying at 100 °C overnight in an oven, the film was punched into 10 mm  $\varnothing$  discs that can be used as electrodes. For a symmetric cell, two equal thin discs isolated by a fiber glass separator impregnated with the electrolyte were placed into the teflon Swagelok body. PTFE front and back ferrules and teflon closing screws were located in both sides as indicate in the scheme displayed in Figure 3.6. Metal plungers press down the cell allowing the flow of current.

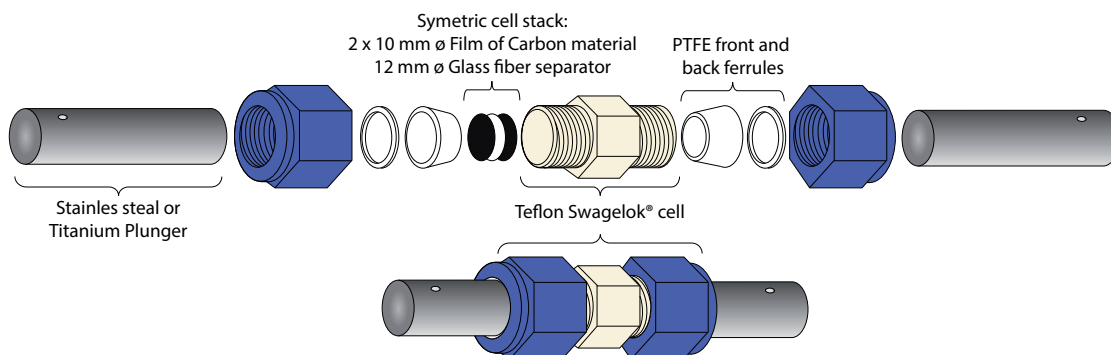


Figure 3.6: Scheme of Swagelok-type cell configuration.

Although, does not exist any standard procedure to test supercapacitors, there

are several techniques widely used that give us information about the electrochemical behavior of the materials which are the Cyclic Voltammetry (CV), Galvanostatic Cyclic with Potential Limitation (GCPL) and Electrochemical Impedance Spectroscopy (EIS).

### 3.4.1 Cyclic Voltammetry (CV)

Cyclic voltammetry (CV) is the most widely used technique for acquiring qualitative information about electrochemical reactions. CV provides information on redox processes, heterogeneous electron-transfer reactions and adsorption processes. It offers a rapid location of redox potential of the electroactive species. CV can also be used to determine the electron stoichiometry of a system, the diffusion coefficient of an analyte, and the formal reduction potential, which can be used as an identification tool. For the study of supercapacitors, CV yields basic information about capacitive parameters including voltage window, capacitance and cycle life.

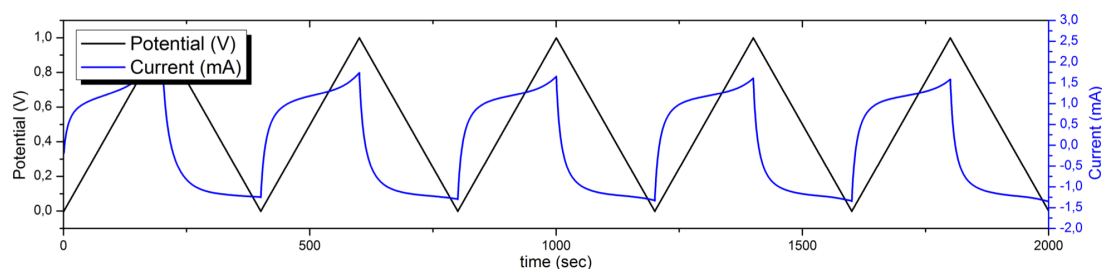


Figure 3.7: Cyclic Voltammetry plot of a supercapacitor where several cycles were measured. Black line represent the voltage applied while the blue line shows the current response as function of time.

A CV consists of scanning linearly the potential of a stationary working electrode along a voltage range (voltage window). During the potential sweep, the potentiostat measures the current resulting from electrochemical reactions (consecutive to the applied potential) often doing repetitively sweeps between both limits (Figure 3.7). The cyclic voltammogram is a current response as a function of the applied potential.

By plotting the current response as function of the applied potential the characteristic "rectangular shape" of a supercapacitor is obtained (Figure 3.8). Several cycles were recorded showing that almost all materials normally require 5 to 10 cycles to reach the steady state (point in which consecutive cycles start to overlap).

The potential window can be determined going to further potentials in both ways, when the current signal starts to increase or decrease exponentially indicating the decomposition of the electrolyte. For example, in aqueous electrolytes, water suffers its electrolysis generating  $O_2$  and  $H_2$ . Those limits determine the effective potential range of our material in a specific electrolyte.

CV is also the most common technique to calculate the capacitance of a material. Integrating the current response ( $i$ ) in a whole cycle (positive and negative charge in absolute value along the entire voltage window) the total charge in amps is obtained, which divided by a factor of 2 (due to the fact that in three electrodes cell the same electrode is working as negative and positive electrode at same time) and the sweep rate ( $\Delta\nu$ ) in volts per seconds directly give the capacitance ( $C$ ) in farads. If additionally the value is divided by the electrode mass ( $m$ ) as shown in the equation 3.6, the gravimetric capacitance ( $C_{grav}$ ) is obtained.

$$C_{grav} = \frac{1}{2m\Delta\nu} \int_{V_1}^{V_2} i(V) \cdot dV \quad (3.6)$$

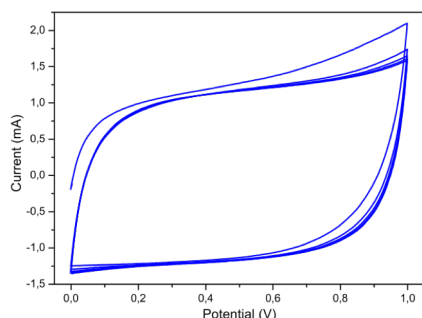


Figure 3.8: CV plot. Current as function of potential.

On an ideal supercapacitor, as the sweep rate increases, the current also increase proportionally. But in real devices, the faster the charge is applied, the less time have the ions to diffuse along the entire surface area of the material and therefore a decay of the capacitance occurs. By recording different CV at increasing sweep rates, that loss of capacitance can be measured giving valuable information about the electrolyte ion diffusion into the pores of the material. Additionally, in CV experiments the cyclic life can also be estimated. If the material starts to degrade or decompose, the capacitance will be strongly affected, and on the CV plots, the cycles are thinner or tilted if the material becomes more resistive.

### 3.4.2 Galvanostatic Cyclic with Potential Limitation (GCPL)

Cyclic Charge/Discharge (CCD) techniques are the standard techniques used to test the performance and cycle-life of batteries and supercapacitors. Between

several different operating modes, the most common is the Galvanostatic Cyclic with Potential Limitation (GCPL) procedure, that consist on apply a constant current (positive for charge and negative for discharge) until a set potential is reached. A repetitive loop of charge and discharge is called a cycle. The plots (see Figure 3.9) show the potential as function of time in which if a constant current is applied, the material reaches the selected voltage. The longer the time the higher is the amount of charge stored and therefore the higher is the capacitance.

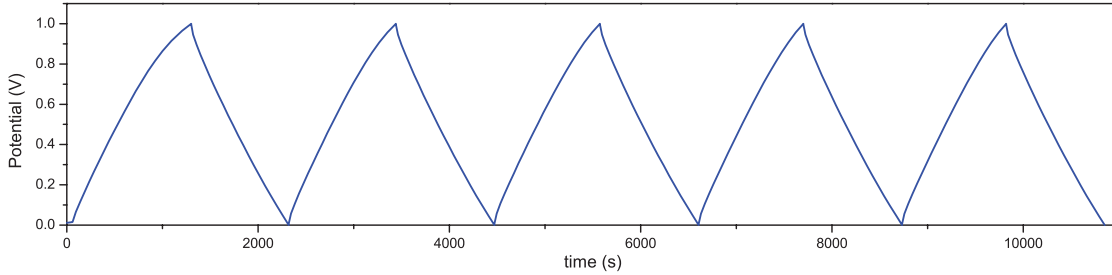


Figure 3.9: Galvanostatic Cyclic with Potential Limitation plot of a supercapacitor where several cycles were measured.

The gravimetric capacitance ( $C_{grav}$ ) can be easily calculated from the charge-discharge slope following equation 3.7. Where  $I$  is the applied current in amps,  $\Delta t$  the elapsed time in seconds,  $\Delta V$  the reached potential in volts and  $m$  the electrode mass in grams.

$$C_{grav} = \frac{2 \cdot I \cdot \Delta t}{m \cdot \Delta V} \quad (3.7)$$

The ideal behavior of a supercapacitor in a GCPL experiment is a straight line with a slope equal to  $\Delta t/\Delta V$ , but in real devices, the line looks a little more curved and the ohmic drop at the beginning of each process is especially noticeable, indicating how conductive the material is. In these experiments, if the applied current is increased, the set potential is reached faster, providing valuable information of the electrochemical behavior of the material like ion diffusion along the material and cycle life.

### 3.4.3 Electrochemical Impedance Spectroscopy (EIS)

Electrochemical Impedance spectroscopy is a powerful method of characterizing many of the electrical properties of materials and their interfaces with electronically

conducting electrodes. It may be used to investigate the dynamics of bound or mobile charge in the bulk or interfacial regions of any kind of solid or liquid material (ionic, semiconducting, mixed electronic-ionic, and even insulators like dielectrics). In supercapacitors, EIS is the preferred method for measuring ESR values, besides allowing the calculation of the capacitance as in other techniques (Macdonald & Johnson, 2018).

The concept of electrical resistance is well known as the ability of a circuit element to resist the flow of electrical current. It can be calculated by dividing the potential by the current following the Ohm's Law:

$$R = \frac{E}{I} \quad (3.8)$$

However, in practice, circuit elements exhibit much more complex behavior than a theoretical resistance, which forces us to abandon that simple concept and in its place we use impedance, a more general circuit parameter. Like resistance, impedance is a measure of the ability of a circuit to resist the flow of electrical current, but unlike resistance, it is not limited by the simplifying properties of an ideal resistor: It follows Ohm's Law at all current and voltage levels, its resistance value is independent of frequency and alternating current and voltage signals though a resistor are in phase with each other (Macdonald & Johnson, 2018).

In this technique an AC potential is applied to the electrochemical cell and then measuring the current through the cell. When a sinusoidal potential excitation is applied, the response to that excitation is an alternating current, but shifted in time from the applied current (phase-shift). In a linear system both the potential ( $E$ ) and current ( $I$ ) can be described in terms of the radial frequency and time as follows:

$$E_t = E_0 \sin(\omega t) \quad (3.9)$$

$$I_t = I_0 \sin(\omega t + \phi) \quad (3.10)$$

Where  $E_t$  and  $I_t$  are the potential and current at time in volts and amps,  $E_0$  and  $I_0$  are the amplitude of each signal,  $t$  is the time in seconds and  $\omega$  is the radial

frequency in radians per second, which is related directly with the frequency of the signal in hertz by the equation:

$$\omega = 2\pi f \quad (3.11)$$

Including the phase-shift  $\phi$  in the current response signal. This current signal can be analyzed as a sum of sinusoidal functions (a Fourier series). The impedance then can be calculate in terms of a magnitude and a phase-shift following an analogous equation to Ohm's Law:

$$Z = \frac{E_t}{I_t} = \frac{E_0 \sin(\omega t)}{I_0 \sin(\omega t + \phi)} = Z_0 \frac{\sin(\omega t)}{\sin(\omega t + \phi)} \quad (3.12)$$

Where the impedance is expressed in terms of a magnitude,  $Z_0$ , and a phase shift,  $\phi$ . The representation of these parameters as function of the frequency is called the Bode plot. However, for a better physical interpretation of impedance data, is more convenient to describe the impedance as a complex number following the Euler's relationship for sinusoidal parameters:

$$Z(\omega) = \frac{E}{I} = Z_0(\cos\phi + j\sin\phi) \quad (3.13)$$

$$Z(\omega) = Z'(\omega) + jZ''(\omega) \quad (3.14)$$

Plotting the real part on the X-axis and the imaginary part on the Y-axis, an impedance representation called "Nyquist plot" is obtained. This is the most common form to defined the impedance in batteries and other energy storage devices and although there is not direct information about the frequency used in each point, is easy to interpretate the resistance nature of the measured cell. In a Nyquist plot, the impedance value is represented with a vector of magnitude equal to  $|Z|$  and an angle from the X-axis called phase angle. By considering the extremes, a pure resistance does not have that imaginary (also called out-of-phase) part, so the phase angle is equal to  $0^\circ$ . On the contrary, a theoretical capacitor, where the signal is totally out-of-phase, the phase angle should be  $-90^\circ$ . A real device has not a pure resistive or capacitive behavior, is always a mixture of both.

The sum of all impedance data measured at different frequencies often results on one or more semicircles which can be interpreted as different resistance interfaces in the device. For an easy interpretation of the data its very helpful to fit the obtained data to an electric circuit model. In the case of supercapacitors, the classic first order equivalent circuit can be seen in Figure 3.10.

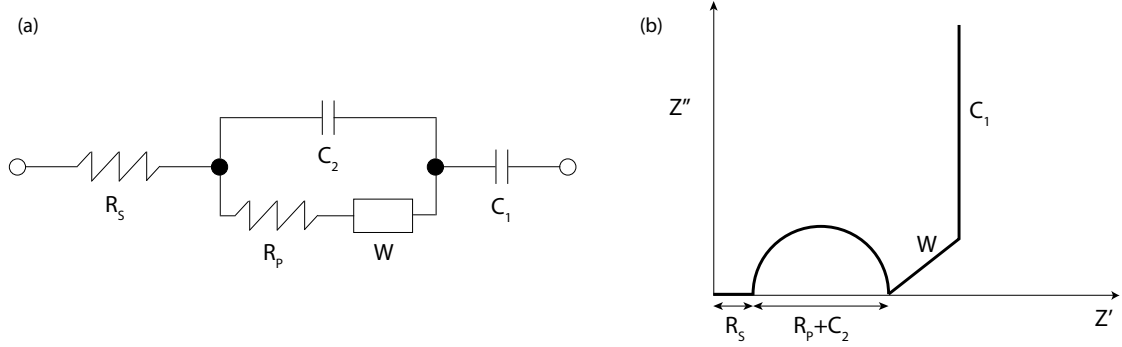


Figure 3.10: (a) First order equivalent circuit of a supercapacitor and (b) its corresponding Nyquist plot.

The first resistance  $R_s$  is related with the intrinsic resistance of the electrolyte. The second resistance  $R_p$  and the capacitor element  $C_2$  in parallel represent the electrical resistance of the cell, defined by the diameter of the semicircle in the Nyquist plot. The Warburg element  $W$  takes into account the diffusion of the electrolyte ions within the carbon material. Its physical meaning comes from the time necessary for the electrolyte ions to fill the accessible pores in the material. Finally, the capacitor element  $C_1$  represents the capacitive behavior of the electrochemical cell. The longer and more parallel to the Y-axis, the higher capacitance and more "pure" capacitive behavior possess.

The capacitance value can also be calculated from impedance data. Considering the supercapacitor as a whole, the follow direct relation can be made:

$$Z(\omega) = \frac{1}{j\omega C(\omega)} \quad (3.15)$$

Then, as the impedance, the capacitance value can also be define as a complex number following the same Euler's relationship used before:

$$C(\omega) = C'(\omega) + jC''(\omega) \quad (3.16)$$

Allowing the calculation of both parts of the capacitance from impedance data as follow:

$$C'(\omega) = \frac{-Z''(\omega)}{\omega|Z(\omega)|^2} \quad (3.17)$$

$$C''(\omega) = \frac{Z'(\omega)}{\omega|Z(\omega)|^2} \quad (3.18)$$

Where the term  $|Z(\omega)|$  represent the magnitude of the impedance vector at each frequency. The real part  $C'(\omega)$  of the capacitance corresponds to the capacitance measured at low frequency and is the capacitance value of the cell. The imaginary part  $C''(\omega)$  can be correlated to an energy dissipation by irreversible processes (Taberna *et al.*, 2003). By representing both values as function of frequency, the real part (Figure 3.11a) shows a sharply increase at low frequencies up to the total capacitance of the cell, meanwhile the imaginary part (Figure 3.11b) shows a maximum defining a time constant characteristic of the whole system, also called dielectric relaxation time (Cole & Cole, 1941), which indicates the time required to the electrolyte ions to completely fulfill the available surface area to neutralize the charge generated on the electrodes, in other words, the time required by the device to be fully charged.

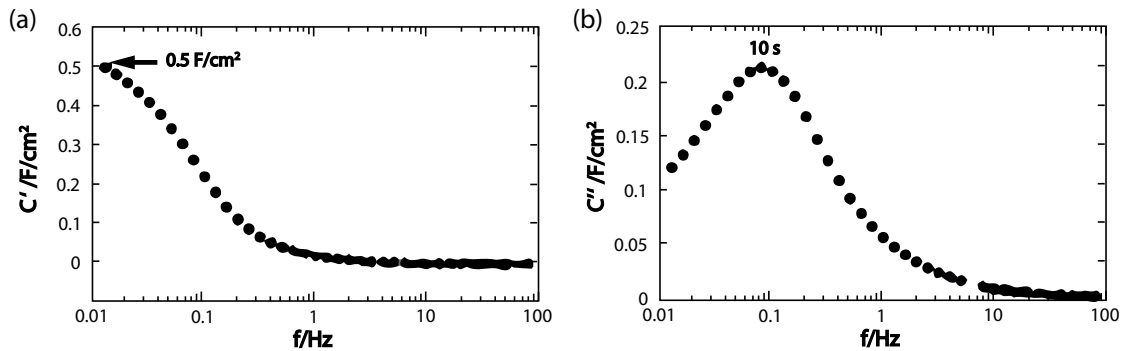


Figure 3.11: (a) Real ( $C'$ ) and (b) imaginary ( $C''$ ) parts of the complex capacitance showing a total capacitance value up to  $0.5 F cm^{-2}$  and a time constant of 10 seconds (after Taberna *et al.*, 2003).



## Bibliography

- AMMRF (2019). Australian microscopy & microanalysis research facility. url <http://www.ammrf.org.au/myscope>. Accessed: 22-03-2019.
- BRUNAUER, S., EMMETT, P. H. & TELLER, E. (1938). Adsorption of gases in multimolecular layers. *Journal of the American Chemical Society* **60**(2), 309–319.
- COLE, K. S. & COLE, R. H. (1941). Dispersion and absorption in dielectrics i. alternating current characteristics. *The Journal of Chemical Physics* **9**(4), 341–351.
- GREGG, S. J. & SING, K. S. W. (1982). *Adsorption, surface area and porosity*. Academic Press, London.
- I. GOLDSTEIN, J., LYMAN, C. E., NEWBURY, D. E., LIFSHIN, E., ECHLIN, P., SAWYER, L., C. JOY, D. & MICHAEL, J. R. (2003). *Scanning Electron Microscopy and X-Ray Microanalysis*. Kluwer Academic.
- JAGIELLO, J. & OLIVIER, J. P. (2013). 2d-nldft adsorption models for carbon slit-shaped pores with surface energetical heterogeneity and geometrical corrugation. *Carbon* **55**, 70–80.
- MACDONALD, J. R. & JOHNSON, W. B. (2018). Fundamentals of impedance spectroscopy. In: *Impedance Spectroscopy; Theory, Experiment, and Applications*. Hoboken, NJ: John Wiley & Sons, Inc., pp. 1–20.
- OLSEN, E. (1990). *Métodos ópticos de análisis*. Editorial Reverté.
- ROUQUEROL, J., ROUQUEROL, F., LLEWELLYN, P., MAURIN, G. & SING, K. (2013). *Adsorption by powders and porous solids*. Academic Press.
- SEATON, N., WALTON, J. & QUIRKE, N. (1989). A new analysis method for the determination of the pore size distribution of porous carbons from nitrogen adsorption measurements. *Carbon* **27**(6), 853–861.
- TABERNA, P., SIMON, P. & FAUVARQUE, J. (2003). Electrochemical characteristics and impedance spectroscopy studies of carbon-carbon supercapacitors. *Journal of The Electrochemical Society* **150**(3), A292–A300.
- WILLIAMS, D. B. & CARTER, C. B. (2009). *Transmission Electron Microscopy*. SPRINGER.

## Chapter 4

# Organometallic-derived carbon with embedded metal nano-oxide composites as improved electrode materials for supercapacitors

The use of organometallic compounds as precursors for carbon materials was firstly reported by Komatsu and Endo in 1985 (Komatsu & Endo, 1985). Iron was commonly used as catalyst in carbon fiber production and researches have the idea of reducing the catalyst material to the minimum particle size in order to improve the efficiency of the method, so they used ferrocene as catalyst. Although the method was not completely satisfactory, the authors obtained various undefined mixtures of fibers and carbon nanoshapes. Years later, ferrocene became the common catalyst used for the production of existing and new carbon nanostructures in chemical vapor deposition (CVD) synthesis. Mainly due to its easy availability, low cost and good stability on air atmosphere (Hummers & Offeman, 1958; Marcano *et al.*, 2010; Pumera, 2009), contributing to establish this CVD technique as one of the most used to synthesize, under appropriate conditions, the so-called Shape Carbon Nanomaterials (SCNMs) (Nyamori *et al.*, 2008) like graphene or CNTs from organometallic precursors (Ansari & Giannelis, 2009; Jiang *et al.*, 2013).

It was not until 2005 that the well known chlorination method in the CDC synthesis was applied to organometallic compounds. Urones *et al.* (Urones-Garrote *et al.*, 2005) firstly employed ferrocene as precursor in the chlorination reaction yielding the first Organometallic-Derived Carbons (ODC) showing several shapes

(tubes, bags, etc.) depending on the temperature and reaction time. The CDC synthesis, as seen in the introduction (pg. 25, section 1.3 Carbon Science), consists of the selective metal etching of the crystalline network of the carbide with halogens (mainly chlorine) at high temperatures forming the corresponding volatile metal halide; being a well-established method to synthesize nanoporous carbon with relative high purity, specific shape, narrow pore size distribution and high surface area (Gogotsi *et al.*, 2003). The fact that the main drawback of this synthetic method relies in the low weight yield due to the loss of the heavier component, encouraged the use of precursors with higher amount of carbon atoms per formula like organometallic compounds. For example, in SiC, TiC and WC the mass percentages of carbon are 29.95, 20.06 and 6.13% respectively meanwhile for ferrocene is 64%. Besides, chlorine can also react with carbon forming  $\text{CCl}_4$ , lowering the final yield (Yushin *et al.*, 2006). In the case of ferrocene, iron was extracted from the metallocene structure and eliminated as a mixture of its iron chlorides ( $\text{FeCl}_2$  and  $\text{FeCl}_3$ ); hence, cyclo-pentadienyl rings provide the carbon source. Owing to its success, in the last years, the same group have reported the synthesis of microporous organometallic-derived carbons with different shapes by chlorination of organometallic precursors such as cobaltocene (Katcho *et al.*, 2007), chromocene (González-García *et al.*, 2013), bis(cyclopentadienyl) tungsten dichloride (González-García *et al.*, 2010) and bis(cyclopentadienyl) titanium dichloride (González-García *et al.*, 2011).

During the chlorination method, metal halides are formed in gas phase as secondary products. When the formed metal halide has a low boiling point and the chlorination temperature is high enough, halides are easily eliminated from the carbon networks, but if the metal halide has a higher boiling point or the chlorination temperature is not enough, the metal halide formed cannot escape out of the ODC matrix, obtaining a composite material constituted by a carbon matrix containing a fine dispersion of metal halide nanoparticles. This phenomenon is observed in the previous case of ferrocene (Urones-Garrote *et al.*, 2005), where the  $\text{FeCl}_2$  formed gets stuck in the ODC due to its relatively high melting point ( $674^\circ\text{C}$ ) or more evident in the products of the chlorination of chromocene (González-García *et al.*, 2013) where the halide remains encapsulated forming core-shell particles consisting of a crystalline nucleus identified as  $\text{CrCl}_3$  surrounded by layers of disordered carbon (Figure 4.1).

In terms of the applicability of these materials as electrodes in supercapacitors devices, they are not apparently useful. Solid nanoparticles subtract surface area to the carbon material reducing its capacitance values and although some metal halides have pseudocapacitance properties, they can be dissolved in acid

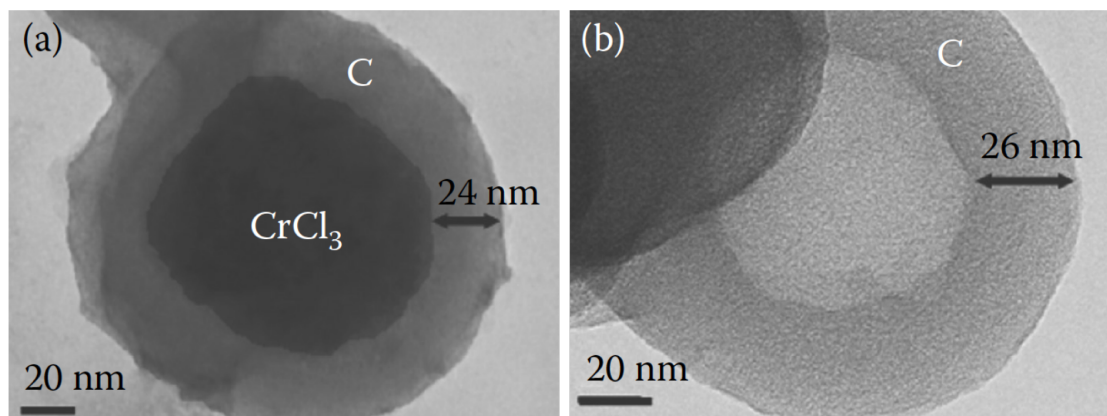


Figure 4.1: (a) Medium-magnification TEM images for a filled sphere at 400 °C and (b) the resulting hollow carbon sphere at 900 °C (b) both obtained from chromocene precursor (González-García *et al.*, 2013).

aqueous electrolyte or transformed into hydroxides/oxides in basic electrolytes. To take advantages of these subproducts of the chlorination reactions at low temperatures, in this chapter we describe the hydrothermal transformation of those halide nanoparticles into the corresponding stable electroactive nano-oxides. In this sense, organometallic compounds based on metals exhibiting pseudocapacitance in their oxide forms, such as nickel or manganese, were selected as precursors for the synthesis of new carbon composite materials where both capacitive and pseudocapacitive energy storage mechanisms could be combined in synergy, improving the total capacitance value of the electrode material.

## 4.1 Nickelocene as precursor of microporous organometallic-derived carbon with confined nickel oxide nanoparticles as supercapacitor electrode

NiO is one of the most promising electrode materials due to its good pseudocapacitive performance, availability, low cost and environmental friendship (Brousse *et al.*, 2015). However, owing to its poor conductivity, cycling stability and rate capability its high specific capacitance potential is limited in practical applications. On the contrary, carbon materials exhibit good conductivity, high power density and long cycle life, however the low specific capacitance limits their further appli-

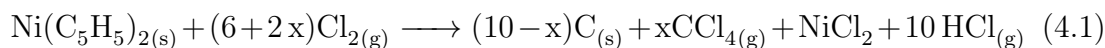
cations. In this sense, the development of novel electrode architectures based on metal oxide nanoparticles@carbon-based composites yielding better electrochemical performances, electrical conductivity and mechanical strength is a promising field to investigate. To reach this goal, new synthetic pathways to load active nanoparticles within a carbon matrix must be developed. In this sense, several synthetic methods such as electrodeposition of  $\text{MnO}_2$  in carbon nanotubes (Zhang *et al.*, 2008), the preparation of carbon xerogel-titanium oxide composites by an inverse emulsion sol-gel method (Elmouwahidi *et al.*, 2018) or NiO-mesoporous carbon composite by a liquid-crystalline (LC) phase-templating method have been described (Chen *et al.*, 2013).

In this section, we describe the synthesis and characterization of microporous three-dimensional flower-like and sphere-like particles formed by disordered graphene-like layers obtained via chlorination of nickelocene  $\text{Ni}(\text{C}_5\text{H}_5)_2$  as carbon precursor (González-García *et al.*, 2017). Moreover, the intermediate temperature material composed by a matrix of highly disordered carbon containing nanocrystals of  $\text{NiCl}_2 \cdot 6\text{H}_2\text{O}$  is successfully transformed into a NiO@carbon composite. The incorporation of NiO nanoparticles enhances the electrochemical performance of the material as electrode in supercapacitor devices, adding a pseudocapacitive energy storage mechanism that works in synergy with the capacitive mechanism of the microporous carbon material.

## Synthesis

Two carbon samples were prepared at 600 °C and 900 °C (labeled as Ni-ODC600 and Ni-ODC900 respectively) in order to evaluate if the composite material synthesized at lower chlorination temperature yields improved electrochemical properties. Bis(cyclopentadienyl)nickel (II),  $\text{Ni}(\text{C}_5\text{H}_5)_2$ , with  $P2_1/a$  space group, ( $a = 1.073$  nm,  $b = 0.786$  nm,  $c = 0.591$  nm,  $\beta = 123.5^\circ$ ), melting point 172 °C (Wells, 1975) (Alfa Aesar, powder purity of 97%) was placed on a quartz crucible and located on a tubular furnace provided with a system capable of supplying argon and chlorine gas and a safety and neutralization system of  $\text{Cl}_2$  at the exit consisting in a one empty gas washing bottle followed by two more containing a saturated NaOH solution. The following heating program was used: a heating rate of 50 °C/min until the selected synthetic temperature (600 and 900 °C), then 1 hour at this temperature followed by switching off the furnace. At this stage, the chlorine gas flow was cut and replaced by argon (25 cm<sup>3</sup>/min) for removal of the excess of chlorine and nickel halides during the reactor cooling to room temperature. The excess of chlorine and the volatile halides formed during the synthesis were

removed by bubbling on a NaOH saturated solution at the exit of the reactor. Finally, the carbon material was washed several times with hot water and dried under dynamic vacuum in order to remove traces of adsorbed Cl<sub>2</sub>. The possible chlorination reaction can be described as follows:



A portion of the material chlorinated at 600 °C, was placed in a Teflon stainless steel hydrothermal chamber with 30 mL of KOH 12 M. The autoclave was heated at 200 °C for 48 h then the sample (labeled as NiO@ODC) was filtered under vacuum, washed with abundant water and the residual black powder was dried at 100 °C overnight.

## Structural Characterization

X-ray diffraction patterns (Figure 4.2) were recorded to follow the chlorination of Ni(C<sub>5</sub>H<sub>5</sub>)<sub>2</sub>. After the first thermal treatment (600 °C), the characteristic maxima of the crystalline precursor disappear suggesting the transformation of the Ni(C<sub>5</sub>H<sub>5</sub>)<sub>2</sub> used as carbon source. In the patterns of the sample produced at 600 °C new diffraction maxima appear, identified as typical of the crystal structure of NiCl<sub>2</sub> · 6H<sub>2</sub>O (Pedro González, 2012). Finally, at 900 °C, the absence of any defined diffraction maxima in the patterns suggests that the reaction has been completed and the obtained materials do not have a well-ordered crystalline structure. In addition, the presence of a broad and not so well-defined diffraction maximum located at 2θ = 24° suggests that the materials present a highly graphite-like disordered nanostructure.

### *Ni-ODC600 Carbon nanostructures*

The morphology of the sample is observed in the SEM image displayed in Figure 4.3a. At this chlorination temperature the sample consists mostly of spherical particles of diameter ranging from 90 to 220 nm. Additionally, in lesser amount, carbon plaques with length ranging from 400 to 950 nm and thickness varying from 30 to 80 nm are observed. In the low magnification TEM image (Figure 4.3b) it is possible to distinguish three different particles: corrugated plaques of irregular shape and thickness, solid spheres of diameter from 70 to 170 nm and

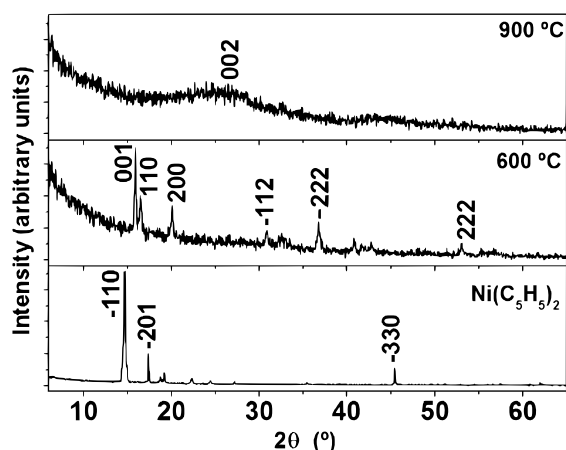


Figure 4.2: X-ray diffraction patterns for samples at different temperatures from nickelocene.

small hollow spheres of diameter from 40 to 55 nm and wall thickness from 5 to 12 nm that seem to be decorating the surface of the solid ones. In some cases, the wall of these hollow spheres looks like open or broken. The corresponding SAED pattern, inset in Figure 4.3b, displays diffuse diffraction rings with  $hk0$  graphite-like reflections, which are characteristic for carbon materials built up by highly disordered graphene-like layers without a three-dimensional stacking at long range. Figure 4.3c shows a HRTEM image recorded at the edge of one solid sphere. The contrast of this image is characteristic of highly disordered carbon materials, where the graphene-like layers are randomly stacked and form a very dense nanostructure. Notice some individual graphene-like layers at the edge of the sphere. Figure 4.3d shows a HRTEM image of one open sphere being less dense than the solid ones. It is clearly observed that it is formed by highly disordered and entangled graphene-like layers; however, it is possible to identify some individual graphene layers at the edge of the walls of this nanosphere. A careful analysis of the HRTEM image reveals the presence of nanocrystals (smaller than 5 nm) of  $\text{NiCl}_2 \cdot 6\text{H}_2\text{O}$ , identified by their chemical composition obtained from the XEDS analysis. Finally, the HRTEM image of Figure 4.3e shows the structure of one carbon plaque. Once again, the contrast of this image suggests that it is formed by two different materials: a matrix of highly disordered carbon and well dispersed  $\text{NiCl}_2 \cdot 6\text{H}_2\text{O}$  nanocrystals of within the matrix.

#### *Ni-ODC900 Carbon nanostructures*

The morphology of the carbon materials obtained at 900 °C chlorination temperature is observed in Figure 4.4. During the SEM observations, micrometric

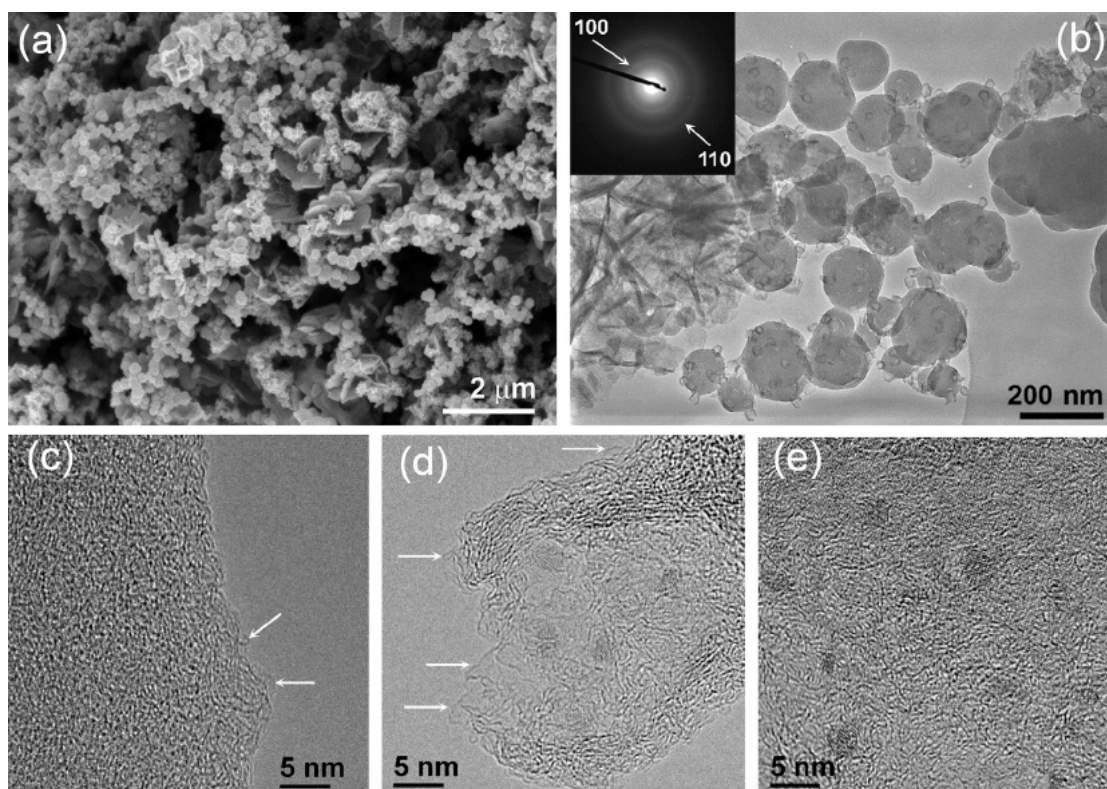


Figure 4.3: (a) SEM micrograph showing conglomerated spheres and some carbon plaques. (b) Low magnification TEM image of the particles (solid spheres decorated with smaller hollow spheres and bended plaques) obtained at 600 °C. Their corresponding HRTEM images show the edge of (c) a solid sphere and reveal presence of nanocrystalline  $\text{NiCl}_2 \cdot 6\text{H}_2\text{O}$  in (d) an open hollow sphere and (e) a carbon plaque. Notice the graphene-like layers marked with white arrows.

structures quite similar to a desert rose have been found in major proportion as it can be seen in Figure 4.4a. A higher magnification micrograph (Figure 4.4b), made on one desert rose, allows observing that the petals of these roses are formed by a coaxial-type stacking of carbon plaques (thickness from 240 to 300 nm) that could be the result of the evolution of the carbon plaques previously detected at lower chlorination temperature. However, thickness of these plaques presents an important increase with the reaction temperature. We have also found some beds of spherical particles, diameter from 90 to 230 nm (almost the same size than the spheres obtained at 600 °C) but conglomerated (Figure 4.4c). These spheres were observed in smaller proportion than the desert roses.

The average nanostructure of these particles was studied by TEM. Figure 4.5a



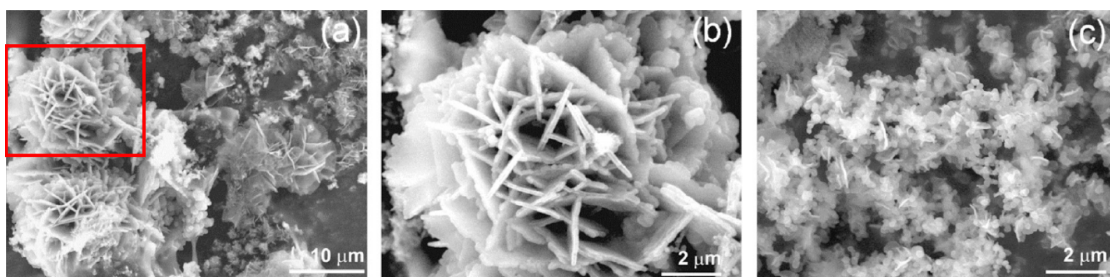


Figure 4.4: (a) SEM micrographs of the materials obtained at 900 °C. Carbon particles of micrometric size similar to a desert rose and spherical particles. (b) Enlargement of the zone squared in (a) revealing that these roses are formed by thick carbon plaques. (c) Conglomerates of carbon spheres and some isolated carbon plaques.

shows a low magnification TEM image of one of the carbon plaques that could be related to the particles that form the petals in the desert rose structure. As observed, contrast of the image suggests that these plaques are corrugated, sometimes bent and have variable shape and thickness. Figure 4.5b shows a group of solid spheres (diameter from 75 to 150 nm) surrounded by smaller hollow spheres (diameter from 35 to 50 nm, wall thickness from 6 to 9 nm), as observed previously in the sample obtained at 600 °C. This curious nanostructure is quite similar to the morphology of *Opuntia ficus-indica*, see inset, a cactus that grows in America, Spain, Italy and Western Africa. The SAED patterns, inset in Figure 4.5a and b, present diffraction rings slightly more defined than the observed at 600 °C, with spacing than can be assigned to the  $hk0$  graphite type reflections, once again, associated to the disorder in the graphene-like layers despite that an incipient local graphitization takes place at this chlorination temperature. Even though the low magnification TEM images do not show a significant change in the nanostructure of the particles obtained at 900 °C, respect to the 600 °C ones, in their respective HRTEM images it is possible to observe an evolution in the local nanostructure of these particles, as suggested by their SAED patterns. Figure 4.5c presents an image that corresponds to one of the carbon plaques. Contrast of this image is characteristic of highly disordered carbon materials; however, it is possible to detect some individual graphene-like layers at the edges of the structure, as well as some small graphitic ribbons formed by the stacking of 2-3 graphene layers. The HRTEM images of the solid and hollow spheres are in Figure 4.5d and e, respectively. Note that both nanostructures are mostly formed by open and disordered graphene-like layers. In some cases, these layers are locally stacked as small local graphitic domains of 2-4 graphene-like layers. At this temperature, Nickelocene is completely transformed into an ODC, without any residual  $\text{NiCl}_2$ .

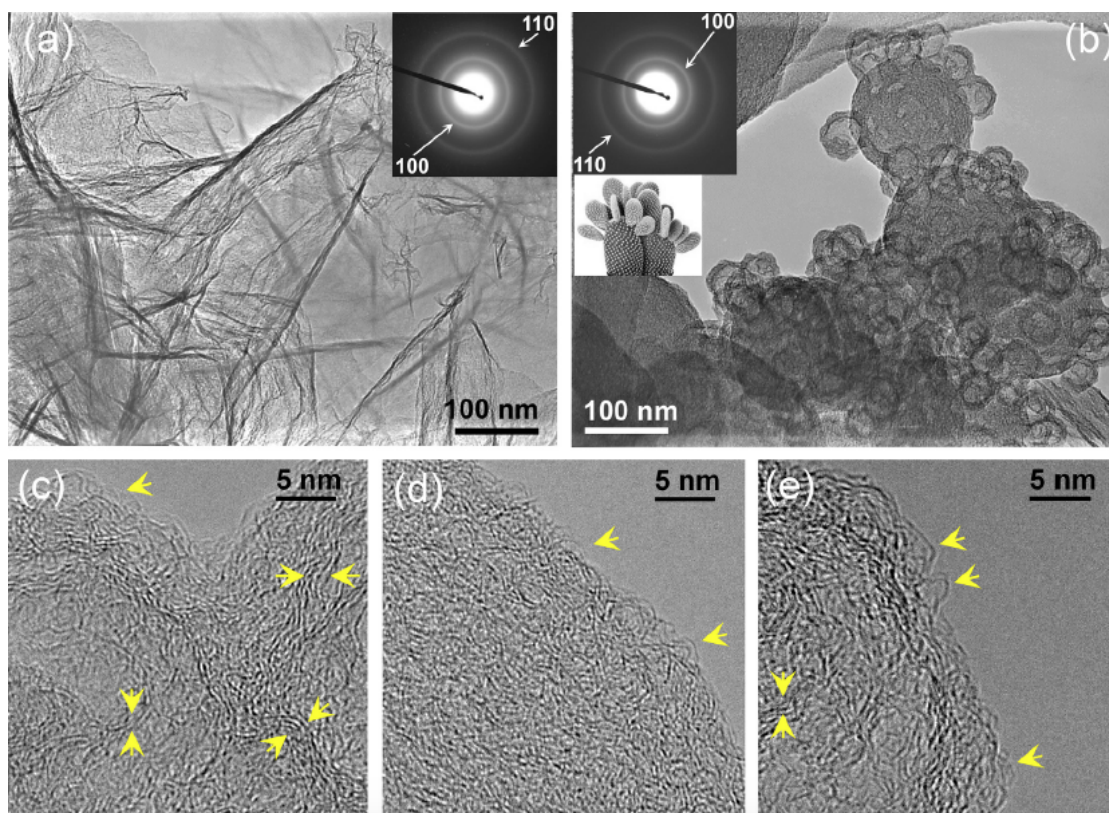
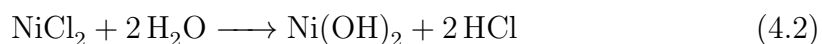


Figure 4.5: Low magnification TEM images of (a) the petals of the desert rose and (b) the group of spherical particles that form the Opuntia cactus shape. HRTEM images of (c) a single carbon plaque, (d) a solid sphere and (e) the edge of a hollow sphere. The graphitic ribbons and individual graphene-like layers are marked with yellow arrows

#### *NiO@ODC composite material*

The formation of such a composite material at 600 °C as an intermediate product in the preparation of the organometallic-derived carbon, suggests the possibility of the transformation of the  $\text{NiCl}_2 \cdot 6\text{H}_2\text{O}$  into NiO nanoparticles yielding a new composite material NiO@ODC. The hydrothermal treatment in basic media converts the  $\text{NiCl}_2 \cdot 6\text{H}_2\text{O}$  nanoparticles according to the following reactions:





The morphology observed by SEM images displayed in Figure 4.6 can be related with the material carbonized at 600 °C. Spherical particles of diameter range (from 90 to 220 nm) similar than the Ni-ODC600 composite and, in minor proportion, carbon plaques of varying thickness can be observed at low magnification (see Figure 4.6a), demonstrating that the carbon material does not seem to have undergone any transformation. However, a closer inspection of these spheres (Figure 4.6b) indicate that the spheres have now a rough and open structure, in some cases broken spheres, instead of the smooth and soft surface observed in the Ni-ODC600 precursor. The new surface morphology suggests an increase of the surface area of the NiO@ODC composite. Additionally, although at this magnification it is impossible to detect such a small NiO nanoparticles in the composite, XEDS analysis detect the presence of nickel and oxygen, characteristic signals of the successful transformation of  $\text{NiCl}_2 \cdot 6\text{H}_2\text{O}$  residue into NiO nanoparticles within the carbon material.

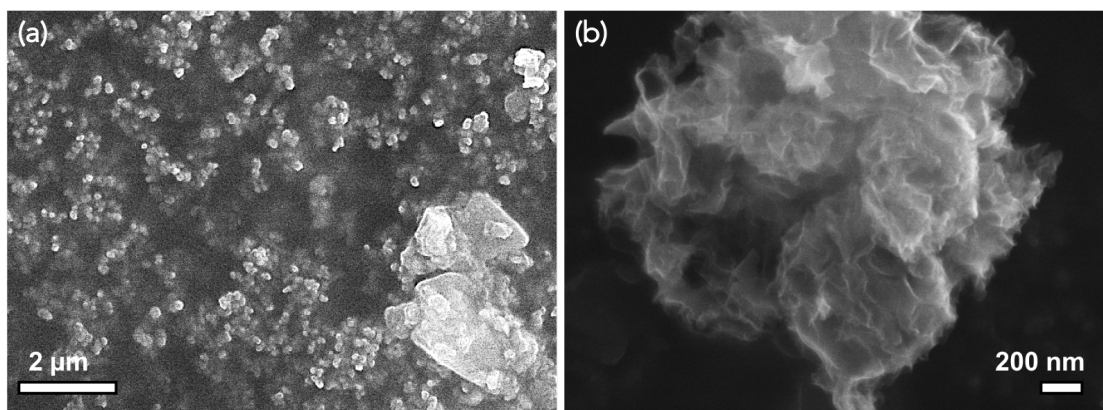


Figure 4.6: (a) SEM micrograph showing conglomerated spheres and some carbon plaques. (b) Detail of conglomerated spheres showing the roughness of their surface.

A closer inspection of the sample in the TEM (Figure 4.7) by High-Angle Annular Dark Field (HAADF) imaging (Figure 4.7a) confirms that the spherical material is composed by a matrix of low atomic number element containing brighter areas of a heavier one. Along with larger nanocrystals, the high magnification image displayed in Figure 4.7b also demonstrates the existence of bright spots all along the carbon matrix consisting of well dispersed nanoparticles smaller than 5 nm in diameter. Some of these small nanoparticles are identified as NiO



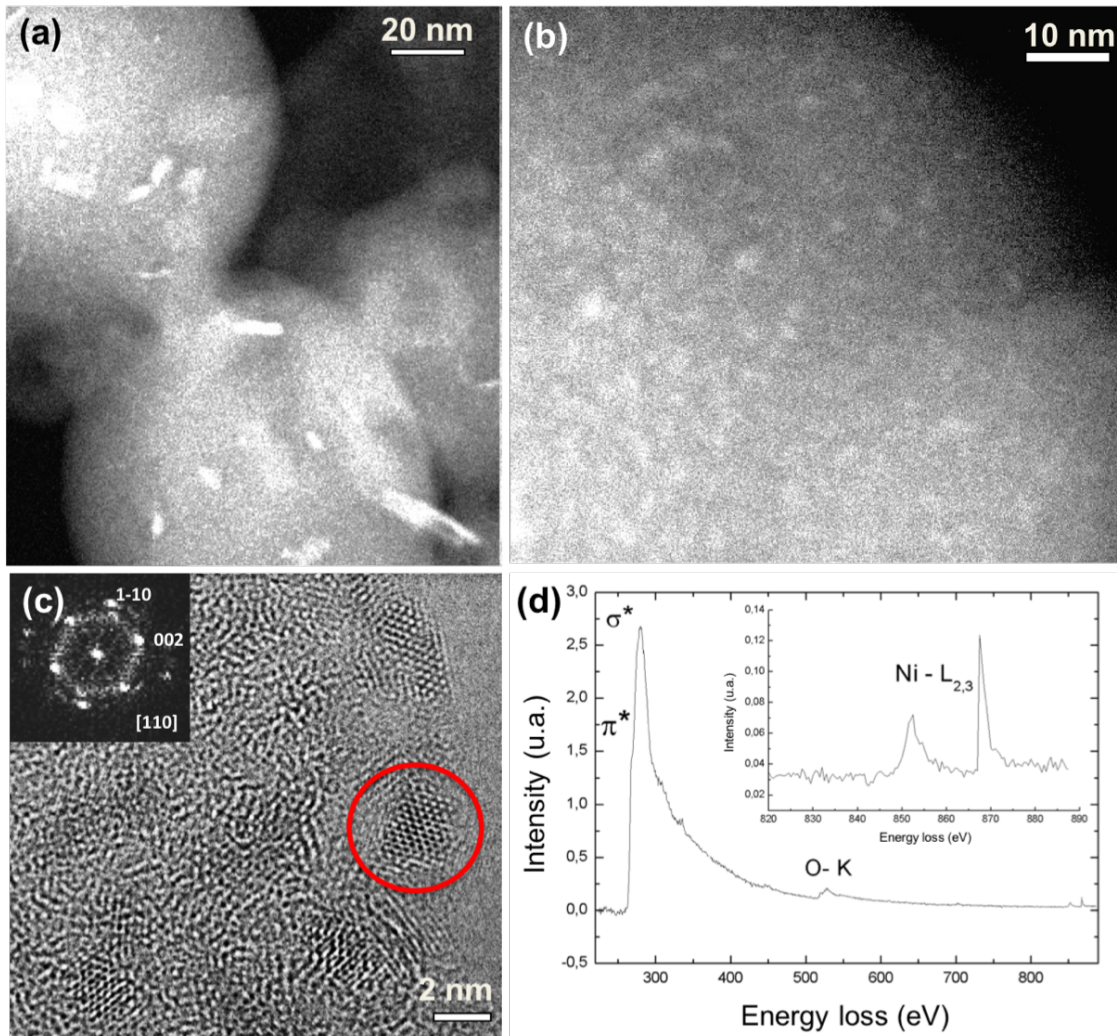


Figure 4.7: (a) Low and (b) high magnification HAADF images of the solid spheres after the hydrothermal process. (c) HRTEM image showing an edge of a solid sphere where well crystalline NiO nanoparticles (identified by inset DDP along the  $[110]$  zone axis) can be observed within highly disordered graphene layers. (d) EEL spectrum from the particle in (c) marked with a red circle showing the characteristic edges of NiO together with the carbon one.

nanocrystallites oriented along the  $[110]$  zone axis in the HRTEM image displayed in Figure 4.7c. Besides, the EELS spectrum recorded in the composite NiO@ODC (Figure 4.7d) shows its characteristic edges as well as the absence of chlorine. The self-assembly of highly dispersed pseudo-capacitive NiO nanoparticles into a carbon matrix improves not only the specific capacitance of the carbon but

also the electrical conductivity and electrode density for its further application in supercapacitors (Chen *et al.*, 2013).

## Textural Characterization

The textural parameters were obtained from the  $N_2$  adsorption-desorption measurements performed on the three materials previously described. Their isotherm plots (Figure 4.8a) can be considered as Type I, related to microporous materials, according to the IUPAC classification (Rouquerol *et al.*, 2013). The isotherms also exhibit a H4 hysteresis loop which is associated to non-rigid slit-shaped pores. The closure of the desorption branch at  $p/p_0 = 0.42$  is almost independent to the morphology of the sample but it is associated to the nature of the adsorptive (Sing *et al.*, 1985). Finally, an important amount of nitrogen is adsorbed at relative pressures  $p/p_0 > 0.7$  revealing the existence of textural porosity formed by the interparticle voids among the carbon packing of all the particles, as it has been observed by SEM (Figures 4.3, 4.4 and 4.6). Results derived from the assessment of the surface area values are collected in Table 4.1. The specific surface area, obtained using the BET theory, is as high as  $710 \text{ m}^2/\text{g}$  for Ni-ODC900, whereas for Ni-ODC600 and NiO@ODC a dramatic reduction is found due to the presence of the  $\text{NiCl}_2 \cdot 6 \text{H}_2\text{O}$  or NiO nanoparticles within the carbon matrix. As displayed in Table 4.1 the microporous surface area (SMic) for all the tested materials comprise almost 80% of the total area, indicating that they are mostly microporous.

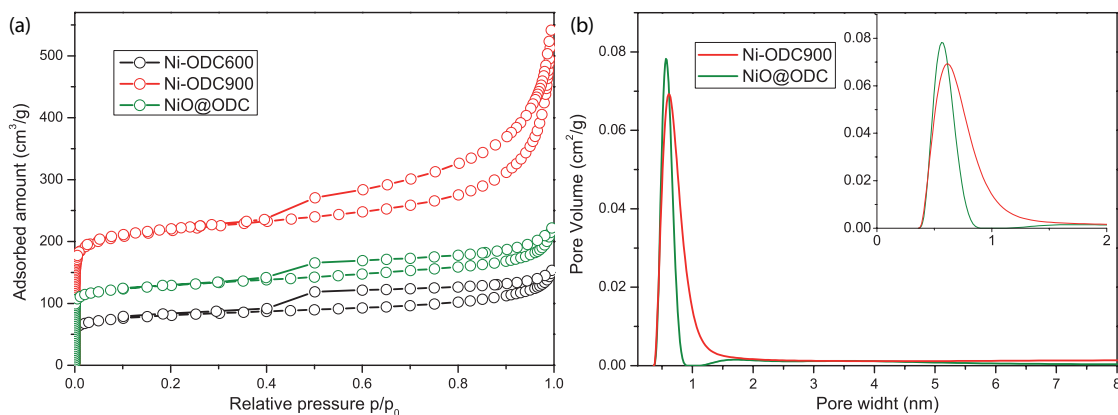


Figure 4.8: (a) Standard nitrogen adsorption-desorption isotherms at 77 K for Ni-ODC600, Ni-ODC900 and NiO@ODC. (b) Representation of the pore size distribution showing the region with pore width  $<50 \text{ nm}$  for Ni-ODC900 and NiO@ODC and the micropore region  $<2 \text{ nm}$  in the inset.

	$S_{\text{Total, BET}}$ ( $\text{m}^2/\text{g}$ )	$S_{\text{Ext. BET}}$ ( $\text{m}^2/\text{g}$ )	$S_{\text{Micr. BET}}$ ( $\text{m}^2/\text{g}$ )	Pore Width $_{2\text{D-NLDFT}}$ (nm)
<i>Ni-ODC600</i>	277	49	227	-
<i>Ni-ODC900</i>	710	136	573	0.61
<i>NiO@ODC</i>	422	80	341	0.56

Table 4.1: Total, exterior and micropore BET surface area and pore width of prepared samples.

The pore size distribution (PSD) plots, derived from the NLDFT method are represented in Figure 4.8b. The graph reveals that both materials exhibit an almost well-defined pore structure with narrow microporosity (0.61 nm and 0.56 nm for Ni-ODC900 and NiO@ODC respectively displayed in the inset of Figure 4.8) and some contributions of wide micropores (up to 2 nm) in the case of Ni-ODC900. In addition, NiO@ODC composite presents some mesopores ranging from 1.59 to 5.71 nm, meanwhile the Ni-ODC900 maintains a similar pore volume up to 44.17 nm with slight maxima at 8.39 and 31.21 nm.

## Electrochemical Characterization

The electrochemical characterization was evaluated in a first step by cyclic voltammetry measurements in a three-electrodes cell. A thin film of the tested materials deposited on top of a glassy carbon rod was fabricated as working electrode, with a platinum wire serving as a counter electrode and a Hg/HgO electrode as reference. A NaOH 1M solution was used as electrolyte in the voltage range between -0.2 and 0.4 V.

The CV curves at a scanning rate of 5 mV/s for the three materials show a nearly rectangular shape (see Figure 4.9) indicating a capacitive nature of the tested electrodes. The nanocomposite NiO@ODC exhibits a highest specific capacitance ( $85 \text{ F g}^{-1}$  at  $5 \text{ mV s}^{-1}$ ) compared with its precursor Ni-ODC600 ( $10 \text{ F g}^{-1}$  at  $5 \text{ mV s}^{-1}$ ) which contains chloride nanoparticles instead of oxide. This behavior indicates that  $\text{NiCl}_2$  nanoparticles are not electrochemically active, and therefore the poor capacitance value of this material is only originated by the electrostatic adsorption of the electrolyte ions on the carbon surface not hidden by the nanoparticles. On the other hand, since the NiO@ODC material was obtained by hydrothermal transformation of the Ni-ODC600 composite, and the increase of the surface area is not significant, it suggests an important contribution of pseudocapacitance from

the NiO nanoparticles. In addition, the NiO@ODC nanocomposite doubles the specific capacitance values of the pure nanoporous carbon Ni-ODC900 ( $47 \text{ F g}^{-1}$  at  $5 \text{ mV s}^{-1}$ ). Although the specific surface area of Ni-ODC900 is larger than the NiO@ODC composite, the combination of the two storage mechanisms on the latter, results in a higher gravimetric capacitance.

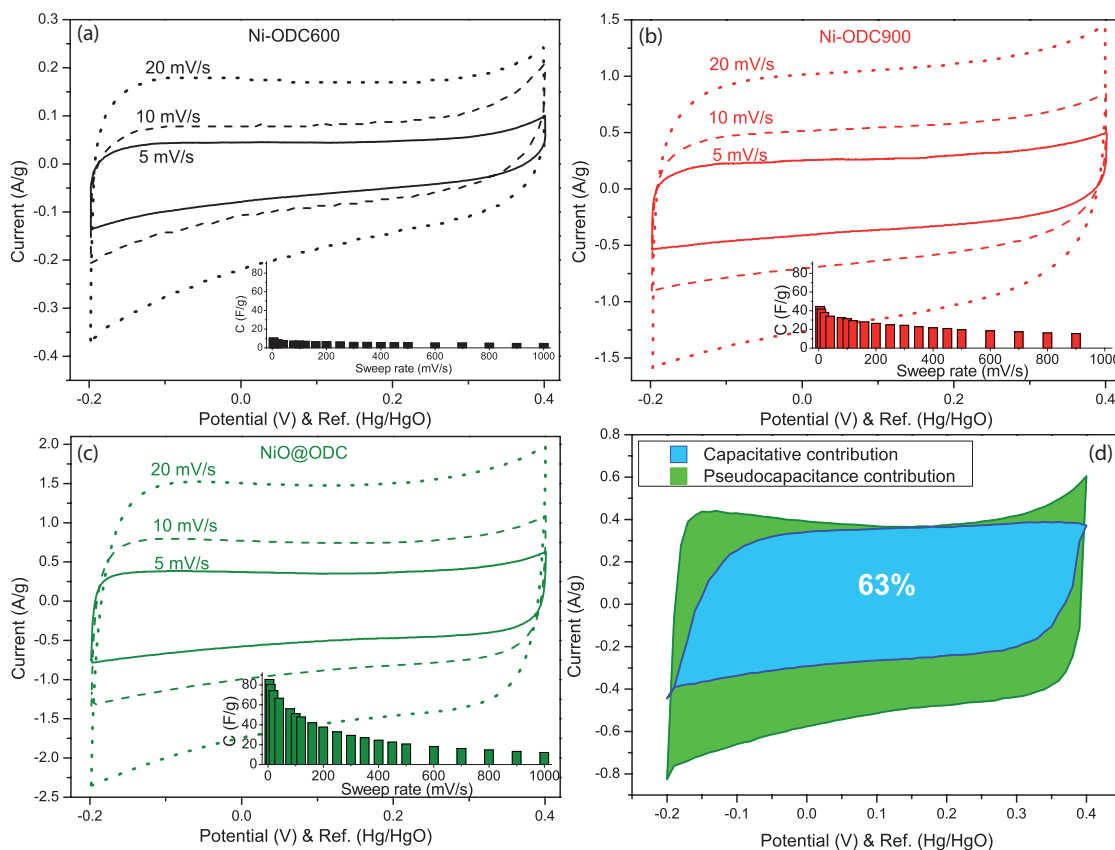


Figure 4.9: Cyclic voltamperometric and capacitance retention at sweep rates from 5 to  $1000 \text{ mV s}^{-1}$  for the carbon material obtained at (a)  $600 \text{ }^\circ\text{C}$ , (b)  $900 \text{ }^\circ\text{C}$  and (c) the composite material NiO@ODC on three-electrode configuration. (d) CV for the composite material NiO@ODC with separate contributions: capacitance (blue) and pseudocapacitance (green).

Several voltammograms were recorded under different scanning rates ranging from 5 to  $1000 \text{ mV s}^{-1}$  in order to evaluate the capacitance retention at highest cycling speeds. The material that better retains capacitance at higher sweep rates is the Ni-ODC600 composite (Fig 4.9a), but this material at  $5 \text{ mV s}^{-1}$  exhibits a capacitance as low as  $10 \text{ F g}^{-1}$ , being probably associated with the fact that only the external surface participates in the electrochemical process. Where ions have not diffusion problem even at high sweep rates. In comparison, the Ni-ODC900

carbon has a higher capacitance loss, approximately 50% at speeds of 1000 mV/s. This disordered carbon material is free of either metal halide nanoparticles or adsorbed chlorine, so the entire microporous area is accessible to the ions. It is in these pores where the ions begin to have diffusion problems, which produces that at higher loading speeds the ions do not have enough time to enter and leave the whole microporous network. In the case of the material NiO@ODC, a carbon-like behavior is observed, very similar to the Ni-ODC900 carbon material. It has the same type of porosity with a similar pore width, and therefore the response at high speeds is similar, but it seems that at low speeds rates the pseudocapacitive mechanism becomes to play an important role by doubling the amount of stored charge.

Additionally, by considering that during the voltammetric experiment, the current response for each sweep rate will vary depending on whether the redox process is diffusion-controlled or surface controlled (capacitive), both contributions can be discriminated and estimated (Augustyn *et al.*, 2014). In a surface capacitive process the current varies directly with the sweep speed ( $\nu$ ), whereas for a diffusion-controlled the current response varies with the square root of the sweep rate ( $\nu^{1/2}$ ) according to the following equation:

$$i(V) = k_1\nu^{1/2} + k_2\nu \quad (4.4)$$

Solving for the values of  $k_1$  and  $k_2$  at each potential allows for the discrimination of the diffusion and capacitive currents, if we rearrange the equation as follows:

$$\frac{i(V)}{\nu^{1/2}} = k_1 + k_2\nu^{1/2} \quad (4.5)$$

Plotting the sweep rate dependence of the current allows us to determine  $k_1$  and  $k_2$  from the slope and the y-axis intercept point of a straight line, respectively, at each fixed potential. After this calculation over the whole potential window we are able to quantify the fraction of the current due to each of these contributions. Figure 4.9d shows the total charge storage of NiO@ODC at a sweep rate of 5 mV/s. These results show that 63% of the total current corresponds to the capacitive mechanism, and the 37% enclosed in the green area is caused by the redox pseudocapacitance of the NiO nanoparticles. Although a capacitive contribution of NiO@ODC similar to that for Ni-ODC600 composite would be expected, since the last is the same material without pseudocapacitive contribution, the slightly



higher value determined for the capacitive contribution of NiO@ODC composite being 63% of the total value, is related to the highest surface area found in this composite material, probably due to the removal of NiCl<sub>2</sub> nanoparticles, hindering the surface of the carbon material, during the solvothermal transformation.

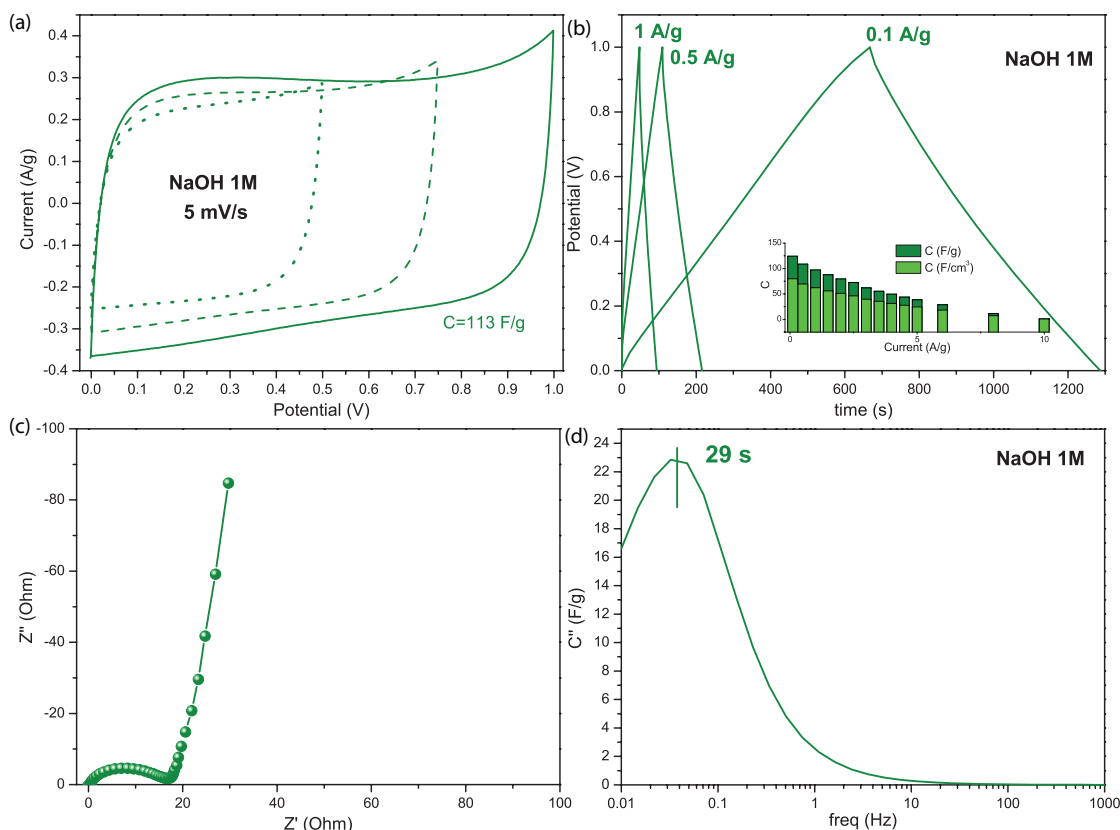


Figure 4.10: Electrochemical Characterization of NiO@ODC composite material on a symmetrical two-electrode cell: (a) CV, (b) GCPL and (c) EIS on Nyquist and (d) complex imaginary capacitance.

Once determined the superior electrochemical performance of the nanocomposite NiO@ODC, this material has been tested in a symmetrical cell. The composite material was processed to make a film and then two disc-electrodes were prepared. They were used both as electrodes separated by a fiberglass impregnated with the NaOH 1M electrolyte in a swagelok cell configuration. CV, GCPL and EIS measurements were performed in order to characterize the cell. The CVs (Figure 4.10a) show a parallelogram shape up to 1 volt at 5 mV s<sup>-1</sup>, indicating a good capacitance behavior as well as for the GCPL plot (Figure 4.10b) where a linear ramp on the charge and discharge process at 0.1 A g<sup>-1</sup> is noticed. The gravimetric capacitance value extracted from the GCPL is 124 F g<sup>-1</sup> at 0.1 A g<sup>-1</sup>, similar to capacitance

values reported for other carbon-metal oxide composites (Lota *et al.*, 2011). On the other hand, a denser electrode ( $0,64 \text{ g cm}^{-3}$ ) has been achieved and yielding a volumetric capacitance of  $79.75 \text{ F cm}^{-3}$  at  $0.1 \text{ A g}^{-1}$ , suggesting that the material could be optimally compressed in manufacturing processes for its potential use as electrode material in portable devices, giving a standard capacitance in less space.

From the nyquist EIS plot displayed in Figure 4.10c we can get the ESR value at the end of the first semicircle, in this case it is about 17 Ohms. The complex impedance plot (Figure 4.10d) show the imaginary ( $C''$ ) part of the complex capacitance (Taberna *et al.*, 2003). The relaxation time constant of the systems, which is the maximum of the graph, is 29 seconds. The time constant is characteristic of each material, and indicates the time needed for the device to be completely charged or discharged.

## Conclusions

Microporous carbon, containing a fine dispersion of NiO nanoparticles, has been synthesized by using a novel and straightforward synthetic route. This was based on the chlorination of  $\text{Ni}(\text{C}_6\text{H}_6)$  at intermediate temperatures, followed by the hydrothermal conversion of the by-product, composed of  $\text{NiCl}_2$  nanoparticles embedded in the carbon matrix, into the target composite NiO@ODC. The success of the proposed procedure has been demonstrated by imaging of the NiO@ODC composite and its respective intermediate  $\text{NiCl}_2$ @ODC, by transmission electron microscopy. This micro/nanostructural study revealed the retention of the shape and microstructure of the carbon matrix, consisting of large solid spheres, decorated on their surface by smaller hollow ones.

Electrochemical studies in a three-electrode configuration demonstrated an improvement in the electrochemical properties of this new composite in comparison with the porous carbon obtained by chlorination of the precursor at  $900 \text{ }^\circ\text{C}$ . The electrochemical characterization in a two-electrodes symmetrical cell displays a capacitive behavior comparable with similar materials, demonstrating the validity of this novel synthesis method in the search for new electrode architectures of electrochemical energy storage materials.

## 4.2 New electrode material based on $\text{Mn}_3\text{O}_4$ nanoparticles embedded in organometallic-derived carbon (ODC)

The previous successful synthesis gave way to extend this two step process of preparing new  $\text{M}_x\text{O}_y$ @ODC composite materials to different precursors than metallocenes, like phthalocyanines or metal acetylacetonates. Among them, the manganese (II) and (III) acetylacetonates were selected as promising precursors for obtaining a composite electrode material with capacitive and pseudocapacitive mechanisms. Manganese presents multitude of possible oxidation states, it is the most abundant metal on earth, after aluminum and iron and has a very low toxicity. There is a great variety of manganese oxides among which there are numerous polymorphs no well understood but related between them, even with their corresponding oxyhydroxides (Wells, 1975). There is a lot of research done on  $\text{MnO}_2$  as electrode material in supercapacitors, including its different polymorphs (Belanger *et al.*, 2008; Chodankar *et al.*, 2016; Huang *et al.*, 2015), as well as composite materials mixing it with different carbon-type materials in order to improve the relatively low electrical conductivity of  $\text{MnO}_2$  (Gambou-Bosca & Belanger, 2015; Xu *et al.*, 2017). But not only  $\text{MnO}_2$  has been studied as electrode component in supercapacitors, other oxidation states like  $\text{MnO}$  (Ramadan *et al.*, 2018),  $\text{Mn}_2\text{O}_3$  (Li *et al.* (2015); Wang *et al.* (2016)) and  $\text{Mn}_3\text{O}_4$  (Shah *et al.*, 2018; Shaik *et al.*, 2016) also have been studied for this purpose, concluding that manganese oxides and their carbon-based composites represent promising and very competitive electrode materials for applications in supercapacitors (Zhang & Chen, 2008).

In this section, following the two-step synthesis successfully applied in the previous section, we describe the synthesis and characterization of microporous ODC composites with embedded  $\text{Mn}_3\text{O}_4$  nanoparticles. Two different precursors with two different manganese oxidation states have been used,  $\text{Mn}(\text{C}_5\text{H}_8\text{O}_2)_2$  and  $\text{Mn}(\text{C}_5\text{H}_8\text{O}_2)_3$ . The structure and physical properties of each precursor determine the morphology and micro/nanostructure of the carbon composite material obtained, along with the electrochemical properties in each case.

### Synthesis

In order to obtain a first carbon material that would combine an adequate porosity and a good quantity of nanoparticles homogeneously dispersed through the carbon

matrix, different chlorination temperatures between 400 °C to 700 °C were carried out, using both 2,4-pentanedione manganese (II) and (III),  $Mn(C_5H_7O_2)_2$  and  $Mn(C_5H_7O_2)_3$ , with  $P2_1/c$  space group, ( $a_{(II)} = 1.118$  nm,  $b_{(II)} = 0.542$  nm,  $c_{(II)} = 1.131$  nm,  $\beta_{(II)} = 106.1^\circ$  and  $a_{(III)} = 1.387$  nm,  $b_{(III)} = 0.746$  nm,  $c_{(III)} = 1.620$  nm,  $\beta_{(III)} = 98.4^\circ$  respectively; Alfa Aesar, powder purity of 100%). This first step allowed to determine the ideal temperature for each precursor, otherwise the carbon resulting material could have too much metal chloride nanoparticles or very large particles that can seal the porous structure, reducing the surface area therefore the capacitive performances; on the contrary, a poor content of nanoparticles or none would not offer pseudocapacitance contribution after the hydrothermal conversion. The optimized conditions to obtain a carbon-based composite material with a compromise between the amount of nanoparticles imbedded and the available surface area was different for each precursor, due to their different thermal stability. In the case of the manganese (III) acetylacetonate ( $Mn(C_5H_7O_2)_3$ , m.p.:159-161 °C (Wells, 1975)) the optimized carbon-base composite was obtained at lower temperature, 500 °C (sample called M3.5 in the following), than in the case of the manganese (II) acetylacetonate ( $Mn(C_5H_7O_2)_2$ , m.p.:248-250 °C (Wells, 1975)) where a temperature of 700 °C was needed (sample that will be called M2.7), according to their different melting points.

Consequently,  $Mn(C_5H_7O_2)_2$  and  $Mn(C_5H_7O_2)_3$  were separately placed in a quartz vessel and heated in the tubular furnace with the same characteristics than in the above NiO@ODC section under argon atmosphere ( $25\text{cm}^3/\text{min}$ ). After 15 min, the argon was replaced by chlorine gas and the furnace was turned on at 50 °C/min until 700 °C and 500 °C respectively. When the temperature is reached, it is maintained for 1 hour before turning off the furnace, replacing chlorine by argon and letting cool down to room temperature. In both synthesis, the raw materials were washed with abundant hot water to remove either traces of  $Cl_2$  or manganese chlorides not imbedded in the carbon matrix.

After structural and textural characterization of the intermediates M2.7 and M3.5 materials, they were dispersed in 30 mL of KOH 12M and placed in a Teflon stainless steel hydrothermal chamber. The autoclave was heated at 200 °C during 48 h and dried at 100 °C overnight after several washings with hot water followed by filtering under vacuum. The new composite materials obtained by hydrothermal conversion will be called  $Mn_3O_4^x@ODC$ , where “ $x$ ” identifies the precursor from which they have been synthesized, 3.5 or 2.7.

## Structural Characterization

*Carbon-based composite material obtained at 500 °C from  $Mn(C_5H_7O_2)_3$*

The TEM study of intermediate M3.5 composite material is shown in Figure 4.11. At low magnification (Figure 4.11) it can be observed that the material consists on large particles (Figure 4.11a) where is possible to identify small dots of darker contrast with size around 4-5 nm. In the high magnification image recorded in a thin edge of the material one of the imbedded nanoparticles of 4 nm in size is clearly imaged (Figure 4.11b). Although the nanocrystal in not oriented and periodicity is only observed along one direction, in the DDP (see inset in Figure 4.11b) this periodicity can be assigned to the 102 plane of  $MnCl_2$ . Besides the XEDS spectrum (Figure 4.11b) detects the signal of manganese and chlorine, together with the one from carbon in higher intensity.

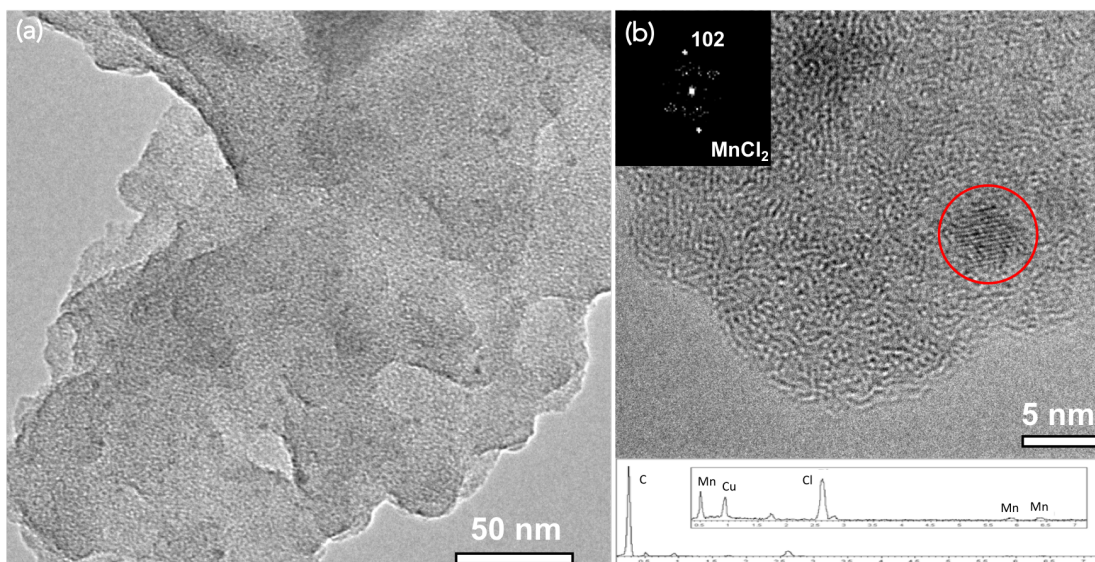
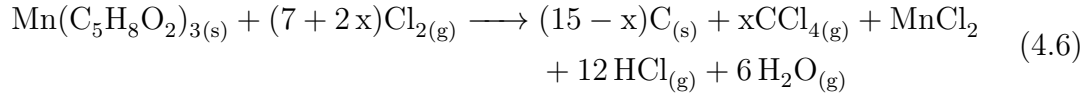


Figure 4.11: TEM micrographs of (a) low and (b) high magnification of compound M3.5 obtained from  $Mn(C_5H_7O_2)_3$  at 500 °C inset of DDP from the nanoparticle encircled in red. Below the XEDS spectrum form this particle is dsplayed.

$MnCl_2$  nanoparticles, with  $CdCl_2$  or  $Cd(OH)_2$ -type structure, have a melting point of 654 °C, above the chlorination temperature, and a boiling point of 1225 °C, even higher. Therefore this compound can remain within the resulting amorphous carbon material in the form of nanoparticles. The chlorination reaction of this compound can be postulated as follows::



Where “ $x$ ” represents the amount of  $CCl_4$  formed decreasing the yield of the carbon mass.

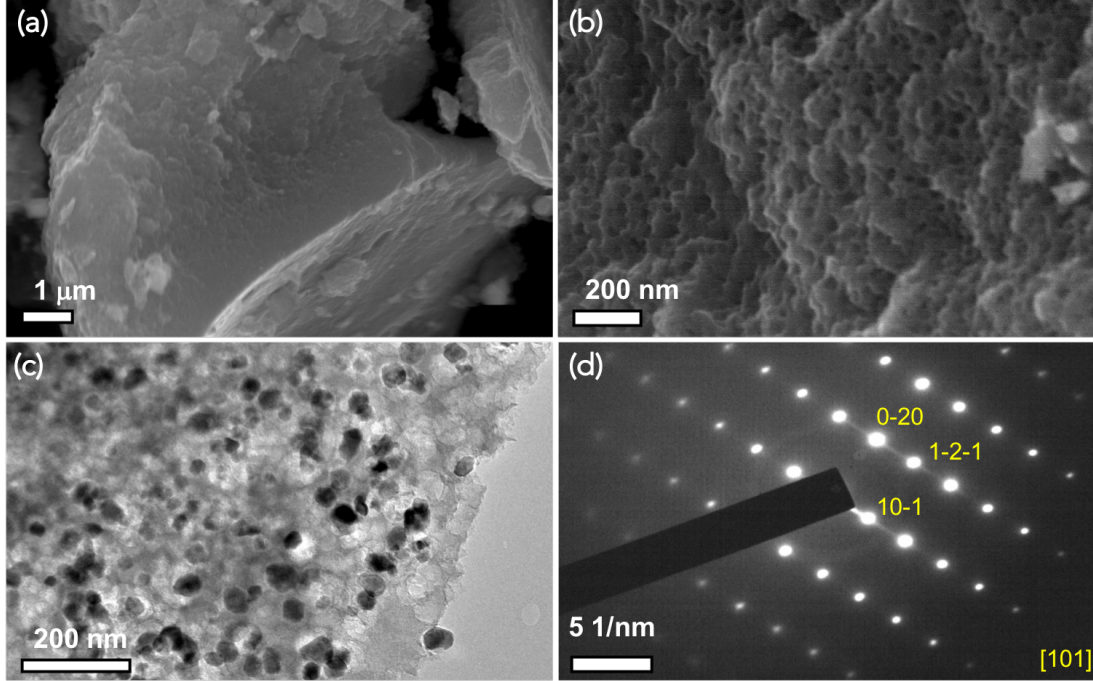
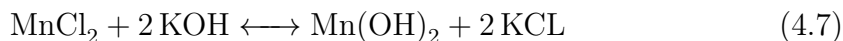


Figure 4.12: SEM micrographs of the composite material  $Mn_3O_4^{3.5}@ODC$  at (a) low and (b) high magnifications. TEM micrographs of the composite at (c) low magnification and (d) diffraction pattern along the  $[101]$  zone axis taken in one of the largest nanocrystals.

After hydrothermal conversion, the  $Mn_3O_4^{3.5}@ODC$  composite material was studied again by electron microscopy (Figure 4.12). In the low magnification SEM image (Figure 4.12a) the composite material is revealed as large particles without any distinguishable shape. A closer inspection at higher magnification (Figure 4.12b) reveals a fluffy surface containing voids of size below 100 nm. The TEM image displayed in Figure 4.12c shows the local structure of the composite material consisting on a matrix of disordered carbon containing empty voids and other containing darker nanocrystals. Those nanocrystals are identified as the hausmanite type  $Mn_3O_4$  through the diffraction pattern recorded along the  $[101]$  of

one of the larger nanoparticles as well as the XEDS analysis. Unfortunately, the size of the nanooxides obtained after the hydrothermal transformation of the manganese halide nanoparticles is notoriously larger. According to the experimental data, the chemical reactions involved in the hydrothermal transformation may be formulated:



In the first stage  $\text{MnCl}_2$  nanoparticles react with  $\text{KOH}$  yielding  $\text{Mn(OH)}_2$ , then the presence of oxygen favors the oxidation of manganese yielding  $\text{Mn}_3\text{O}_4$  which is the first oxidation process following the Pourbaix diagram (White & Labayru, 1991). Since pseudocapacitance is a surface process, homogeneous and small nanoparticles are expected to provide a larger area that increases the capacitance contribution. In the particular case of  $\text{Mn}_3\text{O}_4^{3.5}\text{@ODC}$  material, the microstructural study demonstrates that the previous premises are not fulfilled and therefore promising electrochemical properties are not expected.

*Carbon-based composite material obtained at 700 °C from  $\text{Mn}(\text{C}_5\text{H}_7\text{O}_2)_2$*

The TEM study of the intermediate M2.7 composite material shown in Figure 4.13 reveals a highly porous carbon-based material. In the low magnification image (Figure 4.13a) a characteristic particle showing a homogeneous distribution of pores can be observed. At higher magnification (Figure 4.13b), the pore diameter can be measured ranging from 5 to 25 nm, being in the mesopore range. XEDS analysis performed in different areas of the specimen during the observation detects the presence of manganese and chlorine elements in the material, but in the TEM micrographs the nanoparticles responsible of those signals are not observed. Here, the acquisition of HAADF images (Figure 4.13c), where the contrast is almost proportional to the  $Z$  number of elements, allow the localization of the expected  $\text{MnCl}_2$  in the composite. Since manganese atomic number ( $Z = 25$ ) is greater than carbon ( $Z = 6$ ), the presence of  $\text{MnCl}_2$  nanoparticles can be located as the sharp brightest areas within the carbon material. EELS spectra (Figure 4.13d) performed on these areas show the characteristic carbon  $K$  and manganese  $L_{2,3}$  edges, confirming the presence of  $\text{MnCl}_2$  nanoparticles of such a small size that cannot be easily imaged by conventional HRTEM. Analogously to the previous material, we can postulate the chlorination reaction as follows:



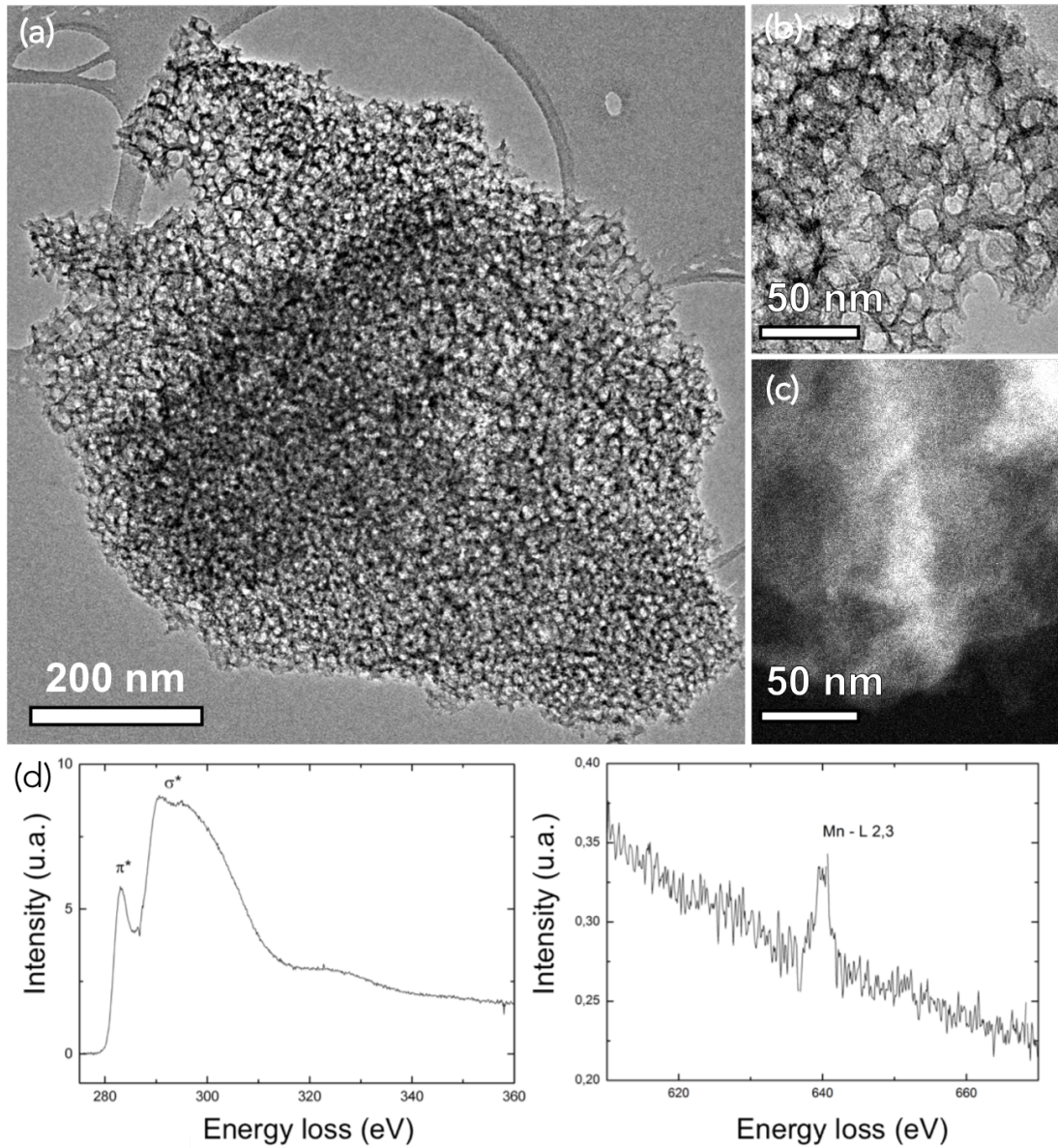
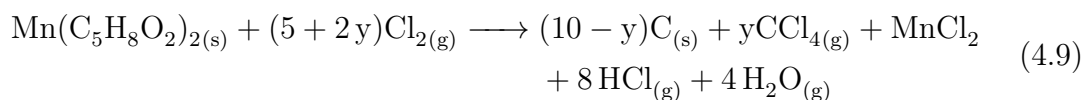


Figure 4.13: TEM micrographs of (a) low and (b) high magnification of the M2.7 intermediate composite material. (c) STEM-HAADF mode image where the brightest zones indicate the presence of a higher Z element than carbon. (d) EELS spectrum where the  $K$  and  $L_{2,3}$  edges of carbon and manganese respectively can be identified.





Where now “ $y$ ” represents the amount of  $\text{CCl}_4$  formed decreasing the yield of the carbon mass.

This composite material was subsequently subjected to the hydrothermal conversion under basic conditions in order to transform the manganese chloride (II) nanoparticles into one of the many manganese oxides or even oxyhydrides with pseudocapacitative properties, but under the same hydrothermal conditions than the previous material the obtention of  $\text{Mn}_3\text{O}_4$  nanoparticles was expected but with lower size taking into account that the  $\text{MnCl}_2$  nanoparticles in the present composite exhibited subnanometric size. The SEM images displayed in Figure 4.14 show the shape and morphology of the obtained composite named  $\text{Mn}_3\text{O}_4^{2.7}\text{@ODC}$ . The composite is formed by large sponge like particles plenty of voids.

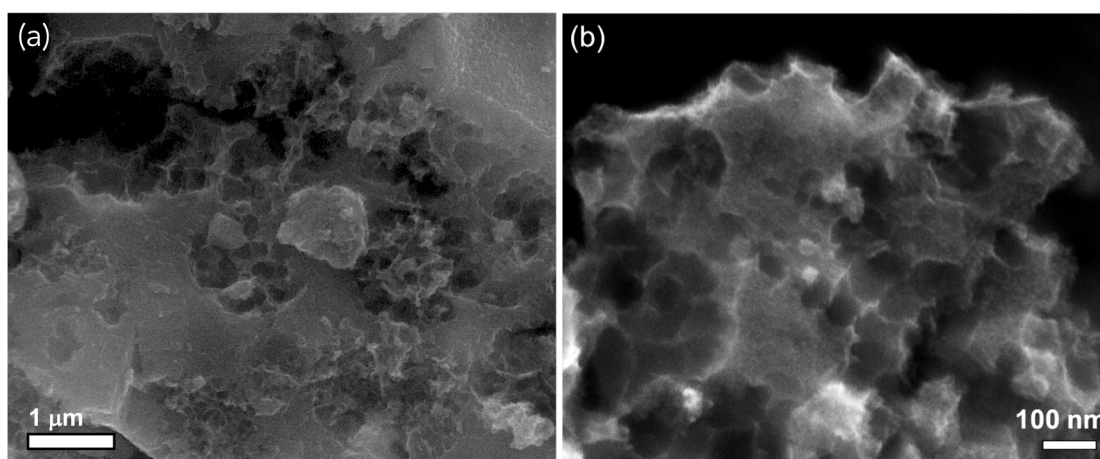


Figure 4.14: SEM micrographs of hybrid materials  $\text{Mn}_3\text{O}_4^{2.7}\text{@ODC}$  at (a) low and (b) high magnifications.

Figure 4.15 shows the TEM study of the obtained composite material. In the low magnification image (Figure 4.15a) it can be appreciated that the carbon matrix has barely changed compared to the precursor imaged in Figure 4.13, but now a darker contrast is clearly observed corresponding to the manganese oxide nanoparticles well dispersed within the carbon matrix. These nanoparticles are better imaged in the HAADF image displayed in Figure 4.15b, where the characteristic mesopores of the carbon matrix is more recognizable and now

brighter nanoparticles ranging from 6 to 20 nm are clearly identified. Again, the hydrothermal process transforms the  $MnCl_2$  nanoparticles in larger nanooxides, however now they are still enough small to provide good electrochemical response. EELS spectra recorded on different particles confirm the presence of manganese showing its  $L_{2,3}$  edge at 644 eV. A closer inspection of the composite at higher magnification (Figure 4.15c) by HRTEM reveals the atomic arrangement of one of these nanoparticles of about 12 nm located at the thin edge of the composite. The crystalline nanoparticle can be identify as expected with the hausmanite phase  $Mn_3O_4$ , oriented along the  $[110]$  zone axis.

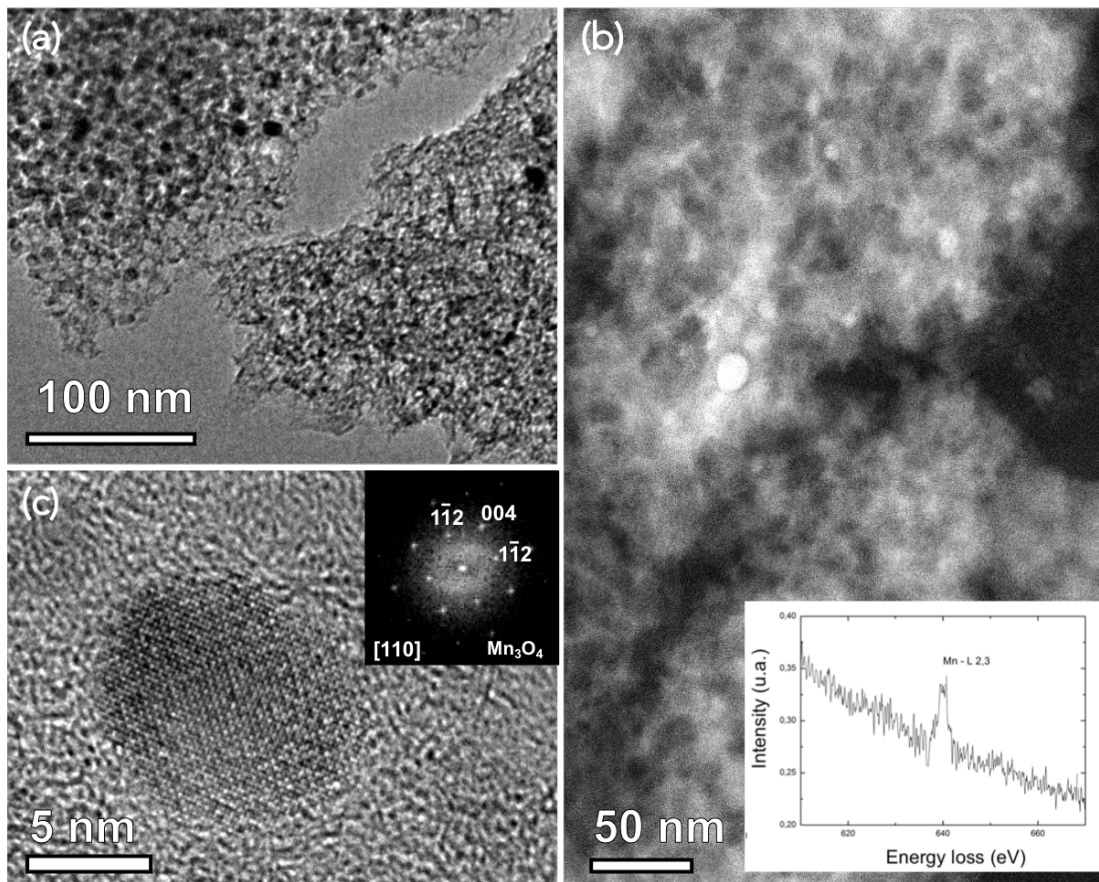


Figure 4.15: (a) TEM and (b) HAADF micrograph of  $Mn_3O_4^{2-7}@ODC$  composite material, inset EELS spectrum with the  $L_{2,3}$  manganese absorption edge. (c) HRTEM image of a single nanoparticle and its digital diffraction pattern that identifies the spinel phase  $Mn_3O_4$  along the  $[110]$  axis zone.

## Textural Characterization

The  $N_2$  adsorption isotherms displayed in Figure 4.16a assert that both materials have a type IV isotherm characteristic of mesoporous materials in combination with a H4 hysteresis loop, which is associated with the presence of micropores. Results derived from the assessment of the surface area values are collected in Table 4.2. The specific surface areas, obtained using the BET theory, are  $512 \text{ m}^2 \text{ g}^{-1}$ , and  $749 \text{ m}^2 \text{ g}^{-1}$  for  $Mn_3O_4^{3.5}@ODC$  and  $Mn_3O_4^{2.7}@ODC$ , respectively. The largest surface area found in  $Mn_3O_4^{2.7}@ODC$  is in agreement with the fact that this material is built up by a low-density carbon matrix containing small size nanoparticles, whereas the presence of large nanoparticles in  $Mn_3O_4^{3.5}@ODC$ , hindering the surface, could be responsible for its lower surface area.

The pore size distribution (PSD) plots, derived from the NLDFIT method, are depicted in Figure 4.16b. The plots confirm for both composites the development of narrow micropores (pore width of 0.6-0.7 nm), however the plot for the  $Mn_3O_4^{2.7}@ODC$  material reveals a more complex pore structure containing narrow (pore width 0.62 nm) and wider (pore width 1.48 nm) microporosity, as well as some mesopores ranging from 3 to 10 nm in diameter (Table 4.2). In this sense, mesoporosity in this material can be attributed to pores formed between the corrugated carbon foils detected by the TEM study (Figure 4.15). As extracted from the textural analysis the combination of micropores and well defined mesopores plus the presence of small oxides nanoparticles makes the composite  $Mn_3O_4^{2.7}@ODC$  a good candidate for supercapacitor whereas the microstructural and textural properties of  $Mn_3O_4^{3.5}@ODC$  foresee worse electrochemical performance of this material.

	$S_{\text{Total BET}}$ ( $\text{m}^2/\text{g}$ )	$S_{\text{Ext. BET}}$ ( $\text{m}^2/\text{g}$ )	$S_{\text{Micr. BET}}$ ( $\text{m}^2/\text{g}$ )	Pore Width $_{2D-NLDFIT}$ (nm)
$Mn_3O_4^{3.5}@ODC$	512	400	112	0.67
$Mn_3O_4^{2.7}@ODC$	749	465	284	0.62, 1.48, 2.09, 3.7, 5.1, 7.6

Table 4.2: Total, exterior and micropore BET surface area and pore width of  $Mn_3O_4^x@ODC$  samples.

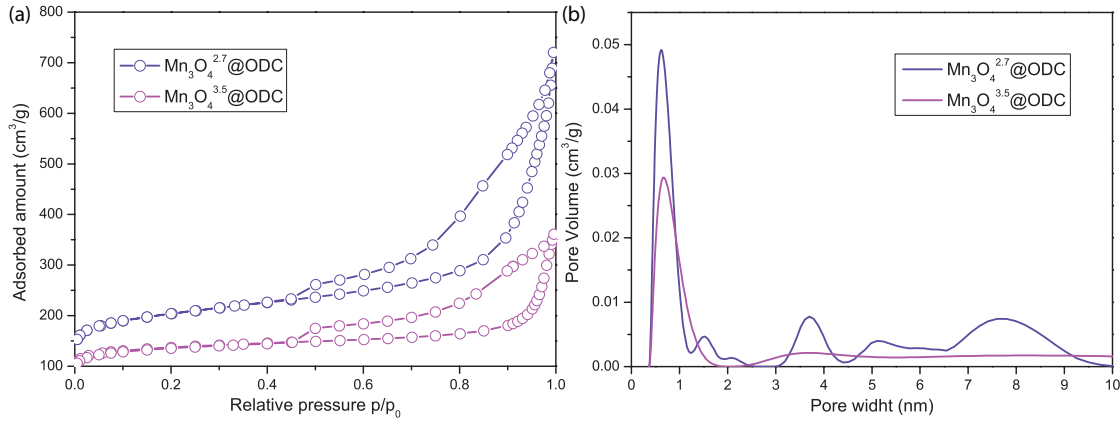


Figure 4.16: (a)  $N_2$  adsorption-desorption isotherms at 77 K of  $Mn_3O_4@ODC$  composite material obtained from each precursor. (b) Graphical representation of the pore size distribution showing the region with pore width <10 nm.

## Electrochemical Characterization

The two composite materials were electrochemically characterized by cyclic voltammetry (CV) on a three-electrode cell using a glassy carbon rod as working electrode where the material was deposited as thin film; platinum wire as counter electrode and two different reference electrodes, hydrogen electrode (RHE) and a Hg/HgO, in order to measure in acid and basic electrolyte respectively.  $H_2SO_4$  0.5 M was used as acid electrolyte and NaOH 1 M as basic electrolyte and measurements were carried out at different sweep rates, from 5 to 1000  $mV s^{-1}$ .

The sample  $Mn_3O_4^{2.7}@ODC$  (Figure 4.17a) show a rectangular shape in both electrolytes, typical of a capacitive behavior, instead that the sample  $Mn_3O_4^{3.5}@ODC$  (Figure 4.17b) in which the shape of CV looks tilted. Both samples behave better on the basic 1 M NaOH electrolyte, the rectangular shape is better maintained because in acid the oxide nanoparticles can be dissolved. Manganese ions released in the medium generate diffusion problems, increasing the electrode resistance. For the composite  $Mn_3O_4^{3.5}@ODC$  a very high electrical resistance is observed, denoted by the tilted parallelogram; the electrolyte is unable to reach the entire surface area of the material due in large part to diffusion problems even at low sweep rates. The porous structure seems blocked, being ineffective in facilitating ion traffic. The capacitance values obtained for this material are quite low: 62  $F g^{-1}$  in  $H_2SO_4$  0.5 M and 14  $F g^{-1}$  in NaOH 1 M. The gravimetric capacitance values for  $Mn_3O_4^{2.7}@ODC$  is 95  $F g^{-1}$  in acid electrolyte ( $H_2SO_4$  0.5 M) and 101  $F g^{-1}$  in basic electrolyte (NaOH 1M), its porous structure seems to be the key for

obtaining better results than the previous material, in addition to having smaller hausmanite nanoparticles, which increases its contribution. Although in  $\text{H}_2\text{SO}_4$  the CVs show slight broadening in the middle, typically assigned to pseudocapacitance behavior of oxygen groups located at the surface of the carbon created during the hydrothermal process (like on a chemical activation, KOH also attacks the carbon surface, leaving oxygen groups on the surface). The contribution of  $\text{Mn}_3\text{O}_4$  nanoparticles cannot be clearly seen. In NaOH that contribution it is shown in the asymmetric distortion at higher voltage in the parallelogram that also remain at higher sweep rates indicating a intercalation pseudocapacitance type.

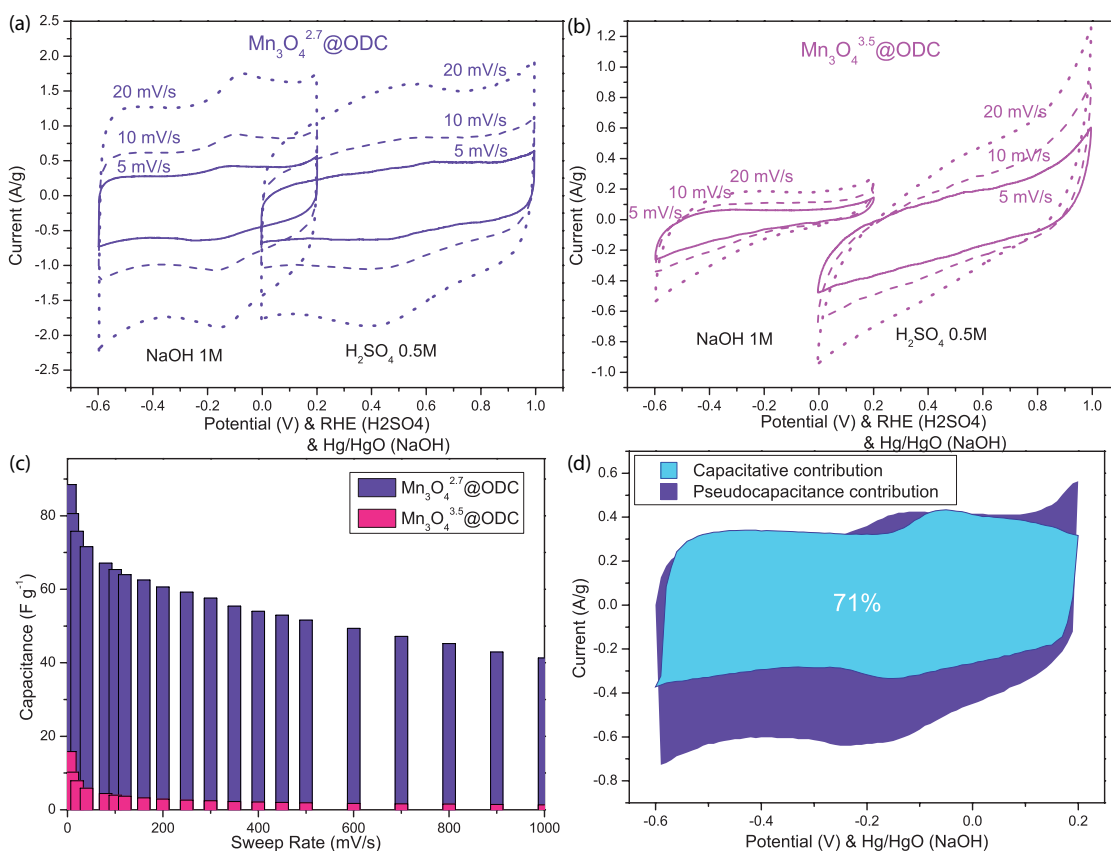


Figure 4.17: Cyclic voltammograms at different sweep rates of (a)  $\text{Mn}_3\text{O}_4^{2.7}\text{@ODC}$  and (b)  $\text{Mn}_3\text{O}_4^{3.5}\text{@ODC}$  in a deaerated, 25 °C,  $\text{H}_2\text{SO}_4$  0.5 M and 1 M NaOH solution on a three-electrode configuration. (c) Fraction of total capacitance retained from 5 to 1000  $\text{mV s}^{-1}$ . (d) Total (purple area) and capacitive contributions (blue area) to charge storage in 1 M NaOH of  $\text{Mn}_3\text{O}_4^{2.7}\text{@ODC}$ .

In order to investigate how accessible the porous structures are for the electrolyte on both materials, measurements at different sweep rates were carried out

from 5 to 1000  $mV s^{-1}$ . In the graph of Figure 4.17c it can be observed that the compound  $Mn_3O_4^{2.7}@ODC$  maintains a 46% of the total capacitance at 1000  $mV s^{-1}$  having a porous structure more appropriate than the composite  $Mn_3O_4^{3.5}@ODC$ , which loses 82% of the capacitance at 200  $mV s^{-1}$  and 92% at 1000  $mV s^{-1}$ .

Considering the approximation made before for the separation of energy storage mechanisms according to its variation with the sweeping speed, direct (capacitive) or its square root (pseudocapacitive), the capacitive contribution of the voltamperogram obtained for the  $Mn_3O_4^{2.7}@ODC$  composite material can be separated (Figure 4.17d). It can be seen how the capacitive contribution in blue represent the 71% of the total capacitance obtained in purple. It is now more evident that the pseudocapacitive contribution takes place in the whole potential window as the purple part of the total voltammogram that is not overlapping by the blue voltamperogram, which represents only the capacitive contribution.

Once confirmed the superior electrochemical properties of the  $Mn_3O_4^{2.7}@ODC$  composite material over the  $Mn_3O_4^{3.5}@ODC$ , it was selected for the two-electrodes experiment. Nevertheless, a new ODC carbon material was synthesized from  $Mn(C_5H_7O_2)_2$  at 900 °C in order to compare the composite with a pure carbon material. The carbon obtained at 900 °C is shown in Figure 4.18 displaying a very similar morphology to the carbon matrix in the  $Mn_3O_4^{2.7}@ODC$ , so it will be considered as the carbon matrix in the composite without any nanoparticle, with comparable specific surface area and microporous distribution.

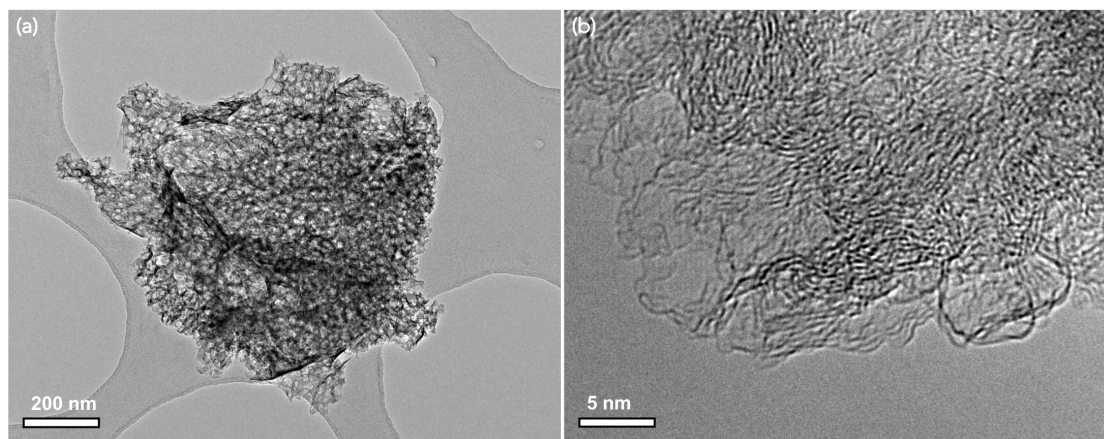


Figure 4.18: (a) Low and (b) high magnification images of the ODC carbon material from  $Mn(C_5H_7O_2)_2$  at 900 °C.

Similarly to the previous electrode material, the composite and the new carbon materials were processed to make a film and then two disc electrodes from

each carbon-film were separated by a fiberglass impregnated with NaOH 1M electrolyte inside a symmetric configuration Swagelok-cell. The CVs of both materials (Figure 4.19a) show a rectangular shape up to 1 Volt, although in the case of the  $\text{Mn}_3\text{O}_4^{2.7}\text{@ODC}$  a peak at 0.1 Volts probably due to some Faradaic reversible reaction of manganese oxide can be observed. The current signal clearly indicates a superior gravimetric capacitance value for the  $\text{Mn}_3\text{O}_4^{2.7}\text{@ODC}$  composite. Thereby the gravimetric and volumetric capacitance from the GCPL plot (Figure 4.19b) for the composite material is  $130 \text{ F g}^{-1}$  and  $58 \text{ F cm}^{-3}$  respectively at  $0.1 \text{ A g}^{-1}$ , higher than for the ODC carbon material that is  $87 \text{ F g}^{-1}$  and  $28 \text{ F cm}^{-3}$ . It is a very low volumetric capacitance as well because of the low density of the carbon,  $0.32 \text{ g cm}^{-3}$  against  $0.45 \text{ g cm}^{-3}$  for the composite. The gravimetric capacitance obtained for the ODC carbon material synthesized at  $900 \text{ }^\circ\text{C}$  represents the 70% of the capacitance of the composite, sustaining the approach done on the three-electrode characterization shown previously. The impedance Nyquist plot (Figure 4.19c) shows a very close behavior between the composite and the ODC carbon materials with a similar ERS value of 4.6 Ohms. The relaxation time constant of the systems is 2.9 seconds calculated from the imaginary part of the complex capacitance (Figure 4.19d) slightly improving the value for the ODC carbon which is 3.2 seconds. The  $\text{Mn}_3\text{O}_4$  nanoparticles increase the total gravimetric capacitance of the composite material besides providing a higher density that enhances the total volumetric capacitance not only without losing conductivity but slightly increasing it. Put all that together with a suitable pore structure for the ion diffusion of the carbon matrix makes it a promising electrode material for high power density supercapacitors.

## Conclusions

$\text{Mn}_3\text{O}_4\text{@ODC}$  composite material has been successfully synthesized by partial chlorination followed by hydrothermal conversion from both Mn(II) and Mn(III) acetylacetonates precursors. Imaging both  $\text{Mn}_3\text{O}_4\text{@ODC}$  composites obtained by transmission electron microscopy revealed a mesoporous carbon containing a fine dispersion of  $\text{Mn}_3\text{O}_4$  nanoparticles for the  $\text{Mn}_3\text{O}_4^{2.7}\text{@ODC}$ , meanwhile for the  $\text{Mn}_3\text{O}_4^{3.5}\text{@ODC}$ , although the porous carbon matrix is very similar, the  $\text{Mn}_3\text{O}_4$  nanoparticles are much more bigger.

Electrochemical studies in a three-electrodes configuration demonstrated that such big nanoparticles in the  $\text{Mn}_3\text{O}_4^{3.5}\text{@ODC}$  composite, probably due to the lower chlorination temperature, obstruct the ions diffusion along the specific surface area which results on a very resistive material. On the other hand, the  $\text{Mn}_3\text{O}_4^{2.7}\text{@ODC}$



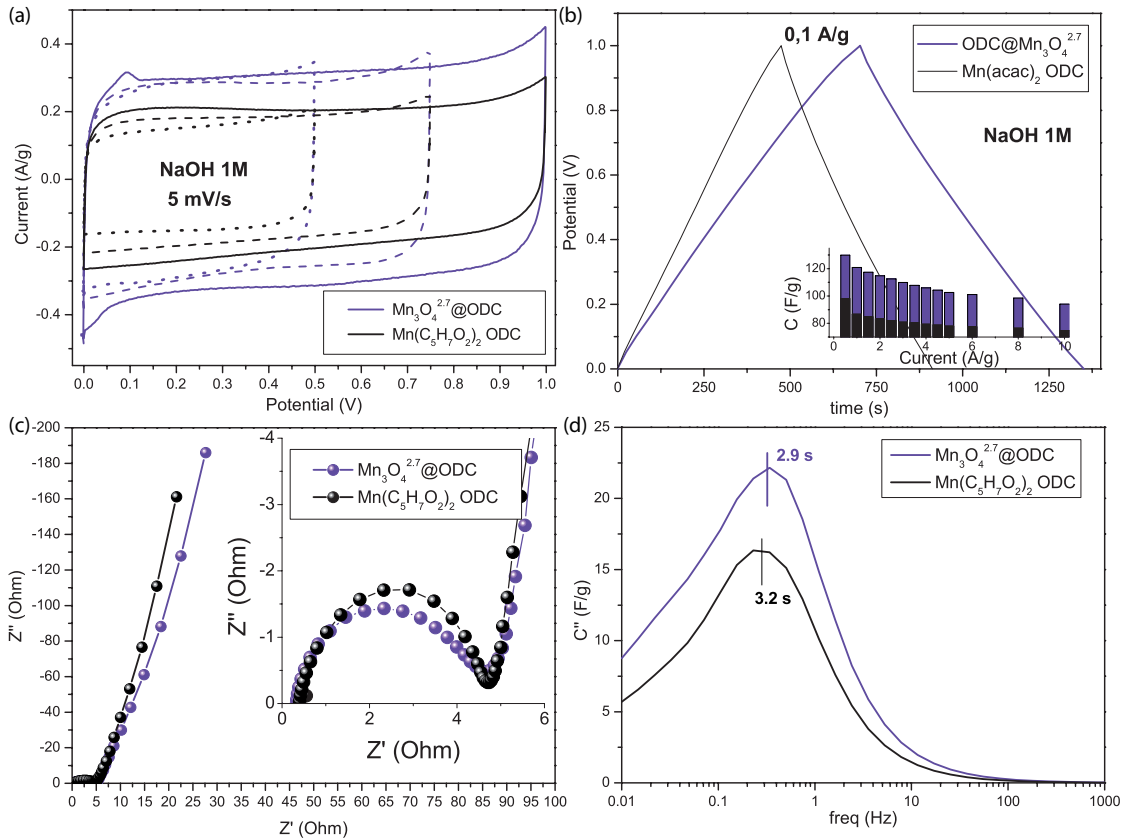


Figure 4.19: Electrochemical Characterization of the  $Mn_3O_4^{2.7}@ODC$  composite and the  $Mn(C_5H_7O_2)_2 ODC$  carbon materials on a symmetrical two-electrode cell: (a) CV, (b) GCPL and (c) EIS on Nyquist and (d) complex imaginary capacitance plot.

composite displays a much better electrochemical behavior even showing pseudo-capacitive contribution of  $Mn_3O_4$  nanoparticles, demonstrating its superior performance as an effective electrode to facilitate fast ion and electron transportations, which are highly desirable for high power supercapacitors. Further studies in a two-electrodes symmetrical cell configuration of this composite gives evidence of its superior capacitance value against the porous carbon obtained by chlorination of the precursors at 900 °C, temperature in which there is not any nanoparticle residue.



## Bibliography

- ANSARI, S. & GIANNELIS, E. P. (2009). Functionalized graphene sheet-poly(vinylidene fluoride) conductive nanocomposites. *Journal of Polymer Science: Part B: Polymer Physics* **47**(9), 888–897.
- AUGUSTYN, V., SIMON, P. & DUNN, B. (2014). Pseudocapacitive oxide materials for high-rate electrochemical energy storage. *Energy and Environmental Science* **7**(5), 1597–1614.
- BELANGER, D., BROUSSE, T. & LONG, J. W. (2008). Manganese oxides: Battery materials make the leap to electrochemical capacitors. *Interface* **17**.
- BROUSSE, T., BELANGER, D. & LONG, J. W. (2015). To be or not to be pseudocapacitive? *Journal of The Electrochemical Society* **162**(5), A5185–A5189.
- CHEN, F., ZHOU, W., YAO, H., FAN, P., YANG, J., FEI, Z. & ZHONG, M. (2013). Self-assembly of nio nanoparticles in lignin-derived mesoporous carbons for supercapacitor applications. *Green Chem.* **15**(11), 3057–3063.
- CHODANKAR, N. R., DUBAL, D. P., GUND, G. S. & LOKHANDE, C. D. (2016). A symmetric mno<sub>2</sub>/mno<sub>2</sub> flexible solid state supercapacitor operating at 1.6v with aqueous gel electrolyte. *Journal of Energy Chemistry* **25**(3), 463–471.
- ELMOUWAHIDI, A., BAILÓN-GARCÍA, E., CASTELO-QUIBÉN, J., PÉREZ-CADENAS, A. F., MALDONADO-HÓDAR, F. J. & CARRASCO-MARÍN, F. (2018). Carbon-tio<sub>2</sub> composites as high-performance supercapacitor electrodes: synergistic effect between carbon and metal oxide phases. *J. Mater. Chem. A* **6**(2), 633–644.
- GAMBOU-BOSCA, A. & BELANGER, D. (2015). Chemical mapping and electrochemical performance of manganese dioxide/activated carbon based composite electrode for asymmetric electrochemical capacitor. *Journal of The Electrochemical Society* **162**(5), A5115–A5123.
- GOGOTSI, Y., NIKITIN, A., YE, H., ZHOU, W., FISCHER, J. E., YI, B., FOLEY, H. C. & BARSOUM, M. W. (2003). Nanoporous carbide-derived carbon with tunable pore size. *Nature Materials* **2**, 591.
- GONZÁLEZ-GARCÍA, P., ARENAS-ESTEBAN, D., ÁVILA-BRANDE, D., URONES-GARROTE, E. & OTERO-DÍAZ, L. (2017). Nickelocene as precursor of microporous organometallic-derived carbon and nickel oxide-carbon nanocomposite. *J. Colloid Interface Sci.* **490**, 410–419.
- GONZÁLEZ-GARCÍA, P., CENTENO, T. A., URONES-GARROTE, E., ÁVILA-BRANDE, D. & OTERO-DÍAZ, L. C. (2011). Porous carbon nanospheres derived from chlorination of bis(cyclopentadienyl)titanium dichloride and their electrochemical capacitor performance. *Materials Chemistry and Physics* **130**(1), 243–250.
- GONZÁLEZ-GARCÍA, P., URONES-GARROTE, E., ÁVILA-BRANDE, D., GÓMEZ-HERRERO, A. & OTERO-DÍAZ, L. C. (2010). Structural study of carbon nanomaterials prepared by chlorination of tungsten carbide and bis(cyclopentadienyl)tungsten dichloride. *Carbon* **48**(13), 3667–3675.

- GONZÁLEZ-GARCÍA, P., URONES-GARROTE, E., CORRO, E. D., ÁVILA-BRANDE, D. & OTERO-DÍAZ, L. C. (2013). The production of carbon particles of different shapes produced by the chlorination of  $\text{Cr}(\text{C}_5\text{H}_5)_2$ . *Carbon* **52**, 90–99.
- HUANG, M., LI, F., DONG, F., ZHANG, Y. X. & ZHANG, L. L. (2015). MnO<sub>2</sub>-based nanostructures for high-performance supercapacitors. *J. Mater. Chem. A* **3**(43), 21380–21423.
- HUMMERS, W. S. & OFFEMAN, R. E. (1958). Preparation of graphitic oxide. *Journal of the American Chemical Society* **80**(6), 1339–1339.
- JIANG, Z., LI, Q., CHEN, M., LI, J., LI, J., HUANG, Y., BESENBACHER, F. & DONG, M. (2013). Mechanical reinforcement fibers produced by gel-spinning of poly-acrylic acid (paa) and graphene oxide (go) composites. *Nanoscale* **5**(14), 6265–6269.
- KATCHO, N. A., URONES-GARROTE, E., ÁVILA-BRANDE, D., GÓMEZ-HERRERO, A., URBONAITE, S., CSILLAG, S., LOMBA, E., AGULLÓ-RUEDA, F., LANDA-CÁNOVAS, A. R. & OTERO-DÍAZ, L. (2007). Carbon hollow nanospheres from chlorination of ferrocene. *Chemistry of Materials* **19**(9), 2304–2309.
- KOMATSU & ENDO (1985). Production of carbon fiber grown in vapor phase.
- LI, W., SHAO, J., LIU, Q., LIU, X., ZHOU, X. & HU, J. (2015). Facile synthesis of porous Mn<sub>2</sub>O<sub>3</sub> nanocubics for high-rate supercapacitors. *Electrochimica Acta* **157**, 108–114.
- LOTA, K., SIERCZYNSKA, A. & LOTA, G. (2011). Supercapacitors based on nickel oxide/carbonmaterials composites. *International Journal of Electrochemistry* **2011**(321473).
- MARCANO, D. C., KOSYNKIN, D. V., BERLIN, J. M., SINITSKII, A., SUN, Z., SLESAREV, A., ALEMANY, L. B., LU, W. & TOUR, J. M. (2010). Improved synthesis of graphene oxide. *ACS Nano* **4**(8), 4806–4814.
- NYAMORI, V. O., MHLANGA, S. D. & COVILLE, N. J. (2008). The use of organometallic transition metal complexes in the synthesis of shaped carbon nanomaterials. *J. Organomet. Chem.* **693**(13), 2205–2222.
- PEDRO GONZÁLEZ, G. (2012). *Nanoestructuras de carbono: síntesis y caracterización estructural y electrónica*. Ph.D. thesis, Universidad Complutense de Madrid.
- PUMERA, M. (2009). Electrochemistry of graphene: new horizons for sensing and energy storage. *The Electrochemical Record* **9**(4), 211–223.
- RAMADAN, M., ABDELLAH, A. M., MOHAMED, S. G. & ALLAM, N. K. (2018). 3d interconnected binder-free electrospun mno@c nanofibers for supercapacitor devices. *Scientific Reports* **8**(1), 7988.
- ROUQUEROL, J., ROUQUEROL, F., LLEWELLYN, P., MAURIN, G. & SING, K. (2013). *Adsorption by powders and porous solids*. Academic Press.
- SHAH, H. U., WANG, F., JAVED, M. S., SHAHEEN, N., ALI, S., AHMAD, M. A. & HE, K. (2018). Mn<sub>3</sub>O<sub>4</sub> nanosheets decorated on flexible carbon fabric for high-performance supercapacitors electrode. *Materials Letters* **210**, 148–152.

- SHAIK, D. P., ROSAIAH, P. & HUSSAIN, O. (2016). Supercapacitive properties of mn<sub>3</sub>o<sub>4</sub> nanoparticles synthesized by hydrothermal method. *Materials Today: Proceedings* **3**(1), 64–73.
- SING, K. S. W., EVERETT, D. H., HAUL, R. A. W., MOSCOU, L., PIEROTTI, R. A., ROUQUÉROL, J. & SIEMIENIEWSKA, T. (1985). Reporting physisorption data for gas/solid systems with special reference to the determination of surface area and porosity. *Pure Appl. Chem.* **57**, 603.
- TABERNA, P., SIMON, P. & FAUVARQUE, J. (2003). Electrochemical characteristics and impedance spectroscopy studies of carbon-carbon supercapacitors. *Journal of The Electrochemical Society* **150**(3), A292–A300.
- URONES-GARROTE, E., ÁVILA-BRANDE, D., KATCHO, N. A., GÓMEZ-HERRERO, A., LANDA-CÁNOVAS, A. & OTERO-DÍAZ, L. C. (2005). Amorphous carbon nanostructures from chlorination of ferrocene. *Carbon* **43**(5), 978–985.
- WANG, R., MA, Y., WANG, H., KEY, J., BRETT, D., JI, S., YIN, S. & SHEN, P. K. (2016). A cost effective, highly porous, manganese oxide/carbon supercapacitor material with high rate capability. *J. Mater. Chem. A* **4**(15), 5390–5394.
- WELLS, A. (1975). *Structural Inorganic Chemistry*. Clarendon Press.
- WHITE, D. A. & LABAYRU, R. (1991). Synthesis of a manganese dioxide-silica hydrous composite and its properties as a sorption material for strontium. *Industrial & Engineering Chemistry Research* **30**(1), 207–210.
- XU, L., JIA, M., LI, Y., JIN, X. & ZHANG, F. (2017). High-performance mno<sub>2</sub>-deposited graphene/activated carbon film electrodes for flexible solid-state supercapacitor. *Scientific Reports* **7**(1), 12857.
- YUSHIN, G., NIKITIN, A. & GOGOTSI, Y. (2006). *Nanomaterials Handbook. Edited by Yury Gogotsi*. Florida, EEUU: EEUU: CRC PRESS, BOCA RATON.
- ZHANG, H., CAO, G., WANG, Z., YANG, Y., SHI, Z. & GU, Z. (2008). Growth of manganese oxide nanoflowers on vertically-aligned carbon nanotube arrays for high-rate electrochemical capacitive energy storage. *Nano Letters* **8**(9), 2664–2668.
- ZHANG, S. W. & CHEN, G. Z. (2008). Manganese oxide based materials for supercapacitors. *Energy Materials* **3**(3), 186–200.

## Chapter 5

# Lignocellulosic-based activated carbons with ingrained metal or metal oxide nanoparticles as composite supercapacitor electrodes

Nowadays, most of the commercial EDLCs are based on AC due to their well-developed manufacturing technologies, easy production in large quantities, relatively low cost and great cycle stability (Burke, 2007; Wei *et al.*, 2011a). During the rapid development of modern society over the 20th century, the production of AC was noticeably increased for their use as clean gas application, air quality control, energy storage/conversion and economic recovery of valued chemicals (González-García, 2018). Most ACs have been synthesized from precursors based on fossil fuels, but the shortage of these resources requires finding new types of affordable and renewable precursors. In recent years, many different natural resources with high biomass content such as wood, bamboo, coconut shell or olive pits have been reported for the preparation of ACs (Ip *et al.*, 2008; Long *et al.*, 2014; Navarro-Suárez *et al.*, 2014; Redondo *et al.*, 2015; Wang *et al.*, 2013).

The chemical composition of AC produced from biomass is mainly composed by C, O, H, N, Ca, and K in order of abundance, containing also Si, Mg, Al, S, Fe, P, Cl, and Na in minor proportion depending on the precursor (Vassilev *et al.*, 2010). The most abundant element of biomass, carbon, is found as component of three different biopolymers: cellulose, hemicellulose and lignin being the last one responsible for the development of microporosity in ACs (Suhas *et al.*,

2007). That is why biomass residues with a high lignin content, such as coconut (59.4% (Jústiz-Smith *et al.*, 2008)) or palm shell (53.4% (Adinata *et al.*, 2007)) have been widely studied as raw materials for the production of microporous AC for supercapacitors (Jain *et al.*, 2013; Misnon *et al.*, 2015).

Although recent research has been focusing on the use of abundant and renewable sources for the production of nanoporous carbon electrodes, for applications like hybrid electric vehicles and portable electronic devices, further development of dense and inexpensive carbon materials with high capacitance per unit volume is critically needed (Wei & Yushin, 2012). In the previous chapter is demonstrated that increasing the electrode material density is a direct way to achieve it. On the other hand, activated carbons suffer of low electric conductivity, as it has been described in the Introduction section, which is reflected in high ESR values. Therefore, the challenge pursued in this chapter is devoted to improve the electrochemical properties of well know microporous ACs obtained from Galician walnut shell (*Juglans regia*) and bamboo (*Guadua angustifolia*) species (Figure 5.1), precursors previously studied in our research group, consisting on highly disordered microporous carbon materials with high surface areas up to  $2000 \text{ m}^2 \text{ g}^{-1}$  and specific capacitances as high as  $161 \text{ F g}^{-1}$  (Pedro González, 2012). One way explored to improve the electrochemical performance of porous carbons consist on the development of composite materials based on faradaic materials (metal nano-oxides) and carbon. This combination, yields synergistic effects between the storage mechanisms of both phases and produces denser materials with higher volumetric capacitance. Moreover, these nanoparticles or even better metallic nanoparticles like gold can improve the electrical conductivity of the composite, contributing to decrease the ERS value of the supercapacitor device.

## 5.1 Walnut shell activated carbon with embedded $\text{MnO}_x$ nanoparticles composite with enhanced electrochemical properties

Ruthenium oxide ( $\text{RuO}_2$ ) is considered the best pseudocapacitive material, being able to deliver gravimetric capacitance values up to  $1000 \text{ F g}^{-1}$  (Sugimoto *et al.*, 2006), with a potential window of 1.4 V in aqueous electrolyte. However the shortage of ruthenium on earth-crust and therefore the high market price of  $\text{RuO}_2$  restrict its applications mostly in military and aerospace industries (Conway, 1999). Manganese is the twelfth most abundant element on the earth-crust,

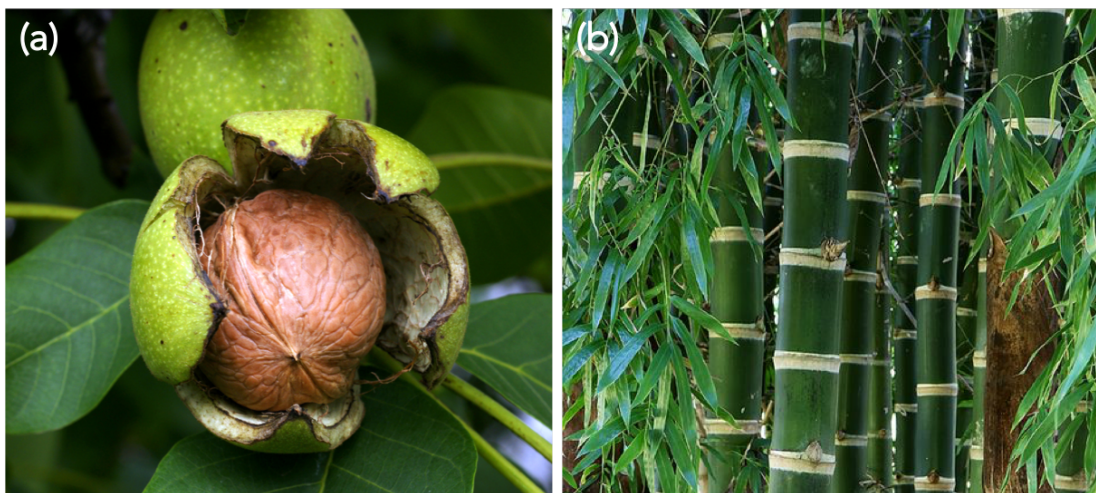


Figure 5.1: Lignocellulosic precursors. *Guadua Angustifolia* (a) and *Juglans regia* (b).

cheap, environmentally benign and available in various oxidation states, becoming the proper replacement element to ruthenium for electrochemical purposes. Manganese oxides ( $\text{MnO}_x$ ) are environmental friendly and only harmful by excessive inhalation or ingest. As it has been described in the previous chapter, manganese oxides ( $\text{MnO}_x$ ) have been widely studied as pseudocapacitive metal oxides used in composite materials for electrochemical capacitors as well as alkaline batteries and lithium ion batteries (Zhang & Chen, 2008), evidencing in all the cases to be a reliable electrode material with high performance. Compared to bulk  $\text{MnO}_x$  materials, nanoparticles acquire larger surface areas, increasing the pseudocapacitive activity (since is a surface process) and reducing the current densities. Nonetheless, the synthesis of  $\text{MnO}_x$  in the form of nanoparticles requires an extra effort than for the same material in bulk. Several and effective synthetic routes have been developed in order to prepare different manganese nano-oxides such as hydrothermal synthesis (Wu *et al.*, 2009; Yu *et al.*, 2009), electrodeposition (Thiagarajan *et al.*, 2011) and colloidal processes in both aqueous (Jana *et al.*, 2007; Luo, 2007) and organic (Jana *et al.*, 2008) medium.

It is obvious that EDLCs and batteries offer both certain distinct advantages. Therefore, hybridization of EDLC and batteries is highly attractive. Nanoscale decoration of carbons with a battery material allows a faradaic charge transfer, enhancing the specific capacity of purely EDLC materials. In this sense, many  $\text{MnO}_x$ @carbon composite systems have been investigated for supercapacitor applications (Bordjiba & Bèlanger, 2009; Chen *et al.*, 2018; Qu *et al.*, 2017).

In this section, in our effort to improve the electrochemical properties found in AC derived from walnut shells (*Juglans Regia*), we describe the preparation of a new composite material by incorporation of ultrasmall and spherical  $\text{MnO}_x$  nanoparticles (aprox. 2 nm size). AC obtained from *Juglans Regia* exhibits a specific capacitance of  $161 \text{ F g}^{-1}$  measured at  $1 \text{ mA cm}^{-2}$ , matching and even surpassing the values quoted in the literature for AC derived from lignocellulosic precursors (González-garcía *et al.*, 2013). However, the specific capacitance markedly decreases due not only to the presence of surface oxygenated acidic groups (Centeno & Stoeckli, 2006) but also due to the low electronic conductivity of activated carbon being in order of 10 to  $100 \text{ S m}^{-1}$  (El-Kady *et al.*, 2012; Sánchez-gonzález *et al.*, 2011). The precursor is first carbonized and then chemically activated by KOH under thermal treatment. Once the carbon guest is obtained, this material is incorporated into a brown colloidal aqueous solution containing 1% of  $\text{MnO}_x$  nanoparticles and after a few seconds they are adsorbed by the activated carbon yielding a transparent supernatant. Consequently, a new composite material, called  $\text{MnO}_x@WAC$  (walnut activated carbon containing MnO nanoparticles), composed by a matrix of highly disordered and entangled graphene layers containing ultrasmall pseudocapacitive MnO nanoparticles is presented. The effect of such small amount of metal oxide nanoparticles in the electrochemical performance of the activated carbon is evaluated.

## Synthesis

### *Walnut shell Activated Carbon (WAC)*

Before carbonization, the walnut shells were smashed in a metal mortar to reduce the particle size to millimeters. Then, 5 g of these particles were placed into a quartz crucible and heated at  $400^\circ\text{C}$  during 10 minutes in a tubular furnace under Ar atmosphere in order to remove their low boiling and melting point organic compounds. Finished the carbonization process, heating was turned off and the system was cooled down to room temperature. For the activation process, the carbon powder and the KOH are homogeneously mixed in a ratio 1:4. Then, the resulting mixture was placed on an alumina crucible inside a tubular furnace under Ar atmosphere, during 60 min at  $700^\circ\text{C}$ . After thermal activation, heating was turned off and the system was cooled down until  $25^\circ\text{C}$ . The activated carbon was neutralized with concentrated HCl solution and washed with abundant distilled water until the total elimination of chemical impurities. The final product labeled as WAC was dried in a stove at  $110^\circ\text{C}$  during 24 h.

*MnO<sub>x</sub> nanoparticles*

MnO<sub>x</sub> nanoparticles were synthesized by a novel route using poly acrylic acid (PAA) as both surfactant and reductor agent of manganese from KMnO<sub>4</sub>. 1.2 mmol of PAA were added to a solution of 20 ml of KMnO<sub>4</sub> 0.02 M. After few minutes the solution change its colour from purple to light brown indicating reduction of the oxidation state of manganese and the formation of a colloidal solution of MnO<sub>x</sub> nanoparticles. The colloid was then dialyzed for 5 days under continuous stirring renewing the water every day to remove excess of PAA in the dispersion. The final colloid dispersion was then washed by centrifugation (4000 rpm, 60 min) and placed on a stove at 80°C overnight. A brown powder is then collected as final MnO<sub>x</sub> nanoparticles product.

*MnO<sub>x</sub>@WAC composite*

The MnO<sub>x</sub>@WAC composite material was prepared following the next procedure. A dispersion of MnO<sub>x</sub> nanoparticles in 5 mL of water was added to an aqueous suspension of WAC (5 mL) in a ratio 1:100. After mixing, it was sonicated for 5 min changing the brown colour of the dispersion from brown into transparent, indicating an incorporation of the MnO<sub>x</sub> nanoparticles within the activated carbon. The MnO<sub>x</sub>@WAC composite was isolated by centrifugation (6000 rpm, 15 min) and dried at 80°C overnight.

**Structural Characterization**

Galician walnut shell is a high lignin content carbon and low cost renewable biomass readily accessible by our research group, which make it a good candidate as precursor material. An elemental analysis (see Table 5.1) was performed demonstrating the high carbon content of the walnut shell and the walnut shell activated carbon (WCA).

	C	N	H	O
<i>Juglans regia</i>	48.04	6.01	0.30	45.51
<i>WAC</i>	85.30	0.32	0.91	13.43

Table 5.1: Elemental analysis from the precursor and the WAC (%)

After the carbonization and chemical activation process, the carbon content (85.3%) almost doubles its amount values as displayed in Table 5.1, but important



concentrations of oxygen and hydrogen suggest the presence of surface oxygenated acidic groups such as hydroquinones or quinones.

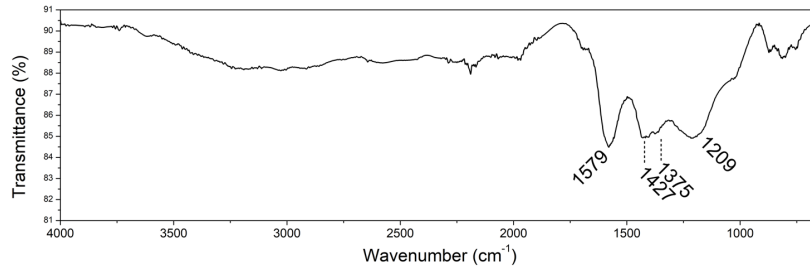


Figure 5.2: Infrared spectrum of WAC.

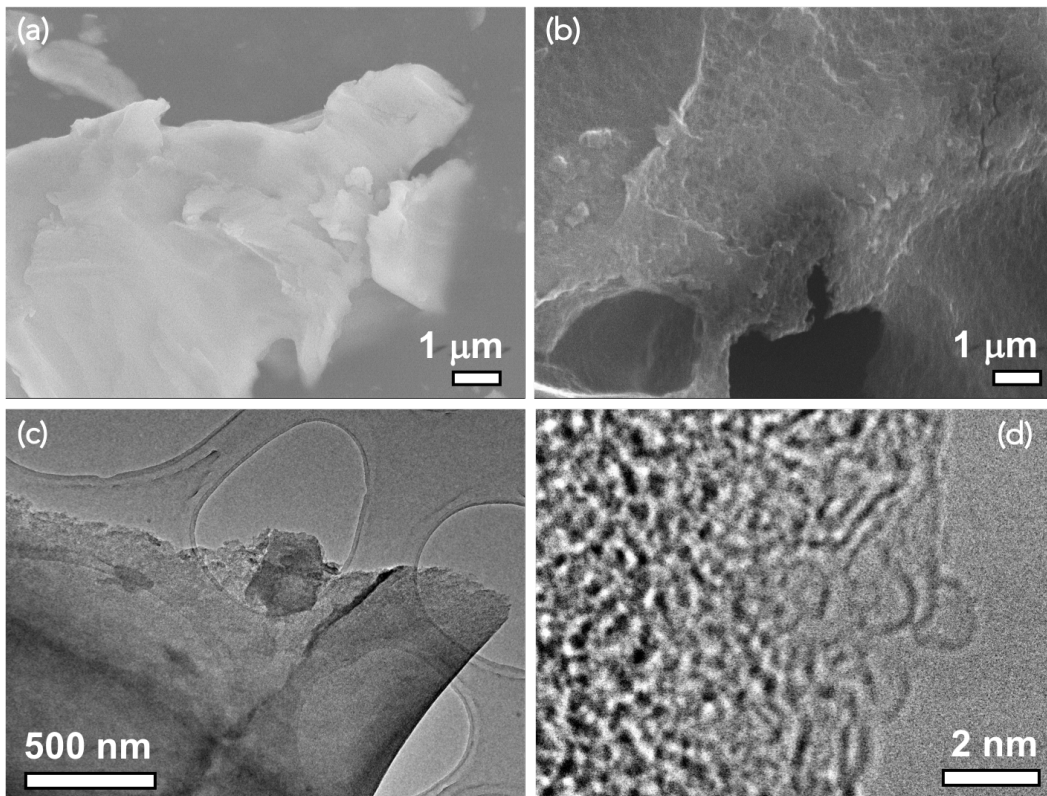


Figure 5.3: SEM images of raw walnut shell (a) and the obtained shell activated carbon (WAC) (b). Low magnification TEM (c) and HRTEM (d) images of WAC.

The identification of these oxygenated surface groups has been carried out by infrared spectroscopy (IR). The spectrum presents a broad band centred at 1579  $\text{cm}^{-1}$  indicating the presence of quinonic groups  $\nu(\text{C}=\text{O})$ . The bands situated at

1375-1427  $\text{cm}^{-1}$  due to the  $\nu(\text{C}-\text{O})$  stretching reveals the formation of xanthenes  $\nu(\text{C}-\text{O})$  and ethers  $\nu(\text{C}-\text{O})$  groups.

The SEM micrographs displayed in Figure 5.3 allow us to compare the morphology of the precursor and the AC. While the precursor exhibits a smooth and plane surface (Figure 5.3a), in the AC a roughness of the surface is clearly observed as result of the activation process (Figure 5.3b). The TEM study at low magnification (Figure 5.3c) shows that the material is formed by large a very thin carbon platelet-like particles. A closer inspection at higher magnification (Figure 5.3d) confirms that the material is composed by highly disordered and entangled graphene layers as building unit, showing even fullerene-like carbon layers at the edge of the particle.

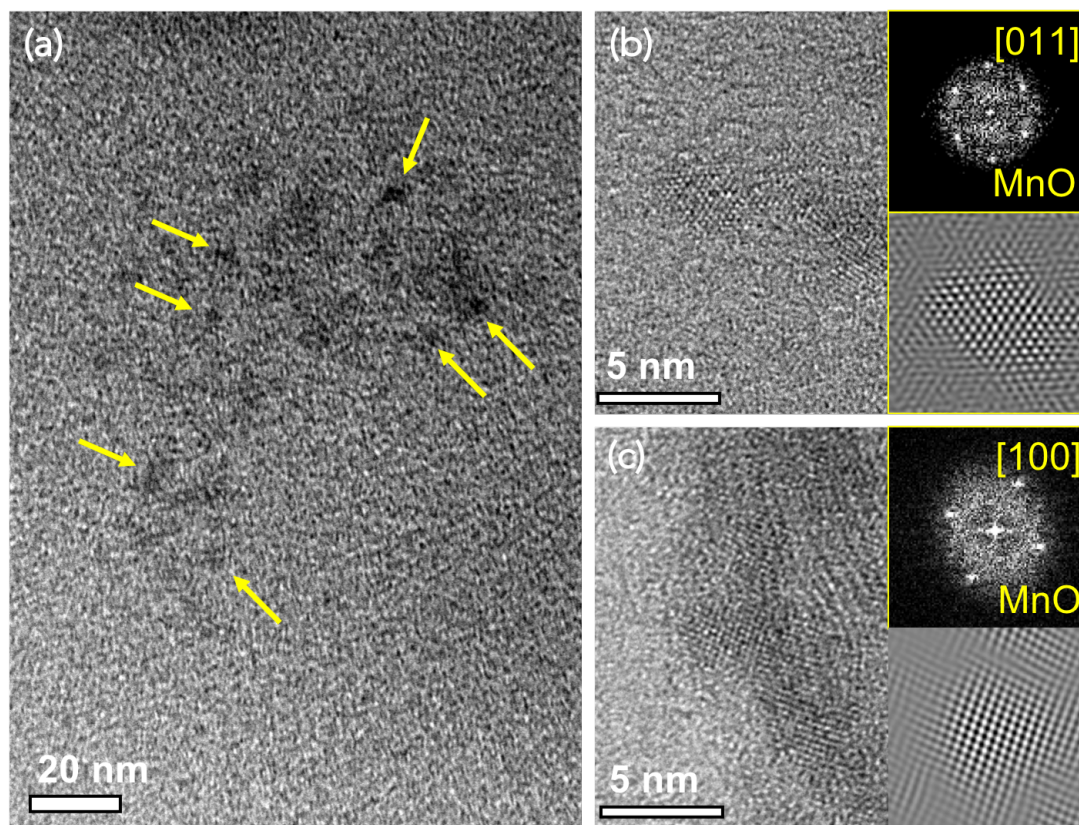


Figure 5.4: (a) Low magnification TEM micrograph of the colloidal  $\text{MnO}_x$ . HRTEM images of the  $\text{MnO}_x$  nanoparticles identified as MnO along the (b) [011] and (c) [100] zone axis. Their corresponding digital diffraction patterns are inset.

On the other hand, the synthesized  $\text{MnO}_x$  nanoparticles are very stable on aqueous solutions. Figure 5.4a shows a low magnification TEM image of the  $\text{MnO}_x$

nanoparticles, identified as the darker contrast of the image (poner flechas en la imagen para indicarlas) with a diameter ranging from 2-4 nm. These nanoparticles are identified as MnO, after recording HRTEM images along the [011] and [100] zone axis.(Figure 5.4b and c). MnO can be described as a cubic close-packing anion structure with all the octahedral holes filled by the cations in a NaCl type structure where all the  $Mn^{2+}$  cations are surrounded by  $O^{2-}$  anions. Although MnO does not exhibits channels in its structure like  $MnO_2$  polymorphs, is still considered one of the more promising candidates as electrode materials in supercapacitors (Ramadan *et al.*, 2018; Wei *et al.*, 2011b), due to its abundance, low cost and environmental compatibility plus its theoretical specific capacitance higher than  $MnO_2$  ( $1360 F g^{-1}$  against  $1110 F g^{-1}$  respectively)(Yang *et al.*, 2014).

The micro/nanostructure of the MnO@WAC composite material is analyzed in Figure 5.5. At first sight, both the low magnification TEM (Figure 5.5a) and the HRTEM images (Figure 5.5b) do not display appreciable contrast variation to ascertain the presence of the MnO nanoparticles within the particle, but we should remain that the nanoparticles are below 4 nm in size and only 1% in weight in the materials. However, the XEDS analyses performed in large areas of the particles (Figure 5.5c) detect the presence of manganese in addition to carbon and oxygen. The relative high intensity of the oxygen signal can be explained by the fact that the activated carbon contains around a 13% of oxygen as it has been previously discussed. In order to localize and image the MnO nanoparticles within the carbon matrix the use of STEM-HAADF mode was necessary. In the images recorded in this operation mode of the TEM, the contrast of the image is almost proportional to the atomic number of the atoms, in this composite material since Mn has the highest Z, we can identify the ultrasmall nanoparticles of MnO as tiny brighter spots well dispersed within the homogeneous darker contrast belonged to the carbon matrix (Figure 5.5d).

## Textural Characterization

$N_2$  adsorption-desorption isotherms measurements at 77 K on the WAC and  $MnO_x$ -@WAC composite material have been performed in order to evaluate the effect of the nanoparticles loading on the porous structure of the host material. The isotherm plots of both materials displayed in Figure 5.6a can be assigned to a type I according with the IUPAC classification, where the porosity consist mainly on micropores (<2nm) although the slight deviations at high pressure values indicate the presence of certain large pores (Gregg & Sing, 1982), however their impact in the total area is only around 5% as reflected in the values of  $S_{Ext. BET}$  displayed



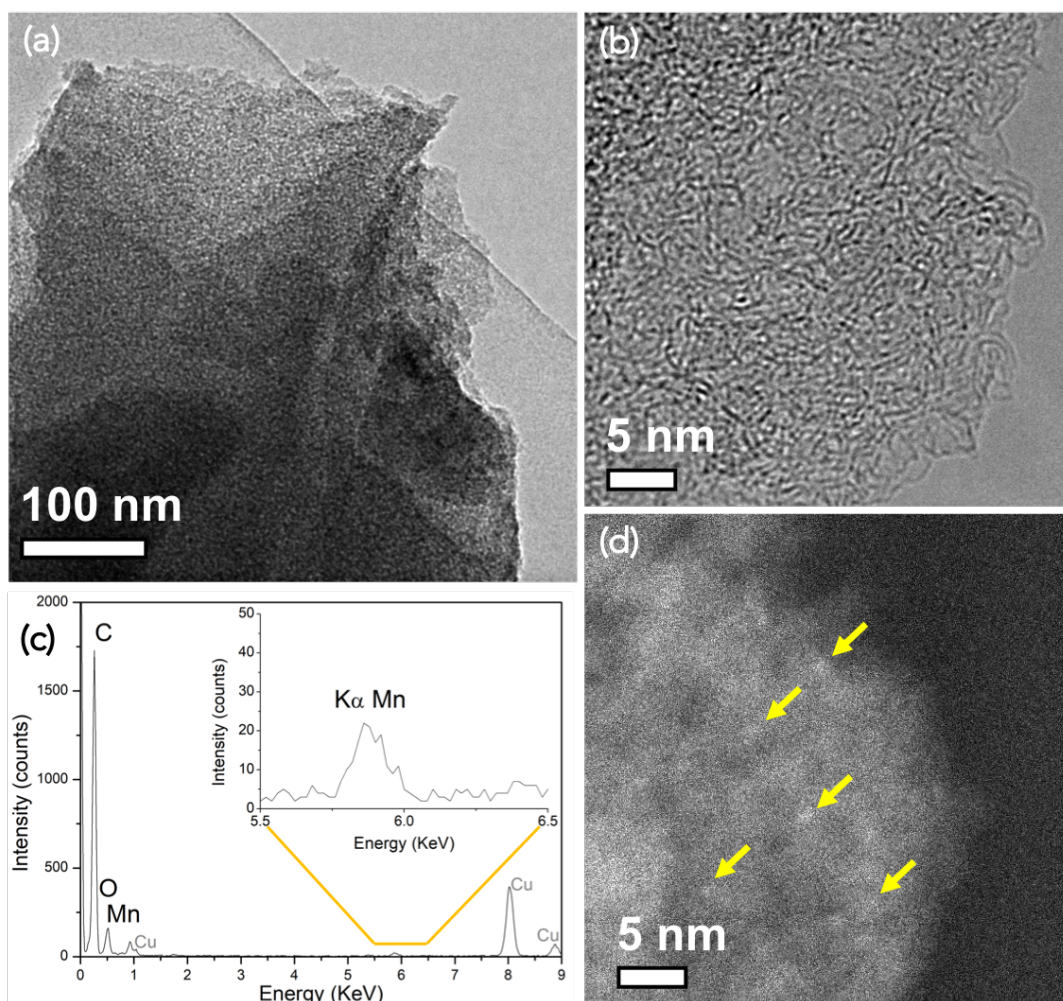


Figure 5.5: TEM micrographs of MnO@WAC composite material at low (a) and high (b) magnification. (c) XEDS spectrum of a carbon particle. On the right top of the spectrum the enlargement of the red squared area allow to identify the characteristic signal of Mn. (d) STEM-HAADF micrograph of the composite material where the MnO nanoparticles can be identify as the bright spots marked by arrows.

in Table 5.2. The comparison of the textural parameters from both materials (see Table 5.2, reveals a decrease of  $900 \text{ m}^2 \text{ g}^{-1}$  as result of the incorporation of 1% of MnO nanoparticles. However, the  $S_{\text{BET}}$  values of these materials are still remarkably larger that the reported by Pedro González (2012) for the same lignocellulosic precursor. The main difference lies in the chemical activation process, being more effective a mixture in solid state of the carbon and KOH that the impregnation of the carbon in a KOH solution. The pore size distributions derived from the

NLDFT method of WAC and  $\text{MnO}_x@WAC$  are depicted in Figure 5.6b. The plots confirm a similar behavior of these materials, showing a well defined pore structure composed by narrow ( $<0.7$  nm) and wide (0.7-2 nm) micropores, with similar values as it can be observed in Table 5.2. The main difference found on the porous structures corresponds to the decrease of wide micropores with size close to 2 nm which corresponds to the lower size of the MnO nanoparticles. Therefore the surface area decrease is originated by adsorption of the MnO nanoparticles within the micropores matching their size.

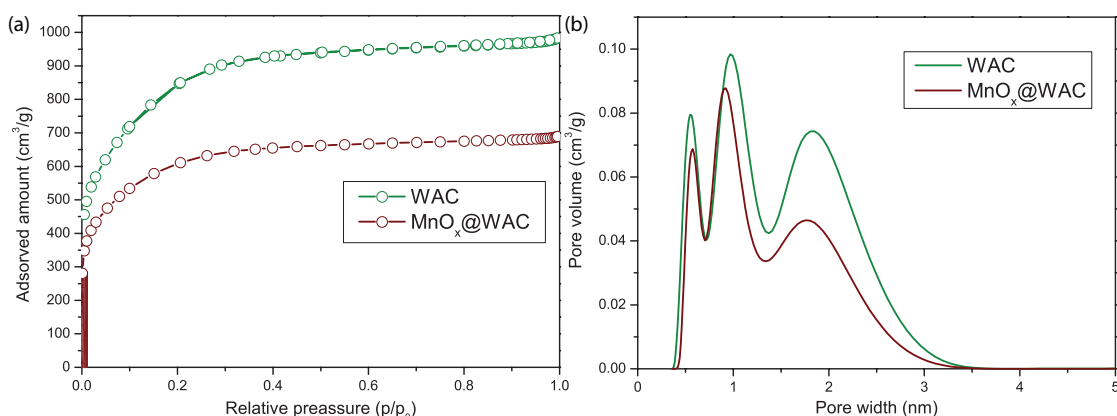


Figure 5.6: (a)  $\text{N}_2$  adsorption/desorption isotherm plots from WAC and  $\text{MnO}_x@WAC$ . (b) Representation of the pore size distributions showing the region with pore width  $\leq 5$ nm.

	$S_{\text{Total, BET}}$ ( $\text{m}^2/\text{g}$ )	$S_{\text{Ext., BET}}$ ( $\text{m}^2/\text{g}$ )	$S_{\text{Micr., BET}}$ ( $\text{m}^2/\text{g}$ )	Pore Width $_{2D-NLDFT}$ (nm)
WAC	2927	140	2786	0.55, 0.97 & 1.82
$\text{MnO}_x@WAC$	2070	84	1985	0.57, 0.92 & 1.76

Table 5.2: Total, external and micropore BET surface area and pore width of WAC and  $\text{MnO}_x@WAC$ .

## Electrochemical Characterization

The WAC carbon and the  $\text{MnO}_x@WAC$  composite material were directly measured in a symmetric Swagelok-type cell by cyclic voltammetry response at  $5 \text{ mV s}^{-1}$  at room temperature. Both samples show the typical pure capacitive behavior

of quasi-rectangular shapes in the CVs (Figure 5.7). The gravimetric capacitance values determined from the CVs displayed in Figure 5.7a yield values of  $168 \text{ F g}^{-1}$  and  $172 \text{ F g}^{-1}$  for the carbon and the composite. In the composite material the capacitance value is 2% higher than the one for the pure carbon. Although the deposition of 1% of MnO nanoparticles provokes a decrease of the surface area (see Table 5.2) and therefore less accessible surface to the electrolyte ions, the pseudocapacitive contribution of such nanoparticles contribute to making balancing the loss of pure capacitance. The slight increase in density in the composite material also increase the volumetric capacitance from 41 to  $59 \text{ F cm}^{-3}$ .

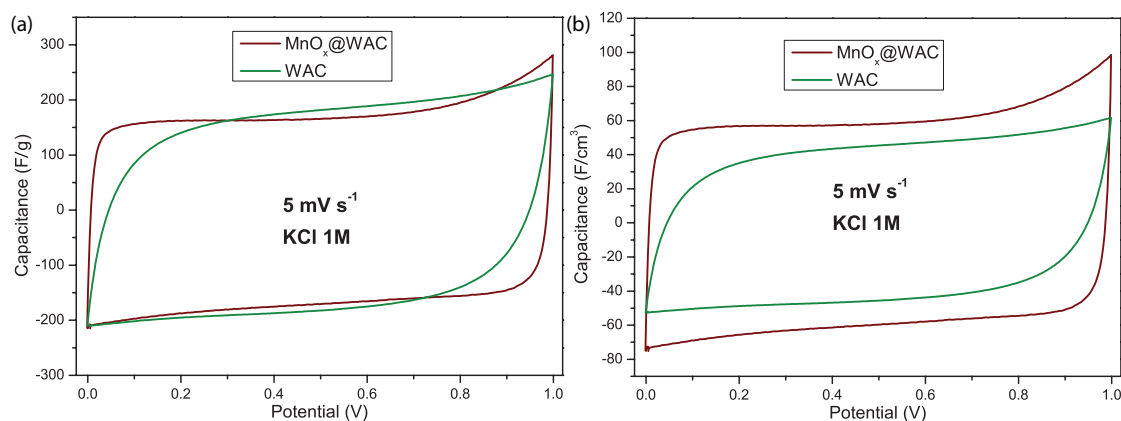


Figure 5.7: Comparison of gravimetric (a) and volumetric (b) capacitance of  $\text{MnO}_x\text{@WAC}$  composite material and NCA carbon material on a symmetric two-electrode cell.

As the sweep rate was increased (see Figure 5.8a), although the shape of the CVs is almost retained in the case of the carbon material, the loss of the shape is more evident and the original volumetric capacitance decrease more rapidly in comparison with the composite. Further characterization of the materials was performed by galvanostatic measurements at different current densities (Figure 5.8b). The charging discharging profiles at  $0.1 \text{ A g}^{-1}$  show linear-like dependencies of the potential versus time in agreement with the capacitive charge storage mechanism and the capacitance obtained from cycling voltammetry. In this case, capacitance values calculated from GCPL shows a higher gravimetric capacitance value for the carbon material than for the composite ( $207 \text{ F g}^{-1}$  and  $191 \text{ F g}^{-1}$  respectively) unlike the values calculated from CVs before. Being such small differences, the capacitance value for both materials can be considered as equal. By increasing the current density from  $0.1$  to  $10 \text{ A g}^{-1}$  (Figure 5.8b inset), the composite  $\text{MnO}_x\text{@WAC}$  holds a 63% of the original capacitance current density, whereas the carbon material suffers a dramatic reduction of the capacitance in the same range.

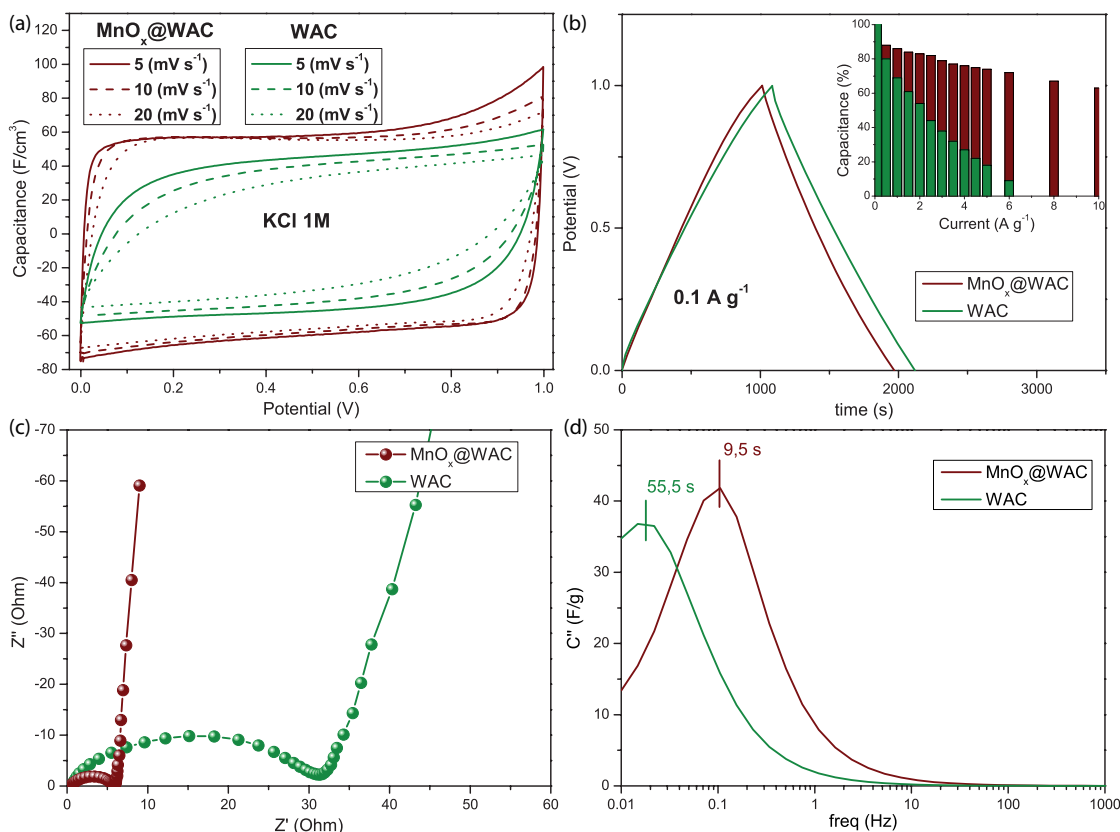


Figure 5.8: (a) Cyclic voltammograms at different scan rates, (b) galvanostatic charge-discharge cycles, (c) Nyquist plot and (d) complex imaginary capacitance from potentiostatic electrochemical impedance spectroscopy for  $\text{MnO}_x@WAC$  and WAC on a symmetric two-electrode cell.

The Nyquist plots obtained after potentiostatic electrochemical impedance spectroscopy (PEIS) measurements are displayed in Figure 5.8c. It is evident that the  $\text{MnO}_x@WAC$  composite exhibits a much smaller diameter of the Nyquist semicircle, indicating a much more efficient charge transfer process at the electrode interface. The equivalent circuit modeling yields ESR values of 31 and 6 ohm respectively, improving the relaxation time constant calculated from the complex impedance data from 55.5 to 9.5 seconds (Figure 5.8d). This result suggests that the incorporation of 1% of  $\text{MnO}$  nanoparticles leads to a much reduced electrical impedance and an increased charge transfer process.

## Conclusions

An activated nanoporous carbon from Galician walnut shells (WAC) with an enormous specific surface area has been successfully synthesized following a dry chemical activation process. As well as ultrasmall  $\text{MnO}_x$  nanoparticles synthesized by a novel method using polyacrylic acid as both surfactant and reductor agent. The combination of both materials in adequate proportions results on the  $\text{MnO}_x$ @WAC composite with improved electrochemical performance due the pseudocapacitance properties of MnO nanoparticles which work in synergy with the capacitive mechanism of WAC, in addition to the increase in the electrical conductivity, indicated in the impedance measurements by a dramatic decrease of the ESR value.

## 5.2 Bamboo activated carbon with embedded gold nanoparticles composite as supercapacitor electrode with enhanced volumetric capacitance

At the present, the ohmic resistance of the activated nanoporous carbon is the main disadvantage at the time to use it as electrode material in supercapacitors. It can substantially be reduced by the incorporation of other carbon additives such as carbon black, graphite or carbon nanotubes (Portet *et al.*, 2005) or a low cost and excellent conductor such as copper nanocrystals (Zhang *et al.*, 2013). Though copper is more economic than noble metals such as gold or platinum and yield also higher volumetric capacity and contribute also to the increase of energy storage through the presence of faradaic reactions, is easily oxidized into CuO in the form of nanoparticles, with a dramatic decrease of the electronic conductivity from  $108 \text{ S m}^{-1}$  into  $0.1\text{-}1 \text{ S m}^{-1}$  (Jeong & Choi, 1996). Therefore, gold may offer an excellent alternative to copper as main composition of nanoparticles within ACs matrices. In this context, gold nanoparticles (AuNPs) have been synthesized in CDCs through wet chemical synthesis of nanocrystals in aqueous solution (Niu *et al.*, 2011). However, due to the inherent difficulties of dispersabilities of hydrophobic ACs in water, and considering the advances of synthesis of gold nanoparticles in non-aqueous solvents (Xia *et al.*, 2009), we consider interesting the use of organic solvents to obtain highly loaded ACs@AuNPs matrices with promising electronic conductivities.

In this section, we report a facile an efficient synthetic method to incorporate



gold nanoparticles in an activated nanoporous carbon matrix, in organic solvent, derived from an abundant natural plant resource: the *Guadua angustifolia* bamboo specie. This precursor has been selected, since the obtained AC, called bamboo activated carbon (BAC), exhibits a high specific capacitance value of  $154 \text{ F g}^{-1}$  at  $1 \text{ mA cm}^{-2}$  (González-garcía *et al.*, 2013). Although, in a similar way than the WAC described in the previous section, the specific capacitance notably decreases as the current density increase. The precursor is first carbonized and then chemically activated by KOH during thermal treatment. Then AuNPs have been incorporated to the carbon matrix by using a method for the large-scale synthesis of organoamine-protected AuNPs (Hiramatsu & Osterloh, 2004). Therefore, a nanostructured AuNPs@BAC composite material is obtained exhibiting a microstructure composed of highly disordered and entangled graphene layers with a 25% of Au inside and decorating the surface. The incorporation of a more dense material like gold in the AC provoked an enhancement of almost double of the volumetric capacitance values ( $47 \text{ F cm}^3$ ) in aqueous electrolyte as well as the drop of one order of magnitude of the internal resistance of the supercapacitor cell. The change in the textural properties of the activated nanoporous carbon upon addition of gold nanoparticles and the reliable synthesis method of these metal-nanoporous carbon composites suggest the possibility of production of many different nanostructured composite electrode materials for electrochemical energy storage applications.

## Synthesis

### *Bamboo Activated Carbon (BAC)*

Prior the carbonization, the lignocellulosic precursor *Guadua angustifolia*, was reduced to 1 cm length. The carbonization process was performed in a similar way than the above nutshell carbon: 5 g of these particles were placed into a quartz crucible and heated at  $400^\circ\text{C}$  during ten minutes in a tubular furnace under Ar atmosphere in order to remove their low boiling and melting point organic compounds. Finished the carbonization process, heating was turned off and the system was cooled down to  $25^\circ\text{C}$ . The carbon obtained from the previous stage was chemically activated with KOH but in this case by solid-liquid interaction, using the impregnation method. A solution of 10 mL containing 10 M KOH and the carbon in weight ratio 4:1 was stirred at  $70^\circ\text{C}$  during 120 min. The resulting slurry was later on dried at  $110^\circ\text{C}$  followed by a thermal activation carried out in a tubular furnace under Ar atmosphere, during 60 min at  $700^\circ\text{C}$ . Elapsed the activation time, heating was turned off and the system was cooled until  $25^\circ\text{C}$ . The

activated carbon was washed in a 0.1 M HCl solution and with abundant distilled water until the total elimination of chemical impurities. The final product was dried in a furnace at 110°C during 24 h.

#### *AuNPs@BAC composite*

For the preparation of the AuNPs@BAC composite, 70 mg of the activated carbon were dispersed by sonication (15 minutes) in 10 mL of toluene, and subsequently mixed with 3.25 mL of oleylamine (OAm) and 35 mg of  $\text{HAuCl}_4 \cdot 3\text{H}_2\text{O}$ . The mixture was stirred during 12 hours at room temperature, to allow complete diffusion of chemicals within the carbon matrix. The mixture was heated to reflux at 150°C during 2 hours. Then at room temperature, the mixture was centrifuged and cleaned twice with toluene (2500 rpm, 10 min) to remove excess of OAm, and the precipitate was redispersed in 0.5 mL of toluene. Finally, the AuNPs@BAC sample was heated under vacuum at 80°C during 1 week to remove traces of solvent.

## Structural Characterization

Bamboo waste is selected as raw material because it is a renewable biomass, it has a high content of carbon (see elemental analysis in Table 6.1), yields a high quality activated carbon and is a low cost precursor (abundance).

	C	N	H	O
<i>Guadua angustifolia</i>	44.84	5.84	0.91	48.41
<i>BAC</i>	82.85	2.88	1.22	13.05

Table 5.3: Elemental analysis from the precursor and the BAC (%)

Generally, a carbonization process at 400°C is needed to enrich the carbon content by eliminating non-carbon species, followed by a chemical activation process with KOH at 700°C to enhance the pore volume, enlarge the diameter of pores and increase the porosity. The success of the activation process is reflected in the doubled carbon content above 80% in the chemical activated carbon from *Guadua angustifolia* (BAC) compared with the raw material (see Table 5.3). The chemical composition of BAC exhibits a concentration of oxygen and hydrogen of 13.05% and 2.88% respectively, suggesting the presence of surface oxygenated acidic and hydroquinone/quinone groups that can be responsible of pseudo-capacitance in the carbon material.

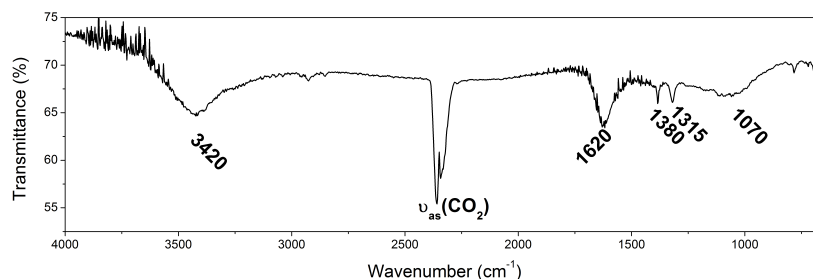


Figure 5.9: Infrared spectrum of BAC

The analysis of the infrared spectrum (5.9) allows the identification of the different groups. The sharpest band at  $1620\text{ cm}^{-1}$  indicates the presence of quinonic groups  $\nu(\text{C}=\text{O})$ , whereas those situated at  $1315$  and  $1380\text{ cm}^{-1}$ , due to the  $\text{C}-\text{O}$  stretching, reveals the formation of xanthenes  $\nu(\text{C}-\text{O})$  and ethers  $\nu(\text{C}-\text{O})$  groups. The single band at  $1070\text{ cm}^{-1}$  reveals that the ethers groups are symmetric ( $\text{R}-\text{O}-\text{R}$ ). Finally, the broad band at  $3240\text{ cm}^{-1}$ , due to the  $\text{H}-\text{O}$  stretching, confirms also the presence of phenolic groups  $\nu_{(\text{H}-\text{O})}$  and the weak and broad bands in the range from  $2850\text{--}2950\text{ cm}^{-1}$ , can be assigned to the asymmetric  $\nu_{\text{as}(\text{C}-\text{H})}$  and symmetric  $\nu_{\text{s}(\text{C}-\text{H})}$   $\text{C}-\text{H}$  stretching.

As it can be seen in Figure 5.10a, the pieces of the raw dried bamboo are formed by fibers since is mainly composed of cellulose, lignin and hemicellulose. A close inspection of the raw material by Scanning Electron Microscopy (SEM) reveals the fibrous nature of the precursor (see Figure 5.10b). The SEM image of BAC displayed in Figure 5.10c clearly shows how the chemical activation modifies the surface of the raw material due to the elimination of volatiles. Notice that the material is composed by fibrous particles showing almost exfoliated very thin carbon flakes and the development of a high amount of pores.

Oleylamine (OAm) is common reagent used in the synthesis of stable and monodisperse nanoparticles (Mourdikoudis & Liz-marza, 2013). In fact, the synthesis of Au nanoparticles is very simple since only involves OAm and  $\text{HAuCl}_4$  in an organic solvent. Here, OAm acts not only as reduction agent of  $\text{Au}^{3+}$  into Au, but also stabilizes grow of the particles through the affinity of the  $\text{NH}_2$  group with the metal. Under these synthetic conditions, it seem feasible that a highly porous structure of an active carbon such as BAC, can act as a nanoreactor where the Au-OAm nanoparticles can be growth yielding an interesting composite AuNPs@BAC. The success of this approximation is clearly demonstrated by the SEM images displayed in Figure 5.10d-f. The image displayed in Figure 5.10d shows a perspective of the AuNPs@BAC composite material where all the particles are decorated by

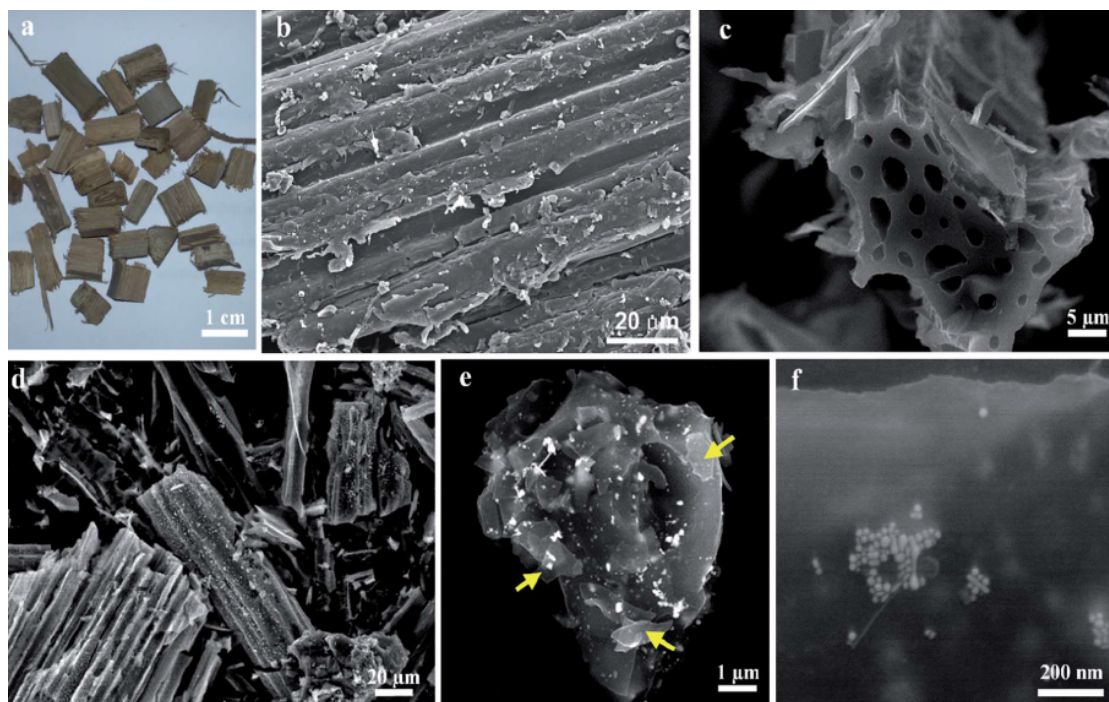


Figure 5.10: (a) Photograph of the dried bamboo pieces before the carbonization, SEM micrograph of the precursor (b) before and (c) after carbonization and chemical activation, low magnification SEM micrographs of (d) AuNPs@BAC composite material and (e) a single particle and (f) high magnification micrograph of the BCA@AuNPs composite.

areas with brighter contrast corresponding to the Au nanoparticles. At higher magnification (Figure 5.10e) a single particle of this material is displayed containing a substantial amount of Au nanoparticles. The most important point is that in those areas the Au nanoparticles are not agglomerated but well-ordered as it can be observed at the high magnification SEM image displayed in Figure 5.10f. Here, we note that the size of the nanoparticles on the surface is not homogeneous, but are well separated by around 2 nm, which is the length of the OAm molecule (Borges *et al.*, 2011). In addition, the blurred bright contrast observed can indicate that also groups of particles are located inside the carbon material.

To further investigate the structure of the prepared composite material AuNPs@BAC, a HRTEM study has been performed. Figure 5.11 displays the HRTEM images at different magnification of this composite material. At low magnification (Figure 5.11a) we observe a very thin layer of active carbon containing darker areas where the Au nanoparticles have grown, exfoliated in the crushing of the microparticles

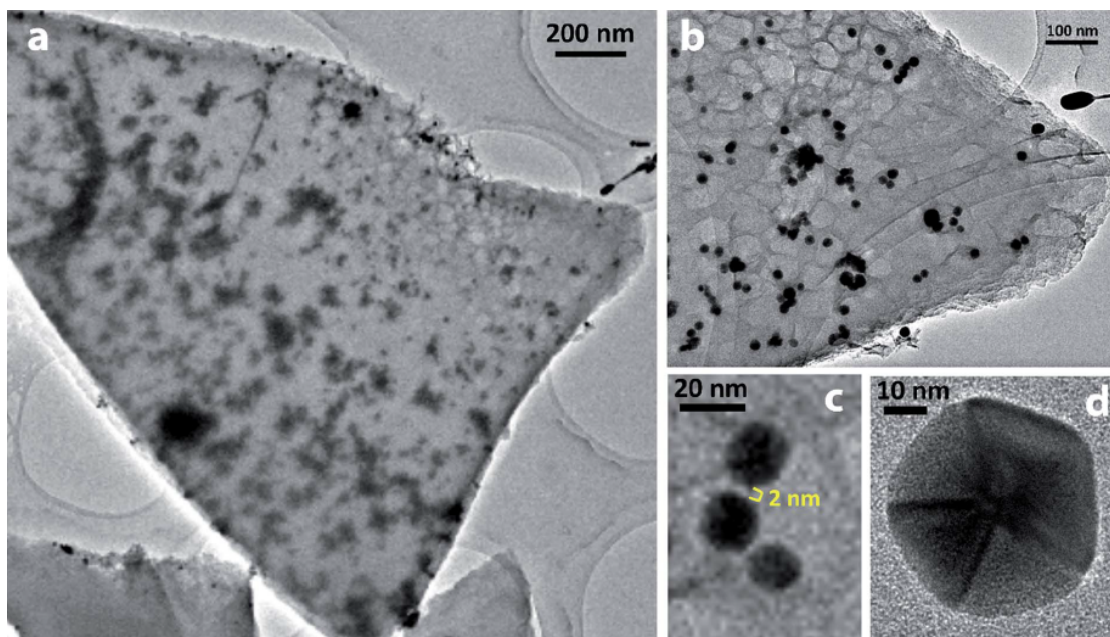


Figure 5.11: (a) Low magnification TEM image of the composite material CAC@AuNPs, where the darker areas reveal the presence of AuNPs. (b) Magnified area from (a) where isolated and ordered AuNPs are clearly identified. (c) Group of AuNPs showing an interparticle distance of 2 nm. (d) Single pentatwinned Au nanocrystal.

observed by SEM during the TEM sample preparation. In fact some of these layers are marked by yellow arrows in Figure 5.10e. At higher magnification (Figure 5.11b) we detect the presence of single but also groups of particles with different size in the surface and inside the carbon layer with a separation between the closest particles 2 nm (Figure 5.11c). The HRTEM images of single Au nanoparticles reveal that their size varies between 15 and 50 nm, and a multiply twinned structure (Figure 5.11d), which is typical for noble metals with a face-centered cubic structure at small sizes (Lu *et al.*, 2008). The amount of gold incorporated to the BAC has been analyzed by thermo-gravimetric analysis of a portion of AuNPs@BAC in air yielding a loss of carbon of 75% and therefore a content of gold of 25%.

## Textural Characterization

The effect on the porous structure with the loading of AuNPs, has been study by the  $N_2$  adsorption-desorption measurements at 77 K on the BAC and the composite



material BAC-AuNPs prepared in this work. The isotherm plots of both materials depicted in Figure 5.12a follow the type I according to the IUPAC classification (Gregg & Sing, 1982). It appears that the porosity consists mainly of micropores (width < 2 nm). The BET surface (SBET) area and the micropore volume of BAC are one order of magnitude larger than in AuNPs@BAC, as effect of the loading of AuNPs (see Table 6.1).

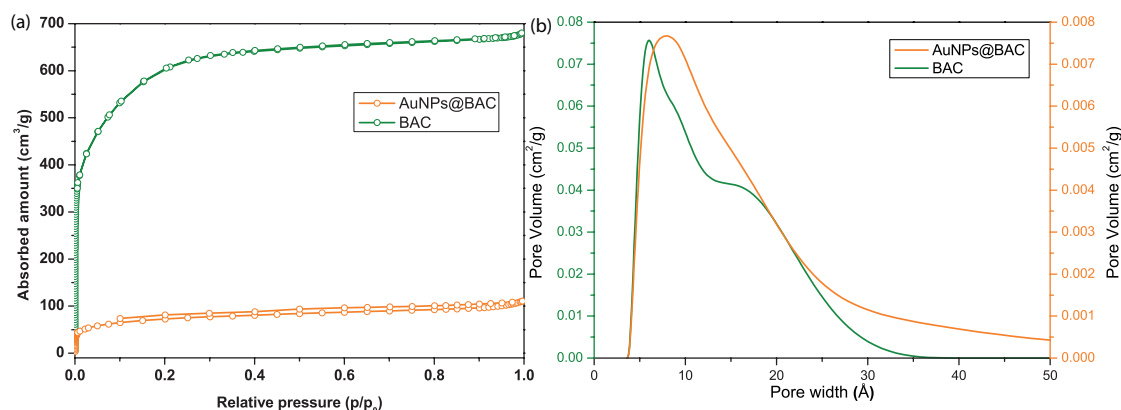


Figure 5.12: (a)  $N_2$  adsorption/desorption isotherm plots from BAC and AuNPs@BAC. (b) Pore size distributions of BAC and AuNPs@BAC on a symmetric two-electrode cell.

	$S_{\text{Total, BET}}$ ( $\text{m}^2/\text{g}$ )	$S_{\text{Ext. BET}}$ ( $\text{m}^2/\text{g}$ )	$S_{\text{Micr. BET}}$ ( $\text{m}^2/\text{g}$ )	Pore Width $_{2\text{D-NLDFT}}$ (nm)
BCA	2187	96	2091	0.57, 0.91 & 1.77
BCA@AuNPs	265	48	217	0.78

Table 5.4: Total, exterior and micropore BET surface area and pore width of prepared samples.

The pore size distribution curves of both materials (see Figure 5.12b) show a similar trend, however whereas the curve of BAC present a maximum value at 0.57 nm and two well defined shoulders centred at 0.91 and 1.77 nm respectively, in the PSD of AuNPs@BAC the maximum is displaced at 0.78 nm and the shoulders disappear due the fact that the ratio of pores with a size between 1.5-2.5 nm are increased respect to smaller pores. Interestingly, the new pore distribution matches the size of the chain length of OAm at the surface of the AuNPs (Wang *et al.*, 2010). Therefore, we have analysed the typical interparticle distance between AuNPs by HRTEM (Figure 5.11c.) that has been determined in 2 nm, showing an interdigitation of the monolayers of OAm between adjacent nanocrystals within

the carbon matrix. This result can be correlated to the increase of the pores with a size between 1.5-2.5 nm observed in the pore size distribution.

## Electrochemical Characterization

Figure 5.13 shows the cyclic voltammetric response of the carbon electrodes containing gold nanoparticles (AuNPs@BAC) and without (BAC) recorded in a supercapacitor cell at  $5 \text{ mV s}^{-1}$  at room temperature in a symmetric two-electrode cell configuration. Both samples shown CVs with rectangular shape, typical of a capacitive behavior. Figure 5.13a shows higher gravimetric capacitance values for BAC ( $100 \text{ F g}^{-1}$ ) than the sample BCA-AuNPs ( $73 \text{ F g}^{-1}$ ). This is because of the presence of higher specific surface ( $2019 \text{ m}^2 \text{ g}^{-1}$  against  $265 \text{ m}^2 \text{ g}^{-1}$ ) in BAC than AuNPs@BAC. However, sample AuNPs@BAC shows superior volumetric capacitance values ( $47 \text{ F cm}^3$ ) in comparison to BAC ( $29 \text{ F cm}^3$ ) as a consequence of the incorporation on its microstructure of gold nanoparticles as it shown in Figure 5.13b.

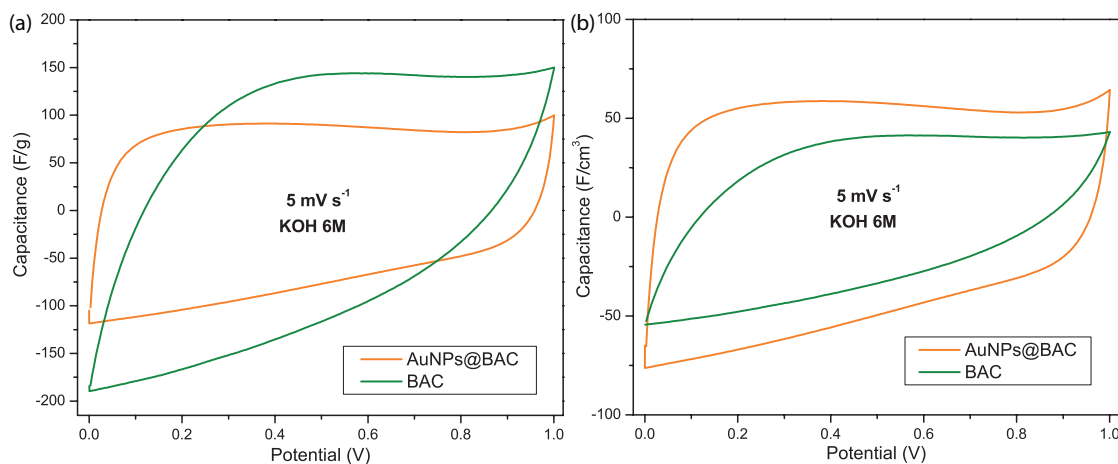


Figure 5.13: (a) Cyclic voltammograms at different scan rates, (b) galvanostatic charge-discharge cycles, (c) Nyquist plot and (d) complex capacitance from potentiostatic electrochemical impedance spectroscopy for BAC@AuNPs and BAC on a symmetric two-electrode cell.

Additional electrochemical measurements performed on the samples BAC@AuNPs and BAC in 6MKOH electrolyte are shown in Figure 5.14. Figure 5.14a shows CVs at different scan rates for AuNPs@BAC sample. The increasing of the ohmic resistance in the bulk electrolyte with increasing the scan rate produced a small distortion in the CVs. The distortion of the electrochemical response was

more pronounced in CAC sample in which a highly resistive behavior during polarization can be observed in Figure 5.14a. The origin of this distortion could be due to the intricate diffusion of the ions inside the pores. However, the textural properties exhibited by both samples comprised the presence of a large amount of micropores accompanied by certain mesoporosity that should be optimum for retention of the capacitive properties as the sweep rate increase (Maletin *et al.*, 2012). In addition, both samples presented enough micropore surface area SDFT (<2 nm) (see Table 6.1) that should allow the accommodation of the electrolyte's ions while cycling up to 1 V without the presence of sieving effect features (Mysyk *et al.*, 2009). Therefore, the distortion might not be only due to the diffusion limitation of the ions into the nanopores but possibly to the presence of a high electrode resistance. The inherent electronic conductivity of the active electrode material is included in the ESR. Then, it would be also possible by impedance spectroscopy analysis to further ascertain the role of functional groups and the inhomogeneous nanoporosity in the ohmic drop of the cell (Gregg & Sing, 2005). Figure 5.14c shows the Nyquist plot of the supercapacitor cell obtained from PEIS data. The vertical increase of the imaginary part of the impedance in both carbon electrodes confirms the capacitive nature of the electrochemical storage. The first semicircle of BAC sample is attributed to the bulk impedance while the second one appearing at lower frequencies suggests the parallel existence of a charge transfer resistance. Thus, it might be possible that faradaic reactions (irreversible) from the presence of functional groups at the surface of the activated carbon are at the origin of the high values of

capacitance observed for sample BAC. We have compared both PEIS data before and after cycling for BAC supercapacitor cell evidencing the disappearance of the interfacial contribution which it was most probably due to the oxygen groups at the surface of the porous carbon. The total interfacial resistance at open circuit voltage is shown to be comparable than the bulk resistance and it was therefore evident how the presence of gold nanoparticles suppressed this effect, which is important for practical applications. The electrochemical series resistance (ESR) measured for AuNPs@BAC reaches the value of 8 ohm cm<sup>2</sup>, one order of magnitude lower than that for sample BAC with an ESR value of 130 ohm cm<sup>2</sup>. Moreover, high electrochemical stability for the nanoporous carbon-gold nanoparticles electrode material was evidenced by PEIS measurements of the supercapacitor cell after cycling. From these measurements, we can also infer that an optimum interaction between carbon surface and gold nanoparticles was achieved. Figure 5.14b shows the galvanostatic charge-discharge cycles at 0.1 A g<sup>-1</sup>. The charging discharging profiles show linear-like dependencies of the potential versus time in agreement with the capacitive charge-storage mechanism and the capacitance obtained from cycling voltammetry.



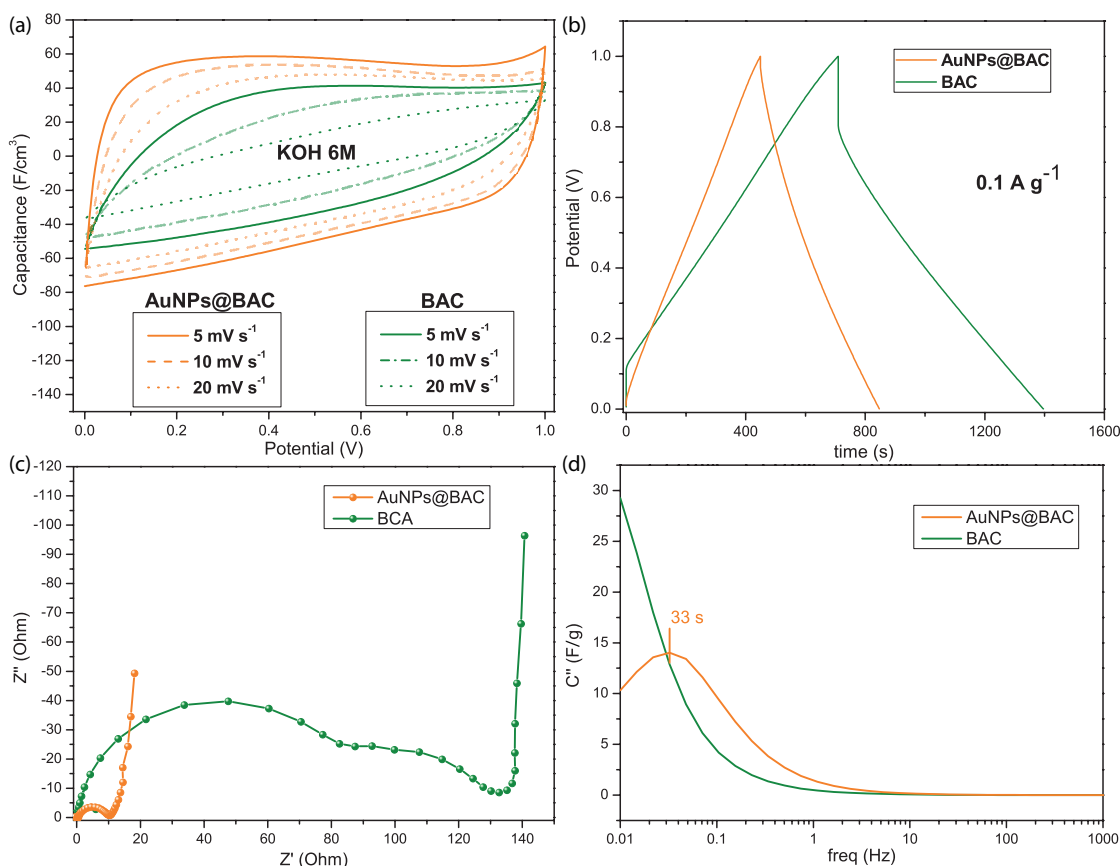


Figure 5.14: (a) Cyclic voltammograms at different scan rates of AuNPs@BAC and BAC samples. (b) Galvanostatic charge-discharge plots for CAC and AuNPs@BAC at 0.1 A g<sup>-1</sup>. Potentiostatic electrochemical impedance spectroscopy of AuNPs@BAC and BAC on (c) Nyquist plot and (d) complex imaginary capacitance.

## Conclusions

In summary, a facile and reproducible new method for the synthesis of activated nanoporous carbon@gold nanoparticles composites has been detailed. This approach yields nanostructured electrode materials with high-volumetric capacitance in aqueous electrolyte (6 M KOH). Interestingly the suppression of the irreversible capacitance caused by the presence of oxygen moieties at the surface of the carbon has also been evidence after gold nanoparticles incorporation into the carbon matrix. The present results are of high significance because bring the possibility to fabricate nanoporous carbon@metal composites with a high potential of being used as the next generation of electrode materials in electrochemical energy storage

applications.

## Bibliography

- ADINATA, D., DAUD, W. M. A. W. & AROUA, M. K. (2007). Production of carbon molecular sieves from palm shell based activated carbon by pore sizes modification with benzene for methane selective separation. *Fuel Processing Technology* **88**(6), 599–605.
- BORDJIBA, T. & BÈLANGER, D. (2009). Direct redox deposition of manganese oxide on multiscaled carbon nanotube/microfiber carbon electrode for electrochemical capacitor. *J. Electrochem. Soc.* **156**(5), A378–A384.
- BORGES, J., RIBEIRO, J. A., PEREIRA, E. M., CARREIRA, C. A., PEREIRA, C. M. & SILVA, F. (2011). Preparation and characterization of dna films using oleylamine modified au surfaces. *J. Colloid Interface Sci.* **358**, 626–634.
- BURKE, A. (2007). R & D considerations for the performance and application of electrochemical capacitors. *Electrochimica Acta* **53**, 1083–1091.
- CENTENO, T. A. & STOECKLI, F. (2006). The role of textural characteristics and oxygen-containing surface groups in the supercapacitor performances of activated carbons. *Electrochim. Acta* **52**(2), 560–566.
- CHEN, L., GUO, X., LU, W., CHEN, M., LI, Q., XUE, H. & PANG, H. (2018). Manganese monoxide-based materials for advanced batteries. *Coordination Chemistry Reviews* **368**, 13–34.
- CONWAY, B. E. (1999). *Electrochemical Supercapacitors*. Kluwer Academic.
- EL-KADY, M. F., STRONG, V., DUBIN, S. & KANER, R. B. (2012). Laser scribing of high-performance and flexible graphene-based electrochemical capacitors. *Science* **335**(6074), 1326–1330.
- GONZÁLEZ-GARCÍA, P. (2018). Activated carbon from lignocellulosics precursors: A review of the synthesis methods, characterization techniques and applications. *Renewable and Sustainable Energy Reviews* **82**, 1393–1414.
- GONZÁLEZ-GARCÍA, P., CENTENO, T. A., URONES-GARROTE, E., ÁVILA-BRANDE, D. & OTERO-DÍAZ, L. C. (2013). Applied surface science microstructure and surface properties of lignocellulosic-based activated carbons. *Appl. Surf. Sci.* **265**, 731–737.
- GREGG, S. J. & SING, K. S. W. (1982). *Adsorption, surface area and porosity*. Academic Press, London.
- GREGG, S. J. & SING, K. S. W. (2005). *Impedance Spectroscopy*. Wiley, New Jersey.
- HIRAMATSU, H. & OSTERLOH, F. E. (2004). A simple large-scale synthesis of nearly monodisperse gold and silver nanoparticles with adjustable sizes and with exchangeable surfactants. *Chemistry of Materials* **16**(13), 2509–2511.

- IP, A., BARFORD, J. & MCKAY, G. (2008). Production and comparison of high surface area bamboo derived active carbons. *Bioresource Technology* **99**(18), 8909–8916.
- JAIN, A., ARAVINDAN, V., JAYARAMAN, S., KUMAR, P. S., BALASUBRAMANIAN, R., RAMAKRISHNA, S., MADHAVI, S. & SRINIVASAN, M. P. (2013). Activated carbons derived from coconut shells as high energy density cathode material for li-ion capacitors. *Scientific Reports* **3**, 3002.
- JANA, S., BASU, S., PANDE, S., GHOSH, S. K. & PAL, T. (2007). Shape-selective synthesis, magnetic properties, and catalytic activity of single crystalline  $\beta$ -mno<sub>2</sub> nanoparticles. *The Journal of Physical Chemistry C* **111**(44), 16272–16277.
- JANA, S., PANDE, S., SINHA, A. K. & PAL, T. (2008). Synthesis of superparamagnetic  $\beta$ -mno<sub>2</sub> organosol: a photocatalyst for the oxidative phenol coupling reaction. *Inorganic Chemistry* **47**(13), 5558–5560.
- JEONG, Y. K. & CHOI, G. M. (1996). Nonstoichiometry and electrical conduction of cuo. *Journal of Physics and Chemistry of Solids* **57**(1), 81–84.
- JÚSTIZ-SMITH, N. G., VIRGO, G. J. & BUCHANAN, V. E. (2008). Potential of jamaican banana, coconut coir and bagasse fibres as composite materials. *Materials Characterization* **59**(9), 1273–1278.
- LONG, C., QI, D., WEI, T., YAN, J., JIANG, L. & FAN, Z. (2014). Nitrogen-Doped Carbon Networks for High Energy Density Supercapacitors Derived from Polyaniline Coated Bacterial Cellulose. *Adv. Funct. Mater. Funct. Mater.* **24**, 3953–3961.
- LU, X., TUAN, H. Y., KORGEL, B. A. & XIA, Y. (2008). Facile synthesis of gold nanoparticles with narrow size distribution by using aucl or aubr as the precursor. *Chemistry - A European Journal* **14**(5), 1584–1591.
- LUO, Y. (2007). Preparation of mno<sub>2</sub> nanoparticles by directly mixing potassium permanganate and polyelectrolyte aqueous solutions. *Materials Letters* **61**(8), 1893–1895.
- MALETIN, Y., STRELKO, V., STRYZHAKOVA, N., ZELINSKY, S., ROZHENKO, A., GROMADSKY, D., VOLKOV, V., TYCHINA, S., GOZHENKO, O. & DROBNY, D. (2012). Carbon based electrochemical double layer capacitors of low internal resistance. *Energy and Environment Research* **3**(2), 156–165.
- MISNON, I. I., ZAIN, N. K. M., AZIZ, R. A., VIDYADHARAN, B. & JOSE, R. (2015). Electrochemical properties of carbon from oil palm kernel shell for high performance supercapacitors. *Electrochimica Acta* **147**, 78–86.
- MOURDIKOU DIS, S. & LIZ-MARZA, L. M. (2013). Oleylamine in nanoparticle synthesis. *Chem. Mater.* **25**, 1465–1476.
- MYSYK, R., RAYMUNDO-PINERO, E., PERNAK, J. & BEGUIN, F. (2009). Confinement of symmetric tetraalkylammonium ions in nanoporous carbon electrodes of electric double-layer capacitors. *The Journal of Physical Chemistry C* **113**(30), 13443–13449.

- NAVARRO-SUÁREZ, A. M., CARRETERO-GONZÁLEZ, J., RODDATIS, V., GOIKOLEA, E., SÉGALINI, J., REDONDO, E., ROJO, T. & MYSYK, R. (2014). Nanoporous carbons from natural lignin: study of structural-textural properties and application to organic-based supercapacitors. *RSC Advances* **4**(89), 48336–48343.
- NIU, J. J., PRESSER, V., KARWACKI, C. J. & GOGOTSI, Y. (2011). Ultrasmall gold nanoparticles with the size controlled by the pores of carbide-derived carbon. *Mater. Express* **1**(4), 259–266.
- PEDRO GONZÁLEZ, G. (2012). *Nanoestructuras de carbono: síntesis y caracterización estructural y electrónica*. Ph.D. thesis, Universidad Complutense de Madrid.
- PORTET, C., TABERNA, P. L., SIMON, P. & FLAHAUT, E. (2005). Influence of carbon nanotubes addition on carbon-carbon supercapacitor performances in organic electrolyte. *Journal of Power Sources* **139**, 371–378.
- QU, D., FENG, X., WEI, X., GUO, L., CAI, H., TANG, H. & XIE, Z. (2017). Synthesis of mno nano-particle@flourine doped carbon and its application in hybrid supercapacitor. *Applied Surface Science* **413**, 344–350.
- RAMADAN, M., ABDELLAH, A. M., MOHAMED, S. G. & ALLAM, N. K. (2018). 3d interconnected binder-free electrospun mno@c nanofibers for supercapacitor devices. *Scientific Reports* **8**(1), 7988.
- REDONDO, E., CARRETERO-GONZÁLEZ, J., GOIKOLEA, E., SÉGALINI, J. & MYSYK, R. (2015). Effect of pore texture on performance of activated carbon supercapacitor electrodes derived from olive pits. *Electrochim. Acta* **160**, 178–184.
- SÁNCHEZ-GONZÁLEZ, J., STOECKLI, F. & CENTENO, T. A. (2011). The role of the electric conductivity of carbons in the electrochemical capacitor performance. *Journal of Electroanalytical Chemistry* **657**, 176–180.
- SUGIMOTO, W., YOKOSHIMA, K., MURAKAMI, Y. & TAKASU, Y. (2006). Charge storage mechanism of nanostructured anhydrous and hydrous ruthenium-based oxides. *Electrochimica Acta* **52**(4), 1742–1748.
- SUHAS, CARROTT, P. & RIBEIRO CARROTT, M. (2007). Lignin-from natural adsorbent to activated carbon: A review. *Bioresource Technology* **98**(12), 2301–2312.
- THIAGARAJAN, S., TSAI, T. H. & CHEN, S.-M. (2011). Electrochemical fabrication of nano manganese oxidemodified electrode for the detection of h<sub>2</sub>o<sub>2</sub>. *Int. J. Electrochem. Sci.* **6**, 2235–2245.
- VASSILEV, S. V., BAXTER, D., ANDERSEN, L. K. & VASSILEVA, C. G. (2010). An overview of the chemical composition of biomass. *Fuel* **89**(5), 913–933.
- WANG, H., XU, Z., KOHANDEHGHAN, A., LI, Z., CUI, K., TAN, X., STEPHENSON, T. J., KING, C. K., HOLT, C. M. B., OLSEN, B. C., TAK, J. K., HARFIELD, D., ANYIA, A. O., MITLIN, D. & AL, W. E. T. (2013). Interconnected carbon nanosheets derived from hemp for ultrafast supercapacitors with high energy. *ACS Nano* **7**(6), 5131–41.

- WANG, Z., WEN, X.-D., HOFFMANN, R., SON, J. S., LI, R., FANG, C.-C., SMILGIES, D.-M. & HYEON, T. (2010). Reconstructing a solid-solid phase transformation pathway in cdse nanosheets with associated soft ligands. *Proceedings of the National Academy of Sciences* **107**(40), 17119–17124.
- WEI, L., SEVILLA, M., FUERTES, A. B., MOKAYA, R. & YUSHIN, G. (2011a). Hydrothermal carbonization of abundant renewable natural organic chemicals for high-performance supercapacitor electrodes. *Advanced Energy Materials* **1**(3), 356–361.
- WEI, L. & YUSHIN, G. (2012). Nanostructured activated carbons from natural precursors for electrical double layer capacitors. *Nano Energy* **1**(4), 552–565.
- WEI, W., CUI, X., WEIXINGCHEN & IVEY, D. G. (2011b). Manganese oxide-based materials as electrochemical supercapacitor electrodes. *Chem. Soc. Rev.* **40**(3), 1697–1721.
- WU, C., XIE, W., ZHANG, M., BAI, L., YANG, J. & XIE, Y. (2009). Environmentally friendly  $\gamma$ -mno<sub>2</sub> hexagon-based nanoarchitectures: Structural understanding and their energy-saving applications. *Chemistry European Journal* **15**(2), 492–500.
- XIA, Y., XIONG, Y., LIM, B. & SKRABALAK, S. E. (2009). Shape-controlled synthesis of metal nanocrystals: Simple chemistry meets complex physics? *Angewandte Chemie International Edition* **48**(1), 60–103.
- YANG, M., ZHONG, Y., ZHOU, X., REN, J., SU, L., WEI, J. & ZHOU, Z. (2014). Ultrasmall mno@n-rich carbon nanosheets for high-power asymmetric supercapacitors. *J. Mater. Chem. A* **2**(31), 12519–12525.
- YU, P., ZHANG, X., WANG, D., WANG, L. & MA, Y. (2009). Shape-controlled synthesis of 3d hierarchical mno<sub>2</sub> nanostructures for electrochemical supercapacitors. *Crystal Growth & Design* **9**(1), 528–533.
- ZHANG, L., CANDELARIA, S. L., TIAN, J., LI, Y., XIA HUANG, Y. & CAO, G. (2013). Copper nanocrystal modified activated carbon for supercapacitors with enhanced volumetric energy and power density. *Journal of Power Sources* **236**, 215–223.
- ZHANG, S. W. & CHEN, G. Z. (2008). Manganese oxide based materials for supercapacitors. *Energy Materials* **3**(3), 186–200.

## Chapter 6

# Carbon-Gold Nanograpes: A novel and tunable electrode nanomaterial for supercapacitor applications

As we learn in previous chapters, the control over the surface area and pore size in carbon materials is not an easy task. Template carbons represent one strategy to obtain carbon materials with controlled pore structure, where it can be customized in the mesoporous range (Centeno *et al.*, 2007; Tang *et al.*, 2016; Yan-su & Cheng-yang, 2010). This process involves several steps, such as template synthesis, infiltration of carbon precursors, carbonization treatment, and removal of the template, all of which increase relatively their production cost (Zhang *et al.*, 2009). The preparation of CDCs with micropores related to the carbide crystalline structure, which can even be tuned in a certain range as a function of the temperature (Gogotsi *et al.*, 2003), is another strategy to control the pore size of carbon materials, as well as the ODCs previously studied in the chapter 4 of this thesis. Nevertheless, CDC production entails again high costs associated with the metal carbide precursors. On the other hand, biomass-derived carbons are more suitable in terms of their cost and environmentally friendly precursors, but for these types of materials, the pore structure is often very heterogeneous and uncontrollable (Jung *et al.*, 2018). Glucose is an abundant and renewable material widely studied as a precursor for carbon nanostructures. This simple sugar can be polymerized by hydrothermal synthesis into polymerized glucose spheres (PGSs) of different sizes by controlling the temperature and reaction time (Li *et al.*, 2017, 2015; Sevilla & Fuertes, 2009a; Zhang *et al.*, 2015). In a subsequent carbonization step, the nanospheres maintain their original size, but an internal micropore

network is formed, albeit without any control over the process.

Another crucial property related to the applicability of carbon materials as electrodes in supercapacitors is their density. Normally, high surface area carbon materials are very lightweight and when they are processed into thin films during the manufacture of supercapacitor devices, a large fraction of the specific surface area is lost. For this reason, the calculation of the volumetric capacitance instead of the gravimetric capacitance is more convenient because the first considers the density of the material (Gogotsi & Simon, 2011).

## 6.1 Carbon-Gold Nanograpes

In this work, we have taken advantage of the ability of glucose to polymerize around metal nanoparticles through encapsulation during hydrothermal synthesis (Khan & MacLachlan, 2015; Sun & Li, 2004; Zhong *et al.*, 2008), producing a new core-shell carbonaceous material, described as Nanograpes (NGs). These are composed of PGSs with a few gold nanoparticles (AuNPs) present in their cores. After carbonization and chemical activation at 500 °C of NGs, composite material (Gr500, prepared at 500 °C) retained the same core-shell structure as the original NGs, while the PGSs carbonaceous polymer became disordered microporous carbon nanospheres (CNSs). Although it was expected that the Gr5 composite would have a lower gravimetric capacitance than CNSs (119 against 171 F g<sup>-1</sup> respectively), the volumetric capacitance reached values of 90 F cm<sup>-3</sup> in these more practical, denser composite. Similar than the volumetric capacitance value of 96 F cm<sup>-3</sup> reached by the CNSs.

Additionally, in order to improve the conductivity of the electrolyte through the micropores of the NGs material, a new composite material denoted as Gr700 (NGs prepared at 700 °C) was also synthesized at a higher carbonization temperature. In contrast to Gr500, the Gr700 material did not maintain the NG core-shell structure. The AuNPs were found to have melted and then flowed out of the spheres, reconditioning the micropore structure of the NG material and recrystallizing at the surface. This resulted in the generation of an improved micropore size distribution that was found to enhance ion diffusion, thus increasing the volumetric capacitance to ca. 115 F cm<sup>-3</sup> in aqueous acidic solutions. It is possible that the recrystallized AuNPs, now found on the outer surface of the carbon NGs, may improve the electrical conductivity through the carbon layer, thus retaining or even improving the characteristics of these supercapacitors at high power densities

(Zhang *et al.*, 2013).

## Synthesis

### *AuNPs*

AuNPs were synthesized following the classical method described by Enüstüna and Turkevich (Enüstün & Turkevich, 1963). A 500 mL aqueous solution of 0.4 mM HAuCl<sub>4</sub> (>99.9%, Sigma-Aldrich) was heated to boiling in a 1 L flask. Then, a second 20 mL aqueous solution of 1 wt% sodium citrate (>99.9%, Sigma-Aldrich) was quickly added under vigorous stirring. The mixture was kept boiling for 10 min until the color changed to red. Then, at room temperature (RT), the mixture was centrifuged (6500 rpm, 90 min) to remove the excess sodium citrate and the precipitate was redispersed and concentrated in water several times. When the concentration of nanoparticles reached 10 mM, 1.7 mg of poly(ethylene glycol) methyl ether thiol (PEG Thiol-6000, Sigma-Aldrich) was added to the solution in a proportion of four molecules per 1 nm<sup>2</sup> of nanoparticle surface area in order to replace the surfactant under stirring overnight. The AuNPs were centrifuged again (1200 rpm, 90 min) to remove any excess surfactant.

### *Nanograpes*

NGs were prepared by hydrothermal synthesis. D-(+)-Glucose (1 mM, >99.5%, Sigma-Aldrich) was dissolved in a 10 mL water dispersion of the above AuNPs (0.5 mM). The mixture was then transferred to a stainless steel autoclave and heated up to 150°C for 20 h. The resulting product was washed with water and collected by centrifugation. Polymeric glucose spheres (PGSs) were also synthesized with the same procedure without AuNPs and heating to 180°C for 6 h.

The obtained NG and PGS carbonaceous materials were placed in a quartz crucible and heated at 500°C (PGSs and NGs) or 700°C (only NGs) during 1 h in a tubular furnace under argon atmosphere. After the carbonization process, heating was turned on and the system was cooled down to RT. The carbon materials obtained from the previous stage were chemically activated with KOH. The weight ratio of carbon to KOH (>84.0% pellets, EMPLURA) was 1:4. Then, the two materials were ground in an agate mortar until an homogeneous mixture was obtained, which was placed in an aluminum oxide crucible, followed by thermal activation in a tubular furnace under argon atmosphere for 60 min at 500°C. After said activation time, the heating was turned off and the system was cooled down to



25°C. The activated carbon was washed with water and dried in a furnace at 110°C overnight. The samples obtained from NGs are labeled as Gr5 (NGs prepared at 500°C) and Gr7 (NGs prepared at 700°C), while the carbon obtained from PGSs is denoted as carbon nanospheres (CNSs).

## Structural Characterization

Glucose-derived carbon materials can be easily nanostructured, since glucose is readily transformed into solid carbonaceous spheres by polymerization during hydrothermal synthesis. The temperature and reaction time are key factors to control the size of the resulting polymerized glucose spheres (PGSs). The PGS synthesis involves the balance between formation and growth of carbon nuclei simultaneously. The higher the temperature, the greater the number of nuclei formed, with

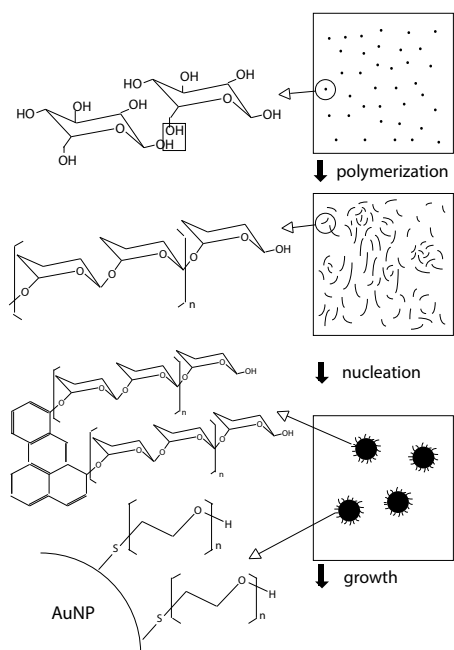


Figure 6.1: Schematic nuclei formation and growth of the polymerized glucose spheres (PGSs) over carbon and PEG-functionalized AuNP cores.

each sphere growing only slowly, thus resulting in carbonaceous material that is composed of many small spheres. In contrast, low temperature synthesis results in the formation of fewer nuclei and favored growth, producing carbonaceous material that is represented by a few large spheres.

The size of the PGSs can also be modulated with the reaction time; in general, the longer the reaction time, the larger the spheres. Glucose polymerization starts with dehydration reactions between the OH groups, forming large hydrophilic chains, which subsequently condense into hydrophobic cores retaining a hydrophilic shell that allows for continuous growth (Li *et al.*, 2011; Sevilla & Fuertes, 2009b), as shown in Figure 6.1. Poly(ethylene glycol) methyl ether thiol (PEG-SH) was chosen as the surfactant polymer to enhance the stabilization of the AuNPs in aqueous solution, as well as to ensure good interactions with glucose, since PEG has been studied for their molecular aggregation, drug encapsulation, and drug release behavior as sugar-PEG-based polymeric architectures (Bhatia *et al.*, 2011). The incorpora-

tion of these PEG-functionalized AuNPs during the hydrothermal synthesis results in the addition of formed cores in the synthesis medium that allow the polymerization of glucose around them, in a similar way than glucose grow over its own core in its polymerization (see Figure 6.1).

In this work, assuming that the AuNPs will be the nuclei of the spheres, a very low temperature of 150 °C compared to that of conventional PGS hydrothermal synthesis was chosen, in addition to a very long reaction time (20 h) in order to suppress the formation of new carbon cores. The SEM micrographs on Figure 6.2 show the obtained NG material as a core-shell composite, consisting of carbonaceous spheres of about 150 nm of diameter with a few AuNPs of 15 nm in diameter at their core. Also, PGSs of the same size without AuNPs were synthesized at a higher temperatures but using shorter reaction times (180 °C for 6 h) for comparison purposes.

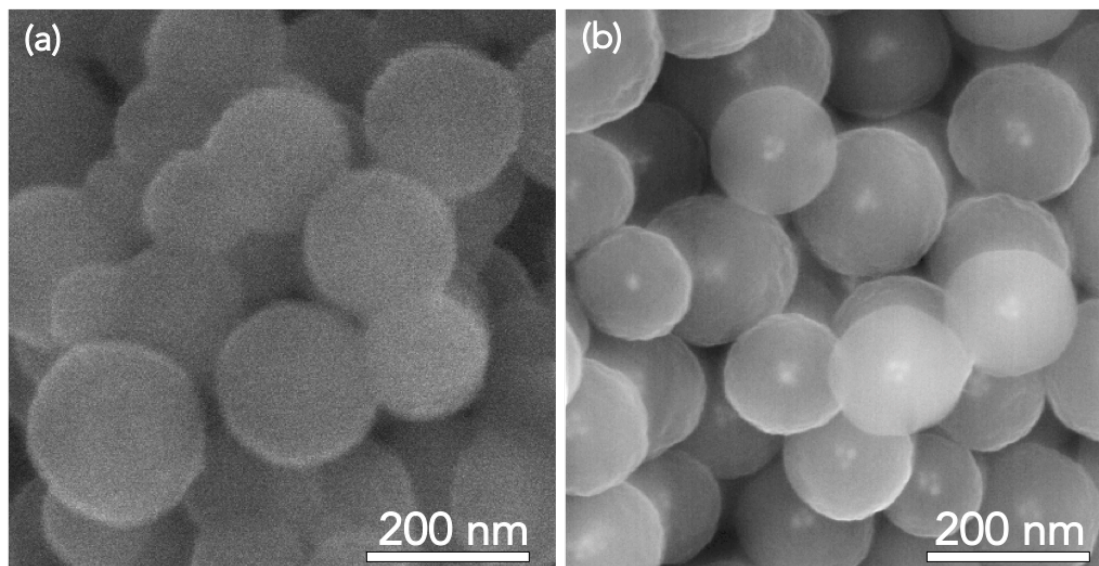


Figure 6.2: Schematic nuclei formation and growth of the polymerized glucose spheres (PGSs) over carbon cores and the mimetic PEG-functionalized AuNP cores.

Assuming that the AuNPs will be the nuclei of the spheres, a very low temperature of 150°C compared to that of conventional PGS hydrothermal synthesis was chosen, addition to a very long reaction time (20 h) in order to suppress the formation of new carbon cores. The SEM micrographs on Figure 6.2 show the obtained NG material as a core-shell composite formed by carbonaceous spheres of about 150 nm of diameter with a few AuNPs of 15 nm in diameter at their

core. Also, PGSs of the same size without AuNPs were synthesized at a higher temperature but shorter reaction time (180°C for 6 h) for comparison purposes.

Normalized infrared spectra provided information on the evolution of the functional groups during the chemical transformations that take place during the polymerization, carbonization and chemical activations processes. PGSs and NGs give very similar spectra but these are quite different from those of their glucose precursors. The main difference is the emergence of a band at 1620  $\text{cm}^{-1}$ , which can be assigned to C=C vibrations from the aromatic rings, as well as the band at 1710  $\text{cm}^{-1}$ , which is assigned to the C=O vibrations corresponding to the carbonyl, quinone, ester, or carboxyl groups that remain inside the nanospheres. The presence of aromatic groups in the PGSs and NGs nanomaterials is also confirmed by the vibration bands seen at 875-750  $\text{cm}^{-1}$ , assigned to aromatic out-of-plane C-H bending vibrations, the bands at 3000-2815  $\text{cm}^{-1}$ , which correspond to stretching vibrations of aliphatic C-H groups, as well as the broad band at 3000-3700  $\text{cm}^{-1}$ , attributed to O-H stretching vibration of the hydroxyl or carboxyl groups, thus confirming the presence of oxygen groups (Sevilla & Fuertes, 2009b). In contrast, in the carbonized and activated samples, the intensity of these bands is significantly reduced in the case of the CNSs, indicating that fewer of these functional groups are present (Zheng *et al.*, 2014). Samples Gr5 and Gr7 still exhibit the bands assigned to aromatic rings, with a less pronounced content of oxygen groups in sample Gr7.

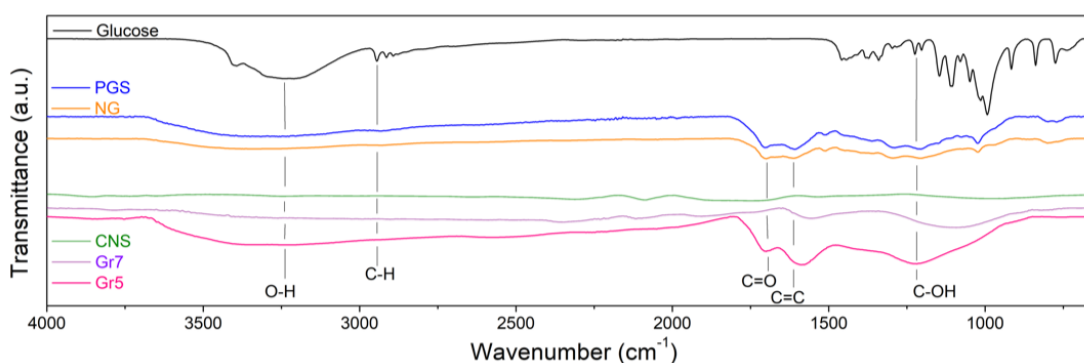


Figure 6.3: FTIR spectra of glucose, PGSs, NGs, CNSs, Gr5, and Gr7.

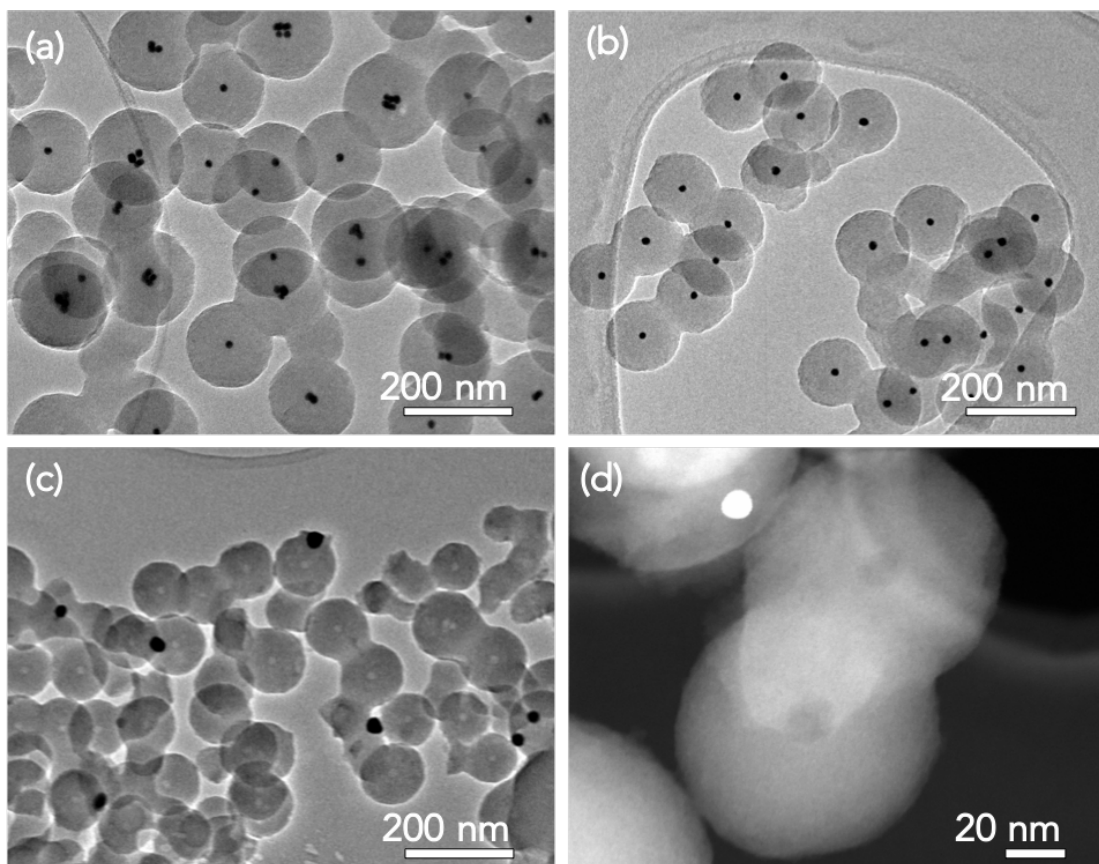


Figure 6.4: TEM micrographs of (a) the CNSs, which retain the original spherical shape, with a 150 nm  $\varnothing$ , (b) the Gr5 composite material composed of carbon spheres with AuNPs at their core, (c) the Gr7 composite material formed from the carbon spheres with a hollow core, containing Au NPs at some surfaces, and (d) a HAADF-STEM image of Gr7, showing the Au NPs at the particle surfaces and the absence of significant Au residue in the inner pores.

After the carbonization and activation processes, the CNSs and Gr5 retain the spherical shape of their respective precursors (Figures 6.4a and 6.4b). Gr7 also conserves a spherical shape, but with the AuNPs located on the outer surface instead of in the core (Figure 6.4c). Moreover, the AuNPs are larger than the pristine nanoparticles of the precursor, which may indicate that they undergo fusion during the carbonization process.

The HAADF-STEM micrograph (Figure 6.4d) of the Gr7 sample clearly shows that the AuNPs not only leave a void in the sphere core but also that no residual

Au remains in the internal pores. However, in-situ TEM experiments showed that, upon heating the NGs up to the synthesis temperature of Gr7, the AuNPs started to melt and mix with the rest of the core nanoparticles, flowing through the microporous structure to the outer surface (Figure 6.5). Based on this scenario, gold from neighboring spheres may also mix, producing larger nanoparticles, in accordance with the observations seen for Gr7 (Figure 6.4 c and d).

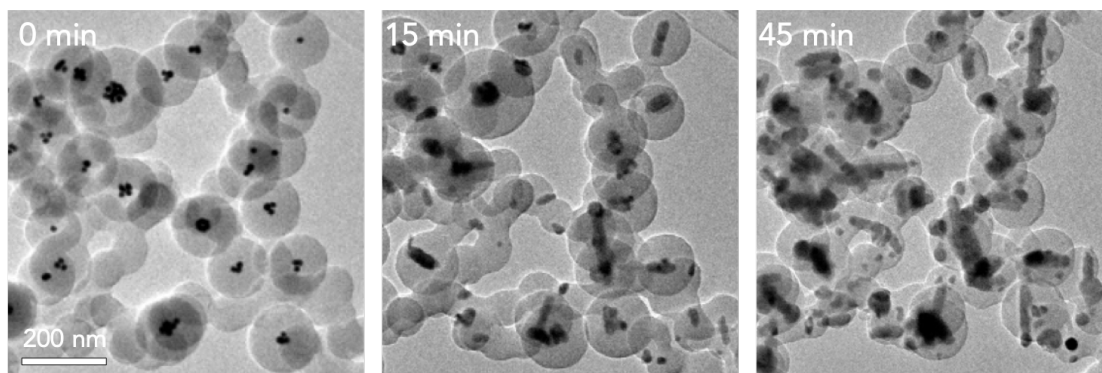


Figure 6.5: TEM micrographs of the nanostructures obtained after increasing times of in-situ heating, where the AuNPs appear to melt and then flow through the microporous structure out of the spheres, where they recrystallize on the outer surface.

After these in-situ experiments, the obtained carbon spheres were seen to contain some residual gold in both the inner pores, the outer surface and the sphere cores, contrary to what was seen for the material obtained in the furnace, suggesting that factors such as the gas flow rate and heating ramp rate used for the carbonization process play an important role in this flow-out mechanism. To understand this more fully, this would require further research, but at this point, it represents a starting point for the control of AuNP diffusion with these carbon nanomaterials, which may enable the tunability of the pore structure of these type of materials.

## Textural Characterization

$N_2$  adsorption isotherms were recorded to determine the specific surface area ( $S_{BET}$ ) of each material, as well as their PSD (Figure 6.6), which are key factors for efficient electrode materials in supercapacitors. All of the isotherms of the carbonized and chemically activated materials exhibit a Type I shape, characteristic of microporous solids (Rouquerol *et al.*, 2013), except for the NG carbonaceous

material, where no  $N_2$  absorption was observed at relatively low pressures. The low  $S_{\text{BET}}$  value of  $23 \text{ m}^2 \text{ g}^{-1}$  for the NGs also indicates the absence of micropores, and thus the surface between the spheres must contribute the majority surface area to  $S_{\text{BET}}$ . The CNS material exhibits a  $S_{\text{BET}}$  of  $720 \text{ m}^2 \text{ g}^{-1}$  and has a PSD with a main contribution centered at  $0.56 \text{ nm}$ , in addition to a minor wider contribution from  $1$  to  $1.5 \text{ nm}$ . The Gr5 composite presents a  $S_{\text{BET}}$  of  $515 \text{ m}^2 \text{ g}^{-1}$ , smaller than that of the CNSs, likely due to the solid core present in the spheres. The PSD is analogous to that of the CNS material, indicating that the AuNPs do not influence the porous structure after carbonization and chemical activation at  $500 \text{ }^\circ\text{C}$ .

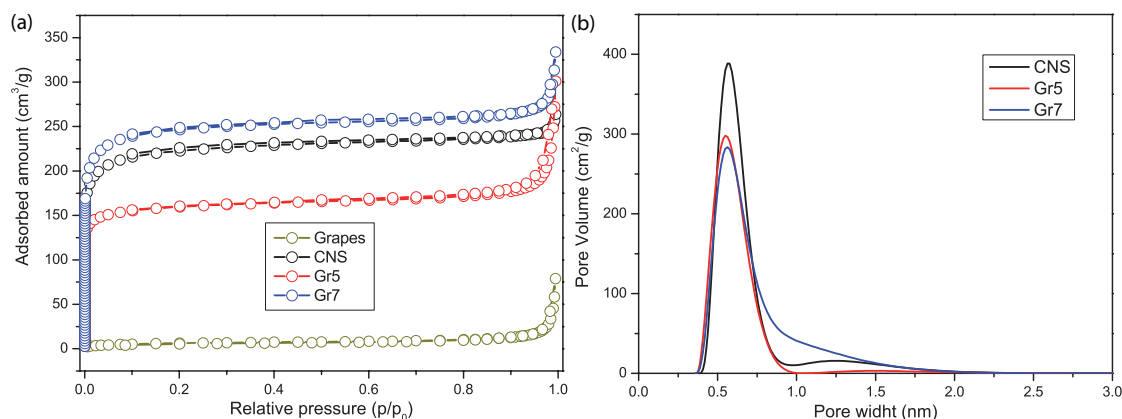


Figure 6.6: (a) Type I  $N_2$  adsorption isotherms for the NG, CNS, Gr5, and Gr7 materials and (b) their PSDs, showing that the main contribution is centered at  $0.56 \text{ nm}$  and revealing minor contributions from  $1$  to  $1.5 \text{ nm}$ , including the broad shoulder unifying both contributions in the case of the Gr7 composite.

	$S_{\text{Total BET}}$ ( $\text{m}^2/\text{g}$ )	$S_{\text{Ext. BET}}$ ( $\text{m}^2/\text{g}$ )	$S_{\text{Micr. BET}}$ ( $\text{m}^2/\text{g}$ )	Pore Width $_{2\text{D-NLDFT}}$ ( $\text{nm}$ )
Grapes	23	8	15	-
CNS	720	26	694	0.56 & 1.24
Gr5	515	25	490	0.55
Gr7	797	23	773	0.56

Table 6.1: Total, exterior and micropore BET surface area and pore width of prepared samples.

For the Gr7 composite,  $S_{\text{BET}}$  increases to  $797 \text{ m}^2 \text{ g}^{-1}$ , higher than that of the CNSs, owing to the hollow space left behind after the AuNPs have left the core of the spheres. Although the main contribution to the PSD in the Gr7 composite is also centered at  $0.56 \text{ nm}$ , in contrast to the above materials, a wide shoulder

unifying bigger porous sizes of up to 1.5 nm is observed. The AuNP flow-out process modifies the pore structure of the material, inducing better interconnectivity between the existing pores.

## Electrochemical characterization

The materials were first tested by cyclic voltammetry (CV) using a three-electrode cell, as shown in 6.7a. The CVs for both the CNS and Gr5 electrode materials exhibit a quasi-rectangle shape with only small peaks centered at 0.45 V, typical for carbon-based supercapacitors. High capacitance values of up to 191 and 205  $\text{F g}^{-1}$  are obtained at a scan rate of  $5 \text{ mV s}^{-1}$  for CNS and GR5, respectively. The Gr7 material achieved a value of  $436 \text{ F g}^{-1}$  at the same sweep rate (Figure 6.7a), with more pronounced redox peaks centered at around 0.5 V, which are typically assigned to the pseudo-capacitive redox activity of the oxygen functional groups anchored on the surface of the carbon material (He, 2018). Since polymerized glucose is the precursor material for PGSs and NGs, it is not surprising to find an abundance of oxygen groups on the CNS, Gr5 and Gr7 surfaces at sites that are accessible to the electrolyte.

Additionally, the Gr7 material is shown to lose only 47% of the capacitance when cycled at  $200 \text{ mV s}^{-1}$  (Figure 6.7b), while CNSs and Gr5 lost approximately 71 and 70%, respectively, of their capacitance at  $50 \text{ mV s}^{-1}$ . This indicates that the pore structure obtained in the Gr7 material allows faster ion diffusion, perhaps consistent with the larger CV charges passed in the CV in Figure 6.7a. That could be due to the modify pore structure in this composite. The wide shoulder up to 1.5 nm in its pore size distribution (Figure 6.6b) favor the ion diffusion along the active surface area.

The high gravimetric capacitance values evidenced in the three-electrode experiments (Figure 6.7) prompted us to process the materials as thin films and perform a second electrochemical characterization in a two-electrode Swagelok-type cell in a symmetrical configuration. This was done in order to calculate the volumetric capacitance from galvanostatic measurements, giving a more reliable capacitance value in terms of applicability (Gogotsi & Simon, 2011). CVs performed (Figure 6.8a) again show a significantly higher current response for the Gr7 composite material in comparison with the CNS and Gr5 electrode materials. The Gr7 composite exhibited a quasi-rectangle CV shape with pseudo-capacitance features at lower potentials than in the 3 electrode measurements. It is also notable that the CNS and Gr5 materials give a more tilted CV, which may indicate that they are



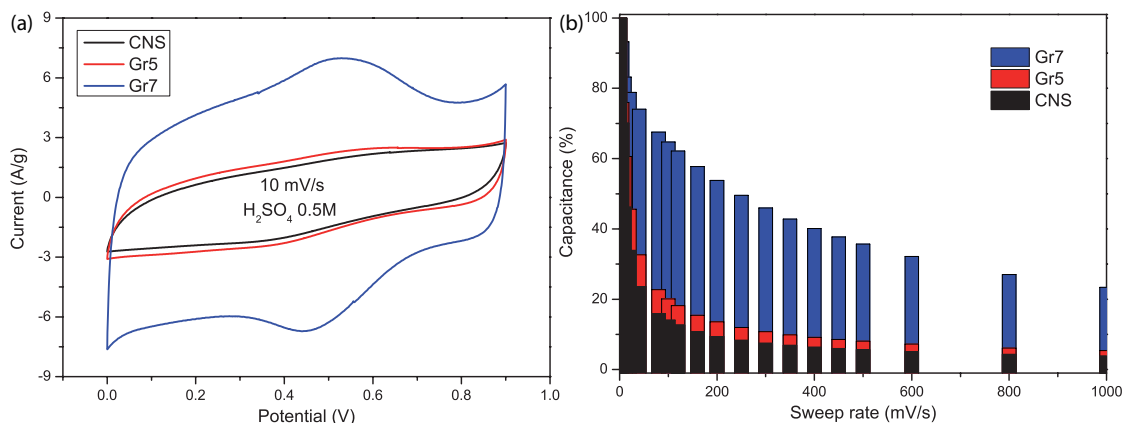


Figure 6.7: (a) The cyclic voltammograms of the CNS, Gr5, and Gr7 materials were performed at  $5 \text{ mV s}^{-1}$  by using a glassy carbon rod as the working electrode (WE), a reversible hydrogen electrode (RHE) as the reference electrode, and platinumized platinum as the counter electrode (CE) in a three-electrode cell configuration. The electrolyte used was deaerated  $0.5 \text{ M H}_2\text{SO}_4$  in deionized water. (b) Capacitance retention of each material with increasing sweep rate.

more resistive materials.

The capacitance values obtained from the galvanostatic charge-discharge curves (Figure 6.8b) show that the Gr7 composite gives the highest gravimetric and volumetric capacitance ( $210 \text{ F g}^{-1}$  and  $114 \text{ F cm}^{-3}$ ) in comparison with the CNS ( $170 \text{ F g}^{-1}$  and  $96 \text{ F cm}^{-3}$ ) and the Gr5 ( $118 \text{ F g}^{-1}$  and  $89 \text{ F cm}^{-3}$ ) materials at  $0.1 \text{ A g}^{-1}$ . These values are higher than seen for carbon spheres in aqueous electrolytes (Zhang *et al.*, 2014; Zhou *et al.*, 2018), showing the superior electrochemical behavior of the Gr7 material in supercapacitive applications, likely as the pore size ( $0.56 - 1.50 \text{ nm}$ ) allows for facile transport of the protons in solution (Li *et al.*, 2011; Zheng *et al.*, 2014). In addition, the high ohmic drop for the CNS and Gr5 materials argues for a lower electrical conductivity of their carbon matrices in comparison with the Gr7 composite material. This is also observed in Figure 6.8b inset, where the capacitance quickly drops to 0% for the CNS and Gr5 materials, meanwhile is better retained for the Gr7 composite.

The impedance analysis of the three materials (Figure 6.8c) allows the calculation of their ESR-define values. While CNS and Gr5 materials show a similar charge transfer resistance with at least two large semicircles and ESR values of 179 and 285 Ohms, respectively, the Gr7 composite exhibits a lower ESR value of 34 Ohms. This clearly shows that Gr7 is the optimum material for use as an electrode in supercapacitors. It should be noted that the vertical response at low frequencies



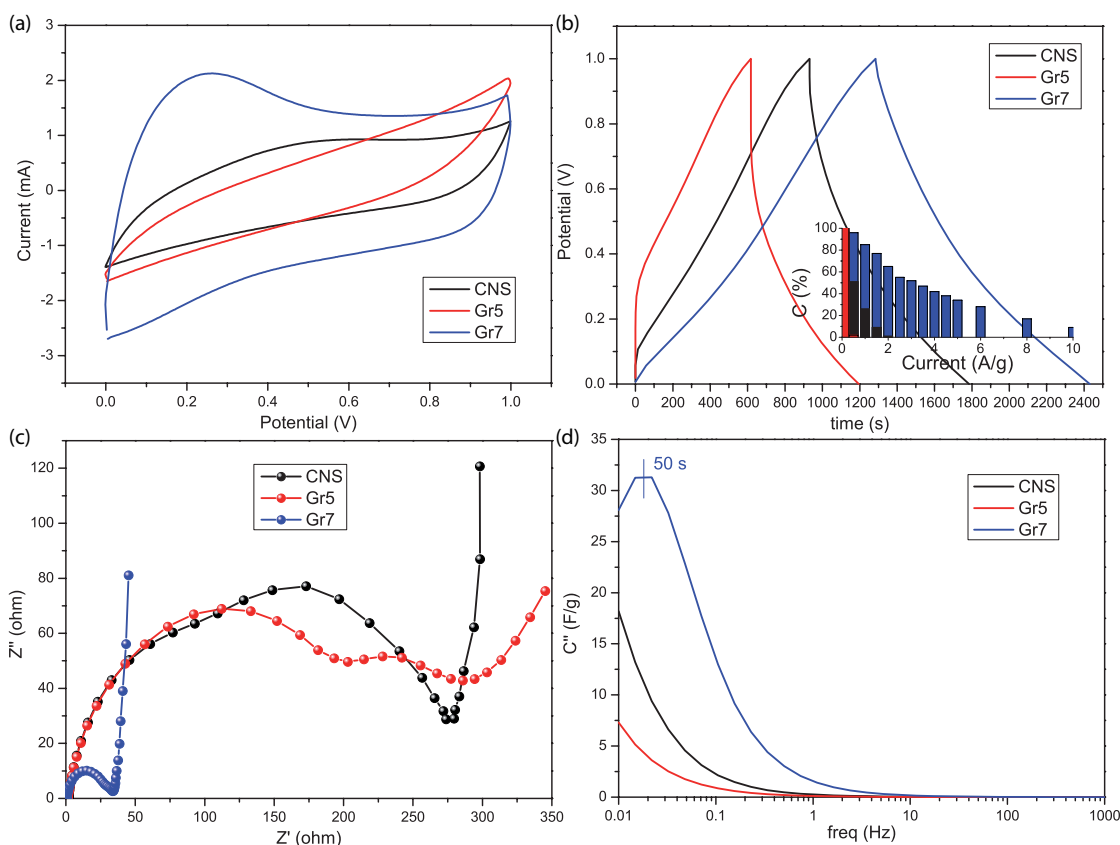


Figure 6.8: (a) Two-electrode Swagelok-type cell cyclic voltammograms at 5 mV s<sup>-1</sup>, (b) galvanostatic charge-discharge at 0.1 mA g<sup>-1</sup>, (c) Nyquist plots, and (d) Complex impedance plots for the imaginary (C'') part of the complex capacitance for the CNS, Gr5, and Gr7 materials in deaerated 0.5 M H<sub>2</sub>SO<sub>4</sub> electrolyte.

is typical of the capacitance of carbon materials (Danoglidis *et al.*, 2019), while the semi-circles reflect the double layer charging process combined with trace redox processes.

The complex impedance plot (Figure 6.8d) show the imaginary (C'') part of the complex capacitance (Taberna *et al.*, 2003). The relaxation time constant of the systems, which is the maximum in the imaginary part, reached values of up to 50 s for the Gr7 composite. However, for the CNS and Gr5 materials, the time constants cannot be calculated because these two materials are quite slow in terms of their electrochemistry such that the maximum lies at a frequency below 10-2 Hz.

## Conclusions

By controlling the temperature and reaction time of the hydrothermal synthesis of glucose polymerization spheres with gold nanoparticles, a new carbonaceous core-shell nanomaterial, denoted as nanograpes, was successfully synthesized. The density of the equivalent carbon spheres was enhanced as well as their electric conductivity due to the inclusion of AuNP. Nanospheres and nanograpes prepared at 500°C showed high gravimetric capacitance on a three-electrode cell of up to 205 F g<sup>-1</sup> at 5 mV s<sup>-1</sup>, but the sample carbonized at 700°C doubled that capacitance value (436 F g<sup>-1</sup>). At such high carbonization temperature, the gold nanoparticles start to melt and flow out of the core of the grapes, creating a more suitable pore structure for ion diffusion as it was evidenced by electrochemical impedance spectroscopy. The Gr7 sample showed the highest capacitance values on a symmetrical two-electrode cell with a gravimetric capacitance of 210 F g<sup>-1</sup> and high volumetric capacitance of up to 114 F cm<sup>-3</sup>.

## Bibliography

- BHATIA, S., MOHR, A., MATHUR, D., PARMAR, V. S., HAAG, R. & PRASAD, A. K. (2011). Biocatalytic route to sugar-peg-based polymers for drug delivery applications. *Biomacromolecules* **12**, 3487–3498.
- CENTENO, T. A., FUERTES, A. B. & STOECKLI, F. (2007). Performance of templated mesoporous carbons in supercapacitors. *Electrochim. Acta* **52**, 3207–3215.
- DANOGLIDIS, P. A., KONSTA-GDOUTOS, M. S. & SHAH, S. P. (2019). Relationship between the carbon nanotube dispersion state, electrochemical impedance and capacitance and mechanical properties of percolative nanoreinforced opc mortars. *Carbon* **145**, 218–228.
- ENÜSTÜN, B. V. & TURKEVICH, J. (1963). Coagulation of colloidal gold. *J. Am. Chem. Soc.* **85**(21), 3317–3328.
- GOGOTSI, Y., NIKITIN, A., YE, H., ZHOU, W., FISCHER, J. E., YI, B., FOLEY, H. C. & BARSOUM, M. W. (2003). Nanoporous carbide-derived carbon with tunable pore size. *Nature Materials* **2**, 591.
- GOGOTSI, Y. & SIMON, P. (2011). True performance metrics in electrochemical energy storage. *Science* **334**(6058), 917–918.
- HE, Y.-T. (2018). Capacitive mechanism of oxygen functional groups on carbon surface in supercapacitors yi-tao he. *Electrochim. Acta* **282**, 618–625.
- JUNG, S., MYUNG, Y., KIM, B. N., KIM, I. G., YOU, I.-K. & KIM, T. (2018). Activated Biomass-derived Graphene-based Carbons for Supercapacitors with High Energy and Power Density. *Sci. Rep.* **8**, 1915.

- KHAN, M. K. & MACLACHLAN, M. J. (2015). Polymer and carbon spheres with an embedded shell of plasmonic gold nanoparticles. *ACS Macro Letters* **4**(12), 1351–1355.
- LI, M., LI, W. & LIU, S. (2011). Hydrothermal synthesis, characterization, and koh activation of carbon spheres from glucose. *Carbohydr. Res.* **346**(8), 999–1004.
- LI, S., LIANG, F., WANG, J., ZHANG, H. & ZHANG, S. (2017). Preparation of mono-dispersed carbonaceous spheres via a hydrothermal process. *Adv. Powder Technol.* **28**(10), 2648–2657.
- LI, Z., LI, D., LIU, Z., LI, B., GE, C. & FANG, Y. (2015). Mesoporous carbon microspheres with high capacitive performances for supercapacitors. *Electrochim. Acta* **158**, 237–245.
- ROUQUEROL, J., ROUQUEROL, F., LLEWELLYN, P., MAURIN, G. & SING, K. (2013). *Adsorption by powders and porous solids*. Academic Press.
- SEVILLA, M. & FUERTES, A. (2009a). The production of carbon materials by hydrothermal carbonization of cellulose. *Carbon N. Y.* **47**(9), 2281–2289.
- SEVILLA, M. & FUERTES, A. B. (2009b). Chemical and structural properties of carbonaceous products obtained by hydrothermal carbonization of saccharides. *Chem. Eur. J.* **15**, 4195–4203.
- SUN, X. & LI, Y. (2004). Colloidal carbon spheres and their core/shell structures with noble-metal nanoparticles. *Angewandte Chemie International Edition* **43**(5), 597–601.
- TABERNA, P., SIMON, P. & FAUVARQUE, J. (2003). Electrochemical characteristics and impedance spectroscopy studies of carbon-carbon supercapacitors. *Journal of The Electrochemical Society* **150**(3), A292–A300.
- TANG, D., HU, S., DAI, F., YI, R., GORDIN, M. L., CHEN, S., SONG, J. & WANG, D. (2016). Self-templated synthesis of mesoporous carbon from carbon tetrachloride precursor for supercapacitor electrodes. *ACS Appl. Mater. Interfaces* **8**(11), 6779–6783.
- YAN-SU, W. & CHENG-YANG, W. (2010). Templated mesoporous carbons and their performance for electric double layer capacitors. *New Carbon Mater.* **25**(5), 376–381.
- ZHANG, C., HATZELL, K. B., BOOTA, M., DYATKIN, B., BEIDAGHI, M., LONG, D., QIAO, W., KUMBUR, E. C. & GOGOTSI, Y. (2014). Highly porous carbon spheres for electrochemical capacitors and capacitive flowable suspension electrodes. *Carbon* **77**, 155–164.
- ZHANG, L., CANDELARIA, S. L., TIAN, J., LI, Y., XIA HUANG, Y. & CAO, G. (2013). Copper nanocrystal modified activated carbon for supercapacitors with enhanced volumetric energy and power density. *Journal of Power Sources* **236**, 215–223.
- ZHANG, L. L., ZHOU, R. & ZHAO, X. S. (2009). Carbon-based materials as supercapacitor electrodes. *J. Mater. Chem.* **38**(29), 2520–2531.
- ZHANG, P., QIAO, Z.-A. & DAI, S. (2015). Recent advances in carbon nanospheres: synthetic routes and applications. *Chem. Commun.* **51**, 9246–9256.

- ZHENG, X., LV, W., TAO, Y., SHAO, J., ZHANG, C., LIU, D., LUO, J., WANG, D. W. & YANG, Q. H. (2014). Oriented and interlinked porous carbon nanosheets with an extraordinary capacitive performance. *Chem. Mater.* **26**(23), 6896–6903.
- ZHONG, Z., SIM, D., TEO, J., LUO, J., ZHANG, H. & GEDANKEN, A. (2008). d-glucose-derived polymer intermediates as templates for the synthesis of ultrastable and redispersible gold colloids. *Langmuir* **24**(9), 4655–4660.
- ZHOU, B., MENG, E. & CHEN, Z. (2018). Synthesis of porous carbon sphere based on starch and its application of electric double layer capacitor. *J. Electrochem. Sci.* **13**, 2441–2447.



# Chapter 7

## Summary and Conclusions

In the present thesis have been presented different approaches aimed to the obtention of new composite materials with improved electrochemical performance for their use as electrodes in supercapacitors devices. Initially, a novel and straightforward synthetic route has been established for the obtention of composite materials made of high specific surface area carbon materials with embebed metal-oxide nanoparticles by the chlorination of organometallic compounds at intermediate temperatures, followed by the hydrothermal conversion of the by-product, composed of metal chloride nanoparticles embedded in a carbon matrix. By this way, micro and mesoporous carbons, containing a fine dispersion of either NiO or Mn<sub>3</sub>O<sub>4</sub> nanoparticles, denoted as **ODC@NiO** and **ODC@Mn<sub>3</sub>O<sub>4</sub>** respectively, have been successfully synthetized from their respective Ni(C<sub>6</sub>H<sub>6</sub>) and Mn(C<sub>5</sub>H<sub>7</sub>O<sub>2</sub>)<sub>2</sub> precursors. The success of the proposed procedure has been demonstrated imaging of the ODC@NiO and ODC@Mn<sub>3</sub>O<sub>4</sub> composites and their respective intermediates, ODC@NiCl<sub>2</sub> and ODC@MnCl<sub>2</sub>, by transmission electron microscopy. This revealed the retention of the shape and microstructure of the carbon matrix, consisting of highly entangled and corrugated carbon foils and large solid spheres, decorated with smaller hollow spheres. Electrochemical studies in a three-electrodes configuration demonstrated an improvement in the electrochemical properties of these new composites in comparison with the porous carbons obtained by chlorination of it precursor at 900°C in the case of the ODC@NiO, increasing the gravimetric capacitance from 47 to 85 F g<sup>-1</sup>; and in comparison with similar composite materials obtained at lower temperature synthesis in the case of the ODC@Mn<sub>3</sub>O<sub>4</sub>, from 14 to 101 F g<sup>-1</sup> in 1M NaOH electrolyte. In addition, the differences in the microstructure of the carbon component, the porous architecture developed as well as the better electronic conductivity of Mn<sub>3</sub>O<sub>4</sub>, are the likely reasons for the supe-

rior electrochemical performance of ODC@Mn<sub>3</sub>O<sub>4</sub> in the symmetrical cell, where capacitance values up to 130 F g<sup>-1</sup> and 58 F cm<sup>-3</sup> were obtained. This study has clearly shown that, depending on the nature of the organic ligand linked to the metal of the organometallic precursor, the final microstructure as well as the textural properties of the carbon component varies significantly. Therefore, since the number of possible organometallic precursors is extremely large and many of them are commercially available, the present results are very promising. This is because this method could lead to the synthesis of a wide range of porous carbon@metal oxide nanoparticle composites for use in the next generation of electrode materials for electrochemical energy storage applications.

As Mn<sub>3</sub>O<sub>4</sub> nanoparticles provide the best result as pseudocapacitive material in the previous composites, boosted us to the creation of similar composite materials by the inclusion of manganese oxide (MnO<sub>x</sub>) nanoparticles in a higher specific surface area materials such as lignocellulosic activated carbons. Thus an activated nanoporous carbon from Galician walnut shells (*Guadua Angustifolia*) and ultrasmall MnO<sub>x</sub> nanoparticles have been synthesized and mixed to form the **WAC@MnO<sub>x</sub>** composite. STEM-HAADF images in conjunction with EDS analysis demonstrate the inclusion of MnO<sub>x</sub> within the carbon matrix as well as the improved electrochemical performance of the composite, reaching gravimetric capacitance values up to 207 F g<sup>-1</sup>, and especially in the dramatic decrease of the ESR value. With a focus on reducing the ESR value of these not much conductive lignocellulosic activated carbons, gold nanoparticles (AuNPs) arise as an ideal material for enhance the electrical conductivity of these composites. In this case, an activated nanoporous carbon from Bamboo (*Juglans regia*) filled with AuNPs has successfully synthesized. The **BAC@AuNPs** composite material display a high volumetric capacitance up to 47 F cm<sup>-3</sup>, due to the increased density given by AuNPs, and a reduction of the ESR value of one order of magnitude.

In order to keep such improvements without reduce the specific surface area of the carbon material the challenge became the synthesis of similar carbon@AuNP with AuNPs relocated outside the surface. A nanostructured composite material composed of spheres of few AuNPs surrounded by a microporous disordered carbon shell was successfully synthesized. The volumetric capacitance and its electric conductivity were enhanced avoiding the reduction on the active specific surface area. Furthermore, for the sample carbonized at 700°C, **Gr7**, TEM in-situ temperature experiment demonstrate that the gold nanoparticles start to melt and flow out of the core of the spheres, creating a more suitable pore structure for ion diffusion, evidenced by the highest gravimetric and volumetric capacitance values of this thesis (210 g<sup>-1</sup> and F cm<sup>-3</sup>).

The state of the art of this thesis can also be seen in the modified Ragone plot of figure 7.1. Taking as reference the same Ragone plot explained in the Introduction chapter (Simon & Gogotsi, 2008), it can be affirmed that the main purpose of this work, which consist in the increase of the specific energy of supercapacitors devices, has been achieved. Except for the BAC@AuNPs, who has a very low specific surface area, all the composite materials syntetized present higher values of specific energy than current supercapacitors. Among which it is worth mentioning the composites with  $\text{MnO}_x$  nanoparticles, ODC@ $\text{Mn}_3\text{O}_4$  and WAC@ $\text{MnMnO}_x$ , which retains also high specific energy values ant higher specific power.

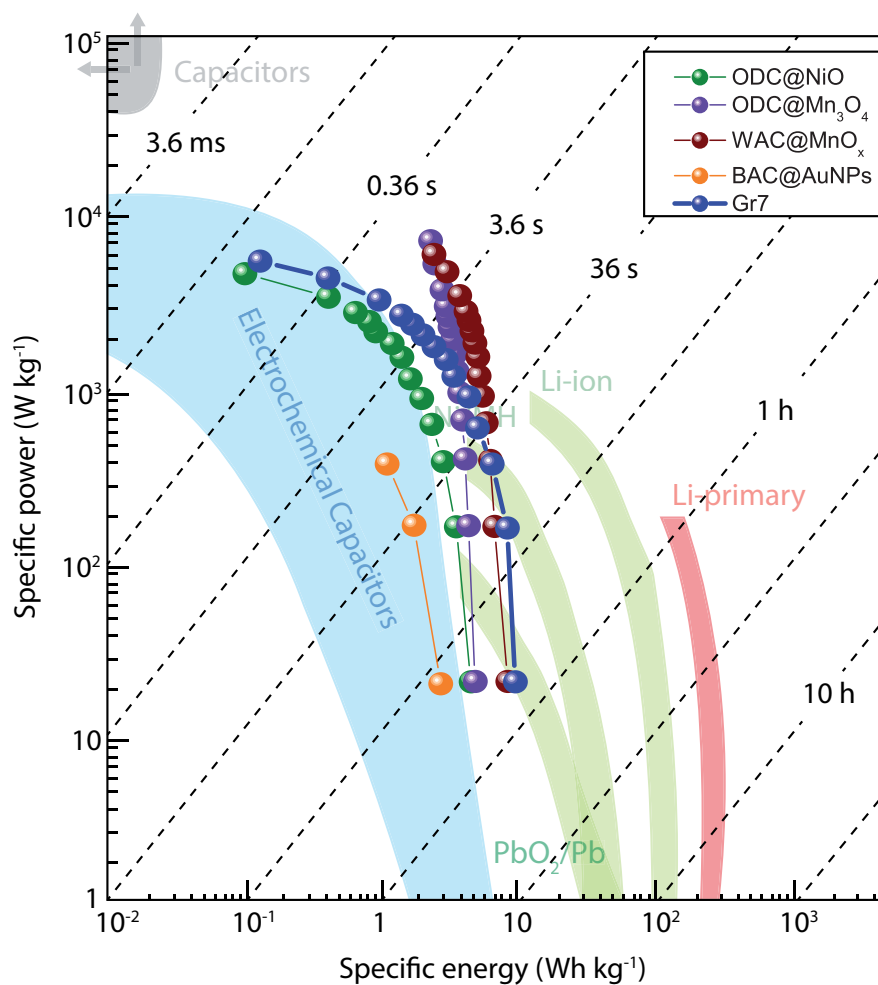


Figure 7.1: Actualized Ragone Plot including the materials studied in the present thesis (modified from Simon & Gogotsi, 2008).





# Appendix I: List of Publications

- Daniel Arenas Esteban, Andrés Guerrero Martínez, Javier Carretero González, Viola I. Birrs, L. Carlos Otero Díaz, David Ávila Brande. *Carbon-gold Nanograpes, a novel nanotunable electrode material for supercapacitors*, To be submitted.
- Daniel Arenas-Esteban, Esteban Urones-Garrote, Javier Carretero-González, Viola I. Birrs, L. Carlos Otero-Díaz, David Ávila-Brande. *Organometallic-derived carbon (ODC)-metal nano-oxide composites as improved electrode materials for supercapacitors*, Inorganic Chemistry, **2019**, submitted.
- Daniel Arenas-Esteban, David Ávila-Brande, L. C. Otero-Díaz, Esteban Urones-Garrote. *New Electrode Material Based on  $Mn_3O_4$  Nanoparticles Embedded in Organometallic-Derived Carbon (ODC)*, Microscopy and Microanalysis, **2016**, 22(S3), 1350-1351.
- Pedro García-González, Daniel Arenas-Esteban, David Ávila-Brande, Esteban Urones-Garrote, L. C. Otero-Díaz. *Nickelocene as precursor of microporous organometallic-derived carbon and nickel oxide-carbon nanocomposite*, Journal of Colloid and Interface Science, **2015**, 490 (105) 86282-86290.
- David Ávila-Brande, Daniel Arenas-Esteban, L. Carlos Otero Díaz, Andrés Guerrero-Martínez, Gloria Tardajos, Javier Carretero-González. *Activated nanoporous carbon-gold nanoparticle composite electrode with enhanced volumetric capacitance*, RSC Advances, **2015**, 5, 86282-86290.
- Joanna RESZCZYNSKA, Daniel ARENAS ESTEBAN, Maria GAZDA, Adriana ZALESKA. *Pr-Doped  $TiO_2$ . The effect of metal content on photocatalytic activity*, Physicochemical Problems of Mineral Processing. **2014**, 50(2), 515-525.



## Appendix II: List of Presentations

- 10<sup>th</sup> International Symposium on Metallic Multilayers, Madrid, Spain, 17<sup>th</sup>-21<sup>st</sup> June, 2019. **Poster Presentation:** *Itinerant room temperature ferromagnetism in Mn doped GaSb*. C. Pulzara-Mora, A. Pulzara-Mora, A. Forero-pico, M. Ayerbe-Salamanca, J. Marqués-Marchán, A. Asenjo, N. M. Nemes, D. Arenas, R. Sáez Puche.
- 1<sup>er</sup> Congreso sobre Materiales Multifuncionales para Jóvenes, Granada, Spain, 3<sup>rd</sup>-4<sup>th</sup> September, 2018. **Oral Presentation:** *Carbon Nanograpes: A New Carbon-Based Composite Material for Application as Electrode in Supercapacitors*. Daniel Arenas Esteban, David Ávila Brande, Javier Carretero Gonzalez, Viola Birss, L. Carlos Otero Díaz.
- CARBON 2018, Madrid, Spain, 1<sup>st</sup>-6<sup>th</sup> July, 2018.
  - **Oral Presentation:** *Carbon Nanograpes: A New Composite Material for Use as Electrode on Supercapacitors*. Daniel Arenas Esteban, David Ávila Brande, L. Carlos Otero Díaz.
  - **Poster Presentation:** *Composite Material Based on Organometallic-Derived Carbon and Metal Oxide Nanoparticles with Improved Electrochemical Performance as Electrode Material for Supercapacitors*. D. Arenas-Esteban, D. Ávila-Brande, E. Urones-Garrote, P. González-García, L.C. Otero-Díaz.
  - **Poster Presentation:** *Self-templated carbon materials from the chlorination of metal organic frameworks (MOFs)*. S. Martín Calvo, D. Arenas Esteban, P. Salcedo Abraira, P. Horcajada, D. Ávila Brande.
- QIES 2018 Tenerife (La Laguna), Spain, 17<sup>th</sup>-20<sup>th</sup> June, 2018.
  - **Oral Presentation:** *Carbon Nanograpes: a new carbon-based composite material for application as electrode in supercapacitors*. Daniel Arenas Esteban, David Ávila Brande, Javier Carretero Gonzalez, Viola Birss, L. Carlos Otero Díaz.
  - **Poster Presentation:** *Self-templated carbon materials from the chlorination of metal organic frameworks (MOFs)*. A. Cendoya Peñaranda, D. Arenas Esteban, P. Salcedo Abraira, P. Horcajada Cortés, J. Carretero Gonzalez, D. Ávila Brande.
- 51<sup>st</sup> Course: Electron Crystallography, Erice, Italy, 1<sup>st</sup>-10<sup>th</sup> June, 2018. **Poster presentation:** *Organometallic derived carbons (ODCs) as promising composite electrode materials in supercapacitors*. D. Arenas-Esteban, D. Ávila-Brande, L. Carlos Otero-Díaz and E. Urones-Garrote.




- European Material Research Society 2017 fall meeting, Warsaw University, Poland, 18<sup>th</sup>-21<sup>st</sup> September, 2017. **Oral Presentation:** *Nutshell Carbon-Manganese Oxide nanoparticles composites as electrode material on high performance supercapacitors.* Daniel Arenas-Esteban, Amalia Ode-Fernández, David Ávila-Brandé, L. Carlos Otero-Díaz.
- XXXVI Reunión Bial de la Sociedad Española de Química, Sitges, Spain, 25<sup>th</sup>-29<sup>th</sup> June 2017. **Oral Presentation:** *Composite Material Based on Nickelocene-Derived Carbon and NiO Nanoparticles with Improved Electrochemical Performance as Electrode Material for Supercapacitors.* D. Arenas-Esteban, D. Ávila-Brandé, E. Urones-Garrote, P. González-García, L.C. Otero-Díaz.
- 2016 Microscopy & Microanalysis, Columbus, Ohio, 24<sup>th</sup>-28<sup>th</sup> July, 2016. **Poster presentation:** *New electrode material based on Mn<sub>3</sub>O<sub>4</sub> nanoparticles embedded in organometallic-derived carbon (ODC).* D Arenas-Esteban, D Ávila-Brandé, LC Otero-Díaz, E Urones-Garrote.
- QIES 2016, Málaga (Torremolinos), Spain, 19<sup>th</sup>-22<sup>sd</sup>.
  - **Poster presentation:** *Desarrollo de nuevos materiales basados en carbono para su aplicación como electrodos en supercondensadores.* D. Ávila-Brandé, D. Arenas-Esteban, L. C. Otero-Díaz, A. Guerrero-Martínez, J. Carretero-González.
  - **Poster presentation:** *Composites carbón-nanoóxido metálico como potenciales materiales de electrodo en supercondensadores.* D. Arenas Esteban, D. Ávila Brandé, E. Urones Garrote, L. C. Otero Díaz.
- I Simposio Anual en Química Avanzada, Universidad Complutense de Madrid (UCM), Madrid, Spain, 13<sup>th</sup>-16<sup>th</sup>. **Oral presentation:** *Materiales de carbon nanoestructurado como electrodos en supercondensadores.* Daniel Arenas Esteban.
- European Material Research Society 2015 fall meeting, Warsaw University, Poland, 15<sup>th</sup>-18<sup>th</sup> September, 2015.
  - **Poster presentation: Phtalocianine derived Supercapacitors.** Ana Sánchez Grande, Daniel Arenas Esteban, David Ávila Brandé, Esteban Urones Garrote, Javier Carretero González, L. Carlos OteroDíaz.
  - **Oral presentation:** *Synthesis and characterization of carbon metal nanoparticle composite as electrode material for supercapacitors.* David Ávila Brandé, Daniel Arenas Esteban, L. Carlos Otero Díaz, Andrés Guerrero Martínez, Gloria Tardajos, Javier Carretero González.
- XXXV Bienal Real Sociedad Española de Química (RSEQ), A Coruña, Spain, 19<sup>th</sup>-23<sup>rd</sup> July, 2015. **Poster presentation:** *Electrodos de carbón nanoporoso decorados con nanopartículas de oro para su aplicación en supercondensadores.* D. Ávila Brandé, D. Arenas Esteban, G. Alepuz Fernández, L.C. Otero Díaz, A. Guerrero Martínez, G. Tardajos, J. Carretero González.

## Appendix III: CV



## Daniel Arenas Esteban

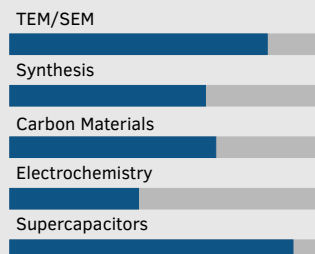
Chemist

-  3 May 1984
-  C/San Sebastián 9  
28902 Getafe, Madrid (SPAIN)
-  +34 695 467 316
-  darenasest@gmail.com

### About me

During my master and PhD studies I have acquired good skills on several synthesis techniques such as solid state, hydrothermal, chlorination, chemical activation, etc., as well as absorption isotherms and electrochemical characterization techniques. Nevertheless, electron microscopy techniques became a fundamental part of all my studies, acquiring valuable experience on morphological and compositional characterization of materials.

### Skills



(\*) [The skill scale is from 0 (Fundamental Awareness) to 6 (Expert).]

### Education

- since 2014 Ph.D. in Advanced Chemistry Universidad Complutense de Madrid  
*Composite materials based on disordered carbon as supercapacitor electrodes. Thesis directors: David Avila Brande, Luis Carlos Otero Diaz.*
- 2013-2014 Master in Science and Chemical Technology Universidad Complutense de Madrid  
*Introduction to Research in Nanoscience and Nanomaterials: Disordered Graphene Nanomaterials. Tutors: David Avila Brande, Luis Carlos Otero Diaz.*
- 2007-2013 B.Sc. in Chemistry Universidad Complutense de Madrid  
*Final Project: "Photocatalytic degradation of phenol under UV-Vis light by Pr-doped TiO<sub>2</sub>". Department of Chemical Technology of the Technical University of Gdansk, Poland. Tutors: Reszcyńska Joanna, Adriana Zaleska.*

### Publications

- 2016 *New Electrode Material Based on Mn<sub>3</sub>O<sub>4</sub> Nanoparticles Embedded in Organometallic-Derived Carbon (ODC).* D. Arenas-Esteban, D. Ávila-Brande, L. C. Otero-Díaz and E. Urones-Garrote. *Microscopy & Microanalysis*, 22, (S3) 1350-1351.
- 2015 *Nickelocene as precursor of microporous organometallic-derived carbon and nickel oxide-carbon nanocomposite.* Gonzalez-García, P., Arenas-Esteban, D., Ávila-Brande, D., Urones-Garrote, E., Otero-Díaz, L.C.. *Journal of Colloid and Interface Science*, 5, (105) 86282-86290.
- 2015 *Activated nanoporous carbon/gold nanoparticle composite electrode with enhanced volumetric capacitance.* David Ávila-Brande, Daniel Arenas-Esteban, L. Carlos Otero Díaz, Andrés Guerrero-Martínez, Gloria Tardajos, Javier Carretero-González. *RSC Advances*, 5, 86282-86290.
- 2014 *Pr-Doped TiO<sub>2</sub>. The effect of metal content on photocatalytic activity.* Joanna RESZCZYNSKA, Daniel ARENAS ESTEBAN, Maria GAZDA, Adriana ZALESKA. *Physicochemical Problems of Mineral Processing*, 20(2), 515-525.

### Experience

- since 2014 Research group member Universidad Complutense de Madrid  
Projects: MAT2017-84385-R Functional materials: magnetic and nanostructured.  
Project: PR26/16-3B-1 New 3D architectures of carbon-based nano-materials for application in energy storage systems.  
Project: MATERENER3CM Materials for energy: electrical, magnetic and superconducting

### Awards

- 2018 First prize in the modality of scientific photographs in the VI Scientific Disclosure Contest for photography entitled "Accomplices crystals" convened by the OTRI.
- 2017 Accessit in the field of Sciences and Engineering in the I Thesis Contest in 3 Minutes with the thesis "Disordered carbon materials for its application as electrodes in supercapacitors".
- 2015 Special Mention in the modality of scientific photographs in the VI Scientific Disclosure Contest for photography entitled "Carbon energy warehouse" convened by the OTRI.

**Congress communications**

- 2019 10<sup>th</sup> International Symposium on Metallic Multilayers, Madrid, Spain. Poster.
- 2018 1<sup>st</sup> Congreso sobre Materiales Multifuncionales para Jóvenes, Granada (Spain). Oral contribution.
- 2018 CARBON Congress, Madrid (Spain). Oral contribution.
- 2018 QIES 2018 La Laguna (Spain). Oral contribution.
- 2018 51<sup>st</sup> Course: Electron Crystallography, Erice, Italy. Poster.
- 2017 European Material Research Society fall meeting, Warsaw University of Technology (Poland). Oral contribution.
- 2017 XXXVI Reunión Bienal de la Sociedad Española de Química, Sitges (Spain). Oral contribution.
- 2016 I Simposio Anual en Química Avanzada, Universidad Complutense de Madrid 2016. Oral contribution.
- 2016 Microscopy & Microanalysis Meeting, Columbus (Ohio). Poster
- 2015 European Material Research Society fall meeting, Warsaw University of Technology (Poland). Poster
- 2015 XXXV Bienal Real Sociedad Española de Química (RSEQ) 2015, A Coruña (Spain). Poster

**Training courses**

- 2018 51<sup>st</sup> Course: Electron Crystallography 2018, Erice (Italia).
- 2017 RSEQ School of Spectroscopy, Segovia (Spain).
- 2016 Transmission electron microscopy: beyond the boundary of atomic resolution. Summer course, San Lorenzo del Escorial (Spain).
- 2016 Short course on MATERIALS FOR SUSTAINABLE ENERGY GENERATION, Universidad Politécnica de Madrid (Spain).
- 2015 IV Training Seminar on Radiological Protection, Universidad Complutense de Madrid.
- 2015 XV Workshops on Materials: Materials for Energy and Environmental Sustainability, Universidad Carlos III de Madrid.
- 2013 Computer courses: Microsoft Excel and Microsoft PowerPoint, Universidad Complutense de Madrid.

**Other merits**

- 2016-2019 Teaching Assistant in the Department of Inorganic Chemistry I, during the courses.
- 2018 Founding President of the ECS Madrid UCM Student Chapter.
- 2018 Organizer Member Contest: "Brain Wars: The future is in your hands".
- 2018 Organizer Member Workshop: "Experimental techniques one step from your laboratory".
- 2018 Organizer Member: II PhDay, Faculty of Chemistry, UCM.
- 2016 Organizing Member: I Annual Symposium in Advanced Chemistry. UCM.